ALMA MATER STUDIORUM · UNIVERSITÀ DI BOLOGNA

Scuola di Scienze
Dipartimento di Fisica e Astronomia
Corso di Laurea Magistrale in Fisica

Measurement of $D^0 - \overline{D}^0$ mixing parameters and search for CP violation with $D^0 \to K^{\pm}\pi^{\mp}$ decays at LHCb

Relatore:
Dott. Angelo Carbone

Correlatore:
Dott. Angelo Di Canto

Presentata da:
Michele Veronesi

Anno Accademico 2015/2016

優へ

Abstract

L'oscillazione dei mesoni neutri è una manifestazione del fatto che gli autostati di massa sono una combinazione lineare degli autostati di *flavour*. Siccome appartengono alla classe di processi a corrente neutra con cambiamento di flavour (*flavour changing neutral currents*), esse non possono essere mediate a livello *tree* nel Modello Standard e costituiscono quindi un banco di prova per testare in maniera indiretta contributi di nuova fisica ad alte energie attraverso processi virtuali. La violazione della simmetria di Carica-Parità può inoltre portare a diverse frequenze di oscillazione per particelle prodotte come mesoni o antimesoni. L'osservazione di asimmetrie di CP più grandi rispetto alle previsioni teoriche potrebbe quindi essere un segnale di fisica oltre il Modello Standard.

L'esperimento LHCb, situato sul *Large Hadron Collider* al CERN, è stato progettato per condurre misure di precisione di decadimenti di particelle con quark *beauty* e *charm*. Nel settore della fisica del charm, l'esperimento LHCb ha ottenuto importanti risultati, quali la prima osservazione delle oscillazioni dei mesoni neutri con charm (D^0) in una singola misura. In questo caso, le oscillazioni sono altamente soppresse e la violazione di CP è prevista essere molto piccola ($\sim \mathcal{O}(10^{-3})$) nel Modello Standard.

L'oggetto di questa tesi è la misura dei parametri di mixing e la ricerca della violazione di CP misurando i rapporti dei tassi di decadimento $D^0 \to K^+\pi^-$ su $D^0 \to K^-\pi^+$ in funzione del tempo e confrontandoli con i processi di di carica coniugati. I campioni di dati utilizzati in questa analisi sono stati registrati da LHCb durante il 2015 e il 2016 in collisioni protone-protone ad un'energia del centro di massa di 13 TeV, corrispondenti ad una luminosità integrata di $0.3\,\mathrm{fb}^{-1}$ e $1.6\,\mathrm{fb}^{-1}$, rispettivamente. Nel limite di conservazione di CP, i valori dei parametri di mixing ottenuti sono $x'^2 = (0.100 \pm 0.027 \pm 0.010) \times 10^{-3}$, $y' = (4.086 \pm 0.52 \pm 0.20) \times 10^{-3}$ e $R_D = (3.553 \pm 0.031 \pm 0.010) \times 10^{-3}$, dove la prima incertezza è statistica mentre la seconda è dovuta ad errori sistematici. Quando la misura è eseguita separatamente per D^0 e $\overline{D}^0$ non vi è evidenza di violazione di CP.

Abstract

The oscillations of neutral mesons are a manifestation of the fact that mass eigenstates are a superposition of flavour eigenstates. Since they belong to the class of *flavour changing neutral current* processes, they cannot be mediated at tree level in the Standard Model and thus constitute a powerful probe of new physics at high energy scales. Violation of the charge-parity symmetry may lead to different mixing rates for a particle produced as a meson or as an anti-meson. The observation of large CP asymmetries would also be a hint of physics beyond the Standard Model.

The LHCb experiment, located at the Large Hadron Collider at CERN, has been designed to perform precision measurements of the decays involving the *beauty* and charm quark. In charm physics, the LHCb experiment realized important measurements, such as the first observation of neutral charmed mesons oscillations (D^0) from a single measurement. Here, oscillations are suppressed and CP violation is expected to be tiny ($\sim \mathcal{O}(10^{-3})$) within the SM.

This thesis aims to measure the charm mixing parameters and search for CP violation with the decay-time-dependent ratio of $D^0 \to K^+\pi^-$ to $D^0 \to K^-\pi^+$ rates and charge conjugate processes. The datasets used in the analysis were recorded by LHCb during 2015 and 2016 in proton-proton collisions at $\sqrt{s} = 13\,\text{TeV}$, corresponding to an integrated luminosity of 0.3fb^{-1} and 1.6fb^{-1}, respectively. In the limit of CP symmetry, the mixing parameters are determined to be $x'^2 = (0.100 \pm 0.027 \pm 0.010) \times 10^{-3}$, $y' = (4.086 \pm 0.52 \pm 0.20) \times 10^{-3}$ and $R_D = (3.553 \pm 0.031 \pm 0.010) \times 10^{-3}$, where the first uncertainty is statistical and the second systematic, respectively. When the measurement is performed separately for D^0 and $\overline{D}^0$ mesons, there is no evidence for CP violation.

Contents

Introduction

Violation of the CP symmetry is one of the most intriguing topics in particle physics, having consequences both at the fundamental interactions level and at the cosmological scale. First of all, CP violating phenomena provide an operational distinction between matter and antimatter. The experimental CP asymmetries measured in the decays of K and B mesons are successfully explained by the Standard Model (SM) through a single complex phase in the quark-mixing matrix entering the charged weak interactions. However, this complex parameter arises from the Yukawa interactions between the Higgs and the quark fields, hence it is related to the generation of charged fermion masses, which is one of the less understood part of the theory. Moreover, when attempting for a dynamically generated baryogenesis, the baryon-antibaryon imbalance observed in the universe does not fit with the level of CP asymmetry measured in elementary particle interactions at accelerator experiments. For these reasons, it is important to search for new dynamics beyond the SM.

Among the available physical systems studied at particle accelerators, the D^0 mesons are one of the most promising probe of new physics at high energy scales and new interactions, since they are the only neutral meson system made of up-type quarks with sufficiently rich phenomenology, allowing for particle-antiparticle oscillations. They thus provide a unique testbed for the SM down-quark sector and its extensions through virtual effects, where new particles and interactions may provide an enhancement to the mixing rate and the size of CP violation. Observing CP asymmetries larger than SM expectations would be a clear sign of new physics.

Measuring mixing with "wrong-sign" (WS) $D^0 \to K^+\pi^-$ decays, proceeding either directly through doubly-Cabibbo-suppressed (DCS) decays or through mixing followed by Cabibbo-favoured (CF) decays $D^0 \to \overline{D}^0 \to K^+\pi^-$, offers several experimental advantages and is sensitive to both CP violation in mixing and in the interference between the CF and mixing amplitudes. In the first place, two-body hadronic decays, consisting of only two charged tracks, are reconstructed with higher efficiency with respect to multibody decays or other decays with neutral particles in the final state, such as a π^0 or a K^0_S. Moreover, the $D^{*\pm}$ production asymmetry, arising from the non-symmetric proton-proton (pp) collisions (with respect to antimatter), and any effects in decay time resolution and detector acceptance cancel out to a high level of approximation in the ratio with the "right-sign" (RS) $D^0 \to K^-\pi^+$ decay, proceeding mainly through CF amplitudes and having a trivial time-dependence.

In this thesis work, a measurement of the $D^0 - \overline{D}^0$ mixing parameters, separately for particles produced as a D^0 or $\overline{D}^0$ in the flavour conserving strong interaction $D^{*+} \to D^0\pi_s^+$ and charge conjugate decays, is reported. The analysis is performed using data corresponding to an overall $1.9\,\mathrm{fb}^{-1}$ of integrated luminosity recorded by the LHCb experiment during the LHC Run 2 between 2015 and 2016 with pp collisions. Approximately 140×10^6 RS decays and 573×10^3 WS decays from "prompt" D^{*+} decays are reconstructed, where the D^{*+} meson is produced in the primary pp interactions. The flavour at production is tagged using the charge of the low momentum ("soft") pion π_s produced in association with the D^0 meson in the D^{*+} decay, while $D^0 \to K^{\pm}\pi^{\mp}$ decays are only nearly flavour specific, and are thus classified as WS or RS depending on the charge of the decay products. CP violation is searched for by comparing the time dependent ratio of D^{*+} and D^{*-} tagged WS to RS decay rates.

This thesis is organized as follows. In Chap. 1 the phenomenology of charm mixing and CP violation is introduced, in relation with the underlying theory of the SM and the current experimental status. In Chap. 2 an overview of the experimental apparatus is given, with a stress on the specific subsystems which are relevant for the achievement of this analysis. In Chap. 3 the analysis strategy is described in detail.

Chapter 1

$D^0 - \overline{D}^0$ mixing and CP violation

This chapter explains the motivations for the measurement carried out in this thesis. To start with, the concept of discrete symmetries and their role in weak interactions is introduced with an historical overview. The theory of the Standard Model and the incorporation of CP violation into its framework is then presented. Subsequently, the formalism used to interpret the phenomenological aspects of meson mixing is developed and the experimental observables which are measured in the analysis can be defined.

1.1 Discrete symmetries

In physics there are three fundamental discrete symmetries. The parity (P), the reflection of space coordinates $\vec{x}$ into $-\vec{x}$, if conserved, implies that left and right are indistinguishable by physical processes. The time reversal (T), the inversion of time coordinates t into $-t$, represents the symmetry under the reversal of time, *i.e.* if conserved by the laws of physics it entails that the reversed process is also allowed. The charge conjugation (C), the conjugation of all internal quantum numbers (such as the electric charge), transforms a particle into its antiparticle (with equal mass, momentum and spin) and it implies, for every charged particle, the existence of an antimatter counterpart, while for a neutral particle this may coincide or differ by other internal quantum numbers.

A series of experiments conducted in the late 1950s [1, 2], prompted by a theoretical survey on the experimental data available at that time [3], showed that neither parity nor charge conjugation were respected by the weak interactions. Subsequently, the observation of a long lived neutral K meson (an eigenstate of the Hamiltonian with negative CP eigenvalue) decaying into two pions (a state of positive CP), demonstrated that also the combined CP symmetry was not conserved by the weak interactions governing the decay [4].

The violation of C and P symmetries is embedded in the theory of electroweak interactions through chiral couplings of the gauge bosons to the quark and lepton fields [5–8]. The incorporation of CP violation in this theoretical framework, as noticed by Kobayashi and Maskawa [9], could be done by introducing a single irremovable complex phase in the charged current weak interactions, the necessary condition for this to happen being the existence of a third generation of quarks, yet undiscovered at that time.

The success of this description comes on one side from the discoveries of the bottom [10] and top quarks [11, 12], confirming the existence of a third family of quarks, and on the other from the following observation of *direct* CP violation in the decay of a neutral K decaying to two charged and neutral pions [13, 14] and in the large CP asymmetries measured in the $B^0 - \overline{B}^0$ system [15, 16].

Although the theory proved to be extremely successful in explaining all the experimental data until now, the study of CP violation remains particularly interesting to probe the effects of possible new physics at high energies measuring the effects of virtual particles circulating in loops. Moreover, it is related to cosmology through the mechanism of baryogenesis, which offers the possibility to dynamically explain the imbalance of matter over antimatter in the universe. One fundamental ingredient to generate this asymmetry is that elementary particles violate CP and C [17]. Nevertheless, model calculations requires a larger level of CP violation than present in the Standard Model to reproduce the observed baryon-antibaryon asymmetry. Many extensions of the Standard Model introduce new sources of CP violation in form of large CP asymmetries, which may be revealed by precise measurements.

In particular, CP violation has not yet been observed in decays of neutral charmed mesons and is predicted to be of $\mathcal{O}(10^{-3})$ in the Standard Model. Furthermore, the neutral D is also the only meson-antimeson system made of up-type quark with mixing. This allows to uniquely test the up-quark sector of the Standard Model and its possible extensions through oscillations and interfering amplitudes. Experimental sensitivity has now reached a level of high precision measurements, thanks to the huge amount of charm decays recorded at the high center of mass energy of the LHC, exploiting the large $c\bar{c}$ production cross section at these energies.

1.2 CP violation in the Standard Model

The Standard Model of particle physics is a relativistic quantum field theory, describing all elementary particles and their interactions through the dynamical principle of local gauge invariance. The matter content is defined by chiral representations of fermionic and scalar fields with respect to the transformations of the symmetry group

$$G_{\text{SM}} = SU(3)_C \times SU(2)_L \times U(1)_Y. \tag{1.1}$$

where $SU(3)$ is the non-abelian group describing the strong forces, while $SU(2)_L \times U(1)_Y$ is the symmetry of the electroweak interactions unified in the Glashow-Weinberg-Salam model.

There are three fermion generations (copies of the same representation, which are assigned the same quantum numbers) each consisting of five representations of G_{SM}

$$Q^I_{Li}(3,2)_{+1/6}, \quad U^I_{Ri}(3,1)_{+2/3}, \quad D^I_{Ri}(3,1)_{-1/3}, \tag{1.2a}$$

$$L^I_{Li}(1,2)_{-1/2}, \quad E^I_{Ri}(1,1)_{-1} \tag{1.2b}$$

and one single scalar, the Higgs field

$$\phi(1,2)_{+1/2}. \tag{1.3}$$

The first number in brackets specifies triplets (the quarks) or singlets (the leptons and the scalar) of $SU(3)_C$, the second specifies doublets (left-handed fermions and the scalar) or singlets (right handed fermions) of $SU(2)_L$ while the subscript denotes the weak hypercharge of $U(1)_Y$. The superscript I indicates interaction eigenstates (states for which the interactions are diagonal and couple only fermions of the same generation) while the subindex $i = 1, 2, 3$ is the generation (or flavour) index.

The most general renormalizable Lagrangian density, consistent with the gauge symmetry (1.1) and particle content (1.2a), (1.2b), (1.3) may be divided into three parts

$$\mathcal{L}_{\text{SM}} = \mathcal{L}_{\text{kinetic}} + \mathcal{L}_{\text{Higgs}} + \mathcal{L}_{\text{Yukawa}} \tag{1.4}$$

The first part contains the kinetic terms of the matter and gauge fields, describing free propagation

$$\begin{aligned}\mathcal{L}_{\text{kinetic}} = &-\frac{1}{4}G_a^{\mu\nu}G_{a,\mu\nu} - \frac{1}{4}W_b^{\mu\nu}W_{b,\mu\nu} - \frac{1}{4}B^{\mu\nu}B_{\mu\nu}\\ &- i\bar{Q}_{Li}\not{D}Q_{Li} - i\bar{U}_{Ri}\not{D}U_{Ri} - i\bar{D}_{Ri}\not{D}D_{Ri} - i\bar{L}_{Li}\not{D}L_{Li} - i\bar{E}_{Ri}\not{D}E_{Ri}\\ &- (D^\mu\phi)^\dagger(D_\mu\phi)\end{aligned} \tag{1.5}$$

with $\not{D} = \gamma_\mu \partial^\mu$. The gauge fields are the eight gluons, the three weak interaction bosons and the single hypercharge boson

$$G_a^\mu(8,1)_0, \quad W_b^\mu(1,3)_0, \quad B^\mu(1,1)_0. \tag{1.6}$$

They have been introduced through the covariant derivative in order to maintain local gauge invariance

$$D^\mu = \partial^\mu + ig_s G_a^\mu L_a + igW_b^\mu T_b + ig'B^\mu Y \tag{1.7}$$

where the L_a's are the generators of $SU(3)_C$ (the 3×3 Gell-Mann matrices $\frac{1}{2}\lambda_a$ for triplets, 0 for singlets), with coupling constant g_s, the T_b's are the generators of $SU(2)_L$ (the 2×2 Pauli matrices $\frac{1}{2}\tau_b$ for doublets, 0 for singlets), with coupling constant g, and the Y's are the $U(1)_Y$ charges, with coupling constant g'. The corresponding gauge field strengths are

$$G_a^{\mu\nu} = \partial^\mu G_a^\nu - \partial^\nu G_a^\mu - g_s f_{abc} G_b^\mu G_c^\nu, \tag{1.8a}$$

$$W_a^{\mu\nu} = \partial^\mu W_a^\nu - \partial^\nu W_a^\mu - g\epsilon_{abc} W_b^\mu W_c^\nu, \tag{1.8b}$$

$$B^{\mu\nu} = \partial^\mu B^\nu - \partial^\nu B^\mu. \tag{1.8c}$$

where f_{abc} and ϵ_{abc} (the Levi-Civita symbol) are the $SU(3)_C$ and $SU(2)_L$ structure constants, respectively. The introduction of the covariant derivative (1.7) in the kinetic part of the Lagrangian (1.5) provides also the interaction terms between the matter and gauge fields. This part of the Lagrangian is always CP conserving, as the coupling constants are necessarily real.

The second part of the Lagrangian is the scalar potential

$$\mathcal{L}_{\text{Higgs}} = -\mu^2\phi^\dagger\phi - \lambda(\phi^\dagger\phi)^2 \tag{1.9}$$

with $\mu^2 < 0$ and $\lambda > 0$. The choice of the vacuum expectation value

$$\langle\phi\rangle = \begin{pmatrix} 0 \\ v/\sqrt{2} \end{pmatrix} \tag{1.10}$$

with $v/\sqrt{2} = \sqrt{2}\mu/\lambda^{1/2}$, breaks the electroweak symmetry spontaneously, leading to three massive gauge bosons, while leaving the color and electromagnetic symmetries conserved

$$G_{SM} \to SU(3)_C \times U(1)_{\mathrm{EM}} \tag{1.11}$$

to which it corresponds massless gauge bosons. Also this part of the Lagrangian, for a minimal scalar sector (namely, one single scalar), is CP conserving.

The last part of the Lagrangian contains the Yukawa interactions between the fermions and the scalar

$$\mathcal{L}_{\mathrm{Yukawa}} = Y^d_{ij}\bar{Q}_{Li}\phi D_{Rj} + Y^u_{ij}\bar{Q}_{Li}\tilde{\phi}U_{Rj} + Y^e_{ij}\bar{L}_{Li}\phi E_{Rj} + \mathrm{h.c.} \tag{1.12}$$

with $\tilde{\phi} = i\tau_2\phi^\dagger$, which are introduced in order to provide the mass terms of the quarks and charged leptons through the mechanism of spontaneous symmetry breaking. The Yukawa matrices Y^f_{ij} are general 3×3 matrices that connects fermions of different generations and may contain complex couplings which are CP violating.

When the scalar acquires a vacuum expectation value (1.10), the Yukawa interactions lead to the following mass terms for the quarks

$$\mathcal{L}^{\mathrm{quarks}}_{\mathrm{Yukawa}} = (M_d)_{ij}\bar{D}^I_{Li}D^I_{Rj} + (M_u)_{ij}\bar{U}^I_{Li}U^I_{Rj} + \mathrm{h.c.} \tag{1.13}$$

where the left-handed quark doublets have been decomposed into their components

$$Q^I_{Li} = \begin{pmatrix} U^I_{Li} \\ D^I_{Li} \end{pmatrix}. \tag{1.14}$$

The mass matrices $M_q = \frac{v}{\sqrt{2}}Y^q$ $(q = u, d)$ are however not diagonal in this basis. In order to find the mass basis, where M_q are diagonal, one as to diagonalize them with unitary matrices V_{qL} and V_{qR} such that

$$V_{qL}M_qV^\dagger_{qR} = M^{diag}_q \tag{1.15}$$

with M^{diag}_q diagonal and real. The quark mass eigenstates are then related to the interaction eigenstates as

$$q_{Li} = (V_{qL})_{ij}q^I_{Lj}, \quad q_{Ri} = (V_{qR})_{ij}q^I_{Rj}. \tag{1.16}$$

The charged current weak interactions, which in the interaction basis are diagonal, couple instead quarks of different generations in the mass basis

$$\mathcal{L}^{\mathrm{quarks}}_{W^\pm} = -\frac{g}{\sqrt{2}}\bar{U}_{Li}\gamma^\mu(V_{uL}V^\dagger_{dL})_{ij}D_{Lj}W^+_\mu + \mathrm{h.c.} \tag{1.17}$$

The down-type quarks in the mass basis are thus defined as a superposition of down-type quarks of the three generations, $D'_{Li} = (V_{\mathrm{CKM}})_{ij}D_{Lj}$, where the rotation matrix, $V_{\mathrm{CKM}} = V_{uL}V^\dagger_{dL}$, is the Cabibbo-Kobayashi-Maskawa quark mixing matrix [9, 18]

$$V_{\mathrm{CKM}} = \begin{pmatrix} V_{ud} & V_{us} & V_{ub} \\ V_{cd} & V_{cs} & V_{cb} \\ V_{td} & V_{ts} & V_{tb} \end{pmatrix} \tag{1.18}$$

1.2.1 The CKM matrix

The CKM matrix is a 3×3 unitary matrix. A generic $N \times N$ unitary matrix may be parametrized by means of $N(N-1)/2$ rotation angles and $N(N+1)/2$ complex phases. The phases of the quarks can be redefined without affecting the Lagrangian

$$\begin{cases} U \to e^{i\phi_U} U \\ D \to e^{i\phi_D} D \end{cases} \Longrightarrow V_{\text{CKM}} \to e^{-i\phi_U} V_{\text{CKM}} e^{i\phi_D}. \tag{1.19}$$

where $e^{i\phi_U}$ and $e^{i\phi_D}$ are diagonal matrices whose elements are pure phases. Since the overall phase does not lead to observable physical quantities, $2N-1$ unphysical phases can be removed from V_{CKM}. A generic $N \times N$ quark mixing matrix thus have $N(N-1)/2$ mixing angles and $(N-1)(N-2)/2$ physical complex phases. The minimum number of fermion generations in order to implement CP violation in the Standard Model through complex Yukawa couplings is thus three. The CKM matrix for 3 fermion generations therefore contains three mixing angles and one complex phase.

The presence of a complex phase in the Yukawa couplings of the quarks is a necessary but not sufficient condition for the manifestation of CP violation. By defining a parametrization invariant J_{CP} through the relation [19]

$$\text{Im}(V_{ij} V_{kl} V_{il}^* V_{kj}^*) = J_{CP} \sum_{m,n} \varepsilon_{ikm} \varepsilon_{jln}, \tag{1.20}$$

one finds that the necessary and sufficient condition to have CP violation in the Standard Model is the non vanishing of the quantity

$$\begin{aligned} \text{Im}(\det[Y^d Y^{d\dagger}, Y^u Y^{u\dagger}]) = 2(m_t^2 - m_c^2)(m_t^2 - m_u^2)(m_c^2 - m_u^2) \times \\ \times (m_b^2 - m_s^2)(m_b^2 - m_d^2)(m_s^2 - m_d^2) J_{CP}. \end{aligned} \tag{1.21}$$

The “Jarlskog invariant” is found to be $J_{CP} = s_{12} s_{13} s_{23} c_{12} c_{23} c_{13}^2 \sin\delta$ in the parametrization adopted by the PDG [20], where $s_{ij} = \sin\theta_{ij}$ and $c_{ij} = \cos\theta_{ij}$ are the sine and cosine of the mixing angles and δ is the CP violating phase. Hence, the following additional conditions must be satisfied, in order for CP violation to occur:

- Same-charge quarks should not be degenerate in mass

$$m_u \neq m_c \neq m_t, \quad m_d \neq m_s \neq m_b; \tag{1.22}$$

- The mixing angles should not be equal to 0 or $\pi/2$

$$\theta_{12},\ \theta_{13},\ \theta_{23} \neq 0,\ \frac{\pi}{2}; \tag{1.23}$$

- The CP violating phase should be different from 0 or π.

$$\delta \neq 0,\ \pi \tag{1.24}$$

The above conditions are related to the fact that if any of these would not be respected, one would be able to perform a unitary transformation on the quark fields so as to remove the complex phase.

The magnitudes of the elements of the CKM matrix may be determined through tree-level processes connecting different quark generations, such as nuclear beta decay or semileptonic decays of flavoured mesons. Only the values of $|V_{td}|$ and $|V_{ts}|$ are extracted from the measurement of $B^0 - \overline{B}^0$ and $B^0_s - \overline{B}^0{}_s$ oscillations, which are mediated by box diagrams containing virtual top quarks. The current knowledge of the values $|V_{ij}|$ is [20]

$$|V_{\mathrm{CKM}}| = \begin{pmatrix} 0.97434^{+0.00011}_{-0.00012} & 0.22506 \pm 0.00050 & 0.00357 \pm 0.00015 \\ 0.22492 \pm 0.00050 & 0.97351 \pm 0.00013 & 0.0411 \pm 0.0013 \\ 0.00875^{+0.00032}_{-0.00033} & 0.0403 \pm 0.0013 & 0.99915 \pm 0.00005 \end{pmatrix}. \quad (1.25)$$

The observed hierarchy $|V_{ub}| \ll |V_{cb}| \ll |V_{us}|, |V_{cd}| \ll 1$ allows to expand V_{CKM} in powers of $\lambda = |V_{us}|$ (the sine of the Cabibbo angle), which, up to $\mathcal{O}(\lambda^3)$, is given by [21]

$$V_{\mathrm{CKM}} = \begin{pmatrix} 1 - \frac{1}{2}\lambda^2 & \lambda & A\lambda^3(\rho - i\eta) \\ -\lambda & 1 - \frac{1}{2}\lambda^2 & A\lambda^2 \\ A\lambda^3(1 - \rho - i\eta) & -A\lambda^2 & 1 \end{pmatrix}, \quad (1.26)$$

where the dependence on three real and one imaginary parameters has been made explicit by the four real quantities λ, A, ρ and η. The above parametrization, is very useful for phenomenology, as it will be shown in the next section, and let one immediately recognize the special features of this matrix: it is almost diagonal, it is almost symmetric and its elements get smaller the more one moves away from the diagonal.

1.2.2 Unitarity triangles

The six off-diagonal relations coming from the unitarity of the CKM matrix, $V_{\mathrm{CKM}}V^\dagger_{\mathrm{CKM}} = \mathbf{1}$, may be represented as triangles in the complex (ρ, η) plane

$$\underbrace{V^*_{ud}V_{us}}_{\mathcal{O}(\lambda)} + \underbrace{V^*_{cd}V_{cs}}_{\mathcal{O}(\lambda)} + \underbrace{V^*_{td}V_{ts}}_{\mathcal{O}(\lambda^5)} = 0, \quad (1.27a)$$

$$\underbrace{V_{ud}V^*_{cd}}_{\mathcal{O}(\lambda)} + \underbrace{V_{us}V^*_{cs}}_{\mathcal{O}(\lambda)} + \underbrace{V_{ub}V^*_{cb}}_{\mathcal{O}(\lambda^5)} = 0, \quad (1.27b)$$

$$\underbrace{V^*_{us}V_{ub}}_{\mathcal{O}(\lambda^4)} + \underbrace{V^*_{cs}V_{cb}}_{\mathcal{O}(\lambda^2)} + \underbrace{V^*_{ts}V_{tb}}_{\mathcal{O}(\lambda^2)} = 0, \quad (1.27c)$$

$$\underbrace{V_{td}V^*_{cd}}_{\mathcal{O}(\lambda^4)} + \underbrace{V_{ts}V^*_{cs}}_{\mathcal{O}(\lambda^2)} + \underbrace{V_{tb}V^*_{cb}}_{\mathcal{O}(\lambda^2)} = 0, \quad (1.27d)$$

$$\underbrace{V_{td}V^*_{ud}}_{(1-\rho-i\eta)A\lambda^3} + \underbrace{V_{ts}V^*_{us}}_{-A\lambda^3} + \underbrace{V_{tb}V^*_{ub}}_{(\rho+i\eta)A\lambda^3} = 0, \quad (1.27e)$$

$$\underbrace{V_{ud}V^*_{ub}}_{(\rho+i\eta)A\lambda^3} + \underbrace{V_{cd}V^*_{cb}}_{-A\lambda^3} + \underbrace{V_{td}V^*_{tb}}_{(1-\rho-i\eta)A\lambda^3} = 0. \quad (1.27f)$$

All the triangles have the same area, equal to $J_{CP}/2$, where, in the Wolfenstein parametrization (1.26), $J_{CP} \sim \lambda^6 A^2 \eta$. In particular, the last two expressions represent triangles with sides of the same order of magnitude, *i.e.* their angles are naturally large. The fact that these triangles do not degenerate into a line represents the occurrence of CP violation. Large angles thus correspond to large measurable CP asymmetries. The triangle in the last expression (1.27f), called the Unitarity Triangle (UT), features angles given by

$$\alpha = \arg\left(-\frac{V_{td}V_{tb}^*}{V_{ud}V_{ub}^*}\right) \simeq \arg\left(-\frac{1-\rho-i\eta}{\rho+i\eta}\right), \tag{1.28a}$$

$$\beta = \arg\left(-\frac{V_{cd}V_{cb}^*}{V_{td}V_{tb}^*}\right) \simeq \arg\left(\frac{1}{1-\rho-i\eta}\right), \tag{1.28b}$$

$$\gamma = \arg\left(-\frac{V_{ud}V_{ub}^*}{V_{cd}V_{cb}^*}\right) \simeq \arg(\rho+i\eta), \tag{1.28c}$$

when its sides are divided by $V_{cd}V_{cb}^*$. In Fig. 1.1 is reported a graphic representation of the UT, along with experimental constraints. These come from:

$|V_{ub}/V_{cb}|$: The magnitudes of the matrix elements V_{ub} and V_{cb} are measured in branching fractions of semileptonic $b \to ul\bar{\nu}$ and $b \to cl\bar{\nu}$ decays, respectively. Their ratio is proportional to $\sqrt{\rho^2+\eta^2}$ and constraints the side of the triangle between the α and γ angles, providing a circular allowed region in the (ρ,η) plane;

$\Delta m_d/\Delta m_s$: The measurement of the mass splittings in the $B^0 - \overline{B}^0$ and $B_s^0 - \overline{B}^0{}_s$ systems, through the observed oscillatory behaviour between particle and antiparticle states, constraints the other side of the triangle, their ratio being proportional to $((1-\rho)^2+\eta^2)$;

ϵ_K: The value of ϵ_K measured in $K^0 - \overline{K}^0$ mixing is proportional to $\eta(1-\rho)$, giving an hyperbolic band in (ρ,η) which constraints the position of the apex;

$\sin 2\beta$: This observable is given by the amplitude of the time dependent oscillatory CP asymmetry in $B \to J/\psi K$ decays and constraints the angle β;

α: This angle is measured through time dependent CP asymmetries in $b \to u\bar{u}d$ transitions, such as $B \to \pi\pi$, $\rho\pi$ and $\rho\rho$ decays;

γ: The measurement of γ can be accomplished through the analysis of $B \to DK$ decays.

The constraints on the parameters of the unitarity triangle play a key role in testing the validity of the CKM picture of CP violation. The consistency between different measurements confirms that CP violation in W-mediated flavour changing processes is dominated by the Kobayashi-Maskawa phase.

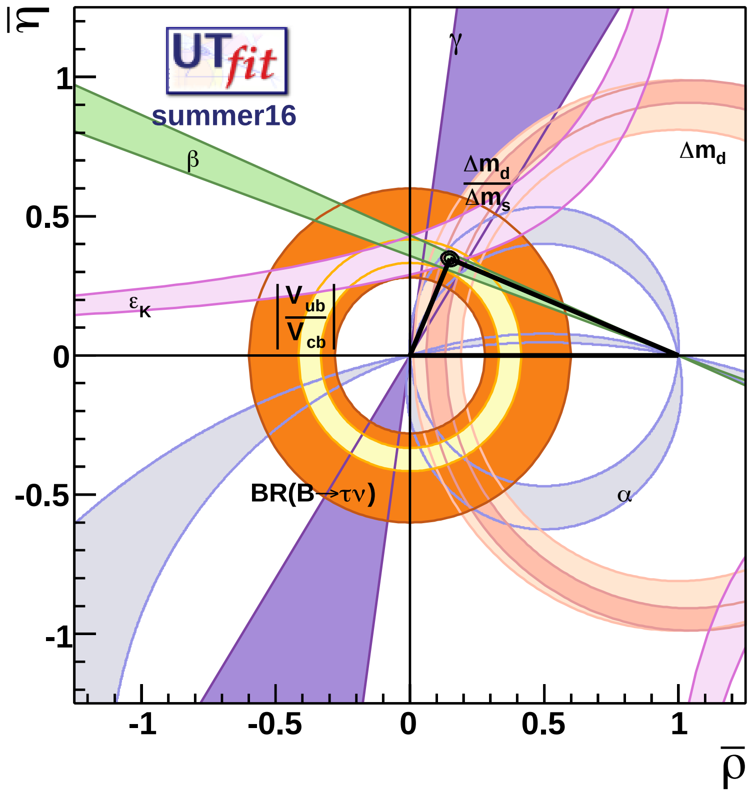

Figure 1.1: Constraints to the unitarity triangle in the ($\bar{\rho}$,$\bar{\eta}$) plane [22].

1.3 Phenomenology of neutral meson mixing

The phenomenology of neutral flavoured mesons is particularly rich because of the possibility of interfering decay and mixing amplitudes. The formalism for the four neutral mesons systems K^0, B^0, B_s^0 and D^0 is the same and their phenomenology differ because of the disparate balance between decay rates and oscillations, as given by their mass and lifetime splitting.

One defines the decay amplitudes of a weakly decaying hadron M and its CP conjugate $\bar{M}$, to a multi-particle final state f and its CP conjugate $\bar{f}$, as

$$\begin{aligned} A_f &= \langle f \,|\, \mathcal{H} \,|\, M \rangle\,, \quad & \bar{A}_f &= \langle f \,|\, \mathcal{H} \,|\, \bar{M} \rangle\,, \\ A_{\bar{f}} &= \langle \bar{f} \,|\, \mathcal{H} \,|\, M \rangle\,, \quad & \bar{A}_{\bar{f}} &= \langle \bar{f} \,|\, \mathcal{H} \,|\, \bar{M} \rangle\,, \end{aligned} \tag{1.29}$$

where $\mathcal{H}$ is the decay Hamiltonian. There are only two types of phases that may appear in A_f and its CP conjugate amplitude $\bar{A}_{\bar{f}}$. "Weak phases" come from complex parameters entering the Lagrangian that contributes to the amplitude. Thus, they will appear with opposite signs in the CP conjugate amplitude. These phases occur within the SM only in the couplings of the $W^{\pm}$ bosons, as described earlier, hence their name. On the other hand, "strong phases", due to rescattering in intermediate on-shell states, may be present even when the Lagrangian is real. Since they are generated by the CP conserving strong interaction, these phases have the same sign in A_f and $\bar{A}_{\bar{f}}$. The phase of a single term contributing in the decay amplitude is convention dependent, while only the difference between two phases in different terms of A_f is physically meaningful, as an overall phase rotation of the amplitude will have no observable consequences.

Writing down each contribution of A_f and $\bar{A}_{\bar{f}}$ in terms of its magnitude $|A_i|$, weak phase ϕ_i and strong phase δ_i

$$A_f = \sum_i |A_i| e^{i(\delta_i + \phi_i)}, \quad \bar{A}_{\bar{f}} = \sum_i |A_i| e^{i(\delta_i - \phi_i)} \tag{1.30}$$

one finds that the necessary condition in order for CP violation to occur in the decay, when $|A_f| \neq |\bar{A}_{\bar{f}}|$, is to have at least two terms with different weak and strong phases, so that the interference term

$$|A_f|^2 - |\bar{A}_{\bar{f}}|^2 = -2 \sum_{ij} |A_i||A_j| \sin(\delta_i - \delta_j) \cos(\phi_i - \phi_j) \tag{1.31}$$

does not vanish.

Neutral flavoured mesons, M^0 and $\bar{M}^0$, are eigenstates of the strong interaction, which conserves flavour, and are usually produced in pair in hadronic collisions. As first noted by Gell-Mann and Pais [23], the flavour eigenstates can be regarded as a superposition of the physical states, with different mass and lifetimes. In addition, basic quantum mechanics allows them to develop a component with opposite flavour during free time propagation. The time evolution of the meson-antimeson system, for times t larger than the typical strong interaction scale, can be described by the approximate Schrödinger equation

$$i \frac{\partial}{\partial t} \begin{pmatrix} M^0(t) \\ \bar{M}^0(t) \end{pmatrix} = \left[\mathbf{M} - \frac{i}{2} \mathbf{\Gamma} \right] \begin{pmatrix} M^0(t) \\ \bar{M}^0(t) \end{pmatrix} \tag{1.32}$$

with effective Hamiltonian $\mathcal{H}_{eff} = \mathbf{M} - i\mathbf{\Gamma}/2$ given by the two 2×2 hermitian matrices $\mathbf{M}$ and $\mathbf{\Gamma}$

$$\mathbf{M} = \begin{pmatrix} M_{11} & M_{12} \\ M_{12}^* & M_{22} \end{pmatrix}, \quad \mathbf{\Gamma} = \begin{pmatrix} \Gamma_{11} & \Gamma_{12} \\ \Gamma_{12}^* & \Gamma_{22} \end{pmatrix} \tag{1.33}$$

whose off-diagonal elements are associated with flavour changing $M^0 \to \bar{M}^0$, $\bar{M}^0 \to M^0$ transitions via off-shell (dispersive) and on-shell (absorptive) intermediate states, respectively, while their diagonal elements describes the flavour conserving time development. Moreover, they must satisfy $M_{11} = M_{22}$ and $\Gamma_{11} = \Gamma_{22}$ in order to comply with CPT invariance.

The physical states are obtained by diagonalizing the Hamiltonian and may be expressed as a linear superposition of the strong interaction eigenstates

$$|M_{L,H}\rangle = p \left| M^0 \right\rangle \pm q \left| \bar{M}^0 \right\rangle \tag{1.34}$$

where L and H denotes the light and heavy state, respectively. The complex parameters p and q must satisfy the normalization condition $|p|^2 + |q|^2 = 1$ and the solution of the eigenvalue problem yields

$$\left(\frac{q}{p} \right)^2 = \frac{M_{12}^* - (1/2)\Gamma_{12}^*}{M_{12} - (1/2)\Gamma_{12}}. \tag{1.35}$$

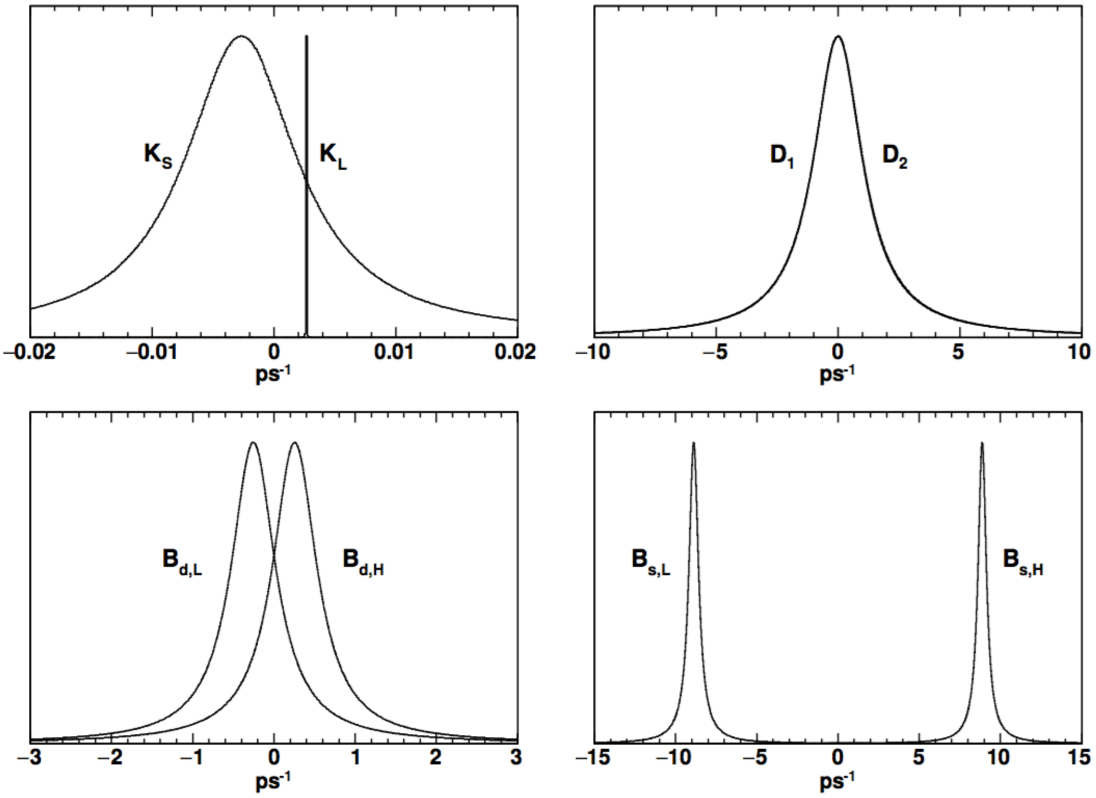

Figure 1.2: Mass and decay width differences for the four neutral meson systems. From [24].

The corresponding eigenvalues are

$$\lambda_{L,H} = \left(M_{11} - \frac{i}{2}\Gamma_{11}\right) \pm \frac{q}{p}\left(M_{12} - \frac{i}{2}\Gamma_{12}\right) \equiv m_{L,H} - \frac{i}{2}\Gamma_{L,H}, \tag{1.36}$$

where the real and imaginary parts have been identified as the masses $m_{L,H}$, with $m_H > m_L$ by definition, and decay widths $\Gamma_{L,H}$ of the two eigenstates, respectively. In Fig. 1.2 the difference in mass and decay width for the four neutral meson systems is displayed, with the values of the parameters as reported by the PDG [20]. In particular, for the neutral K, the two physical states are well defined by their difference in lifetime. Hence, it is possible to obtain a pure long-lived state after waiting that all the short lived component has decayed. This allowed the discovery of CP violation in [4], since in the approximation of CP commuting with the Hamiltonian, the long-lived neutral K would be a CP-odd state. Conversely, B meson mass eigenstates are characterized by their mass separation. This is particularly relevant for the B_s, where large mass splitting leads to fast oscillations, as explained later. No sizeable difference in mass nor in lifetime is present in the D^0 mass eigenstates, which approximately coincide with the eigenstates of CP.

Using the effective Hamiltonian approximation of Eq. (1.32), one obtains, for an initially pure $|M^0\rangle$ and $|\bar{M}^0\rangle$ state, the following time evolutions

$$|M^0_{phys}(t)\rangle = g_+(t)\,|M^0\rangle - (q/p)g_-(t)\,|\bar{M}^0\rangle\,, \tag{1.37a}$$

$$|\bar{M}^0_{phys}(t)\rangle = g_+(t)\,|\bar{M}^0\rangle - (p/q)g_-(t)\,|M^0\rangle\,, \tag{1.37b}$$

where

$$g_{\pm}(t) \equiv \frac{1}{2}\left(e^{-im_H t-\frac{1}{2}\Gamma_H t} \pm e^{-im_L t-\frac{1}{2}\Gamma_L t}\right). \tag{1.38}$$

represents the time dependent probability to conserve flavour (+) or to oscillate into the opposite one (−). The time dependent oscillation probabilities are thus given by

$$P(M^0_{phys}(t) \to \bar{M}^0) = \frac{1}{2}\left|\frac{q}{p}\right|^2 e^{-\Gamma t}(\cosh(y\Gamma t) - \cos(x\Gamma t)) \tag{1.39a}$$

$$P(\bar{M}^0_{phys}(t) \to M^0) = \frac{1}{2}\left|\frac{p}{q}\right|^2 e^{-\Gamma t}(\cosh(y\Gamma t) - \cos(x\Gamma t)) \tag{1.39b}$$

while the probability to conserve flavour is

$$P(M^0_{phys}(t) \to M^0) = P(\bar{M}^0_{phys}(t) \to \bar{M}^0) = \frac{1}{2}e^{-\Gamma t}(\cosh(y\Gamma t) + \cos(x\Gamma t)). \tag{1.40}$$

and the mixing parameters are defined as

$$x \equiv \frac{\Delta m}{\Gamma}, \quad y \equiv \frac{\Delta\Gamma}{2\Gamma}, \tag{1.41}$$

where $\Delta m \equiv m_H - m_L$ and $\Delta\Gamma \equiv \Gamma_H - \Gamma_L$ are the mass and width splitting, while $\Gamma \equiv (\Gamma_H + \Gamma_L)/2$ is the average decay width. The oscillatory term is governed by the mass difference of the physical states, encoded in x, while difference in decay widths determines a non oscillating change of the exponential decay through y. CP is violated in mixing if the probability of the process $M^0 \to \bar{M}^0$ is different from $\bar{M}^0 \to M^0$. This happen when $|q/p| \neq 1$, as manifest in Eqs. (1.39a).

As shown in Fig. 1.3, the phenomenology of neutral particle oscillations varies in the four neutral meson systems, due to the differences in mass and in lifetime scales. Oscillations in the neutral kaons were the first to be established [25], and these feature sizeable differences both in mass and decay width, with mixing parameter of $\mathcal{O}(1)$. Considerable $B^0 - \overline{B}^0$ oscillations came somehow unexpected when they were first measured [26], since the large mass difference of the physical B state, giving $x \sim \mathcal{O}(1)$, is enhanced in virtual loop diagrams involving the heavy top quark, whose mass was then still unknown. On the other hand, the contributions from intermediate on-shell state is here suppressed by the structure of the CKM matrix, giving $y \sim \mathcal{O}(10^{-3})$. Even faster mixing rate were observed in the B^0_s system [27], due to size of the element V_{ts}, where $x \sim 25$ required high proper time resolution to be measured. Finally, evidence of $D^0 - \overline{D}^0$ mixing came with the combination of BaBar, Belle and CDF results [28–30]. Low mixing rates are due to small CKM elements in loops containing the b quark and GIM suppression for the d and s quarks contributions. Long distance effects due to intermediate on-shell states may ultimately dominate. Mixing parameters are therefore of $\mathcal{O}(10^{-3})$. Hence, huge data samples are needed in order to perform analysis with the required sensitivity. Only recently, observation of $D^0 - \overline{D}^0$ oscillations from one single measurement were reported by LHCb [31].

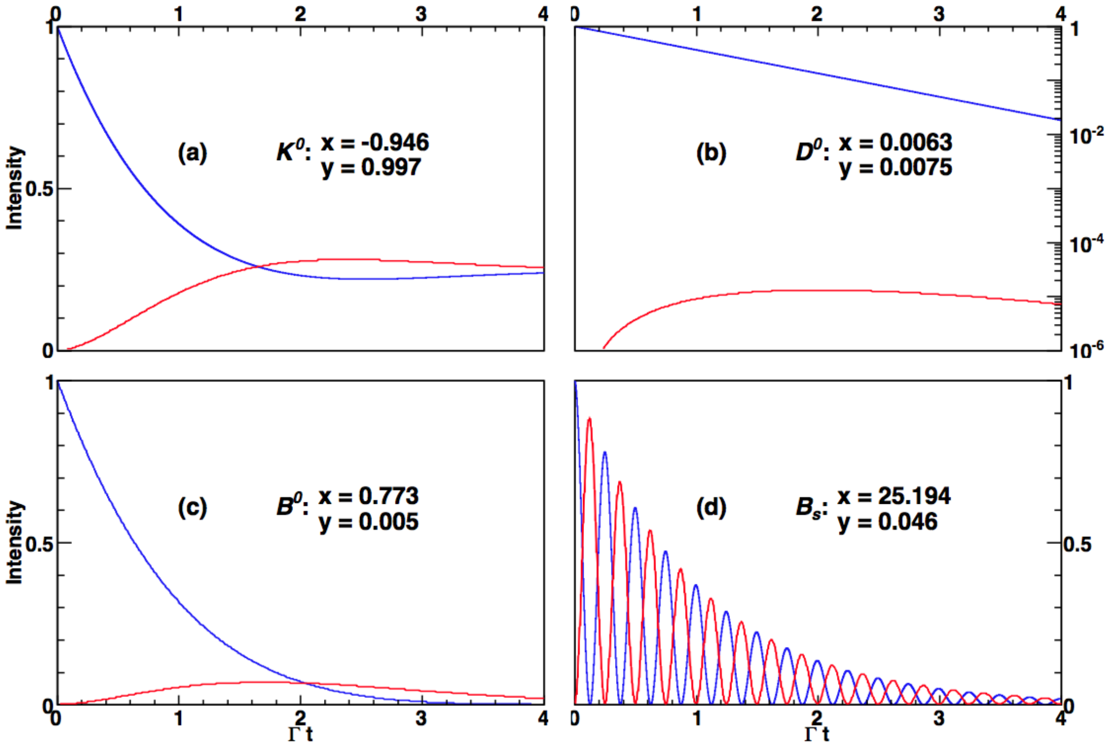

Figure 1.3: Mixed (red) and unmixed (blue) intensities for an initially pure K^0 (a), D^0 (b), B^0 (c) and B^0_s (d) state, as a function of the number of lifetimes (Γt), assuming $|q/p| = 1$. From [32].

Considering decays to a final state f, one obtains for the time dependent decay rates [33]

$$\begin{aligned}\frac{d\Gamma}{dt}(M^0_{phys}(t) \to f) = \frac{e^{-\Gamma t}}{2}|A_f|^2[&(1-|\lambda_f|^2)\cos(x\Gamma t) + (1+|\lambda_f|^2)\cosh(y\Gamma t) \\ &- 2\mathrm{Im}(\lambda_f)\sin(x\Gamma t) + 2\mathrm{Re}(\lambda_f)\sinh(y\Gamma t)],\end{aligned} \tag{1.42a}$$

$$\begin{aligned}\frac{d\Gamma}{dt}(\bar{M}^0_{phys}(t) \to f) = \frac{e^{-\Gamma t}}{2}|\bar{A}_f|^2[&(1-|\lambda_f^{-1}|^2)\cos(x\Gamma t) + (1+|\lambda_f^{-1}|^2)\cosh(y\Gamma t) \\ &- 2\mathrm{Im}(\lambda_f^{-1})\sin(x\Gamma t) + 2\mathrm{Re}(\lambda_f^{-1})\sinh(y\Gamma t)]\end{aligned} \tag{1.42b}$$

with

$$\lambda_f \equiv \frac{q}{p}\frac{\bar{A}_f}{A_f} \quad \text{and} \quad \lambda_{\bar{f}} \equiv \frac{q}{p}\frac{\bar{A}_{\bar{f}}}{A_{\bar{f}}}. \tag{1.43}$$

Decays to CP conjugate final states $\bar{f}$ are obtained by the substitutions $A_f \to A_{\bar{f}}$, $\bar{A}_f \to \bar{A}_{\bar{f}}$ and $\lambda_f \to \lambda_{\bar{f}}$ in the above equations. The terms proportional to $|A_f|^2$ or $|\bar{A}_f|^2$ are related to decays without net $M^0 \leftrightarrow \bar{M}^0$ oscillations, while those proportional to $|\lambda_f|^2$ or $|\lambda_f^{-1}|^2$ are associated with decays following a net oscillation. The $\sinh(y\Gamma t)$ and $\sin(x\Gamma t)$ terms are instead associated with the interference between the two cases. One may thus realize that CP violation can also happen in the interference of a decay following a net oscillation and one without mixing to a common final state. This occurs when the parameter λ in (1.43) carries a complex phase different from zero.

1.3.1 CP asymmetries

CP violating observables in meson decays may be expressed as combinations of the decay amplitudes in Eq (1.29) and, for neutral mesons, the parameters q and p of Eq. (1.34). While in charged mesons decays they depend only on the ratio $|\bar{A}_{\bar{f}}/A_f|$, in neutral mesons they may depend additionally on $|q/p|$ and λ_f of Eq. (1.43), because of the possibility of mixing and interference in the decay process. Eventually, one distinguishes three types of CP violating effects in meson decays:

(i) CP violation in decay, occurring when

$$|\bar{A}_{\bar{f}}/A_f| \neq 1. \tag{1.44}$$

In charged mesons and all baryons decays, this is the only source of CP violation. One may define the observable CP asymmetry as

$$\mathcal{A}_{CP} \equiv \frac{\Gamma(\bar{M} \to \bar{f}) - \Gamma(M \to f)}{\Gamma(\bar{M} \to \bar{f}) + \Gamma(M \to f)} = \frac{|\bar{A}_{\bar{f}}/A_f|^2 - 1}{|\bar{A}_{\bar{f}}/A_f|^2 + 1}. \tag{1.45}$$

(ii) CP violation in mixing, occurring when

$$|q/p| \neq 1. \tag{1.46}$$

This is the only source of CP violation in charged current semileptonic decays, where $f = l^+X$, $|A_f| = |\bar{A}_{\bar{f}}|$ and $A_{\bar{f}} = \bar{A}_f = 0$. One may define an asymmetry as

$$\begin{aligned}\mathcal{A}_{CP}(t) &\equiv \frac{d\Gamma(\bar{M}^0_{phys}(t) \to f)/dt - d\Gamma(M^0_{phys}(t) \to \bar{f})/dt}{d\Gamma(\bar{M}^0_{phys}(t) \to f)/dt + d\Gamma(M^0_{phys}(t) \to \bar{f})/dt} \\ &= \frac{1 - |q/p|^4}{1 + |q/p|^4}\end{aligned} \tag{1.47}$$

where the final state can only be reached through oscillations.

(iii) CP violation in the interference between mixing and decay, occurring when

$$\mathrm{Im}(\lambda_f) \neq 0. \tag{1.48}$$

This form of CP violation may be observed in decays to final CP eigenstates f_{CP}, by means of the following asymmetry

$$A_{f_{CP}}(t) \equiv \frac{d\Gamma(\bar{M}^0_{phys}(t) \to f_{CP})/dt - d\Gamma(M^0_{phys}(t) \to f_{CP})/dt}{d\Gamma(\bar{M}^0_{phys}(t) \to f_{CP})/dt + d\Gamma(M^0_{phys}(t) \to f_{CP})/dt}. \tag{1.49}$$

1.4 Mixing and CP violation in neutral charmed mesons

The $D^0 - \overline{D}^0$ system oscillates at a small rate. Mixing receives contributions from both box diagrams, proceeding through a double weak boson exchange (short distance contributions, Fig. 1.4 left), and from intermediate on shell states, which are accessible to both D^0 and $\overline{D}^0$ states (long distance contributions, Fig. 1.4 right). The long range contributions are affected by large theoretical uncertainties, due to non perturbative QCD effects, and may ultimately dominate the mixing rate. Non precise SM predictions of D^0 mixing make it difficult to identify potential enhancement due to non-SM physics. Nevertheless, it is essential to constrain the mixing parameters in order to deepen the understanding of SM dynamics. CP violation in charm mixing is predicted to be of $\mathcal{O}(10^{-3})$. Thus, the observation of CP violating observables $\gg \mathcal{O}(10^{-2})$ would be a hint of new physics.

1.4.1 "Wrong-Sign" $D^0 \to K^+\pi^-$ decays

The measurement $D^0 - \overline{D}^0$ mixing and CP violation parameters can be performed by comparing the time dependent ratio of $D^0 \to K^+\pi^-$ to $D^0 \to K^-\pi^+$ decay rates with corresponding ratio for the charge conjugate processes. The $D^0 \to K^-\pi^+$ decay is referred to as "right-sign" (RS) decay and mainly proceeds through a Cabibbo-favoured (CF) amplitude. On the other hand, the $D^0 \to K^+\pi^-$ decay, referred to as "wrong-sign" (WS), arises from the interference of the doubly Cabibbo-suppressed (DCS, proportional to $\sin^2\theta_C$) $D^0 \to K^+\pi^-$ decay amplitude and the CF $\overline{D}^0 \to K^+\pi^-$ decay amplitude following a $D^0 \to \overline{D}^0$ oscillation, each with similar magnitude.

The decay amplitudes for tree level dominated decays can in general be written as

$$\begin{aligned} A_f &= A^T_f e^{+i\phi^T_f}, \quad & A_{\bar f} &= A^T_{\bar f} e^{i(\delta_f + \phi^T_{\bar f})}, \\ \bar A_{\bar f} &= A^T_f e^{-i\phi^T_f}, \quad & \bar A_f &= A^T_{\bar f} e^{i(\delta_f - \phi^T_{\bar f})}, \end{aligned} \tag{1.50}$$

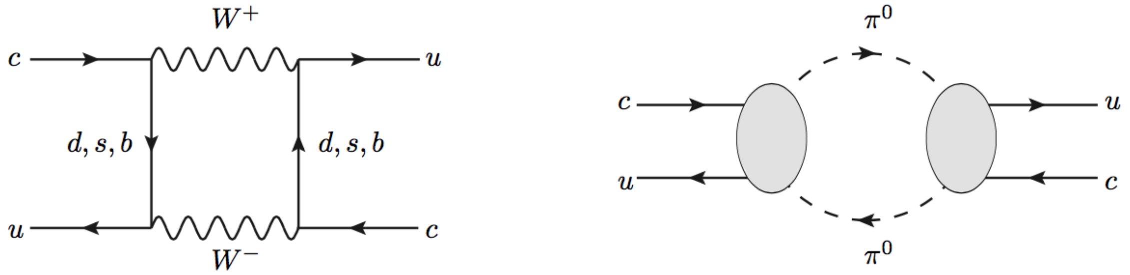

Figure 1.4: Feynman diagrams describing the short (left) and long (right) distance contributions to $D^0 - \overline{D}^0$ mixing. The former proceeds through a double W boson exchange, where all possible down-type quarks can circulate in the loop, while the latter flows through intermediate on-shell meson states in common to the D^0 and $\overline{D}^0$ state.

where A_f^T and $A_{\bar{f}}^T$ are the magnitudes of the dominant SM tree-level processes; ϕ_f^T and $\phi_{\bar{f}}^T$ are the weak (CP violating) phases appearing with opposite signs in CP conjugate amplitudes; δ_f is the strong (CP conserving) phase difference between the final states f and $\bar{f}$, appearing with same signs in CP conjugate amplitudes.

For decays to final states that are not CP eigenstates, such as $D^0 \to K^\pm\pi^\mp$, the parameter λ_f of Eq. (1.43), appearing in the expression of time dependent decay rates of Eq. (1.42), and its CP conjugate counterpart $\lambda_{\bar{f}}$, become

$$\lambda_f = -\left|\frac{q}{p}\right| R_f e^{i(\phi+\delta_f)}, \quad \lambda_{\bar{f}} = -\left|\frac{q}{p}\right| R_{\bar{f}} e^{i(\phi-\delta_f)}, \tag{1.51}$$

where $R_{\bar{f}}^{-1} = R_f \equiv A_{\bar{f}}^T/A_f^T$ and ϕ is the relative weak phase between the mixing and decay amplitudes. In $D^0 \to K^\pm\pi^\mp$ decays, δ is the strong phase difference between DCS and CF amplitudes.

Taking into account the small value of $\tan^2\theta_C$ and of the mixing parameters x and y, one can expand the expression of the decay rates in Eq. (1.42) to quadratic order in (Γt) for the WS decays, with $A_{\bar{f}}$ chosen to be the DCS amplitude, i.e. $\bar{f} = K^+\pi^-$, yielding [34]

$$\frac{d\Gamma}{dt}(D^0(t) \to \bar{f}) \simeq e^{-\Gamma t}|A_f|^2 \left[(R_f^+)^2 + R_f^+ y'^+ \Gamma t + \frac{(x'^+)^2 + (y'^+)^2}{4}(\Gamma t)^2\right], \tag{1.52a}$$

$$\frac{d\Gamma}{dt}(\overline{D}^0(t) \to f) \simeq e^{-\Gamma t}|\bar{A}_{\bar{f}}|^2 \left[(R_f^-)^2 + R_f^- y'^- \Gamma t + \frac{(x'^-)^2 + (y'^-)^2}{4}(\Gamma t)^2\right], \tag{1.52b}$$

where $x'^\pm$ and $y'^\pm$ are related to the indirect CP violating parameters, as

$$x'^\pm = \left|\frac{q}{p}\right|^{\pm 1} (x'\cos\phi \pm y'\sin\phi), \tag{1.53a}$$

$$y'^\pm = \left|\frac{q}{p}\right|^{\pm 1} (y'\cos\phi \mp x'\sin\phi), \tag{1.53b}$$

and x' and y' are related to the mixing parameters through a rotation by an angle corresponding to the strong phase difference δ, as

$$x' = x\cos\delta + y\sin\delta, \tag{1.54a}$$

$$y' = y\cos\delta - x\sin\delta. \tag{1.54b}$$

$R_f^+ = |A_{\bar{f}}/A_f|$ and $R_f^- = |\bar{A}_f/\bar{A}_{\bar{f}}|$ in Eq. 1.52 are the magnitudes of DCS to CF amplitudes ratios for D^0 and $\overline{D}^0$ decays. These are related to the CP averaged ratio of wrong-sign to right-sign $D^0 \to K^\pm\pi^\mp$ decay rates, R_D, and the corresponding direct CP violating asymmetry in DCS decays, A_D, as

$$R_D \equiv \frac{(R_f^+)^2 + (R_f^-)^2}{2}, \tag{1.55a}$$

$$A_D \equiv \frac{(R_f^+)^2 - (R_f^-)^2}{(R_f^+)^2 + (R_f^-)^2}. \tag{1.55b}$$

As the decay time t approaches zero, the WS rate is dominated by DCS amplitudes, where negligible direct CP violation is expected. The term linear in decay time in Eq. (1.52) arises from the interference between DCS and mixing amplitudes while the CF amplitudes associated with oscillations into the corresponding antiparticle produce a pure mixing rate proportional to $(\Gamma t)^2$.

On the other hand, the time dependence of the RS decays is to good approximation exponential in (Γt), and is given by

$$\frac{d\Gamma}{dt}(D^0(t) \to f) \simeq e^{-\Gamma t}|A_f|^2, \tag{1.56a}$$

$$\frac{d\Gamma}{dt}(\overline{D}^0(t) \to \bar{f}) \simeq e^{-\Gamma t}|\bar{A}_{\bar{f}}|^2. \tag{1.56b}$$

Assuming negligible CP violation, the CP averaged time dependent ratio of WS to RS decay rates

$$R(t) = \frac{d\Gamma(D^0 \to K^+\pi^-)/dt + d\Gamma(\overline{D}^0 \to K^-\pi^+)/dt}{d\Gamma(D^0 \to K^-\pi^+)/dt + d\Gamma(\overline{D}^0 \to K^+\pi^-)/dt} \tag{1.57}$$

is therefore approximated by taking the ratios of Eqs.(1.52) and (1.56), with $f = K^-\pi^+$, and is given by

$$R(t) \approx R_D + \sqrt{R_D}y' \left(\frac{t}{\tau}\right) + \frac{x'^2 + y'^2}{4}\left(\frac{t}{\tau}\right)^2 \tag{1.58}$$

where $\tau = 1/\Gamma$ is the mean lifetime and R_D is the ratio of DCS to CF branching fractions of Eq. (1.55a). Considering separately the ratios of WS to RS decay rates of initially produced D^0 and $\overline{D}^0$ mesons, the $R^+(t)$ and $R^-(t)$ rates become, respectively

$$R(t)^\pm = R_D^\pm + \sqrt{R_D^\pm}y'^\pm \left(\frac{t}{\tau}\right) + \frac{(x'^\pm)^2 + (y'^\pm)^2}{4}\left(\frac{t}{\tau}\right)^2 \tag{1.59}$$

with independent set of mixing parameters which can be used to constrain the CP violating parameters $|q/p|$ and ϕ, as in Eq. (1.53), with the measurement of δ as external input, and $R_D^\pm = (R_f^\mp)^2$ of Eq. (1.52), that are sensitive to direct CP violation in DCS amplitudes, as in Eq. (1.55b).

Taking the ratio of WS to RS decay rates gives the advantage of cancelling out several experimental nuisance parameters, such as the $D^{*\pm}$ production asymmetry and the detector decay time acceptance, as outlined in Chap. 3.

1.4.2 Current experimental status

Mixing of neutral charmed mesons and indirect CP violation is described by four theoretical parameters:

- x and y, the two parameters governing mixing;

- $|q/p|$ and $\phi = \text{Arg}(q/p)$, the parameters may indicate CP violation in mixing amplitudes, when $|q/p| \neq 1$ is observed, and in the interference between mixing and decay amplitudes, if $\phi \neq 0$ is measured.

When combining measurements coming from different observables, as done by the *Heavy Flavour Averaging Group* (HFAG) [35], in order to determine the above mentioned parameters, there are other six nuisance parameters that are fitted, describing the physics of the different decay modes. These are:

- $\delta_{K\pi}$ and $\delta_{K\pi\pi}$, the strong phase difference between DCS $\overline{D}^0 \to K^-\pi^+$ and CF $D^0 \to K^-\pi^+$ decay amplitudes, and between the DCS $\overline{D}^0 \to K^-\rho^+$ and CF $D^0 \to K^-\rho^+$ amplitudes, respectively;
- R_D, the ratio of DCS to CF decay rates, $R_D \equiv [\Gamma(D^0 \to K^+\pi^-) + \Gamma(\overline{D}^0 \to K^-\pi^+)]/[\Gamma(D^0 \to K^-\pi^+) + \Gamma(\overline{D}^0 \to K^+\pi^-)]$;
- A_D, A_K and A_π, the direct CP violating asymmetries in DCS $D^0 \to K^+\pi^-$ and in singly Cabibbo suppressed (SCS) $D^0 \to K^+K^-$ and $D^0 \to \pi^+\pi^-$ decays.

The experimental observables that are related to the above fundamental quantities come from different decay modes:

- Semileptonic WS $D^0 \to K^+\ell^-\nu$ decays, which can occur only through mixing, and multibody hadronic WS $D^0 \to K^+\pi^-\pi^+\pi^-$ decays, from which it is possible to measure the mixing rate, defined as

  $$R_M = \frac{x^2 + y^2}{2}. \tag{1.60}$$

- Decays to CP eigenstates $D^0 \to K^+K^-$ and $D^0 \to \pi^+\pi^-$, whose observables are y_{CP} and A_Γ, related to $|q/p|$, ϕ, x and y as

  $$2y_{CP} = \left(\left|\frac{q}{p}\right| + \left|\frac{p}{q}\right|\right) y\cos\phi - \left(\left|\frac{q}{p}\right| - \left|\frac{p}{q}\right|\right) x\sin\phi, \tag{1.61a}$$

  $$2A_\Gamma = \left(\left|\frac{q}{p}\right| - \left|\frac{p}{q}\right|\right) y\cos\phi - \left(\left|\frac{q}{p}\right| + \left|\frac{p}{q}\right|\right) x\sin\phi. \tag{1.61b}$$

  y_{CP} has also been measured using the CP-odd component of the decay $D^0 \to K^0_S K^+K^-$.

- The two-body hadronic WS $D^0 \to K^+\pi^-$ decays, defined in the preceding section;
- The amplitude analysis of mixing and CP violation in $D^0 \to K^0_S\pi^+\pi^-$ decays gives direct access to the mixing and CP violation parameters x, y and $|q/p|$, ϕ, while the analyses of $D^0 \to K^0_S K^+K^-$ and $D^0 \to \pi^0\pi^+\pi^-$ have been only carried out in the hypothesis of no CP violation to date, giving direct access to the mixing parameters x and y.

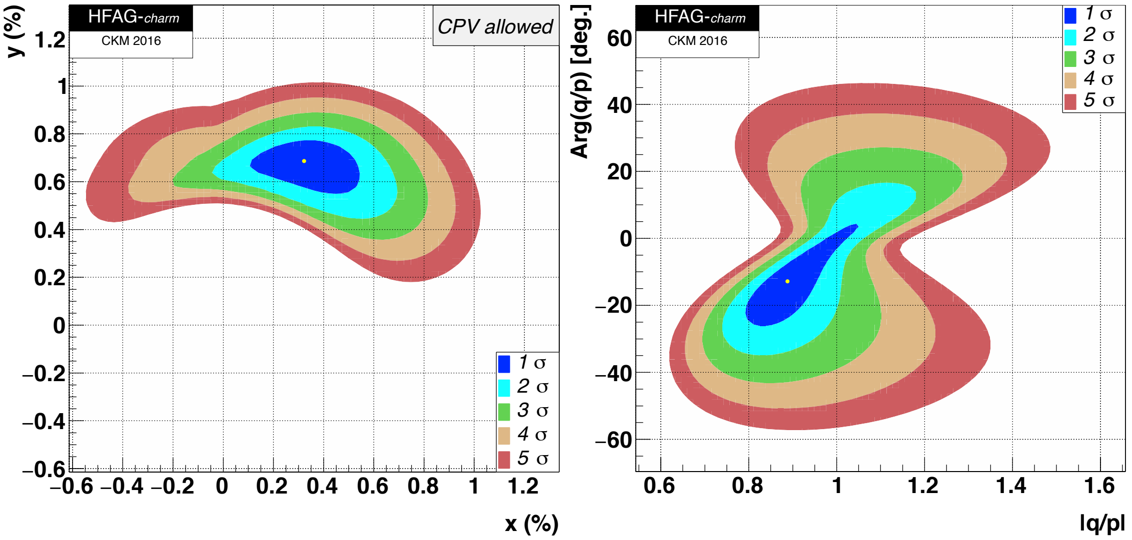

Figure 1.5: Two dimensional contours for the charm mixing parameters (x, y) (left) and CP violating parameters $(|q/p|, \phi)$ (right), with $\phi = \text{Arg}(q/p)$. The no-mixing/no-CP violation case correspond to the point $(0, 0)/(1, 0)$, respectively. From [35].

- The WS $D^0 \to K^+\pi^-\pi^0$ decays are sensitive to the observables x'' and y'', corresponding to the rotated mixing parameters

$$x'' = x\cos\delta_{K\pi\pi} + y\sin\delta_{K\pi\pi}, \tag{1.62a}$$

$$y'' = y\cos\delta_{K\pi\pi} - x\sin\delta_{K\pi\pi}. \tag{1.62b}$$

- It is possible to measure the strong phase $\delta_{K\pi}$ between DCS and CF decay amplitudes exploiting quantum correlations at charm production threshold $\psi(3770) \to D^0\overline{D}^0$.

The HFAG performs a global fit on 49 independent measurements as of 2016 [35], in order to average the charm mixing parameters. When all kind of CP violation is allowed (all parameters free to float), the values of the mixing parameters return

$$x = (0.32 \pm 0.14)\%, \qquad y = (0.69^{+0.06}_{-0.07})\%, \tag{1.63}$$

and for the indirect CP violating parameters

$$|q/p| = 0.89^{+0.08}_{-0.07}, \qquad \phi = (-12.9^{+9.9}_{-8.7})^\circ. \tag{1.64}$$

Their two-dimensional contours, corresponding to 1-5 standard deviations, are shown in Fig. 1.5. The no-mixing hypothesis ($x{=}y{=}0$) is excluded at $> 11.5\sigma$. The parameter x is different from zero by 1.9σ, while y differs from zero by 9.4σ. Thus, the CP-even state is the shorter lived state (as in $K^0 - \overline{K}^0$ mixing), while as x appears to be positive the CP-even eigenstate would also be the heavier state (unlike $K^0 - \overline{K}^0$ mixing). No evidence of CP violation either in mixing or from a phase difference between the mixing and decay amplitude has been observed so far.

Chapter 2

The LHCb experiment

This chapter is dedicated to the illustration of the Large Hadron Collider (LHC) machine and one of its experiments, the Large Hadron Collider beauty (LHCb) experiment, focusing on the subsystems relevant for the analysis of two-body hadronic charm decays, such as the tracking, particle identification and trigger systems.

2.1 The Large Hadron Collider

The LHC represents the state of the art of hadronic particle accelerators. With its 27 km circumference and superconducting dipole magnets, it is designed to collide protons up to 14 TeV centre of mass energy at $10^{34}\,\mathrm{cm}^{-2}\mathrm{s}^{-1}$ instantaneous luminosity and heavy ions (lead nuclei) with 2.8 TeV per nucleon at $10^{27}\,\mathrm{cm}^{-2}\mathrm{s}^{-1}$ peak luminosity. It is located at the final stage of the CERN's accelerator complex, represented in Fig. 2.1, receiving bunches of protons of 450 GeV from the *Super Proton Synchrotron* (SPS) and further accelerating them in two storage rings into opposite directions. Each of them stores 2808 proton bunches at nominal regime, where a bunch contains about 1.1^{11} protons. The two beams cross at four position along the LHC circumference, where the main experiments are placed, and collisions happen at a 40 MHz bunch crossing rate.

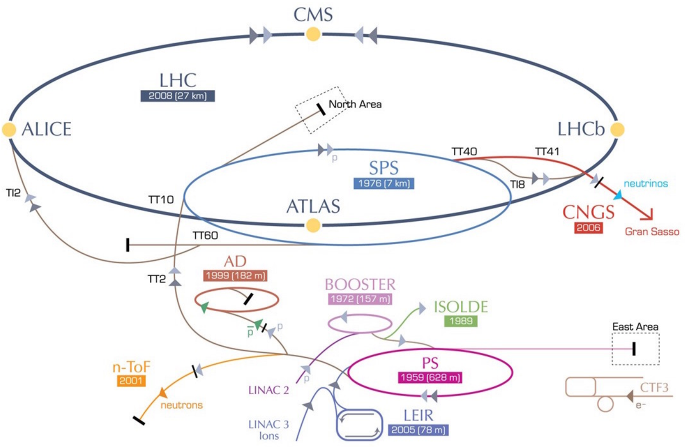

Figure 2.1: CERN's accelerator complex and its main experiments.

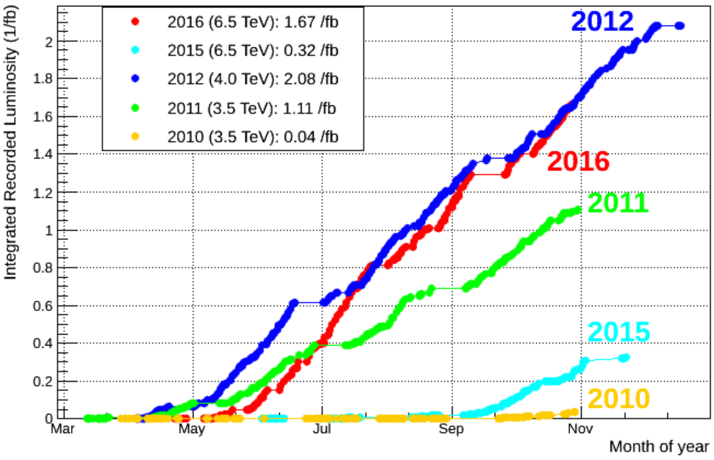

Figure 2.2: LHCb recorded integrated luminosity between 2010 and 2016 in proton-proton collisions.

LHCb started data taking in 2010. Run 1 data taking period ended in 2012, when LHCb collected data corresponding to $3\,\text{fb}^{-1}$ integrated luminosity. During 2015 and 2016 LHC operated at a centre of mass energy of $\sqrt{s} = 13\,\text{TeV}$, finally reaching its design luminosity in June 2016. LHCb operates instead at a lowered luminosity of about $3.5 \times 10^{32}\,\text{cm}^{-2}\text{s}^{-1}$, due to detector and trigger constraints. In this period, it recorded an integrated luminosity of $0.3\,\text{fb}^{-1}$ and $1.6\,\text{fb}^{-1}$, respectively. The instantaneous luminosity recorded by the experiment since 2010 is shown in Fig. 2.2.

2.2 The LHCb detector

LHCb is a single-arm forward spectrometer, designed to study the physics of heavy flavoured mesons and baryons, containing the b or c quark. A schematic vertical cross section of the detector and its components is given in Fig. 2.3. It covers an angular region between 10 and 300 mrad in the horizontal (bending) plane and between 10 and 250 mrad in the vertical plane. Its geometrical acceptance is motivated by the fact that in pp collisions, both $b\bar{b}$ and $c\bar{c}$ pairs are produced with a boost along the beam line, due to the average momentum imbalance of partons constituting the protons. This results in a preferentially small polar angle distribution, as depicted in Fig. 2.4. The pseudorapidity range for tracks reconstructed inside the detector acceptance is therefore $1.8 < \eta < 4.9$, where $\eta \equiv -\ln\tan(\theta/2)$. The coordinate system used by LHCb is a right-handed Cartesian system, with z axis oriented along the beam and y axis pointing vertically upwards. As a result, the x axis points away from the centre of the LHC ring. From this, the azimuthal ϕ and polar θ angle, used in the definition of the pseudorapidity, are also deduced.

The main features of the detector, required in order to carry out its physics programme, are the following:

- Excellent vertex resolution. Many analysis, such as the one discussed in this thesis, require time dependent measurements of decay rates. Thus, it is re-

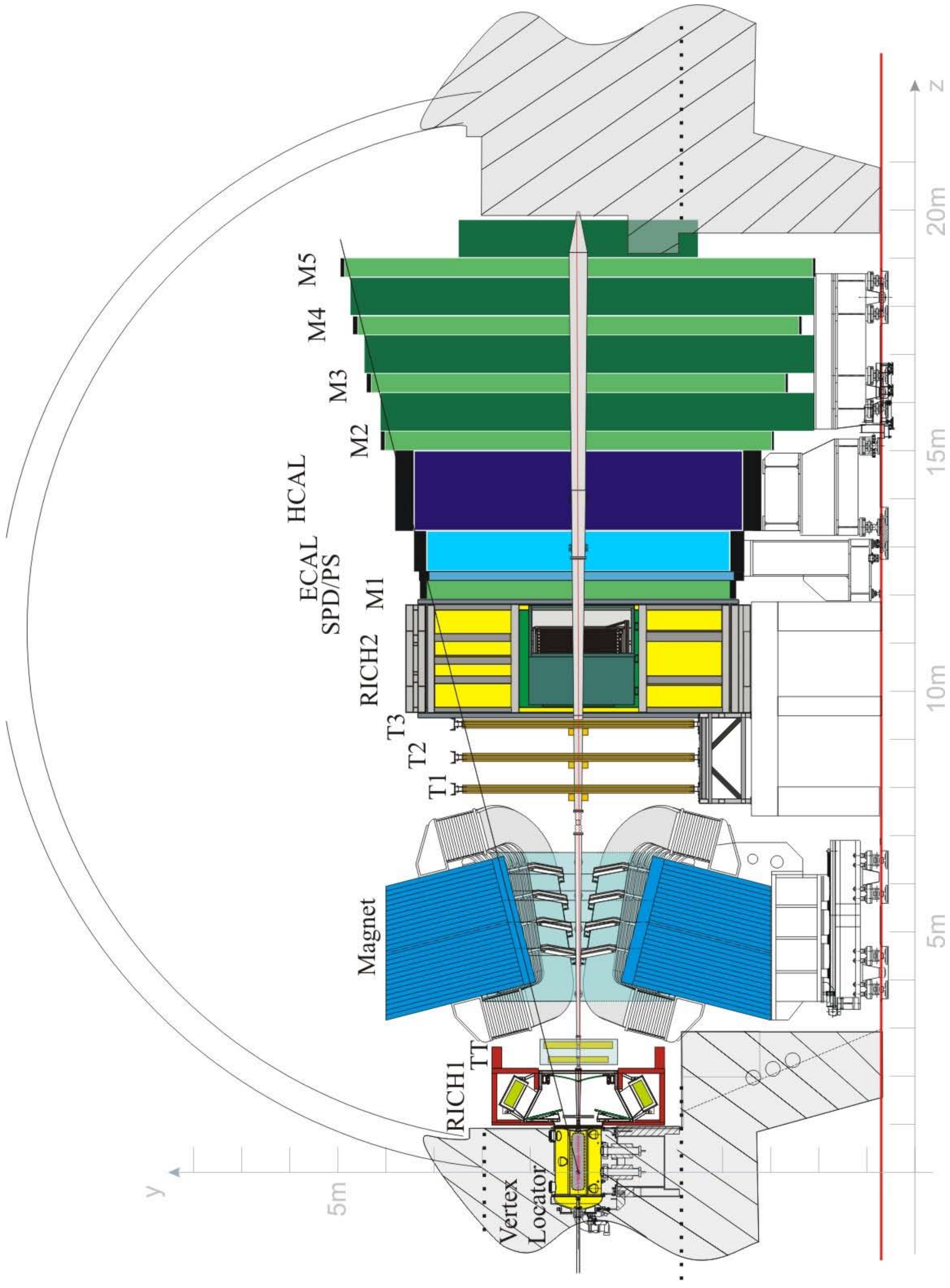

Figure 2.3: Overview of the LHCb detector and its subdetectors.

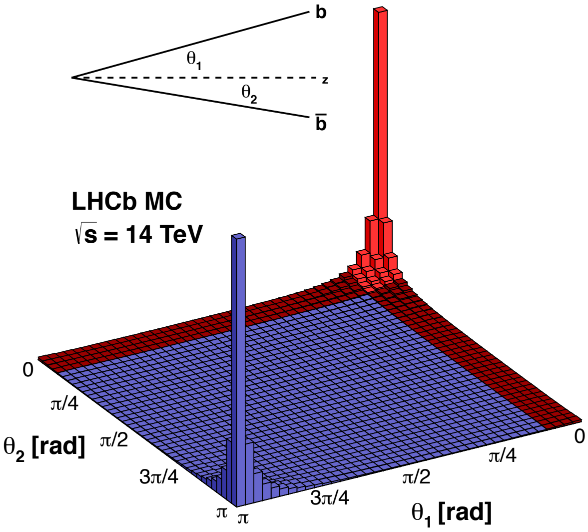

Figure 2.4: Simulated polar angle distribution of $b\bar{b}$ pair produced in pp collisions at $\sqrt{s} = 14\,\text{TeV}$. The LHCb angular acceptance is coloured in red.

quired a high precision on the pp interaction vertices and on the decay vertices of heavy hadrons, from whose distance the decay time is inferred.

- High discrimination between long lived charged particles. Analysis studying two-body and multibody hadronic decays of heavy hadrons need to separate with high accuracy between charged pions, kaons and protons in a wide momentum range (between a few GeV/c up to 100 GeV/c). Together with electrons and muons, these are the five stable particles whose tracks are revealed (and momenta are measured) inside the spectrometer and whose identity is discerned.

- High invariant mass resolution. This depends in turn on the momentum resolution and hence on the precision in measuring charged tracks in a busy hadronic environment. Such a need comes from the necessity to distinguish between particles with similar invariant mass and separate signals from combinatorial background.

- Efficient trigger system. At the centre of mass energies of the LHC, the minimum bias cross section is about three order of magnitudes higher than the $b\bar{b}$ or $c\bar{c}$ cross section. Hence, in order to reduce the acquired data sample to a manageable size and decrease the input rate to a few ten of kHz, it is necessary to retain only the interesting events. This is done in two steps, with increasing order of selection complexity.

In the following, the many subdetectors making up the whole experimental apparatus are described, with attention on what they measure, how they measure it and the technology employed to achieve their purpose.

2.3 Tracking System

The tracking system measures the trajectories of charged particles inside the LHCb acceptance. The vertex detector (VELO) resolves the production and decay vertices of heavy hadrons, decaying after a few centimetres from the interaction point, thus providing a measurement of their decay time. The tracking stations (TT and T1-T2-T3), placed upstream and downstream the magnet, provide a measurement of the charge and momentum of the decay products of those heavy particles decaying in the VELO, by means of their curvature in a magnetic field. The resolution on the momentum achieved for tracks traversing the whole detector results to be $\Delta p/p \sim 0.4 - 0.6\%$.

2.3.1 Vertex Locator

Heavy flavoured mesons have a lifetime of $\sim 1\,\mathrm{ps}$ and, due to their heavy boost, can travel a distance of approximately 1 cm before decaying. The *Vertex Locator* (VELO) is the subdetector placed closest to the interaction point, whose aim is to precisely localize primary and secondary vertices. Its composition is sketched in Fig. 2.5. It is made of 21 silicon modules arranged along the z-direction. These are constituted of $220\,\mu m$ thick silicon microstrips sensors, divided in two halves, in order to allow the opening of the VELO during injection and provide a fully closed configuration during data taking. Since these sensors operate at a distance of 8 mm to the beam, both detectors and readout electronics are housed inside a vacuum vessel. Each half module is constituted on one side of a R-sensor, measuring the

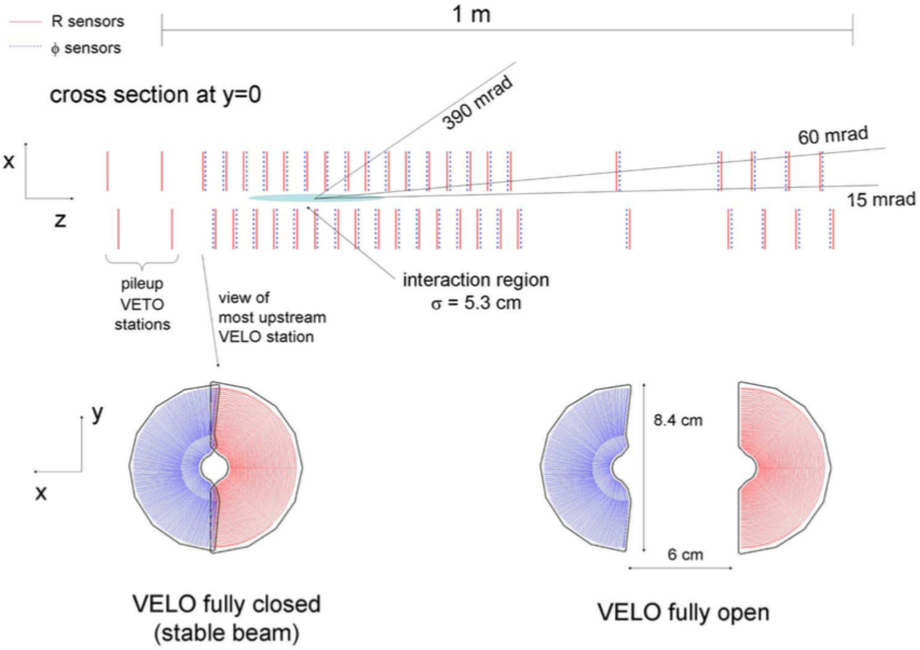

Figure 2.5: Top (top) and front (bottom) view of the VELO silicon sensors, with semicircular modules in both closed (left, stable beam) and open (right, unstable beam) positions [36].

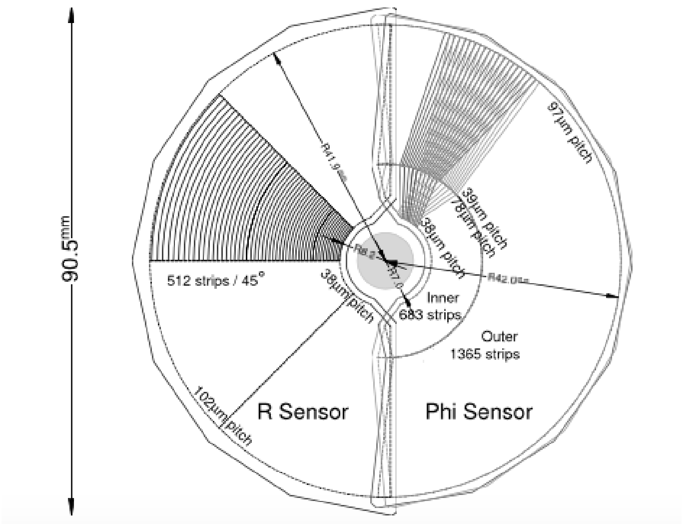

Figure 2.6: A schematic view of the geometry of the R (left) and ϕ (right) sensors making up the VELO.

radial distance, and on the other of a ϕ-sensor, measuring the azimuthal angle. In this way it is possible to localize a 2D spacial point on each plane which combined with the z coordinate of the module gives a 3D space point. R sensors are designed in a semicircular shape (see Fig. 2.6) with varying strip pitch, from 38 μm at the centre to 101.6 μm at the largest radius; ϕ sensors are divided in two region, the inner one having a strip pitch of 78.3 μm while the outer one of 39.3 μm. Inner and outer regions are oriented with a different stereo angle, of 20° and 10° to the radial direction, respectively. The single hit resolution thus achieved is of 7 μm at best, depending on the angle of the track.

The VELO is designed to measure particles in the region $1.6 < |\eta| < 4.9$ and $|z| < 10.6$ cm, which pass at least through three modules. It achieves a spatial resolution in the x and y coordinates ranging from 35μm to 10μm, depending on the number of tracks per event fitted into the vertex, while for the z coordinate

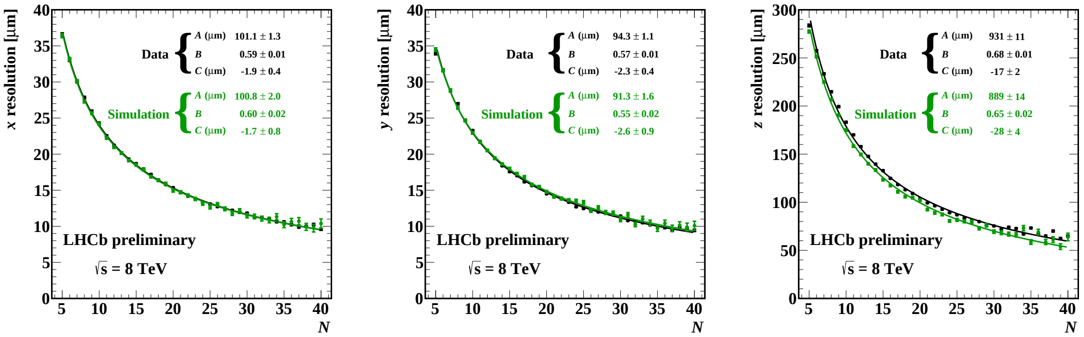

Figure 2.7: Performances of the VELO in the reconstruction of the primary vertex for each spatial coordinate as a function of the number of tracks fitted per event, for one reconstructed primary vertex.

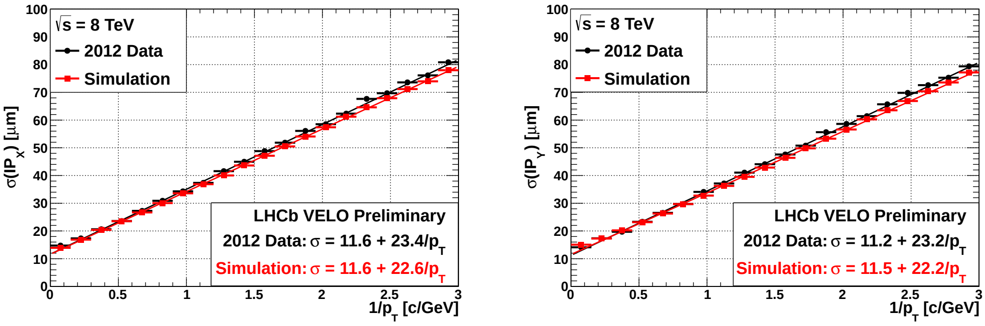

Figure 2.8: Performances of the VELO in the reconstruction of the x and y component of the impact parameter as a function of $1/p_T$.

it varies between 300 μm and 50 μm, as shown in Fig. 2.7. The spatial resolution translates into a decay time resolution of $\sim$ 45 fs. It is possible to the determine the impact parameter, the minimum distance of a track to the primary vertex, with a minimum resolution of $\sim$ 10 μm, varying as $1/p_T$ of the track, as shown in Fig. 2.8.

2.3.2 Tracker Turicensis

The *Tracker Turicensis* (TT) is placed before the magnet, in a region where a residual magnetic field is present. This allows the reconstruction of low-momentum particles, bent out of the downstream acceptance, and long lived particles, such as the K^0_S and the Λ^0, mostly decaying after the VELO. Moreover, it helps combining tracks coming from the VELO with those reconstructed after the magnet, thus improving the resolution in momentum. It consists of two pairs of double layers, arranged in a x-u-v-x configuration. The inner u and v planes are tilted of $\pm 5°$ to the vertical direction in order to allow the determination of the y coordinate. Each plane of the TT is made of several half modules, consisting of a row of seven silicon microstrip sensors with a readout system at the end (see Fig. 2.9). Silicon microstrip sensors have a 200 μm strip pitch. Half modules are joined together to form full modules, which extend into a 150 cm wide and 130 cm high rectangular region covering the whole detector acceptance. The TT stations provide a 50 μm single hit resolution.

2.3.3 Tracking Stations

The three *tracking stations* T1-T2-T3 are placed after the magnet and use a silicon microstrip technology in the inner region (*inner tracker*, IT), where the particle flux is higher, and a gas drift tubes detector in the outer region (*outer tracker*, OT). Each station is made of four detection planes in a x-u-v-x arrangement, as for the TT. Each plane comprises an IT and a OT. The IT uses silicon microstrips with 200 μm strip pitch, covering and 120 cm high and 40 cm wide rectangular region around the beam pipe. The IT gives a 50 μm hit resolution. The OT employs drift tubes of 5 mm diameter, filled with Argon (70%) and CO_2 (30%), giving a drift time of $\sim$ 50 ns. Each OT plane consists of two rows of overlapping tubes, as depicted in

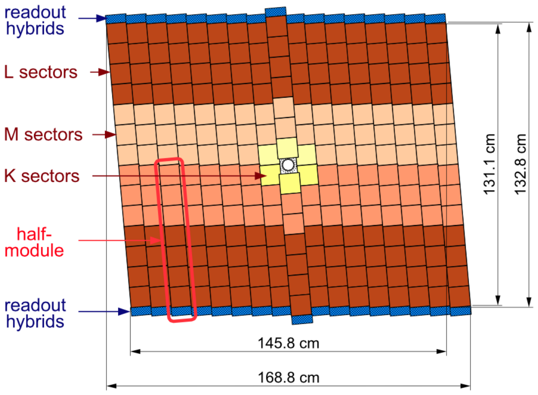

Figure 2.9: Representation of the v plane of the TT station, showing the detector modules and readout system [36].

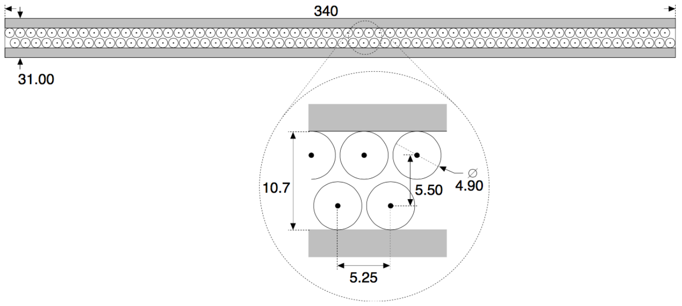

Figure 2.10: Cross section of the OT plane showing the straw drift tubes arrangement [36].

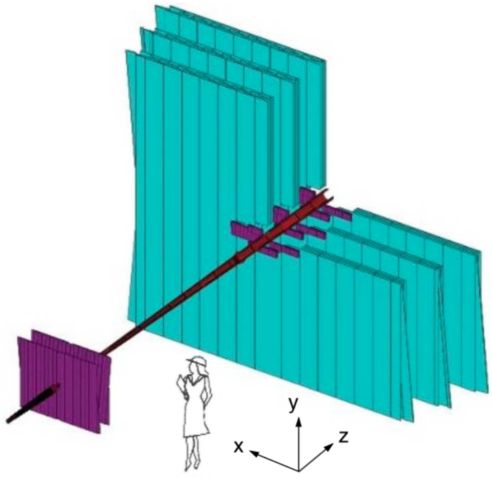

Figure 2.11: Arrangement of the IT (purple) and OT (cyan) modules placed before and after the magnet, respectively [36].

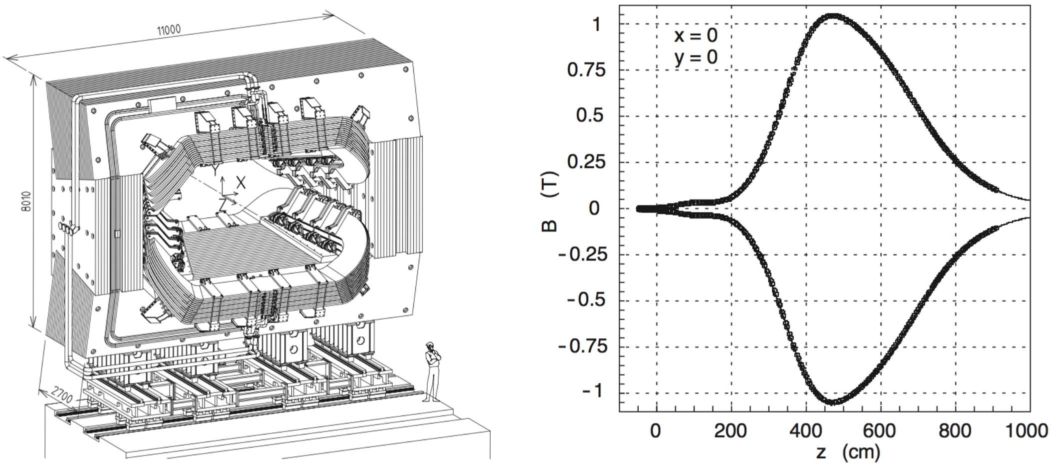

Figure 2.12: LHCb dipole magnet with coordinate system (left) and magnetic field in the x-y plane, along the z direction (right) [36].

Fig. 2.10. The OT covers a large area of $\sim 6 \times 5\,\mathrm{m}^2$ and achieves a $200\,\mu$m spatial resolution. The arrangement of the IT and OT modules is depicted in Fig. 2.11.

2.3.4 Dipole Magnet

The LHCb apparatus is furnished with a warm dipole magnet, providing an integrated magnetic field of 4Tm, with peak intensity of 1Tm. The coils shape, following the profile of the detector acceptance and related coordinate system, is displayed in Fig. 2.12, together with the magnetic field intensity along the z axis. The polarity of the magnet can be reversed, allowing the evaluation of any difference of the detection efficiency in the right and left part of the detector. These affect asymmetrically the detection of positively and negatively charged particles, which bends in opposite direction in the presence of a magnetic field.

2.3.5 Tracks reconstruction

Tracks of charged particles are reconstructed using the hits from the VELO, TT, IT and OT. They can be divided into different categories, depending on their trajectory (see Fig. 2.13):

- Long tracks, releasing hits in all the subsystems used for tracking. These tracks have the best determined momentum and are the kind of tracks used in this analysis;

- Upstream tracks, traversing the VELO and TT, they belong to low momentum particles bent out the rest of the detector by the magnetic field. An estimate of their momentum may be inferred thanks to the residual magnetic field present between the VELO and TT. They can also release a signal in RICH1 if their velocities are above the Cherenkov threshold and may thus be used for its calibration;

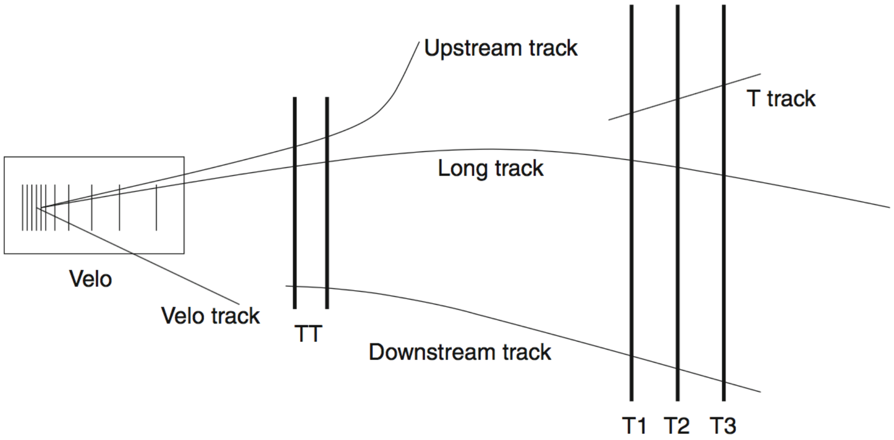

Figure 2.13: Charged track types in the LHCb detector.

- Downstream tracks, originating from long-lived particles decaying after the VELO, they release hits only in the TT and T stations;
- VELO tracks, coming from particles produced at a wide angle with respect to the beamline, they exit the detector acceptance before the TT and are useful in the determination of primary vertices;
- T tracks, produced in secondary decays, they may be useful in the calibration of RICH2.

Seed tracks are searched for by combining almost aligned hits in the VELO and TT, where the magnetic field is low, forming straight lines. Hits from different detectors are then matched to form trajectories that are then refitted with a Kalman filter, taking into account multiple scattering and energy loss from particle interaction. The χ^2 of the track fit is used to discriminate the quality of the track and a clone killer algorithm is run to remove tracks with hits in common. A track is further defined as a *ghost* if it is not matched with a charged particle in the event. They originate from uncorrelated signal and noise hits and typically show a low momentum.

2.4 Particle Identification

In order to reconstruct the invariant mass of a heavy particle decaying in the LHCb acceptance, it is necessary to know the identity of its decay products, whose charged tracks and momenta are measured. The assignment of a mass hypothesis to charged hadrons and leptons is achieved with the aid of imaging Cherenkov devices, calorimetric techniques and the muon detectors.

2.4.1 RICH

Two *Ring Imaging Cherenkov* detectors (RICH1 and RICH2) are dedicated to the identification of charged hadrons, namely pions, kaons and protons. They measure the opening angle of the cone of light emitted by charged particles travelling faster

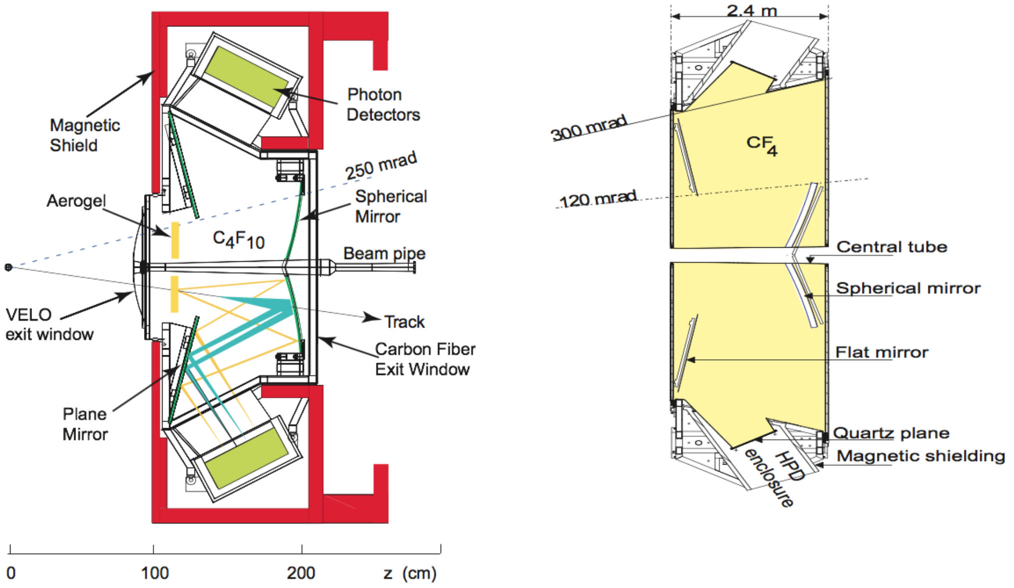

Figure 2.14: Schematic view of RICH1 (left) in the yz plane and RICH2 (right) in the xz plane [36].

than the speed of light in the medium. The opening angle θ_c is related to the velocity v of the charged particle by $\cos\theta_c = c/(nv)$, where n is the refractive index of the medium. By knowing its velocity and momentum, it is thus possible to obtain the mass of the charged particle. The first station, RICH1, is placed upstream the magnet, between the VELO and the TT. It distinguishes Cherenkov angles of particles in a momentum range $\sim$ 1-60 GeV/c. It uses aerogel and C_4F_{10} as radiators and it is designed to cover the whole detector acceptance. Its minimum angular coverage is limited by the beam pipe, resulting in ±25 mrad. A schematic view of the detector, composed of spherical and flat mirrors, bringing Cherenkov light outside the detector acceptance, and *Hybrid Photons Detectors* (HPDs), detecting photons in a wavelength range of $200 - 600$nm, is reported on the left hand side of Fig. 2.14. The HPDs are placed inside MuMetal cylinders, shielding from magnetic fields up to 50 mT. The second station, RICH2, is placed downstream the magnet, between the tracking stations and the first muon station. It distinguishes particles of higher momenta, in a range between $\sim$ 15 GeV/c to 100 GeV/c and beyond. It is filled with CF_4 radiator and covers the angular region closest to the horizontal plane, ±120 mrad in the horizontal plane and ±100 mrad in the vertical, where most high momentum particles are present. As RICH1, its angular coverage is limited to a minimum ±25 mrad due to the beam pipe. Its design is shown on the right hand side of Fig. 2.14.

2.4.2 Calorimeters

The calorimeter system is used to identify electrons, photons and events which are hadronic in nature. It also provides an estimate of the transverse energy $E_T \equiv E\sin\theta$, which is used in the Level 0 trigger decisions. It consists of a *Scintillator Pad Detector* (SPD), a *Pre-Shower* (PS) detector, an *Electromagnetic Calorime-*

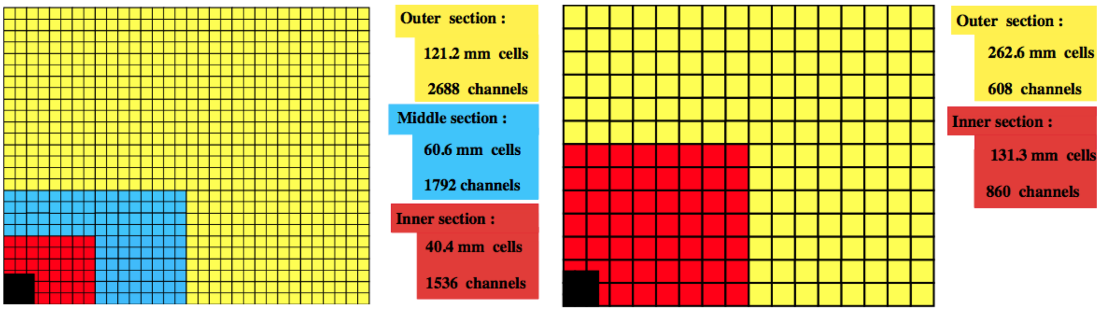

Figure 2.15: Lateral segmentation of SPD/PS and ECAL (left) and the HCAL (right), for one quarter of the detector front face [36].

ter (ECAL) and a *Hadronic Calorimeter* (HCAL). All the subdetectors making up the calorimeters system are made of segmented scintillators, acting as active material, and light is transported by wavelength shifting fibers and read out by photomultipliers. The SPD and PS are both made of scintillating fiber and are separated by a 15 mm thick lead converter. The SPD is used to discriminate between electrons and photons in the L0 trigger and it provides also a fast online estimation of the number of charged tracks in the event. By comparing the number of hits in the SPD and PS, it is possible to separate electrons and the background of charged pions from their longitudinal shower dispersion. The ECAL is made of alternating lead converters and plastic scintillators, for a total material budget of 25 radiations lengths and 1.1 nuclear interaction lengths. The HCAL is made of scintillating square tiles and iron layers, for a total material budget corresponding to 5.6 nuclear interaction lengths. All detectors have a variable lateral segmentation, with increasing sensor size from the beam pipe to external regions of lower occupancy (see Fig. 2.15). The nominal ECAL resolution is $\sigma_E/E = 1\% \oplus 10\%/\sqrt{E}$, where E is in GeV and $\oplus$ indicates quadratic sum, while for the HCAL is $\sigma_E/E = 80\%/\sqrt{E} \oplus 10\%$.

2.4.3 Muon system

Muons are minimum ionizing particles traversing all the detector without suffering major energy losses. The muon stations are therefore placed at the end of the detector, where mainly muons are present, and provide muon identification and standalone track reconstruction and p_T calculation for trigger purposes. One muon station (M1) is placed upstream the calorimeters, providing an improved p_T measurement for the trigger, while the remaining four stations (M2-M5) are placed downstream the calorimeters and are interleaved with 80 cm thick iron plates. The iron absorbers stops the remaining hadrons surviving after the HCAL and select the most penetrating muons, so that only muons with a minimum 6 GeV/c momentum arrive at the M5. A layout of the muon system is given in Fig. 2.16. Muon stations are made of multiwire proportional chambers, except for the inner part of the M1 station, made of triple-GEM (*gas electron multiplier*) detectors, which provide better radiation hardness in the presence of high particle fluxes. Each muon station is subdivided into four parts (R1-R4) with increasing segmentation for diminishing distance from the beam pipe, allowing for an equally distributed particle occupancy.

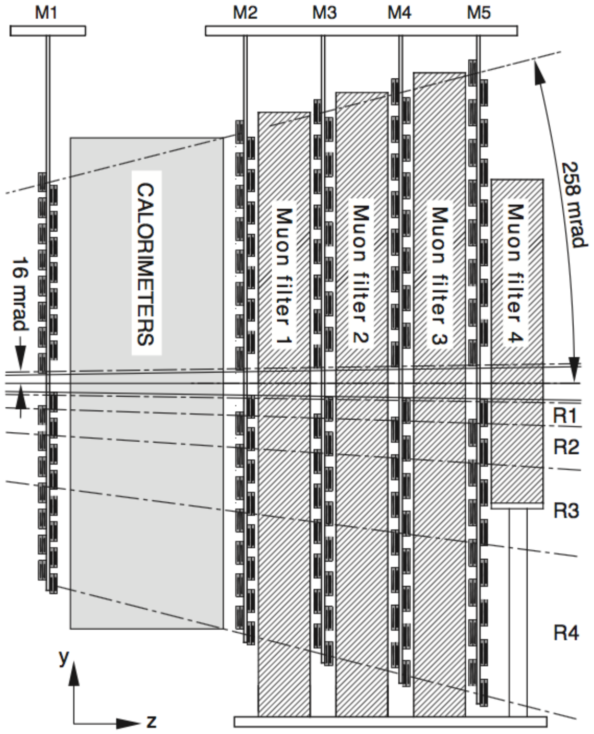

Figure 2.16: Side view of the muon system in the y-z plane [36].

2.4.4 Mass hypothesis likelihood

The informations coming from the RICH detectors, the calorimeters and the muon stations are combined into a log-likelihood difference $\Delta\log\mathcal{L}_{h-\pi}$ between a given particle hypothesis (with $h = K$, p, μ or e) and the arbitrary pion hypothesis taken as a reference

$$\Delta\log\mathcal{L}_{h-\pi} = \log\mathcal{L}(h) - \log\mathcal{L}(\pi) \tag{2.1}$$

where $\mathcal{L}(h)$ is the likelihood of a given track being a particle h. The larger the value of $\Delta\log\mathcal{L}_{h-\pi}$ is, the more likely the particle is of h type. For pions, small or negative values of $\Delta\log\mathcal{L}_{h-\pi}$ indicates h being a pion. The likelihood hypothesis for a particle type is formed multiplying each detector contribution

$$\mathcal{L}(p) = \mathcal{L}^{\text{RICH}}(p) \cdot \mathcal{L}^{\text{CALO}}(\text{non}\, e) \cdot \mathcal{L}^{\text{MUON}}(\text{non}\, \mu) \tag{2.2a}$$

$$\mathcal{L}(K) = \mathcal{L}^{\text{RICH}}(K) \cdot \mathcal{L}^{\text{CALO}}(\text{non}\, e) \cdot \mathcal{L}^{\text{MUON}}(\text{non}\, \mu) \tag{2.2b}$$

$$\mathcal{L}(\pi) = \mathcal{L}^{\text{RICH}}(\pi) \cdot \mathcal{L}^{\text{CALO}}(\text{non}\, e) \cdot \mathcal{L}^{\text{MUON}}(\text{non}\, \mu) \tag{2.2c}$$

$$\mathcal{L}(\mu) = \mathcal{L}^{\text{RICH}}(\mu) \cdot \mathcal{L}^{\text{CALO}}(\text{non}\, e) \cdot \mathcal{L}^{\text{MUON}}(\mu) \tag{2.2d}$$

$$\mathcal{L}(e) = \mathcal{L}^{\text{RICH}}(e) \cdot \mathcal{L}^{\text{CALO}}(e) \cdot \mathcal{L}^{\text{MUON}}(\text{non}\, \mu) \tag{2.2e}$$

where the hadron discriminating power comes mostly from the RICH detectors, that are optimized to provide an excellent K/π separation over a broad momentum

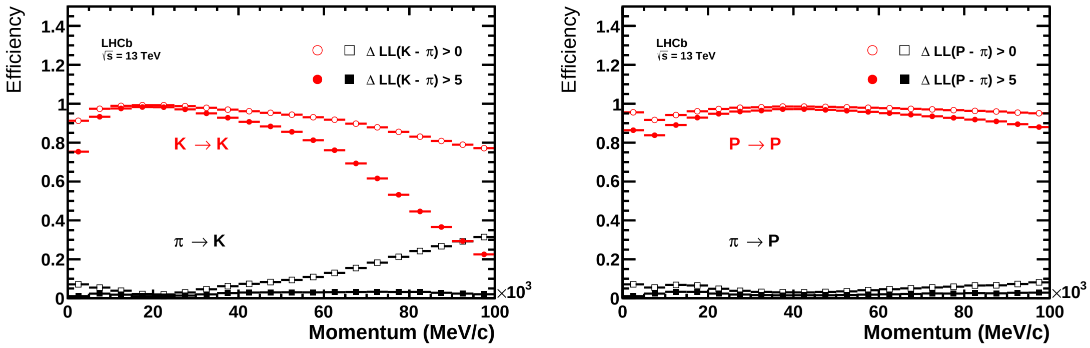

Figure 2.17: Particle identification efficiencies (red) and misidentification probabilities (black) for different PID requirements, for π and K (left) and for p and π (right), measured with 2015 data as a function of track momentum.

range (see Fig. 2.17). The minimum momentum required for a muon to pass the calorimeter and reach the $M2$ station is $p > 3\,\mathrm{GeV/c}$. Tracks trigger the muon decision if they are associated to a certain number of hits in the five muon stations, depending on their momentum. To build the likelihood $\mathcal{L}^{CALO}$, used to identify electrons and neutral particles, the information coming form the energy deposited in the ECAL is used.

In this analysis, K-π separation is particularly important to discriminate RS decays from WS decays. In particular, RS decays whose decay products are doubly misidentified (assigning a π mass hypothesis to the K and vice versa) constitutes a source of systematic bias in the WS signal yield. Tight PID requirements are therefore applied on the K and π mass hypothesis, in order to reduce this bias to a minimum.

2.5 Trigger

LHC collides bunches of protons every 25 ns, corresponding to a frequency of 40 MHz. Since the inelastic cross section is much higher than the $b\bar{b}$ and $c\bar{c}$ production cross sections, only a fraction of events are interesting for physics analysis and only these must be retained in order to cope with technological and cost limits. This is achieved in multiple steps, with higher level of selection complexity. The *level-0* trigger (L0) is hardware based and operates synchronously with the LHC clock, reducing the rate to 1 MHz. The high-level trigger (HLT) is software based and processes the output of the L0 in parallel on the *event filter farm* (EFF), which uses > 20k commercial CPUs. The HLT is divided in two stages: HLT1 performs a partial inclusive event reconstruction, reducing the rate by a factor of 20, while the HLT2 performs a full online event reconstruction and reduces the rate to about 12.5 kHz (2015 running conditions, see Fig. 2.18) to be sent to mass storage.

2.5.1 L0 Trigger

The L0 trigger is implemented on custom made electronic boards integrated in the front end electronics of the detector. It searches for signatures of heavy particles decays, whose daughter particles are produced with large transverse momentum with respect to minimum bias events. These are:

- The highest E_T hadrons, electron and photon clusters in the calorimeters. The L0 calorimeter trigger searches for clusters of calorimeter cells with highest E_T which are tagged either as electron (`L0Electron`), photon (`L0Photon`) or hadron (`L0Hadron`), depending on the energy deposits in the SPD, PS, ECAL and HCAL. The total number of hits in the SPD is also used to reject events with high charged track multiplicity. These correspond to events with high occupancy which exceeds the timing capabilities of both online and offline reconstruction.

- The two highest p_T muons in the muon stations. The L0 muon trigger searches for hits in the muon stations giving a straight line pointing towards the interaction point. A value for the p_T of the muon is thus extrapolated. The two highest-p_T tracks are taken for decision (`L0Muon` and `L0DiMuon`).

Decisions must be taken within $4\,\mu$s of latency, in order to cope with the read-out chips buffer time. All the informations are gathered by a L0 decision unit (DU), which accepts the event if at least one of the subsystems satisfies the selection requirement. The input rate is thus reduced to an L0 output rate of 1 MHz, which is the maximum rate at which the informations from the whole detector can be read out.

2.5.2 HLT1

The HLT1 exploits informations from the VELO by reconstructing 3D points and evaluating the number of primary vertices (PVs) in the event. Before track reconstruction is performed, events with an OT occupancy higher than 20% are rejected because they would take too long to be processed. Several trigger decisions are run in parallel:

- Single displaced high quality tracks with high momentum are looked for, those having a large impact parameter (IP) with respect to the primary vertex (PV) and low impact parameter significance squared ($\chi^2(IP)$), calculated refitting the tracks with a bidirectional Kalman filter;

- Requirements are applied on the momentum of the particles and on the invariant mass of the objects which are reconstructed by matching the VELO tracks with the muon tracks from the L0 decision;

- Electrons and photons are triggered based on the informations from the ECAL.

Decisions are taken in $\sim$ 10-15 ms per event. The HLT1 reduces the rate to approximately 50 kHz, at which a complete event reconstruction in the HLT2 is possible.

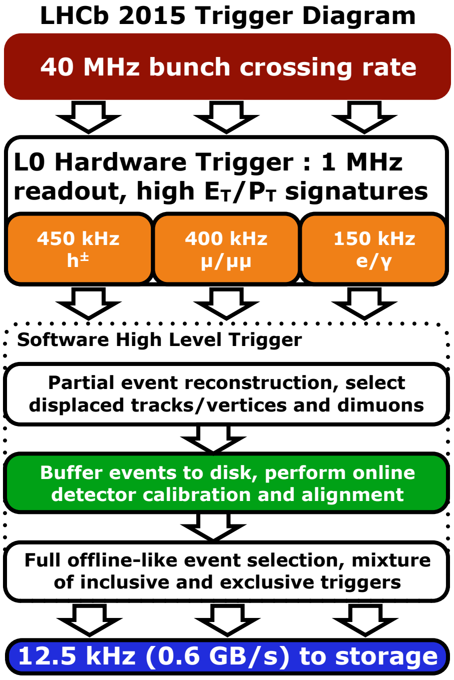

Figure 2.18: LHCb trigger scheme during Run II.

2.5.3 HLT2

While HLT1 is only able to reconstruct tracks in the VELO and primary vertices, HLT2 performs an almost full event reconstruction and is thus able to apply criteria on secondary vertices and composed particles. The total number of reconstructed tracks is used to discard events with high multiplicity which would slow processing time. Inclusive and exclusive selections are applied in order to consider the largest possible set of final states. The n-body topological lines are designed to build multi-body candidates while dedicated lines for specific analysis are used. These lines are based on multivariate algorithms (Boosted Decision Trees), in order to provide a higher background rejection and signal efficiency than a cut-based approach. The HLT2 selected events can then be stored on disk at an output rate of $\sim 12.5\,\text{kHz}$, as of 2015.

2.5.4 The Turbo stream

The introduction of a buffer stage between HLT1 and HLT2 (shown in green in Fig. 2.18), receiving input at the level of kHz from the HLT1, gives enough time to calibrate and align the detector, run an offline-like reconstruction and to calculate offline-like particle identification likelihoods. This allows to be more selective in HLT2 and save only candidates selected by the trigger. The Turbo stream, taking up $\sim 2.5\,\text{kHz}$ of the total output rate in 2015, is the means by which events reconstructed in trigger are persisted to perform physics analysis. They feature an offline-like reconstruction quality and are an order of magnitude smaller in size than events from the full stream, occupying a smaller portion of the total bandwidth for the same output rate. This is particularly essential for charm physics, which is limited by trigger output rate constraints. This analysis uses data from the Turbo lines and is also aimed at validating this new approach. In the LHCb upgrade, an output bandwidth from HLT to storage of 5 GB/s is foreseen, so that a total event rate of 1 MHz could be saved using the Turbo stream.

Chapter 3

Determination of the mixing parameters

In this chapter it is described the procedure followed in the analysis in order to measure the D^0 mixing parameters from $D^0 \to K^{\pm}\pi^{\mp}$ decays using RUN 2 data and search for CP violation in mixing. In the first section, a general overview of the analysis is given, where in particular the main challenges are highlighted, namely how to control the various sources of background and systematic uncertainties. In the second section, the selection adopted to reduce background to a minimum level is described. The third section addresses the mass fit model used in the fit and reports the signal yields and the corresponding WS to RS ratios in the decay time bins. In the fourth section it is evaluated the residual contribution of the peaking backgrounds, which is one the main systematic uncertainty that needs to be taken into account in the final mixing fit. The other sources of systematic uncertainties are briefly described in the fifth section. Eventually, the time dependent fit to extract the mixing parameters is shown and the impact of the results on the precision of the mixing and CP violating parameters is evaluated.

3.1 Analysis overview

To determine the $D^0 - \overline{D}^0$ mixing parameters and search for CP violation, the time dependent ratio of WS to RS decay rates is determined separately for D^0 and $\overline{D}^0$ mesons. The neutral D flavour at production is determined by the charge of the low momentum pion ("soft" pion, π_s), in the flavour conserving strong interaction decay $D^{*+} \to D^0\pi_s^+$, and charge conjugate process. This analysis is restricted to "prompt" D^* candidates, which are directly produced in pp collisions. As a consequence, the D mesons coming from a b-hadron decay, incorrectly identified as originating from the primary vertex, represent an important source of systematic uncertainty.

The WS and RS signal yields are evaluated in different decay time bins and the time dependence of their ratio is determined according to the expression in Eq. (1.59). Experimental effects, such as production asymmetries and differences in detection efficiency of positively and negatively charged particles, may bias the observed ratio and thus the mixing and CP violation measurement. Assuming that the efficiency in detecting the three final state particles factorizes as the efficiencies in detecting the D^0 decay products $\epsilon(K^+\pi^-)$, and the efficiency in the reconstruction of the soft pion $\epsilon(\pi_s^\pm)$, the number of reconstructed D^{*+} and D^{*-} tagged RS and WS decays becomes

$$N_{RS+}^{obs} = N_{D^{*+}}\mathcal{B}(D^{*+} \to D^0\pi^+)\mathcal{B}(D^0 \to K^-\pi^+)\epsilon(K^-\pi^+)\epsilon(\pi_s^+), \tag{3.1a}$$

$$N_{WS+}^{obs} = N_{D^{*+}}\mathcal{B}(D^{*+} \to D^0\pi^+)\mathcal{B}(D^0 \to K^+\pi^-)\epsilon(K^+\pi^-)\epsilon(\pi_s^+), \tag{3.1b}$$

$$N_{RS-}^{obs} = N_{D^{*-}}\mathcal{B}(D^{*-} \to \overline{D}^0\pi^-)\mathcal{B}(\overline{D}^0 \to K^+\pi^-)\epsilon(K^+\pi^-)\epsilon(\pi_s^-), \tag{3.1c}$$

$$N_{WS-}^{obs} = N_{D^{*-}}\mathcal{B}(D^{*-} \to \overline{D}^0\pi^-)\mathcal{B}(\overline{D}^0 \to K^-\pi^+)\epsilon(K^-\pi^+)\epsilon(\pi_s^-), \tag{3.1d}$$

where $N_{D*^\pm}$ is the number of produced $D^{*\pm}$ mesons, $\mathcal{B}(D^{*+} \to D^0\pi^+)$ and $\mathcal{B}(D^{*-} \to \overline{D}^0\pi^-)$ are the branching ratio of the charge-symmetric strong interaction $D^{*+} \to D^0\pi_s^+$ and $D^{*-} \to D^0\pi_s^-$ decays and $\mathcal{B}(D^0 \to K^\pm\pi^\mp)$ and $\mathcal{B}(\overline{D}^0 \to K^\pm\pi^\mp)$ are the effective branching ratio of neutral D decays, including the $D^0 - \overline{D}^0$ oscillation rate. Assuming negligible direct CP violation in RS decay, as it is dominated by tree-level decay amplitudes, one gets $\mathcal{B}(D^0 \to K^-\pi^+) = \mathcal{B}(\overline{D}^0 \to K^+\pi^-)$, and the observed charge WS to RS yield ratios $R^{obs\pm}$ are related to $R^\pm$ of Eq. (1.59) as

$$R^{obs+} = \frac{N_{WS+}^{obs}}{N_{RS+}^{obs}} = R^+\frac{\epsilon(K^+\pi^-)}{\epsilon(K^-\pi^+)}, \tag{3.2a}$$

$$R^{obs-} = \frac{N_{WS-}^{obs}}{N_{RS-}^{obs}} = R^-\frac{\epsilon(K^-\pi^+)}{\epsilon(K^+\pi^-)}. \tag{3.2b}$$

The mass of the D^0 candidates, indicated in the following as $M(K\pi)$, is calculated using the vector sum of the two final state particles momenta and the $K\pi$ mass hypothesis, as given by the particle identification subsystems, in the calculation of energy. In an analogous way, the D^* candidates mass, indicated as $M(D^0\pi_s)$, is reconstructed using the vector sum of the three particles momenta in the final state and the known D^0 and π masses, namely

$$\begin{aligned} M(D^0\pi_s) &= \sqrt{E_{D^*}^2 - p_{D^*}^2}, \\ E_{D^*} &= \sqrt{m_{D^0}^2 + p_{D^0}^2} + \sqrt{m_\pi^2 + p_{\pi_s}^2} \\ \vec{p}_{D^*} &= \vec{p}_{D^0} + \vec{p}_{\pi_s} \\ \vec{p}_{D^0} &= \vec{p}_+ + \vec{p}_- \end{aligned} \tag{3.3}$$

where $\vec{p}_+$ and $\vec{p}_-$ are the momenta of the positively and negatively charged tracks. This quantity offers the advantage of being independent of the mass hypothesis assigned to the D^0 decay products, therefore all the $D^{*+} \to D^0(\to h^+h^{(\prime)-})\pi_s^+$ decays have the same $D^0\pi_s$ distribution, while partially reconstructed multibody decays exhibits larger distributions, as explained next.

Signal and background are discriminated using $M(K\pi)$ and $M(D^0\pi_s)$ distributions, as shown in Fig. 3.1. Signal candidates show a narrow peak in both mass distributions, consistent with experimental resolution. Two body charm decays, in which one final state particle has been misidentified, feature a rapidly falling distribution in $M(K\pi)$, negligibly contributing into the signal region around the nominal D^0 mass, while peaking in $M(D^0\pi_s)$, due to the D^0 mass assignment in the determination of the D^{*+} energy. Doubly-misidentified two body charm decays show a broad $M(K\pi)$ distribution around the nominal D^0 mass and a peaking $M(D^0\pi_s)$ distribution. Multibody partially reconstructed D^0 decays have a smooth distribution in $M(K\pi)$ and a broad peaking structure in $M(D^0\pi_s)$. The dominant background, formed by real D^0 decays associated with random pions, is indistinguishable from signal in $M(K\pi)$ but features a square root-like shape in $M(D^0\pi_s)$, which is subtracted from the signal when a D^{*+} mass fit is performed. Three random tracks which accidentally meet the selection requirements have a smooth $M(K\pi)$ distribution and the same square root-like shape in $M(D^0\pi_s)$.

In order to extract the signal yields, the $M(D^0\pi_s)$ distribution is fitted for candidates lying in a narrow signal region in $M(K\pi)$ around the nominal D^0 mass. The shape parameters and the signal and background yields are determined independently in each decay time bin for D^{*+} and D^{*-} decays. In order to exploit the larger RS statistics and assuming that the RS and WS decays have the same signal shape in the $M(D^0\pi_s)$ distribution, the signal shape parameters are determined from the RS sample and then fixed in the WS fit. The observed WS to RS signal ratios $\tilde{R}$, are then related to the ratios R as [38]

$$\tilde{R}(t)^{\pm} = \epsilon_r^{\pm} R(t)(1 - \Delta_B^{\pm}) + p^{\pm} \tag{3.4}$$

where $\epsilon_r^{\pm} \equiv \epsilon(K^+\pi^-)/\epsilon(K^-\pi^+)$ is the ratio of the $K^{\pm}\pi^{\mp}$ detection efficiencies, accounting for instrumental asymmetries in the $K\pi$ reconstruction efficiencies, mainly caused by the K^- mesons having a larger interaction cross section with matter than K^+ mesons; Δ_B accounts for biases due to the contamination of secondary D^0 candidates coming from b-hadron decays whose reconstructed decay time is systematically larger because calculated with respect to the primary vertex which does not coincide with the D^0 production vertex; $p^{\pm}$ describes backgrounds peaking in $M(D^0\pi_s^+)$ of the WS sample which bias the signal yield, coming from RS events whose both final

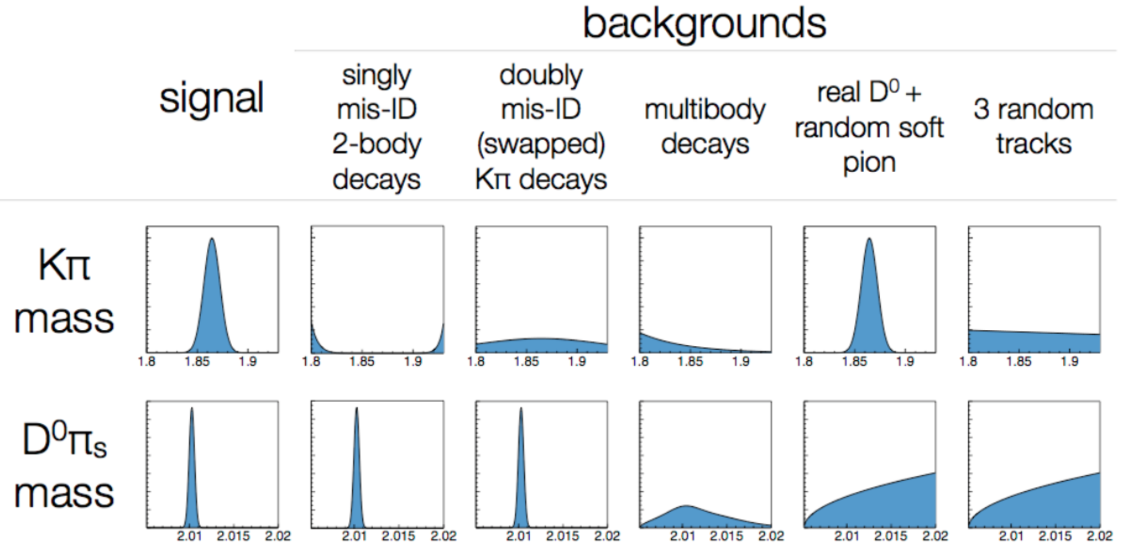

Figure 3.1: Distributions in the $M(K\pi)$ and $M(D^0\pi_s)$ mass for signal and the various background components [37].

state particles mass hypotheses have been misidentified. The presence of secondary D^0 decays and peaking backgrounds is reduced through highly selective requirements on signal candidates, as described in the following. Their residual contribution must then be evaluated. The production asymmetry between D^{*+} and D^{*-} cancel out in the ratio, as well as the asymmetries in detecting soft pions of different charges and thus they do not appear in Eq. (3.4). Decay time resolution and acceptance effects, affecting symmetrically WS and RS samples, cancel to a high level of approximation in the ratio.

3.2 Data sample and events selection

The data sample used in this analysis corresponds to 0.3fb^{-1} and 1.6fb^{-1} of integrated luminosity recorded at $\sqrt{s} = 13\text{TeV}$ during 2015 and 2016, respectively.

The RS (WS) candidates are reconstructed on-line at the second stage of the software trigger (Hlt2). All tracking quantities used in the analysis (*e.g.* momenta of particles and decay time of the D^0 candidate) are refitted offline with a primary vertex constraint, in order to improve mass resolution and thus increase the signal purity. Impact parameter related quantities are instead not required to meet this constraint, in order to avoid refitting biases.

The software trigger requirements, together with the offline selection, are displayed in Tab. 3.1. In the offline selection, RS and WS candidates are required to meet specific conditions on the trigger category, namely the D^0 candidate to be `TOS` on `L0Hadron` or the D^{*+} candidate to be `TIS` with respect to `L0Global` trigger algorithm, and the D^0 candidate to be `TOS` on the logical or of `Hlt1TrackMVA` and `Hlt1TwoTrackMVA` trigger algorithm, where (`D0` and `Dst` are the particles associated with the decay products firing the specific trigger category)

- `L0` is the hardware trigger, where `Hadron` uses the informations coming from the hadronic calorimeter, while `Global` uses the informations coming from all the subsystems involved in the hardware trigger;

- `Hlt1` is the first stage of the software trigger, where `TrackMVA` and `TwoTrackMVA` are multivariate algorithms running on variables related to single tracks and combinations of two tracks, respectively;

- `TOS` (Trigger On Signal) applies the trigger selection to decay products of the signal candidate while `TIS` (Trigger Independent of Signal) to all the decay products not coming from the signal candidate in the same event.

The contamination from misidentified $h^+h^{(\prime)-}$ events is reduced by imposing tighter particle identification criteria, with respect to the trigger selection, on the kaon and the pion coming from the D^0 decay, namely $\Delta\log\mathcal{L}_{K-\pi}(K) > 8$ and $\Delta\log\mathcal{L}_{K-\pi}(\pi) < -5$, where $\Delta\log\mathcal{L}_{K-\pi}(P)$ has been defined in Eq. (2.2). The contribution from D^0 coming from b-hadron decays is suppressed by imposing the significance of the impact parameter, IPχ^2, of the D^0 and soft pion candidates not to exceed 9 and 25, respectively. Nevertheless, the residual amount of doubly misidentified RS events and secondary D^0 decays need to be estimated, separately for $D^{*\pm}$

tagged events and decay time bins, since their potentially different time evolution may mimic CP violation in mixing.

WS events whose D^0 candidate is in common with a RS event having $|M(D^0\pi_s) - m_{D^{*+}}| < 0.9\,\mathrm{MeV/c}^2$ (corresponding to approximately 3σ around the central value $m_{D^{*+}}$, σ being the experimental resolution on $M(D^0\pi_s)$), where $m_{D^{*+}}$ is the nominal D^{*+} mass ($2010.26\,\mathrm{MeV/c}^2$), are then removed from the WS sample, further reducing the combinatorial background in the WS sample. Due to the relative abundance of RS versus WS signal, candidates matching this criterion are more likely to be genuine RS decays and are therefore vetoed from the WS sample.

Figure 3.2 shows the $M(K\pi)$ distributions for the selected RS (left) and WS (right) candidates, separately for 2015 (top) and 2016 (bottom) data. In order to extract the signal yields, D^0 candidates are selected in a narrow signal region of $M(K\pi)$, corresponding to $|M(K\pi) - m_{D^0}| < 24\,\mathrm{MeV/c}^2$ (approximately 3σ around the central value m_{D^0}, σ being the experimental resolution on $M(K\pi)$), where m_{D^0} is the nominal D^0 mass ($1864.83\,\mathrm{MeV/c}^2$). They are further required to satisfy $|M(KK) - m_{D^0}| > 40\,\mathrm{MeV/c}^2$ and $|M(\pi\pi) - m_{D^0}| > 40\,\mathrm{MeV/c}^2$ ($\approx 5\sigma$ away from m_{D^0}), where $M(KK)$ and $M(\pi\pi)$ are the D^0 masses calculated with KK and $\pi\pi$ mass hypotheses for the decay products, respectively, in order to reduce the contamination from singly misidentified $D^0 \to K^+K^-$ and $D^0 \to \pi^+\pi^-$ decays and minimize the contribution from other misreconstructed multibody charm decays. The combinatorial background is subtracted thanks to the distinctive square root-like shape in $M(D^0\pi_s)$ and further reduced with a multivariate selection.

	Requirement		
Quantity	Hlt2	Offline	Units
$p_T(K,\pi)$	> 800	–	MeV/c
$p(K,\pi)$	> 5	–	GeV/c
IP$\chi^2(K,\pi)$	> 4	–	–
$\Delta\log\mathcal{L}_{K-\pi}(K)$	> 5	$> 8^*$	–
$\Delta\log\mathcal{L}_{K-\pi}(\pi)$	< 5	$< -5^*$	–
$p_T(D^0)$	> 2	–	GeV/c
IP$\chi^2(D^0)$	–	$< 9^*$	–
D^0 vertex fit χ^2/ndf	< 10	–	–
D^0 pointing angle (a.k.a. acosDIRA)	> 17.3	–	mrad
Distance of closest approach of D^0 daugthers (a.k.a. DOCA)	> 0.1	–	mm
p_T of at least one of the D^0 daugthers	> 1.5	–	GeV/c
$M(K\pi)$	$[1.715, 2.015]$	$[1.84084, 1.88884]^*$	GeV/c^2
$\|M(KK,\pi\pi) - m_{D^0}\|$	–	$> 40^*$	MeV/c^2
$p_T(\pi_s)$	> 100	–	MeV/c
IP$\chi^2(\pi_s)$	–	$< 25^*$	–
D^* vertex fit χ^2/ndf	< 25	–	–
$M(K\pi\pi_s) - M(K\pi)$	< 160	–	MeV/c^2
`D0_L0Hadron_TOS || Dst_L0Global_TIS`	–	True*	–
`D0_Hlt1TrackMVA_TOS || D0_Hlt1TwoTrackMVA_TOS`	–	True*	–
D^* candidates per event (a.k.a. `totCandidates`)	–	1^*	–
BDT output	–	> 0	–
Veto on WS candidates matched to RS candidates	–	True	–

Table 3.1: Summary of the selection criteria. Offline requirements marked with an asterisk are applied before the data-driven optimization of the BDT cut.

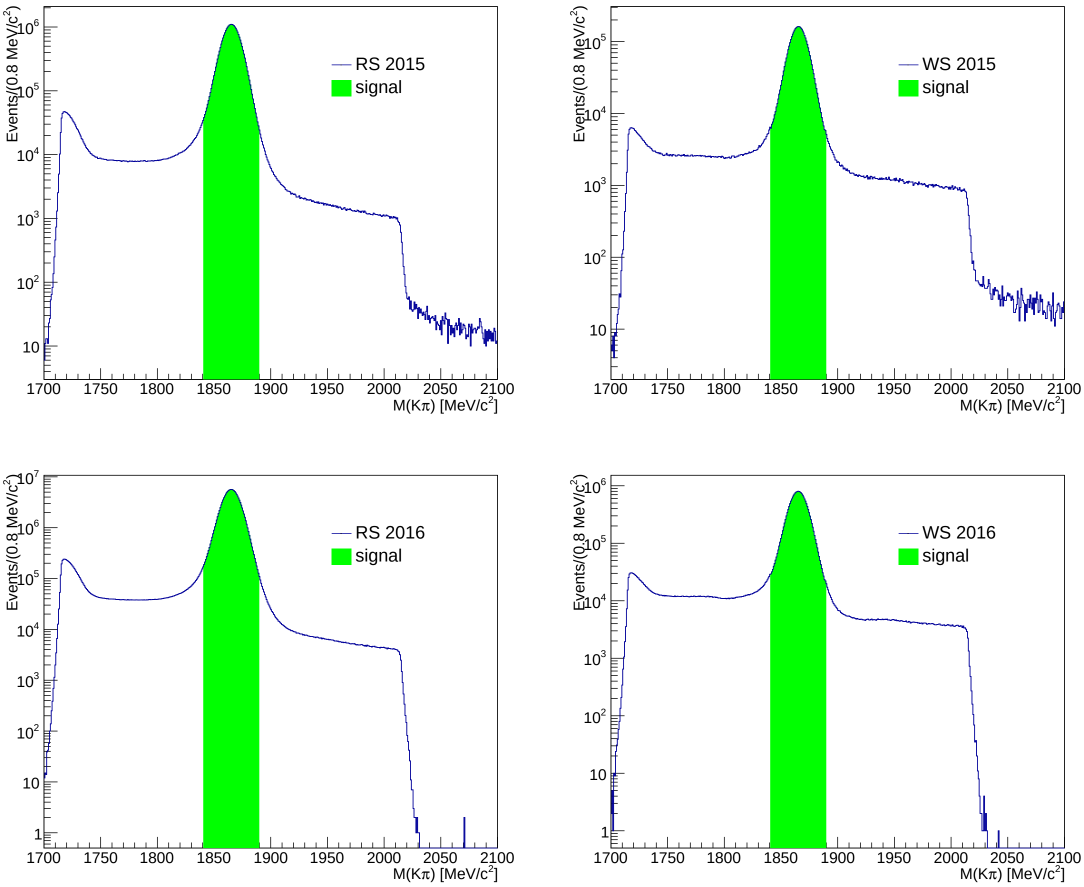

Figure 3.2: $K\pi$-mass distribution of selected RS (left) and WS (right) candidates, separately for 2015 (top) and 2016 (bottom) data. The signal regions are highlighted in green and a logarithmic scale is used on the vertical axis.

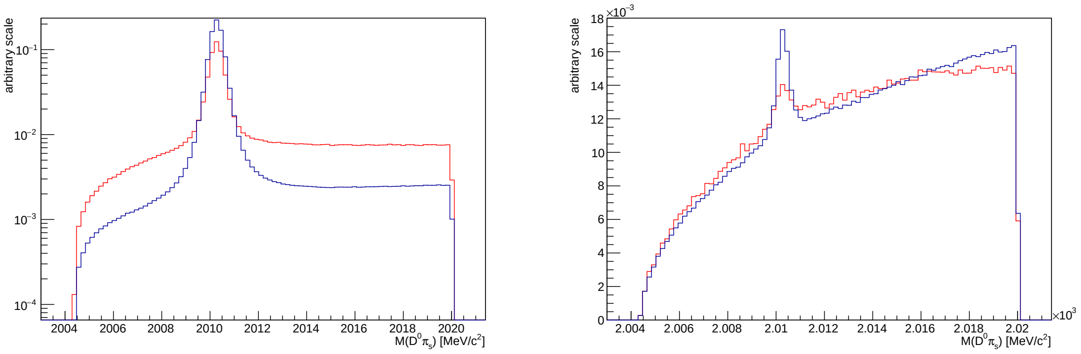

Figure 3.3: Normalized RS (left) and WS (right) $M(D^0\pi_s)$ distributions for one candidate per event (blue) and more than one candidate per event (red) before applying the multivariate optimization. The RS (WS) subsample with more than one candidates per event corresponds to $\approx 15\%$ ($\approx 22\%$) the size of the subsample with one candidate per event in the selected invariant mass region.

3.2.1 Optimization of the offline selection

It is observed that the dominant background in the WS sample, coming from real D^0 decays associated with uncorrelated pions from the primary vertex (random-pions), can be suppressed by removing events where more than one WS or RS candidate per event is present, with only a small loss in signal efficiency. In fact, the $M(D^0\pi_s)$ distribution of WS candidates coming from events with more than one candidate (shown in red in Fig. 3.3, right) exhibits a low signal purity, and are therefore vetoed from the sample under analysis.

The random-pion component is further suppressed with a multivariate selection based on a boosted decision tree (BDT) algorithm (AdaBoost). The BDT is implemented in TMVA [39] and discriminates between various kinematic, particle identification and track fit quality variables of the π_s and the number of tracks in the event. The classifier receives in input the variable distributions of RS events with one candidate per event in the $|M(D^0\pi_s) - m_{D^*}| < 0.9\,\mathrm{MeV}/c^2$ invariant mass window, which are almost pure in signal (see Fig. 3.4, bottom right, in blue), as representative of the WS signal sample. WS events with more than one D^0 candidate per event and $2004.4 < M(D^0\pi_s) < 2020\,\mathrm{MeV/c}^2$ are used as background samples. The invariant mass window is chosen such as their D^{*+} mass distribution is highly enriched in combinatorial background (see Fig. 3.4, bottom right, in red), as expected for suppressed decays. The signal and background distributions of the variables used to train the BDT are shown in Fig. 3.4. Their statistical separation is reported in Tab. 3.2, while their correlation matrices are reported in Fig. 3.5. The cut on the BDT output variable is chosen by maximizing the $S/\sqrt{S+B}$ figure of merit, where S is the RS signal yield scaled by 0.4%, corresponding to the time integrated fraction of WS decays. B is the combinatorial background fitted in the RS sample. The BDT output variable distribution is shown in Fig. 3.6, along with the signal significance and the efficiencies on signal and background samples as a function of the lower BDT threshold. The optimal cut is found to be BDT>0, corresponding to a 79% signal efficiency versus a 48% background efficiency.

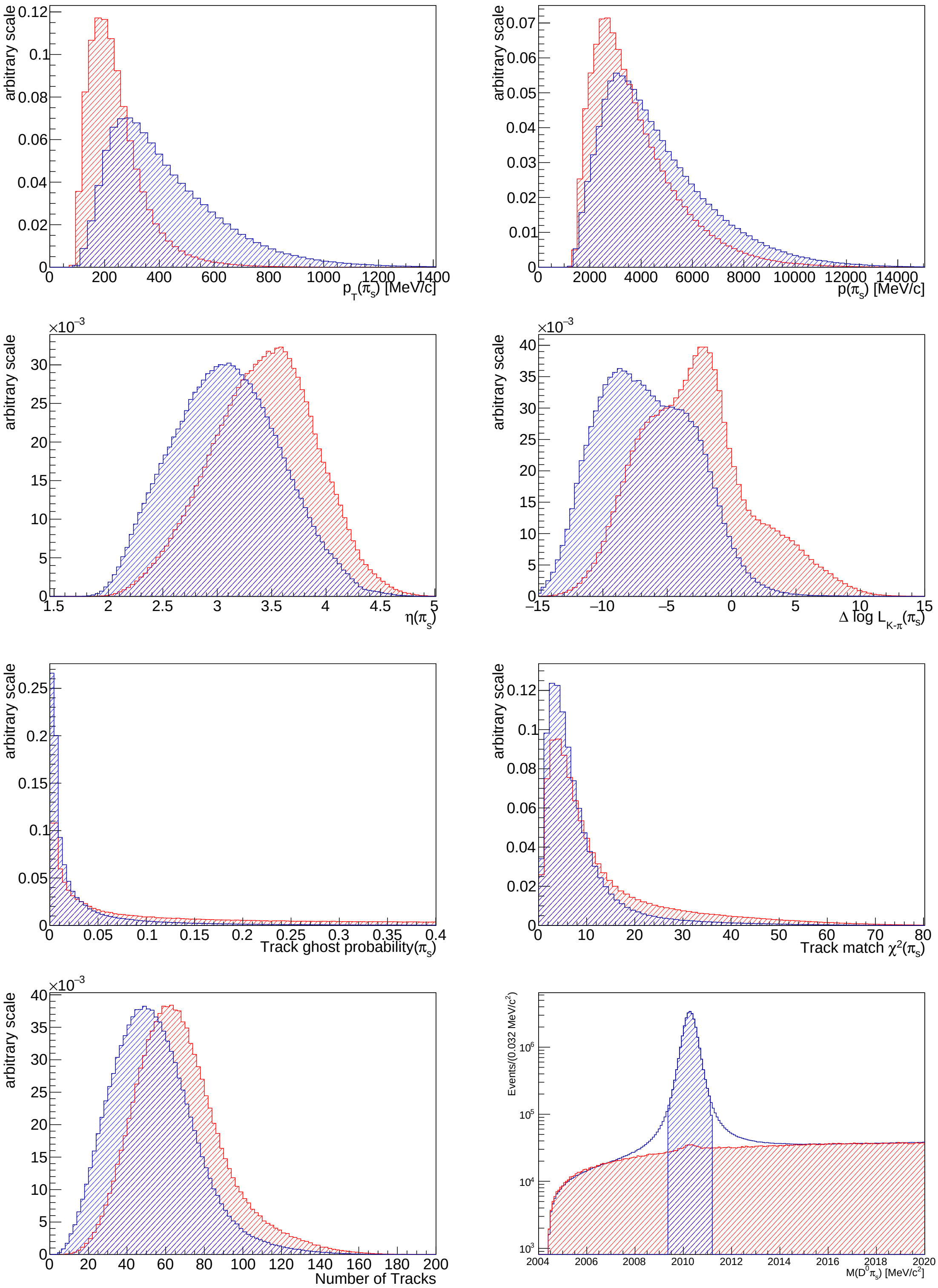

Figure 3.4: Signal (blue) and background (red) distributions used to train the multivariate classifier and D^{*+} mass distributions (bottom right) of the subsamples representing signal and background (in logarithmic scale, highlighted in blue and in red, respectively, the background distribution is scaled by a factor of five).

Quantity	Statistical separation
$p_T(\pi_s)$	0.2771
$\Delta\log\mathcal{L}_{e-\pi}(\pi_s)$	0.1858
Track ghost probability of the π_s	0.1386
$\eta(\pi_s)$	0.1086
$\#$ of tracks in the event	0.0927
$p(\pi_s)$	0.0491
Track match-χ^2 of the π_s	0.0456

Table 3.2: List of discriminating variables used as input to the BDT, together with their signal-to-background statistical separation.

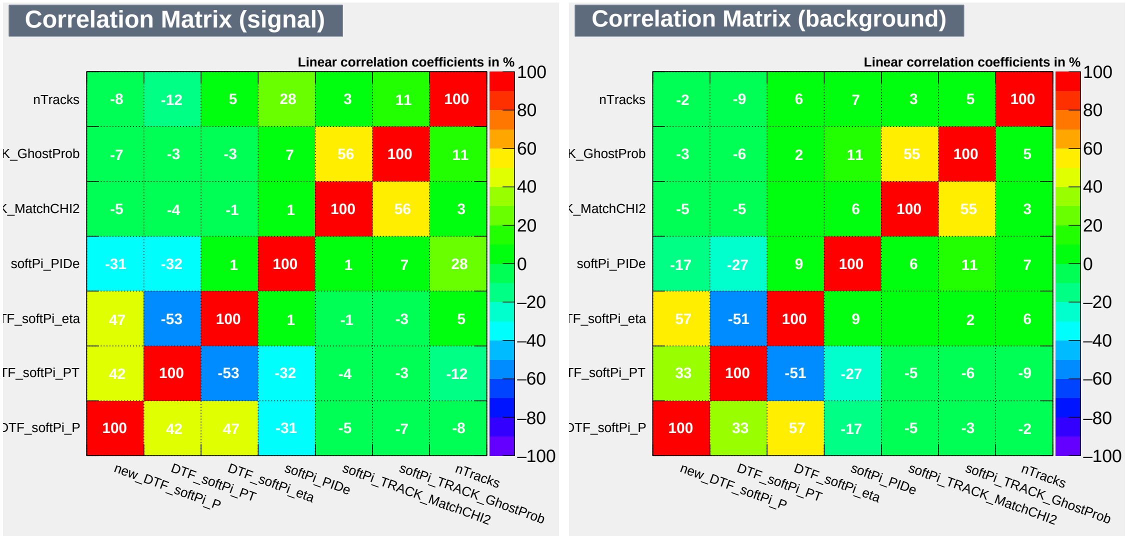

Correlation Matrix (signal)

	new_DTF_softPi_P	DTF_softPi_PT	DTF_softPi_eta	softPi_PIDe	softPi_TRACK_MatchCHI2	softPi_TRACK_GhostProb	nTracks
nTracks	-8	-12	5	28	3	11	100
K_GhostProb	-7	-3	-3	7	56	100	11
_MatchCHI2	-5	-4	-1	1	100	56	3
softPi_PIDe	-31	-32	1	100	1	7	28
TF_softPi_eta	47	-53	100	1	-1	-3	5
TF_softPi_PT	42	100	-53	-32	-4	-3	-12
DTF_softPi_P	100	42	47	-31	-5	-7	-8

Correlation Matrix (background)

	new_DTF_softPi_P	DTF_softPi_PT	DTF_softPi_eta	softPi_PIDe	softPi_TRACK_MatchCHI2	softPi_TRACK_GhostProb	nTracks
nTracks	-2	-9	6	7	3	5	100
K_GhostProb	-3	-6	2	11	55	100	5
_MatchCHI2	-5	-5		6	100	55	3
softPi_PIDe	-17	-27	9	100	6	11	7
TF_softPi_eta	57	-51	100	9		2	6
TF_softPi_PT	33	100	-51	-27	-5	-6	-9
DTF_softPi_P	100	33	57	-17	-5	-3	-2

Figure 3.5: Correlation matrices for signal (left) and background (right) variables used to train the BDT.

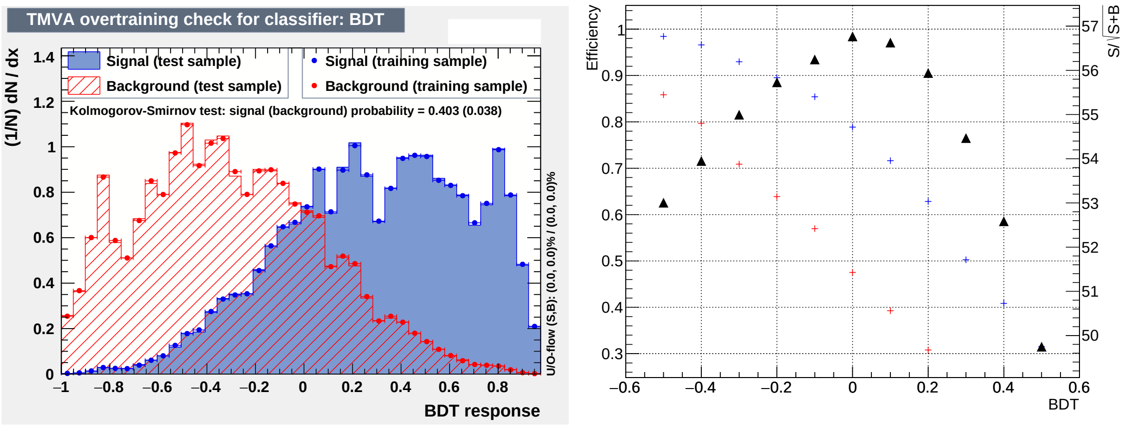

Figure 3.6: Left: BDT distributions for signal (blue) and background (red), separately for the training (points) and test samples (solid lines). Right: signal significance as a function of the lower BDT threshold (black triangles), signal and background efficiencies (blue and red crosses, respectively).

3.3 Determination of WS and RS yields

Signal yields are extracted from the invariant mass distributions of D^{*+} and D^{*-} events, which feature a narrower resolution with respect to the D^0 invariant mass. The invariant mass distribution is modelled by taking into account the signal and combinatorial background shapes, in order to separate their contributions in the fit. The data sample is then divided in bins of the D^0 decay time in order to study the time evolution of the WS over RS yield ratios.

3.3.1 Mass fit model

The signal is described by a Johnson SU function [40],

$$\mathscr{J}(x|\mu,\sigma,\delta,\gamma) = \frac{e^{-\frac{1}{2}\left[\gamma \,+\, \delta\,\sinh^{-1}\left(\frac{x-\mu}{\sigma}\right)\right]^2}}{\sqrt{1+\left(\frac{x-\mu}{\sigma}\right)^2}}, \tag{3.5}$$

that accounts for most of the asymmetric tail of the distribution, mainly due to the radiative energy loss of the charged kaons in the final state, added to three independent Gaussian distributions for the central core, yielding

$$\begin{gathered}\wp_{\rm sgn}(m|\boldsymbol{\theta}_{\rm sgn}) = f_J\,\mathscr{J}(m|m_{D^*}+\mu_J,\sigma_J,\delta_J,\gamma_J) + (1-f_J)\left[f_{G1}\mathscr{G}(m|m_{D^*}+\mu_{G1},\sigma_{G1})\right.\\ \left.+(1-f_{G1})f_{G2}\mathscr{G}(m|m_{D^*}+\mu_{G2},\sigma_{G2}) + (1-f_{G1})(1-f_{G2})\mathscr{G}(m|m_{D^*}+\mu_{G3},\sigma_{G3})\right].\end{gathered} \tag{3.6}$$

The signal parameters $\boldsymbol{\theta}_{\rm sgn}$ include the relative fraction f_J between the Johnson and the Gaussian components; the relative fraction f_{Gi} of each Gaussian; the shift from the known D^{*+} mass of the Johnson distribution's core μ_J, and the three Gaussians means μ_{Gi}; the widths of the Johnson distribution's core σ_J and the three Gaussians widths, σ_{Gi}. The parameters δ_J and γ_J determine the asymmetry in the Johnson distribution's tails.

The background from random associations of a pion with a genuine D^0 decay is purely combinatoric in origin and modelled using an empirical shape, given by

$$\wp_{\rm bkg}(m|\boldsymbol{\theta}_{\rm bkg}) = \frac{1}{\mathscr{N}_B}\,\left[m-(m_{D^0}+m_\pi)\right]^b e^{-c[m-(m_{D^0}+m_\pi)]}.$$

The total probability density function reads

$$\wp(m) = N_{\rm sgn}\wp_{\rm sgn}(m|\boldsymbol{\theta}_{\rm sgn}) + N_{\rm bkg}\wp_{bkg}(m|\boldsymbol{\theta}_{\rm bkg}),$$

where each function is defined for masses greater than a threshold value of $m_{D^0} + m_{\pi^+} \approx 2.004\,\mathrm{GeV/c^2}$ and is properly normalized in the fit range, which extends from threshold up to $2.02\,\mathrm{GeV/c^2}$.

Shape parameters and size of both signal and random pions background are determined by the fit independently in each decay-time bin for the D^{*+} and D^{*-} samples, with the only assumptions that WS and RS $M(D^0\pi_s^+)$ signal shapes are the same. For each decay-time bin, it is first fitted the $M(D^0\pi_s^+)$ distribution of

RS candidates, leaving all parameters free to float. The resulting signal shape parameters are then used as fixed quantities in the subsequent fit to the $M(D^0\pi_s^+)$ distribution of WS candidates. This approach exploits the much larger RS sample to precisely determine the signal shape, and how it varies as a function of decay time, to fit precisely the WS sample.

3.3.2 2015-2016 time integrated yields

Figure 3.7 shows the time-integrated, CP-averaged $D^0\pi_s$ mass distribution for the RS (left) and WS (right) candidates in the corresponding D^0 signal windows, for 2015 (top) and 2016 (bottom) data, with fit projections overlaid. Clean D^{*+} signals are visible overlapping a background dominated by random associations of real D^0 decays with uncorrelated pions. This background is almost negligible in the RS sample. The mass distributions of WS candidates matched to RS events in a 3σ signal region in the RS $D^0\pi_s$ mass are also reported. They show no visible peaking structure and they are therefore removed from the WS sample, in order to reduce background and increase signal purity.

In 2015 [2016] time integrated data sample, $(93.0 \pm 0.5) \times 10^3$ $[(480 \pm 1) \times 10^3]$ WS and $(22.86 \pm 0.01) \times 10^6$ $[(117.34 \pm 0.02) \times 10^6]$ RS events are reconstructed, corresponding to a total yield that is approximately 2.5 times larger than that of the Run 1 analysis [37].

3.3.3 Time dependent yield ratios

The signal yields are then determined in each decay-time interval, separately for 2015 and 2016 data and for magnet polarity, using binned chi-square fits of the $M(D^0\pi_s)$ distributions. The signal yields measured in the D^{*+} and D^{*-} samples are reported in Tabs. 3.3 and 3.4 along with the WS to RS ratios used to determine the mixing parameters in the mixing fit. The decay time bins are chosen so as to equally distribute the available statistic in the whole decay time range. Mass fits projections used to extract the signal yields in decay time bins and for different magnet polarity are reported in App. A.

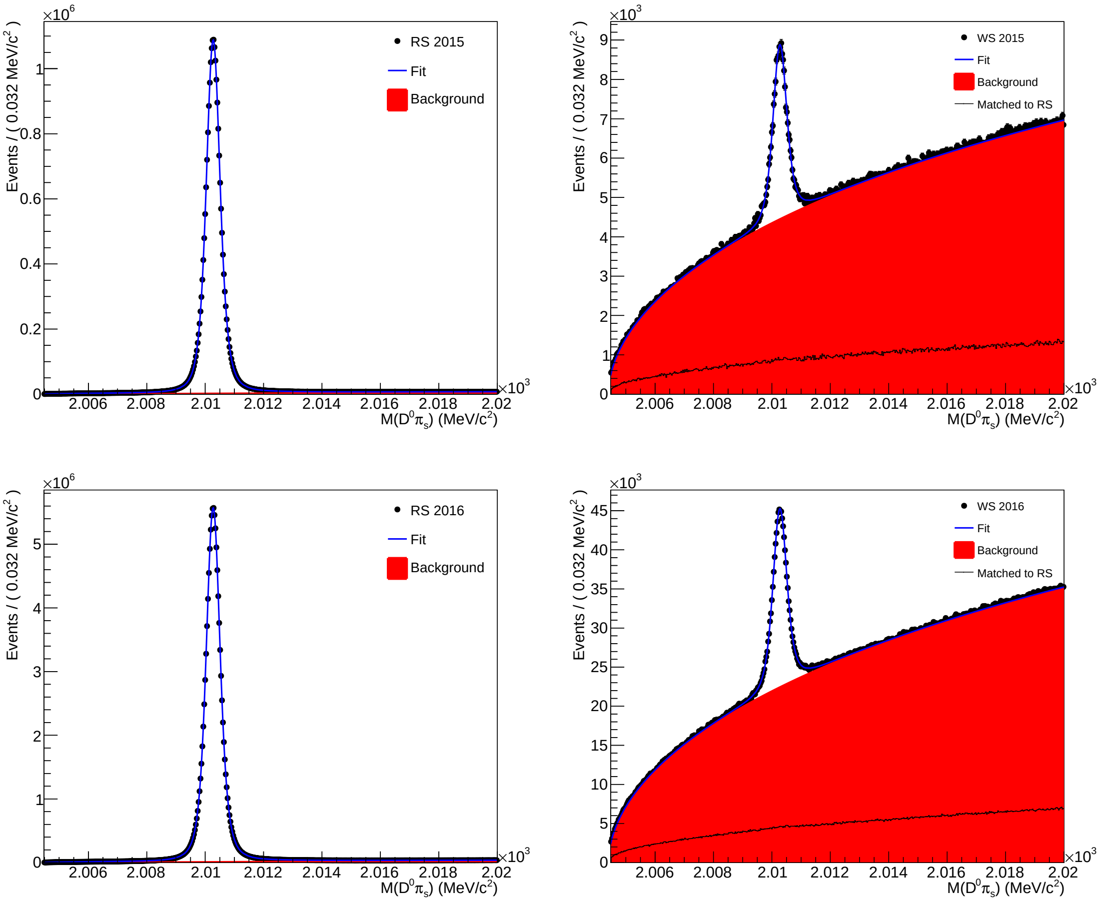

Figure 3.7: $D^0\pi_s^+$-mass distribution for the RS (left) and WS (right) candidates selected in the corresponding $M(K\pi)$ signal regions in 2015 (top) and 2016 (bottom) data.

Decay-time bin	$\langle t \rangle$	$\langle t^2 \rangle$	RS^+ (10^4)	RS^- (10^4)	WS^+ (10^4)	WS^- (10^4)	R^+ (10^{-3})	R^- (10^{-3})
0.00 - 0.80	0.640	0.522	64.79 ± 0.18	67.64 ± 0.12	0.246 ± 0.009	0.253 ± 0.009	3.80 ± 0.14	3.74 ± 0.13
0.80 - 1.00	0.901	0.869	52.48 ± 0.21	55.09 ± 0.17	0.200 ± 0.008	0.200 ± 0.008	3.81 ± 0.15	3.63 ± 0.15
1.00 - 1.20	1.098	1.264	50.07 ± 0.19	52.53 ± 0.27	0.202 ± 0.008	0.208 ± 0.008	4.03 ± 0.16	3.96 ± 0.15
1.20 - 1.35	1.274	1.666	33.94 ± 0.19	35.26 ± 0.14	0.128 ± 0.007	0.127 ± 0.007	3.77 ± 0.21	3.60 ± 0.20
1.35 - 1.50	1.424	2.070	30.21 ± 0.13	31.72 ± 0.18	0.120 ± 0.006	0.128 ± 0.006	3.97 ± 0.20	4.04 ± 0.19
1.50 - 1.75	1.621	2.698	42.93 ± 0.17	45.13 ± 0.21	0.181 ± 0.008	0.178 ± 0.008	4.22 ± 0.19	3.94 ± 0.18
1.75 - 2.00	1.870	3.569	34.36 ± 0.21	36.09 ± 0.19	0.141 ± 0.007	0.140 ± 0.007	4.10 ± 0.21	3.88 ± 0.20
2.00 - 2.25	2.120	4.567	27.44 ± 0.17	29.04 ± 0.24	0.121 ± 0.006	0.119 ± 0.006	4.41 ± 0.22	4.10 ± 0.21
2.25 - 2.50	2.370	5.688	21.39 ± 0.16	22.38 ± 0.11	0.081 ± 0.005	0.091 ± 0.006	3.79 ± 0.24	4.07 ± 0.27
2.50 - 3.00	2.729	7.594	29.58 ± 0.11	31.32 ± 0.12	0.124 ± 0.006	0.127 ± 0.007	4.19 ± 0.20	4.05 ± 0.22
3.00 - 4.00	3.419	11.970	29.09 ± 0.07	30.65 ± 0.10	0.132 ± 0.006	0.138 ± 0.007	4.54 ± 0.21	4.50 ± 0.23
4.00 - 5.00	4.418	19.805	10.86 ± 0.05	11.55 ± 0.13	0.064 ± 0.004	0.064 ± 0.004	5.89 ± 0.37	5.54 ± 0.35
5.00 - 20.0	6.011	37.145	6.52 ± 0.07	6.82 ± 0.03	0.040 ± 0.004	0.040 ± 0.003	6.13 ± 0.62	5.87 ± 0.44
0.00 - 0.80	0.643	0.525	101.41 ± 0.30	101.73 ± 0.19	0.394 ± 0.011	0.386 ± 0.011	3.89 ± 0.11	3.79 ± 0.11
0.80 - 1.00	0.901	0.869	84.82 ± 0.29	84.66 ± 0.18	0.321 ± 0.010	0.313 ± 0.010	3.78 ± 0.12	3.70 ± 0.12
1.00 - 1.20	1.098	1.264	80.68 ± 0.28	81.15 ± 0.16	0.317 ± 0.010	0.309 ± 0.010	3.93 ± 0.12	3.81 ± 0.12
1.20 - 1.35	1.274	1.666	54.50 ± 0.18	54.82 ± 0.16	0.215 ± 0.008	0.203 ± 0.008	3.94 ± 0.15	3.70 ± 0.15
1.35 - 1.50	1.424	2.070	49.10 ± 0.18	49.29 ± 0.17	0.193 ± 0.008	0.191 ± 0.008	3.93 ± 0.16	3.88 ± 0.16
1.50 - 1.75	1.621	2.699	69.13 ± 0.18	69.92 ± 0.25	0.267 ± 0.010	0.272 ± 0.010	3.86 ± 0.15	3.89 ± 0.14
1.75 - 2.00	1.870	3.571	55.68 ± 0.24	56.27 ± 0.21	0.231 ± 0.009	0.218 ± 0.009	4.15 ± 0.16	3.87 ± 0.16
2.00 - 2.25	2.120	4.567	44.02 ± 0.13	44.44 ± 0.16	0.200 ± 0.008	0.189 ± 0.008	4.54 ± 0.18	4.25 ± 0.18
2.25 - 2.50	2.370	5.688	34.39 ± 0.10	34.86 ± 0.10	0.151 ± 0.007	0.143 ± 0.007	4.39 ± 0.20	4.10 ± 0.20
2.50 - 3.00	2.730	7.595	48.11 ± 0.13	49.04 ± 0.25	0.229 ± 0.008	0.220 ± 0.008	4.76 ± 0.17	4.49 ± 0.16
3.00 - 4.00	3.419	11.972	47.20 ± 0.14	47.80 ± 0.13	0.237 ± 0.008	0.226 ± 0.008	5.02 ± 0.17	4.73 ± 0.17
4.00 - 5.00	4.418	19.802	17.65 ± 0.09	17.69 ± 0.05	0.088 ± 0.005	0.093 ± 0.005	4.99 ± 0.28	5.26 ± 0.28
5.00 - 20.0	6.010	37.133	10.57 ± 0.08	10.64 ± 0.08	0.057 ± 0.004	0.057 ± 0.004	5.39 ± 0.38	5.36 ± 0.38

Table 3.3: RS and WS signal yields and their ratios, for D^{*+} and D^{*-} candidates separately, as resulting from the mass fits in each decay time bin for 2015 magnet-up (top) and magnet-down (bottom) data.

Decay-time bin	$\langle t \rangle$	$\langle t^2 \rangle$	RS^+ (10^4)	RS^- (10^4)	WS^+ (10^4)	WS^- (10^4)	R^+ (10^{-3})	R^- (10^{-3})
0.00 - 0.80	0.641	0.523	393.21 ± 0.56	404.99 ± 0.45	1.519 ± 0.021	1.500 ± 0.021	3.86 ± 0.05	3.70 ± 0.05
0.80 - 1.00	0.901	0.869	315.63 ± 0.39	328.15 ± 0.35	1.206 ± 0.020	1.224 ± 0.019	3.82 ± 0.06	3.73 ± 0.06
1.00 - 1.20	1.099	1.265	309.14 ± 0.52	321.32 ± 0.38	1.207 ± 0.020	1.197 ± 0.019	3.90 ± 0.07	3.73 ± 0.06
1.20 - 1.35	1.274	1.666	215.15 ± 0.53	223.01 ± 0.36	0.849 ± 0.017	0.846 ± 0.017	3.95 ± 0.08	3.79 ± 0.08
1.35 - 1.50	1.424	2.070	194.47 ± 0.28	202.97 ± 0.36	0.766 ± 0.016	0.792 ± 0.016	3.94 ± 0.08	3.90 ± 0.08
1.50 - 1.75	1.621	2.699	280.25 ± 0.41	293.40 ± 0.47	1.129 ± 0.019	1.138 ± 0.019	4.03 ± 0.07	3.88 ± 0.07
1.75 - 2.00	1.870	3.570	227.60 ± 0.37	236.88 ± 0.34	0.938 ± 0.018	0.963 ± 0.018	4.12 ± 0.08	4.07 ± 0.08
2.00 - 2.25	2.120	4.567	181.14 ± 0.31	189.23 ± 0.33	0.767 ± 0.016	0.764 ± 0.016	4.23 ± 0.09	4.04 ± 0.08
2.25 - 2.50	2.370	5.690	142.95 ± 0.25	149.91 ± 0.39	0.632 ± 0.014	0.621 ± 0.014	4.42 ± 0.10	4.14 ± 0.09
2.50 - 3.00	2.730	7.595	201.07 ± 0.26	209.68 ± 0.28	0.904 ± 0.017	0.934 ± 0.017	4.50 ± 0.08	4.45 ± 0.08
3.00 - 4.00	3.419	11.970	199.03 ± 0.27	207.96 ± 0.27	0.959 ± 0.017	0.937 ± 0.017	4.82 ± 0.09	4.51 ± 0.08
4.00 - 5.00	4.419	19.810	74.71 ± 0.33	77.96 ± 0.25	0.384 ± 0.011	0.384 ± 0.011	5.14 ± 0.15	4.93 ± 0.14
5.00 - 20.0	6.011	37.159	44.34 ± 0.10	46.87 ± 0.30	0.262 ± 0.009	0.263 ± 0.009	5.91 ± 0.20	5.61 ± 0.20
0.00 - 0.80	0.642	0.524	436.08 ± 0.57	440.32 ± 0.44	1.664 ± 0.022	1.616 ± 0.022	3.82 ± 0.05	3.67 ± 0.05
0.80 - 1.00	0.901	0.869	359.65 ± 0.61	362.82 ± 0.44	1.408 ± 0.021	1.362 ± 0.021	3.91 ± 0.06	3.75 ± 0.06
1.00 - 1.20	1.099	1.264	347.43 ± 0.64	350.53 ± 0.47	1.378 ± 0.021	1.338 ± 0.021	3.97 ± 0.06	3.82 ± 0.06
1.20 - 1.35	1.274	1.666	235.48 ± 0.42	238.12 ± 0.35	0.925 ± 0.018	0.913 ± 0.017	3.93 ± 0.08	3.83 ± 0.07
1.35 - 1.50	1.424	2.070	212.10 ± 0.41	215.58 ± 0.50	0.870 ± 0.017	0.834 ± 0.016	4.10 ± 0.08	3.87 ± 0.07
1.50 - 1.75	1.621	2.698	300.17 ± 0.36	304.23 ± 0.42	1.246 ± 0.020	1.221 ± 0.020	4.15 ± 0.07	4.01 ± 0.07
1.75 - 2.00	1.870	3.570	242.67 ± 0.51	244.14 ± 0.33	1.048 ± 0.018	0.989 ± 0.018	4.32 ± 0.07	4.05 ± 0.07
2.00 - 2.25	2.120	4.567	192.17 ± 0.40	193.98 ± 0.32	0.827 ± 0.016	0.813 ± 0.016	4.30 ± 0.08	4.19 ± 0.08
2.25 - 2.50	2.370	5.689	151.43 ± 0.38	152.43 ± 0.26	0.665 ± 0.015	0.632 ± 0.014	4.39 ± 0.10	4.15 ± 0.09
2.50 - 3.00	2.730	7.595	211.09 ± 0.32	213.69 ± 0.34	0.943 ± 0.017	0.945 ± 0.017	4.47 ± 0.08	4.42 ± 0.08
3.00 - 4.00	3.419	11.970	207.80 ± 0.27	210.50 ± 0.29	0.977 ± 0.018	0.986 ± 0.017	4.70 ± 0.09	4.68 ± 0.08
4.00 - 5.00	4.419	19.806	77.72 ± 0.22	78.45 ± 0.20	0.411 ± 0.011	0.396 ± 0.011	5.29 ± 0.14	5.05 ± 0.14
5.00 - 20.0	6.010	37.129	46.33 ± 0.18	47.13 ± 0.27	0.283 ± 0.009	0.271 ± 0.009	6.11 ± 0.20	5.75 ± 0.19

Table 3.4: RS and WS signal yields and their ratios, for D^{*+} and D^{*-} candidates separately, as resulting from the mass fits in each decay time bin for 2016 magnet-up (top) and magnet-down (bottom) data.

3.4 Peaking backgrounds

In this section, the impact of residual tails of misreconstructed and misidentified decays surviving the PID requirements in the accepted range of the D^0 mass is estimated. Such backgrounds are capable to produce a narrow enhancement in the $M(D^0\pi_s)$ distribution and therefore constitute potential sources of systematic biases. Kinematic correlations are used to study the contamination of $D^0 \to h^+h^{(')-}$ decays in which one or both final-state particles has been misidentified.

3.4.1 Kinematic separation of $D^0 \to h^+h^{(')-}$ decays

The invariant mass of two charged particles of momenta $\vec{p}_+$ and $\vec{p}_-$ and masses m_+ and m_- is given by

$$M_{+-}^2 = \left(\sqrt{p_+^2 + m_+^2} + \sqrt{p_-^2 + m_-^2}\right)^2 - \left(\vec{p}_+ + \vec{p}_-\right)^2 . \tag{3.7}$$

If the two charged particles originate from the two body decay of a D^0 meson, then $M_{+-}^2 = m_{D^0}^2$. In LHCb, one assigns a mass hypothesis, m_1 and m_2, to the two charged tracks, based on the information coming from the particle identification subsystems (in this case, from the two Ring-Imaging Cherenkov detectors, in order to distinguish between kaons and pions in a wide momentum range). The calculated mass for the two body object is thus given by

$$M_{12}^2 = \left(\sqrt{p_+^2 + m_1^2} + \sqrt{p_-^2 + m_2^2}\right)^2 - \left(\vec{p}_+ + \vec{p}_-\right)^2 . \tag{3.8}$$

If the mass hypothesis is wrongly assigned to one of the decay products ($m_+ \neq m_1$ and/or $m_- \neq m_2$) then the calculated two body mass is shifted with respect to the nominal D^0 mass

$$M_{12}^2 = m_{D^0}^2 - \Delta M^2, \tag{3.9}$$

where $\Delta M^2 = M_{+-}^2 - M_{12}^2$ is the difference between the two body mass calculated with correct and wrong mass hypothesis for the D^0 decay products. Taking into account the expressions in Eq. (3.7) and (3.8)

$$\begin{aligned} \Delta M^2 &= (m_+^2 - m_1^2) + (m_-^2 - m_2^2) \\ &+ 2p_+p_- \left(\sqrt{1+\left(\frac{m_+}{p_+}\right)^2}\sqrt{1+\left(\frac{m_-}{p_-}\right)^2} - \sqrt{1+\left(\frac{m_1}{p_+}\right)^2}\sqrt{1+\left(\frac{m_2}{p_-}\right)^2}\right) \end{aligned} \tag{3.10}$$

one obtains an approximated expression by expanding to first order in m/p the terms under square roots

$$\begin{aligned} \Delta M^2 &\approx (m_+^2 - m_1^2) + (m_-^2 - m_2^2) \\ &+ p_+p_- \left[\left(\frac{m_+}{p_+}\right)^2 + \left(\frac{m_-}{p_-}\right)^2 - \left(\frac{m_1}{p_+}\right)^2 - \left(\frac{m_2}{p_-}\right)^2\right] \\ &= \left(1+\frac{p_-}{p_+}\right)(m_+^2 - m_1^2) + \left(1+\frac{p_+}{p_-}\right)(m_-^2 - m_2^2) \\ &= \frac{2}{1+\beta^*}(m_+^2 - m_1^2) + \frac{2}{1-\beta^*}(m_-^2 - m_2^2) \end{aligned} \tag{3.11}$$

with signed momentum imbalance defined as

$$\beta^* \equiv q(\pi_s)\beta, \quad \beta = \frac{p_+ - p_-}{p_+ + p_-}, \tag{3.12}$$

where $q(\pi_s)$ is the charge of the tagging soft pion, useful when considering charged conjugated decays from $\overline{D}^0$ mesons, where $\beta \to -\beta$, in order to obtain the same relations for charged conjugate processes. The RS, WS and decays to two kaons and two pions final states are best separated in the $M_{12}-\beta^*$ plane when M_{12} is calculated with the pion mass hypothesis for both charged decay products, as expressed by the following equations, derived from Eq. 3.9 when considering Eq. 3.11,

$$\begin{aligned}
M^2(\pi^-\pi^+)[D^0 \to K^-\pi^+] &\approx m^2_{D^0} - \frac{2}{1-\beta^*}(m^2_K - m^2_\pi), \\
M^2(\pi^+\pi^-)[D^0 \to K^-\pi^+] &\approx m^2_{D^0} - \frac{2}{1+\beta^*}(m^2_K - m^2_\pi), \\
M^2(\pi^+\pi^-)[D^0 \to K^+K^+] &\approx m^2_{D^0} - \frac{4}{1-\beta^{*2}}(m^2_K - m^2_\pi), \\
M^2(\pi^+\pi^-)[D^0 \to K^+K^+] &= m^2_{D^0}.
\end{aligned} \tag{3.13}$$

A graphical representation of the dependence between the D^0 mass, calculated using the arbitrary $\pi^+\pi^-$ mass assignment to its decay products, $M(\pi^+\pi^-)$, and β^* for each $D^0 \to h^+h^{(\prime)-}$ decay mode is given in Fig. 3.8.

The same distribution for 2015 and 2016 data is reported in Fig. 3.9, where the contributions from $D^0 \to \pi^+\pi^-$ and $D^0 \to K^+K^-$ decays are clearly visible.

The possible physical backgrounds (*i.e.* not combinatorial) whose D^0 mass distribution tails can contribute into the signal region are the following:

- Hadronic three body $D^0 \to h^+h^{(\prime)-}\pi^0$ decays, such as $D^0 \to K^-\pi^+\pi^0$ ($BR \sim 14.3\%$), $D^0 \to \pi^+\pi^-\pi^0$ ($BR \sim 1.4\%$) and $D^0 \to K^+K^-\pi^0$ ($BR \sim 0.3\%$),

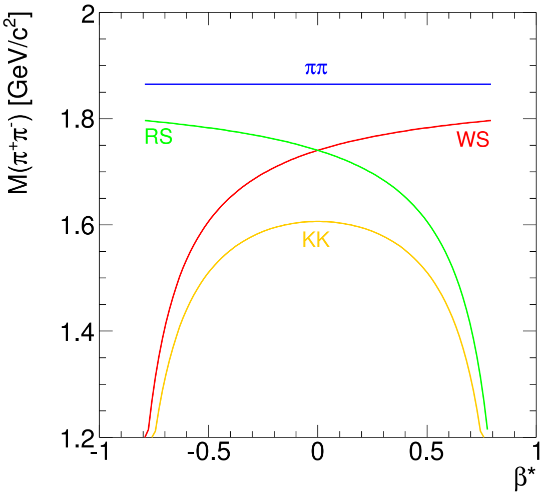

Figure 3.8: Analytic expressions of $M(\pi^+\pi^-)$ as a function of β^* for the four D^*-tagged $D^0 \to h^+h^{(\prime)-}$ decays modes

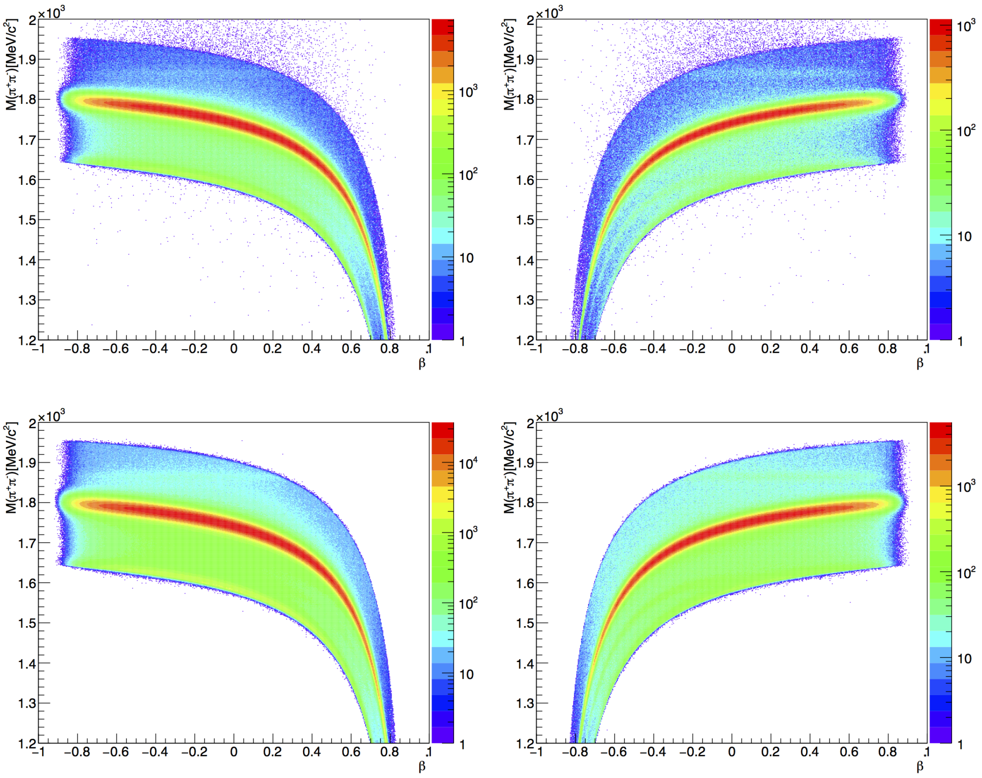

Figure 3.9: $M(\pi\pi)$ versus β^* distribution of RS (left) and WS (right) decays from the 2015 (top) and 2016 (bottom) data sample.

where the π^0 is not reconstructed and the kaon and/or the pion is assigned the pion and/or kaon mass hypothesis, respectively. These events fall in the low D^0 mass region, below the RS and WS bands of Fig. 3.8 (since one particle is lost), and their impact into the signal region is thus expected to be negligible;

- Semileptonic $D^0 \to h^-\ell^+X$ decays, such as $D^0 \to K^-e^+\nu_e$ ($BR \sim 3.5\%$), $D^0 \to K^-\mu^+\nu_\mu$ ($BR \sim 3.3\%$), where the lepton gets the pion mass hypothesis and the neutrino is not revealed, and $D^0 \to \pi^-e^+\nu_e$ ($BR \sim 0.3\%$), $D^0 \to \pi^-\mu^+\nu_\mu$ ($BR \sim 0.2\%$), where the pion gets the kaon mass hypothesis and the lepton the pion mass hypothesis (or vice versa) and the neutrino is not revealed. Their tails reach the high mass region, above the RS and WS bands of Fig. 3.8 (since the lepton gets a higher mass hypothesis), and are thus expected to contribute into the signal region. An upper bound on their contamination is derived below;

- Two body $D^0 \to h^+h^{(\prime)-}$ decays, such as $D^0 \to K^+K^-$ ($BR \sim 0.4\%$) and $D^0 \to \pi^+\pi^-$ ($BR \sim 0.1\%$), where the one of the kaons (pions) is assigned the pion (kaon) mass hypothesis. These backgrounds populate the low and high mass region, respectively. Doubly misidentified $D^0 \to K^\pm\pi^\mp$ decays, where the kaon-pion mass hypothesis is swapped, contribute into the D^0 mass signal region, as shown in Fig. 3.8, where the RS and WS bands cross. They thus constitute the most problematic source of systematic uncertainty.

3.4.2 D^0 mass sidebands

By restricting the sample to events populating particular regions of the $(\beta^*, M(\pi^+\pi^-))$ plane where no signal is expected, it is possible to select independent samples enriched in a specific background source and extrapolate their contribution into the signal region. The following sidebands are studied, all independent of the D^0 signal region:

- $K\pi$ sideband, defined by requiring $|M(K\pi) - m_{D^0}| > 40\text{MeV/c}^2$;
- KK sideband, enriched in singly-misidentified singly-Cabibbo suppressed $D^0 \to K^+K^-$ decays, defined by $|M(K^+K^-) - m_{D^0}| < 24\text{MeV/c}^2$, where $M(K^+K^-)$ is the two body mass calculated with KK mass hypothesis;
- $\pi\pi$ sideband, enriched in singly-misidentified singly-Cabbibo suppressed $D^0 \to \pi^+\pi^-$ decays, defined by $|M(\pi^+\pi^-) - m_{D^0}| < 24\text{MeV/c}^2$, where $M(\pi^+\pi^-)$ is the two body mass calculated with $\pi\pi$ mass hypothesis;
- $K\pi$-swap sideband, defined by $|M(K\pi_{\text{sw}}) - m_{D^0}| < 24\text{MeV/c}^2$ and $|M(K\pi) - m_{D^0}| > 40\text{MeV/c}^2$, where the $M(K\pi_{sw})$ is calculated by swapping the mass hypothesis of the D^0 final state particles with respect to the standard $M(K\pi)$.

The $D^0 \to \pi^+\pi^-$ and $D^0 \to K^+K^-$ decays are severely suppressed in the signal region by the $|M(KK) - m_{D^0}| > 40\,\text{MeV/c}^2$ and $|M(\pi\pi) - m_{D^0}| > 40\,\text{MeV/c}^2$ requirements. The KK and $\pi\pi$-enriched sidebands are however studied to better constrain the composition of events populating the $K\pi$ sideband. The swapped $K\pi$ sideband probes the presence of doubly misidentified candidates that are expected to make it into the signal region, because the WS and RS bands overlap for small values of $|\beta^*|$, as shown in Fig. 3.8. The four sidebands and the signal region are highlighted in the $(\beta^*, M(\pi^+\pi^-))$ space for the RS and WS samples, jointly for 2015 and 2016 data, in Figs. 3.10 and 3.11, respectively. Their content for each region is studied in the corresponding $M(D^0\pi_s)$ distributions.

In the RS sample, candidates peaking in $M(D^0\pi_s)$ from the $K\pi$ sideband are $\approx 5\%$ of the RS signal yield. These candidates feature a degraded $M(D^0\pi_s)$ resolution with respect to the signal and are attributed to multibody partially reconstructed decays such as semileptonic $D^0 \to h^-\ell^+X$ and hadronic $D^0 \to h^+h^{(\prime)-}\pi^0$ decays. The semileptonic component is probably dominant, as suggested by the visible broad bump in the higher-mass $\pi\pi$-enriched sideband, where only semileptonic decays can contribute because of kinematic constraints. Narrower peaking structures are observed in the KK-enriched and $\pi\pi$-enriched sidebands, indicating also the presence of misidentified $D^{*+} \to D^0(\to K^+K^-)\pi_s^+$ and $D^{*+} \to D^0(\to \pi^+\pi^-)\pi_s^+$ events. Because the $M(K\pi)$ distribution of partially reconstructed decays is smoothly falling (see Fig. 3.1), the extrapolated fraction of peaking background in the RS signal region (which is approximately four times smaller than the sideband) would be $\ll 1\%$ and therefore induce a negligible bias in the WS-to-RS ratio.

In the WS sample, candidates peaking in $M(D^0\pi_s)$ from the $K\pi$ sideband are $\approx 22\%$ of the WS signal yield. These events feature a signal-like $M(D^0\pi_s)$ resolution and are attributed to misidentified $D \to h^+h^{(\prime)-}$ decays. By looking at the $M(D^0\pi_s)$

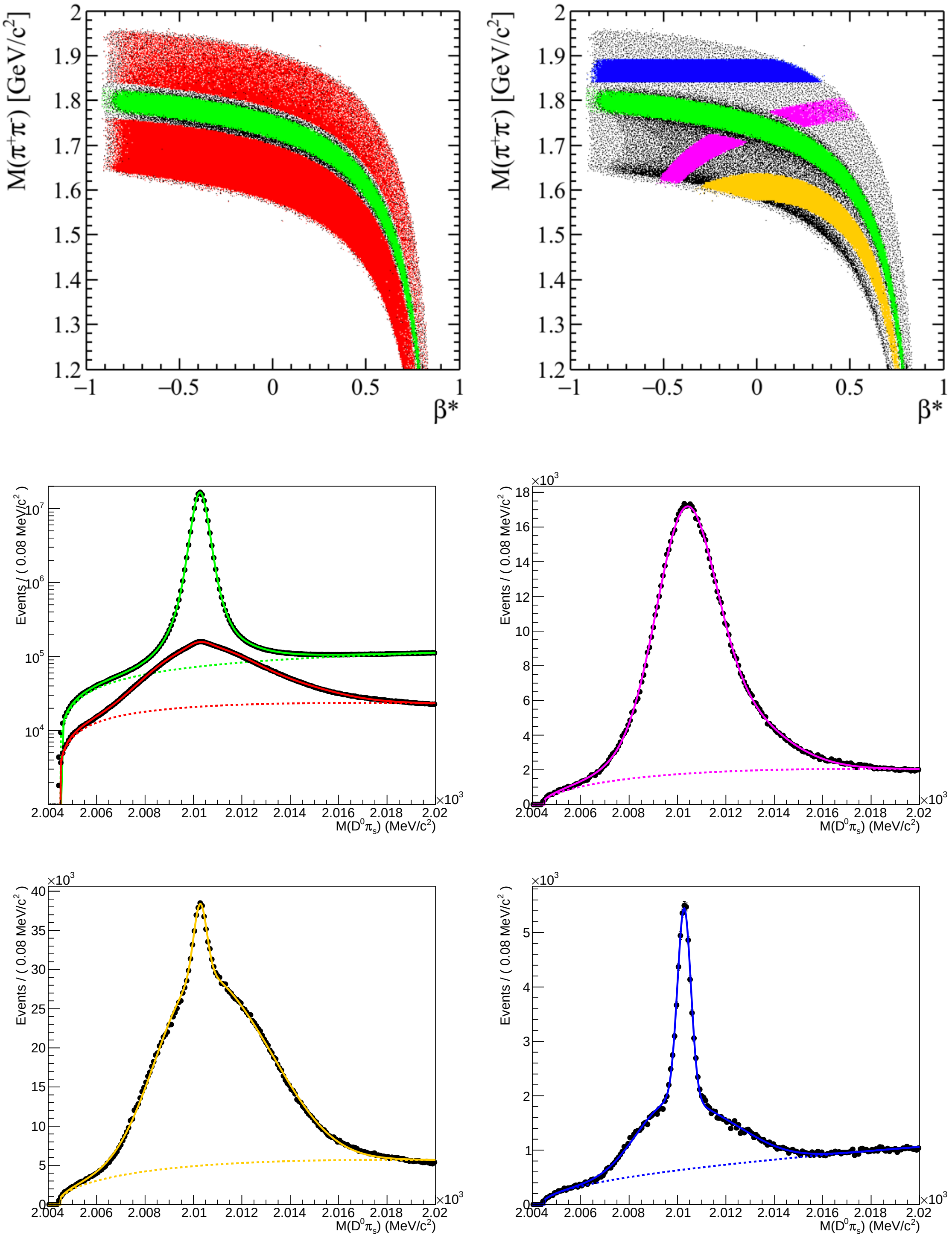

Figure 3.10: Top row: $M(\pi^+\pi^-)$ distribution as a function of β^* for RS candidates with (green) signal region and (red) $K\pi$, (yellow) KK-enriched, (blue) $\pi\pi$-enriched and (magenta) swapped $K\pi$ sidebands highlighted. Middle and bottom rows: for each region the corresponding $M(D^0\pi_s)$ distribution is also shown.

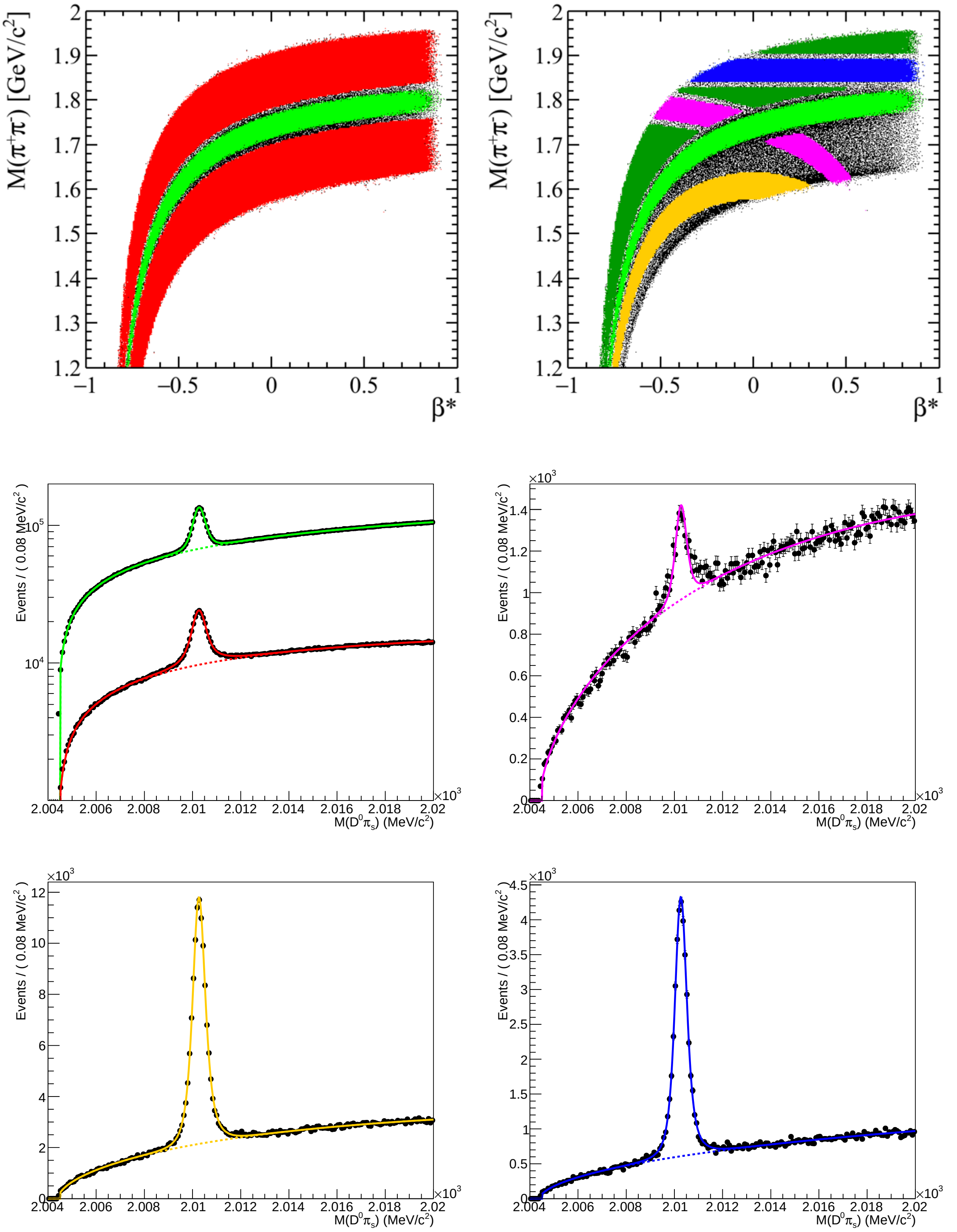

Figure 3.11: Top row: $M(\pi^+\pi^-)$ distribution as a function of β^* for WS candidates with (green) signal region and (red) $K\pi$, (yellow) KK-enriched, (blue) $\pi\pi$-enriched and (magenta) swapped $K\pi$ sidebands highlighted. Middle and bottom rows: For each region the corresponding $M(D^0\pi_s)$ distribution is also shown.

distributions of the other sidebands, the total $\approx 22\%$ fraction is found to be composed by $\approx 15\%$ of $D^{*+} \to D^0(\to K^+K^-)\pi_s^+$, $\approx 6\%$ of $D^{*+} \to D^0(\to \pi^+\pi^-)\pi_s^+$ and $\approx 0.7\%$ of doubly misidentified RS candidates. The left panel of Fig. 3.12 shows the $M(D^0\pi_s)$ distributions of candidates satisfying $|M(\pi^+\pi^-) - m_{D^0}| > 40\,\mathrm{MeV/c^2}$ and $M(K\pi) > m_{D^0} + 40\,\mathrm{MeV/c^2}$, corresponding to the dark green region of the top-right plot of Fig. 3.11. No significant peaking structures are observed. This indicates that contributions from misreconstructed semileptonic decays are absent, as expected in the WS sample, and $D^0 \to h^+h^{(\prime)-}\pi^0$ decays are negligible. A quantitative upper bound on the contamination from partially reconstructed multibody decays can be inferred from the right panel of Fig. 3.12, showing the D^*-sideband-subtracted $M(K\pi)$ distribution of candidates passing a veto on the swapped $K\pi$ mass. The veto $|M(K\pi_{\mathrm{sw}}) - m_{D^0}| > 40\,\mathrm{MeV/c^2}$ removes the dominant background from doubly misidentified candidates and allows to isolate any potential presence of other background contributions. The $D^0 \to \pi^+\pi^-$ and K^+K^- contributions are indeed clearly visible, but no other background component seem to be present. The continuous blue line represent an exponential function constrained to pass through the minima of the data distribution at $\approx 1.81\,\mathrm{GeV/c^2}$ and $\approx 1.91\,\mathrm{GeV/c^2}$. It indicates that the contamination in the signal region from a possible smoothly-distributed background from multibody decays cannot be larger than 0.01% of the WS signal yield.

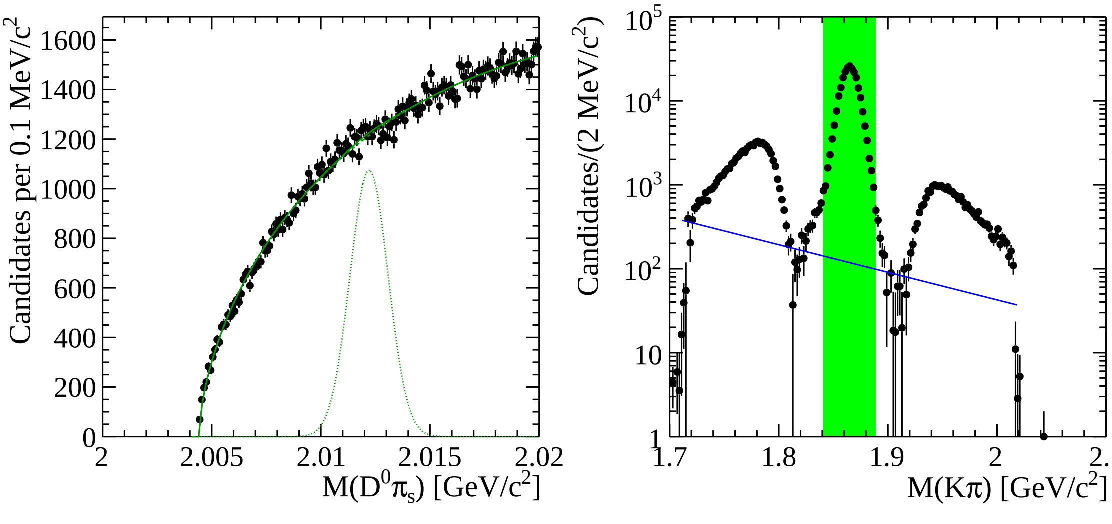

Figure 3.12: Left: $M(D^0\pi_s)$ distributions of candidates populating the dark green region of the top-right plot of Fig. 3.11, with fit projection overlaid. The fit includes a peaking component that is shown by the dotted-dashed line after having multiplied its normalisation by 100. Right: D^{*+}-sideband-subtracted $M(K\pi)$ distribution of candidates passing the $|M(K\pi_{\mathrm{sw}}) - m_{D^0}| > 40\,\mathrm{MeV/c^2}$ veto. The continuous blue line represent an exponential function constrained to pass through the minima of the data distribution. The hatched green area indicates the signal region.

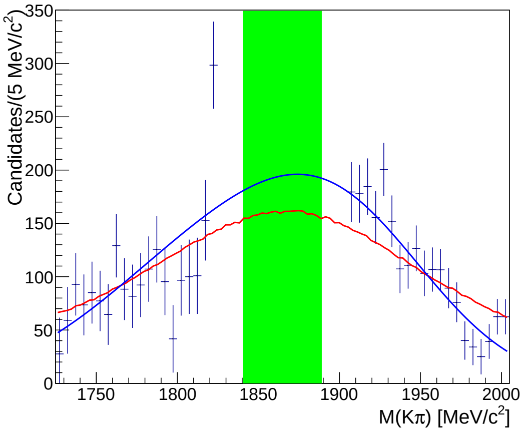

Figure 3.13: D^{*}-sideband-subtracted $M(K\pi)$ distribution of the WS candidates populating the swapped $K\pi$ sideband with two alternative fit projections overlaid. The highlighted green area indicates the signal region.

3.4.3 Doubly misidentified RS events

The dominant peaking background consists in doubly misidentified RS candidates that survive the PID requirements of the WS selection. The fraction of doubly misidentified candidates observed in the swapped $K\pi$ sideband is extrapolated into the signal region by fitting the corresponding $M(K\pi)$ distribution subtracted by the events in the D^{*+}-sideband as shown in Fig. 3.13. The extrapolation is done using two alternative hypotheses for the mass shape of the doubly misidentified candidates. The first one is an empirical double Gaussian function with separate mean values and widths to account for possible asymmetries in the distribution. The second is a non-parametric shape derived using RS candidates with swapped mass hypothesis. In each case, the extrapolation factor corresponds to the ratio of the function integral in the signal region (in green) over the integral in the sideband region (where the function is fitted to the entries of the histogram). The average between the two factors derived in this way and their absolute difference, namely $\epsilon = 0.39 \pm 0.10$, are used to extrapolate the peaking background into the signal region and take into account the systematic uncertainty deriving from choice of the shape. The estimated time-integrated and 2015-2016 averaged fraction of doubly misidentified RS candidates that pollute the WS signal region is thus $(0.261 \pm 0.068)\%$ of WS signal yield.

Its contribution, if dependent on decay time and/or charge asymmetric, can mimic a mixing/CP-violation signal and therefore bias the final measurement. The time evolution of such background (Fig. 3.14), separately for D^{*+} and D^{*-} decays, shows that the fraction of background candidates is essentially charge symmetric and constant as a function of decay time. The plots also show that the contamination is consistent between 2015 and 2016 data.

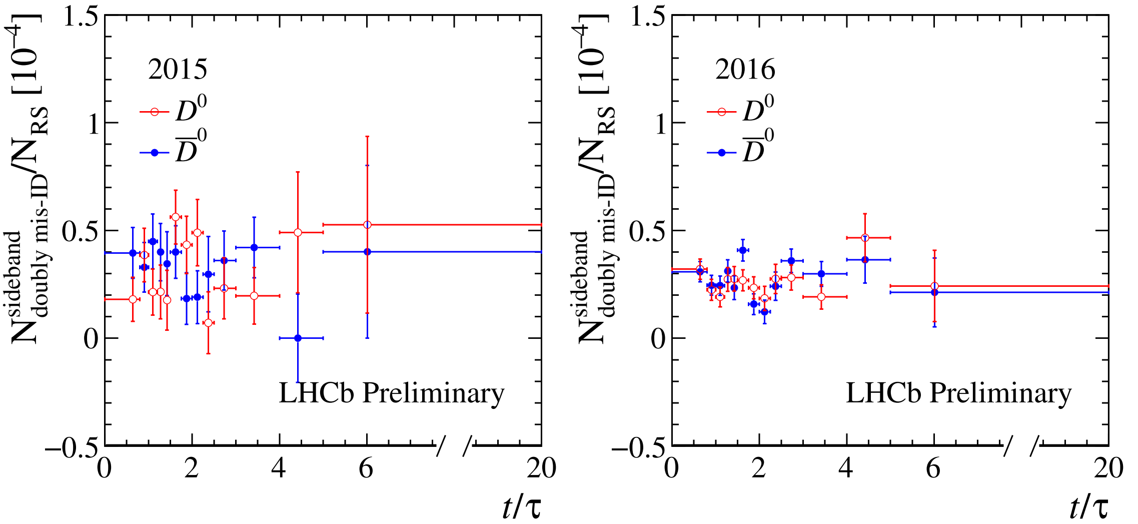

Figure 3.14: Decay-time evolution of the number of doubly misidentified RS candidates observed in the swapped $K\pi$ sideband of the WS sample normalized to the RS signal yield, separately for D^{*+} and D^{*-} and (left) 2015 and (right) 2016 data. These fractions to be extrapolated in the signal region should be multiplied by $\epsilon = 0.39 \pm 0.10$.

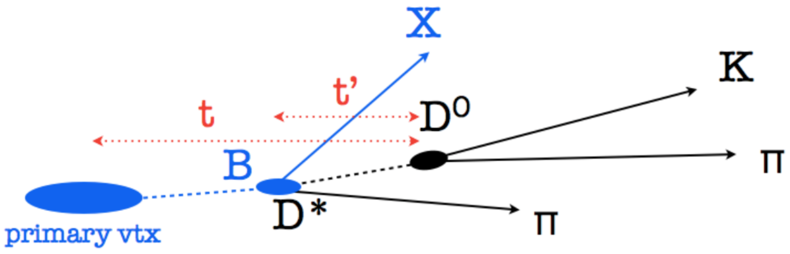

Figure 3.15: Illustration of a secondary D decay showing that the reconstructed decay time t is overestimated with respect to the real decay time t'.

3.5 Other sources of systematic uncertainties

Other sources which constitutes systematic biases for the final measurement are D meson produced in b-hadron decays (secondary D decays) and instrumental asymmetries in the reconstruction of the $K^{\pm}\pi^{\mp}$ final state. A brief overview of their estimation and magnitude is reported, as they will be considered in the final mixing fit.

3.5.1 Secondary D decays

The reconstructed decay time of D mesons coming from b-hadron decays is systematically larger than their real decay time because calculated with respect to the primary vertex, which does not coincide with the D^0 production vertex (see Fig. 3.15). When their contribution is not accounted for, the observed WS/RS yield ratio becomes [41]

$$R(t) = [1 - \Delta_B(t)], \tag{3.14}$$

where $R(t)$ is the ratio of promptly produced candidates and Δ_B is positively defined and bounded as

$$0 \le \Delta_B(t) \le f_B^{RS}(t)\left[1 - \frac{R_D}{R(t)}\right], \tag{3.15}$$

where

$$f_B^{RS}(t) \equiv \frac{N_B^{RS}(t)}{N^{RS}(t) + N_B^{RS}(t)}, \tag{3.16}$$

and is evaluated by fitting in each decay time bin the D^{*+}-sideband subtracted distribution of the $\log(\mathrm{IP}\chi^2)$ and extrapolating the fraction of secondaries into the selection region (defined by $\mathrm{IP}\chi^2 < 9$).

The resulting secondary fraction as a function of decay time, extrapolated for candidates meeting the $\mathrm{IP}\chi^2(D^0) < 9$ requirement of the analysis, is displayed in Fig. 3.16, separately for 2015 and 2016 data and for D^{*+} and D^{*-} candidates. The secondary contamination is consistent with being charge symmetric, but it is different between 2015 and 2016 data samples.

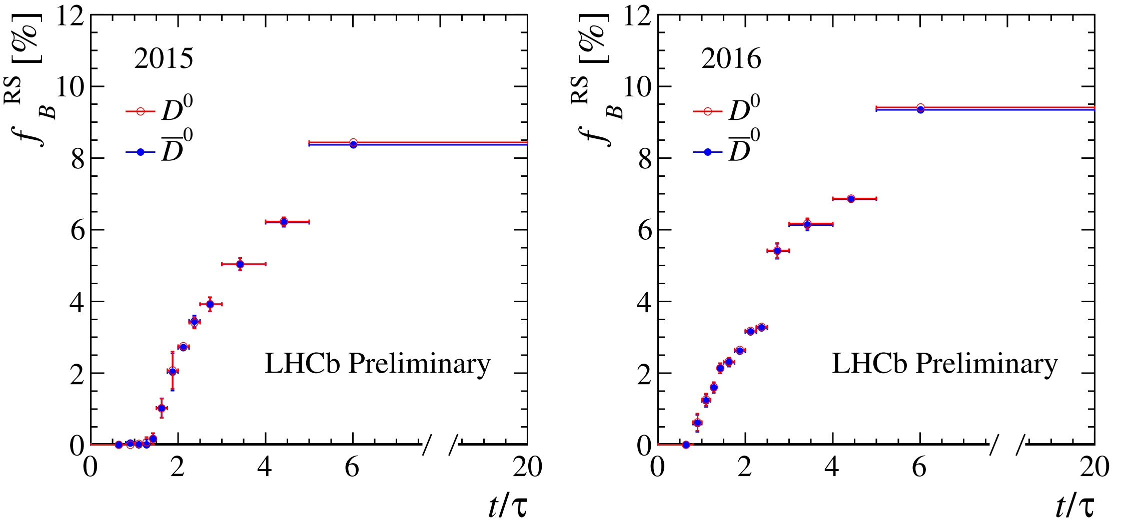

Figure 3.16: Fraction of secondary D decays in the RS sample as a function of decay time for (left) 2015 and (right) 2016 data and separately for (open red dots) D^{*+} and (closed blue dots) D^{*+} candidates.

3.5.2 Instrumental asymmetries

Experimental effects such as different efficiencies for reconstructing WS or RS decays may bias the observed ratio of reconstructed events and the corresponding measurement of mixing parameters. Assuming that the efficiency for detecting the three final-state particles factorizes as the product of efficiencies of the D^0 decay products, $\epsilon(K^{\mp}\pi^{\pm})$, and the efficiency for reconstructing the charged soft pion, $\epsilon(\pi_s^{\pm})$, the charge-specific observed WS-to-RS yield ratios can be written as

$$R^{\rm obs\pm} = \frac{N^{\rm obs}_{WS\pm}}{N^{\rm obs}_{RS\pm}} = R^{\pm}\frac{\epsilon(K^{\pm}\pi^{\mp})\,\epsilon(\pi_s^{\pm})\,(1\pm A_p)}{\epsilon(K^{\mp}\pi^{\pm})\,\epsilon(\pi_s^{\pm})\,(1\pm A_p)} = R^{\pm}\frac{\epsilon(K^{\pm}\pi^{\mp})}{\epsilon(K^{\mp}\pi^{\pm})}. \tag{3.17}$$

The asymmetry in kaon-pion detection efficiency is the only relevant instrumental nuisances, since the production asymmetry (A_p) between D^{*+} and D^{*-} and asymmetries in detecting soft pions of different charge cancel out.

The size of $K\pi$ asymmetry is determined using a combination of Cabibbo-favored D^{*+} decays appropriately reweighted so as the relevant kinematic distributions reproduce those observed in the signal sample. The method is based on the following relationship [42]

$$\frac{\epsilon(K^+\pi^-)}{\epsilon(K^-\pi^+)} = \frac{N(D^-\to K^+\pi^-\pi^-)}{N(D^+\to K^-\pi^+\pi^+)}\frac{N(D^+\to K^0_S\pi^+)}{N(D^-\to K^0_S\pi^-)}. \tag{3.18}$$

The instrumental $K\pi$ asymmetry is then calculated as

$$A_{K\pi} = \frac{\epsilon(K^+\pi^-)-\epsilon(K^-\pi^+)}{\epsilon(K^+\pi^-)+\epsilon(K^-\pi^+)} \tag{3.19}$$

and is obtained to be $A_{K\pi} = (0.69\pm0.23)\%$ for 2015 data and $A_{K\pi} = (0.87\pm0.10)\%$ for 2016 data.

3.6 Mixing fit

The dependence of the yield ratios (Tabs. 3.3 and 3.4) on decay time is fit, simultaneously for D^{*+} and D^{*-}, in order to determine the mixing and CP-violation parameters. The fit minimizes a χ^2 variable that includes terms for the difference between the observed and predicted ratios and for systematic deviations of parameters,

$$\chi^2 = \sum_i \left[\left(\frac{r_i^+ - \tilde{R}_i^+}{\sigma_i^+} \right)^2 + \left(\frac{r_i^- - \tilde{R}_i^-}{\sigma_i^-} \right)^2 \right] + \chi^2_\epsilon + \chi^2_B + \chi^2_p \,. \tag{3.20}$$

The measured WS-to-RS yield ratio and its statistical uncertainty in the decay-time bin i are denoted by $r_i^\pm$ and $\sigma_i^\pm$, respectively. The predicted value for the WS-to-RS yield ratio $\tilde{R}^\pm$ corresponds to the time-integral over bin i of Eq. (1.59) including bin-specific corrections:

$$\tilde{R}^\pm = \epsilon_r^\pm R_i^\pm \left(1 - \Delta^\pm_{B\,i}\right) + p_i, \tag{3.21}$$

$$\epsilon_r^\pm = \frac{1 \pm a_{K\pi}}{1 \mp a_{K\pi}}, \quad \Delta^\pm_{B\,i} = b_i \left(1 - \frac{R_D^\pm}{R_i^\pm}\right), \tag{3.22}$$

$$R_i^\pm = R_D^\pm + \sqrt{R_D^\pm} y'^\pm \langle t \rangle_i + \frac{x'^{2\pm} + y'^{2\pm}}{4} \langle t^2 \rangle_i \,. \tag{3.23}$$

These account for biases due to the decay-time evolution of the secondary D^0 decays ($\Delta_{B\,i}$) and the component of background from misreconstructed charm decays that peak in the signal region (p_i). The relative efficiency $\epsilon_r^\pm$ accounts for the effect of instrumental asymmetries in the $K\pi$ reconstruction efficiencies. The parameters associated with these corrections vary independently in the fit within their χ^2 constraints:

$$\chi^2_\epsilon = \left(\frac{a_{K\pi} - A_{K\pi}}{\sigma_{A_{K\pi}}} \right)^2, \qquad \chi^2_p = \sum_j \left(\frac{p_j - P_j}{\sigma_{P_j}} \right)^2, \qquad \chi^2_B = \sum_l \left(\frac{b_l - B_l}{\sigma_{B_l}} \right)^2 \tag{3.24}$$

where $A_{K\pi} \pm \sigma_{A_{K\pi}}$, $P_j \pm \sigma_{P_j}$ and $B_l \pm \sigma_{B_l}$ are the measured values and associated uncertainties of the $K\pi$ detection asymmetry, fraction of peaking backgrounds and secondary D^0 decays, respectively, determined separately for year of data-taking and, in the latter two cases, for each decay time bin.

Three fits are performed under each of the following hypotheses

No CP violation – the fit parameters are R_D, y' and x'^2 with the following conditions $R_D = R_D^+ = R_D^-$, $y' = y'^+ = y'^-$ and $x'^2 = x'^{2+} = x'^{2-}$;

No direct CP violation – the fit parameters are R_D, y'^+, y'^-, x'^{2+}, x'^{2-} with $R_D = R_D^+ = R_D^-$;

Direct and indirect CP violation – all parameters are free to float.

The fit results to the data are listed in Tab. 3.5. Fig. 3.17 shows the fits' projections on data and Fig. 3.18 the corresponding confidence regions in the (x'^2, y') plane. Detailed fit results, comprehensive of fitted nuisance parameters and corresponding constraints are reported in App. B.

No CP violation				
Parameters		Correlations		
		R_D	y'	x'^2
R_D $[10^{-3}]$	3.553 ± 0.033	1.000	-0.934	0.830
y' $[10^{-3}]$	4.086 ± 0.551		1.000	-0.957
x'^2 $[10^{-3}]$	0.100 ± 0.028			1.000
χ^2/ndf	73.966/101			

No direct CP violation						
Parameters		Correlations				
		R_D	y'^+	x'^{2+}	y'^-	x'^{2-}
R_D $[10^{-3}]$	3.553 ± 0.033	1.000	-0.865	0.718	-0.866	0.719
y'^+ $[10^{-3}]$	4.12 ± 0.60		1.000	-0.938	0.719	-0.599
x'^{2+} $[10^{-3}]$	0.102 ± 0.033			1.000	-0.598	0.499
y'^- $[10^{-3}]$	4.06 ± 0.59				1.000	-0.938
x'^{2-} $[10^{-3}]$	0.099 ± 0.033					1.000
χ^2/ndf	73.757/99					
p-value wrt no CPV	90%					

Direct and indirect CP violation							
Parameters		Correlations					
		R_D^+	y'^+	x'^{2+}	R_D^-	y'^-	x'^{2-}
R_D^+ $[10^{-3}]$	3.566 ± 0.046	1.000	-0.923	0.821	-0.015	-0.005	0.003
y'^+ $[10^{-3}]$	3.92 ± 0.78		1.000	-0.957	-0.005	0.004	-0.003
x'^{2+} $[10^{-3}]$	0.111 ± 0.040			1.000	0.003	-0.003	0.003
R_D^- $[10^{-3}]$	3.541 ± 0.046				1.000	-0.924	0.823
y'^- $[10^{-3}]$	4.25 ± 0.78					1.000	-0.958
x'^{2-} $[10^{-3}]$	0.090 ± 0.040						1.000
χ^2/ndf	73.604/98						
p-value wrt no CPV	95%						

Table 3.5: Results of the fit to the data.

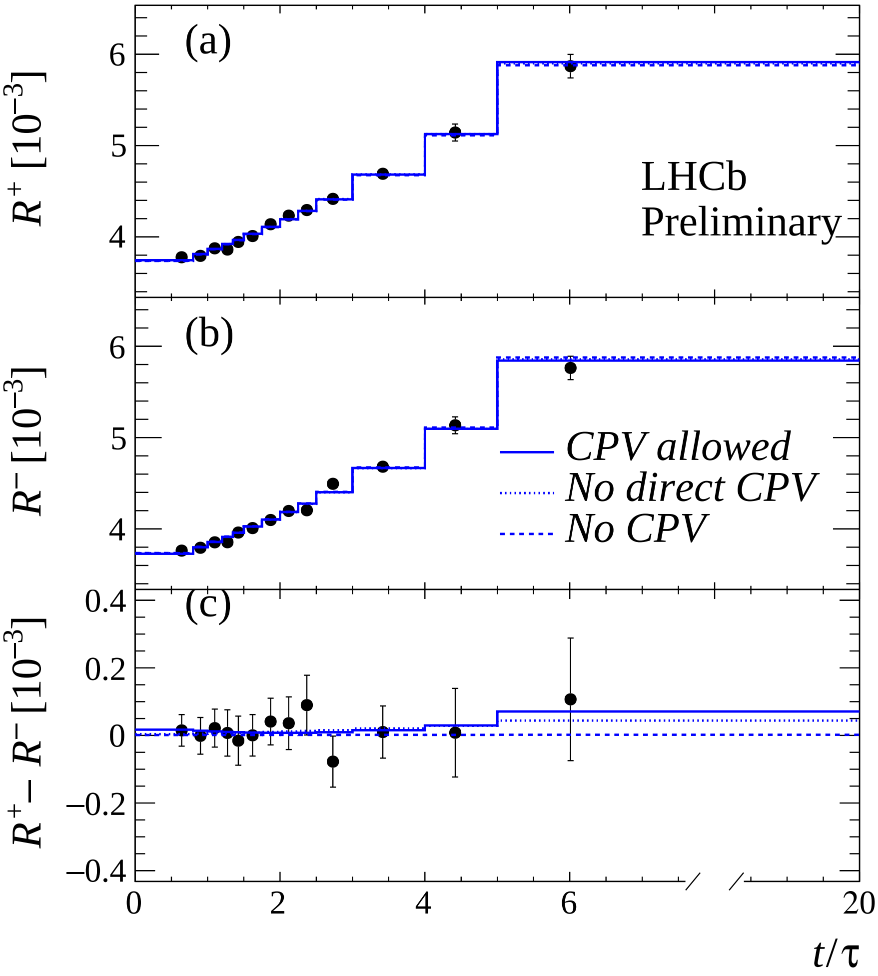

Figure 3.17: Efficiency-corrected ratios of WS-to-RS yields for (a) D^{*+} decays, (b) D^{*-} decays, and (c) their differences as functions of decay time in units of D^0 lifetime. Projections of fits allowing for no CP violation (dashed line), no direct CP violation (dotted line), and any CP violation (solid line) are overlaid. The abscissa of the data points corresponds to the average decay time over the bin; the error bars indicate the statistical uncertainties.

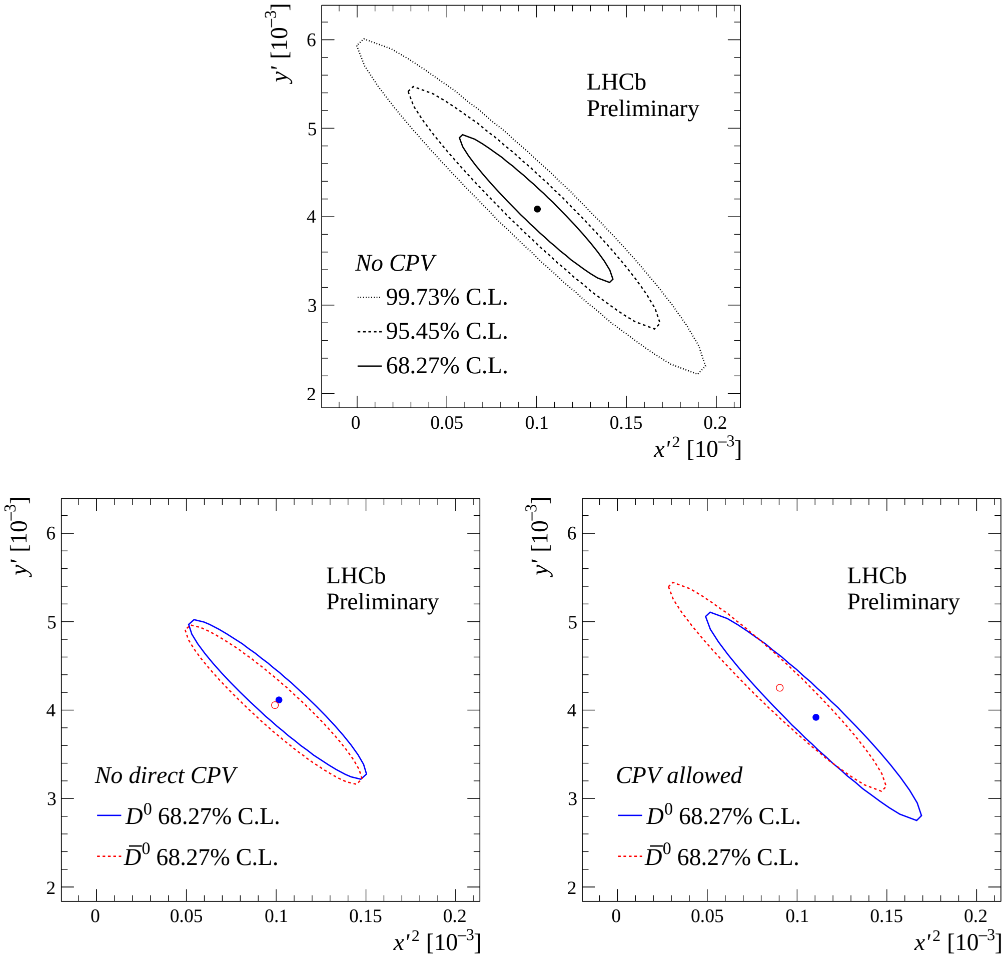

Figure 3.18: Two-dimensional confidence regions in the (x'^2, y') plane obtained assuming no CP violation (top), no direct CP violation (bottom, left), and any CP violation allowed (bottom, right). The best-fit value is shown with a point. Systematic uncertainties are included.

	No CPV fit		
Source	R_D [10^{-3}]	y' [10^{-3}]	x'^2 [10^{-3}]
Instrumental asymm.	0	0	0
Peaking background	±0.003	±0.05	±0.002
Secondary D decays	±0.009	±0.19	±0.009
Total syst. uncertainty	±0.010	±0.20	±0.010
Statistical uncertainty	±0.031	±0.52	±0.027

	No direct CPV fit				
Source	R_D [10^{-3}]	y'^+ [10^{-3}]	y'^- [10^{-3}]	x'^{2+} [10^{-3}]	x'^{2-} [10^{-3}]
Instrumental asymm.	< 0.001	±0.11	±0.10	±0.004	±0.004
Peaking background	±0.003	±0.05	±0.05	±0.002	±0.002
Secondary D decays	±0.009	±0.20	±0.20	±0.011	±0.011
Total syst. uncertainty	±0.010	±0.23	±0.23	±0.012	±0.012
Statistical uncertainty	±0.031	±0.55	±0.55	±0.030	±0.030

	CPV allowed fit					
Source	R_D^+ [10^{-3}]	R_D^- [10^{-3}]	y'^+ [10^{-3}]	y'^- [10^{-3}]	x'^{2+} [10^{-3}]	x'^{2-} [10^{-3}]
Instrumental asymm.	±0.007	±0.006	< 0.01	< 0.01	< 0.001	< 0.001
Peaking background	±0.003	±0.003	±0.05	±0.05	±0.002	±0.002
Secondary D decays	±0.012	±0.013	±0.26	±0.27	±0.013	±0.013
Total syst. uncertainty	±0.015	±0.015	±0.27	±0.27	±0.013	±0.014
Statistical uncertainty	±0.044	±0.044	±0.73	±0.73	±0.037	±0.038

Table 3.6: Summary of systematic uncertainties. In case of no CPV, the instrumental asymmetry due to the different $K\pi$ detection efficiency cancels out (top table, first row)

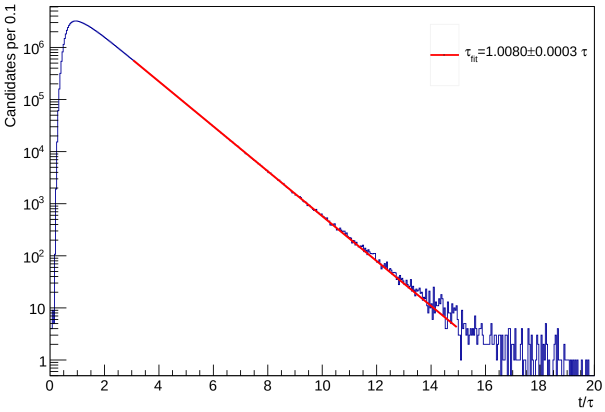

Figure 3.19: Fit to the decay time distribution of the RS candidates for $t > 3\tau$.

3.6.1 Systematic uncertainties

Systematic biases induced by instrumental asymmetries, D^0 mesons originated from b-hadron decays and unmodeled backgrounds from misidentified charm decays, that peak in the $M(D^0\pi_s^+)$ distribution, are already included as nuisance parameters in the time-dependent fit. The fit uncertainties, therefore, incorporate both statistical and systematic contributions due to these sources. To determine the statistical uncertainty and to separate the contribution from the different systematic sources, separate fits to the data are performed, with nuisance parameters fixed to their input values. The systematic components are then calculated by subtraction in quadrature. The measurement's precision is driven by the statistical uncertainties, as shown in Tab. 3.6.

The normalized decay time, t/τ, is calculated using the world average value of the D^0 lifetime [43], which is known with relative uncertainty of $\approx 0.4\%$ and is neglected in the measurement. A simple exponential fit to the decay-time distribution of RS candidates with $t > 3\tau$ (to avoid the modeling of the low-decay-time acceptance) gives a lifetime of $\sim 1\tau$, and confirms that the data sample has a lifetime statistically consistent with the PDG average (see Fig. 3.19).

3.6.2 Consistency checks

Various consistency checks are done looking for possible unexpected variations of the measured parameters as a function of different observables related to the kinematic and topology of the decay or different conditions of the detector. The whole dataset is divided in independent subsamples selected in mutually exclusive ranges of the following variables:

- the number of primary vertices in the events (Tab. 3.7), in order to check for possible biases in the decay time, which is calculated with respect to the primary vertex;
- the impact parameter χ^2 of the low momentum pion (Tab. 3.8), in order to check that the systematic due to secondary D^0 decays is under control;

- the level 0 trigger decision on the hadronic decay products (Tab. 3.9), in order to check for biases arising from the different efficiency of the trigger on the charged decay products;
- the magnet polarity (Tab. 3.10), in order to check for biases induced by detector asymmetries.

The time dependent decay fits are repeated for each of the subsamples. The compatibility of the values of the parameters that are fitted in the hypothesis of all CP violation is checked by building a χ^2 variable (see Eq. (3.25) in the following), accounting for their uncertainties and correlations. Then, a p-value is evaluated. The results obtained with independent subsamples exhibit good agreement and the 68% confidence level projections in the (x'^2, y') plane (shown in Fig. 3.20) demonstrate consistency between the measured values of the mixing parameters

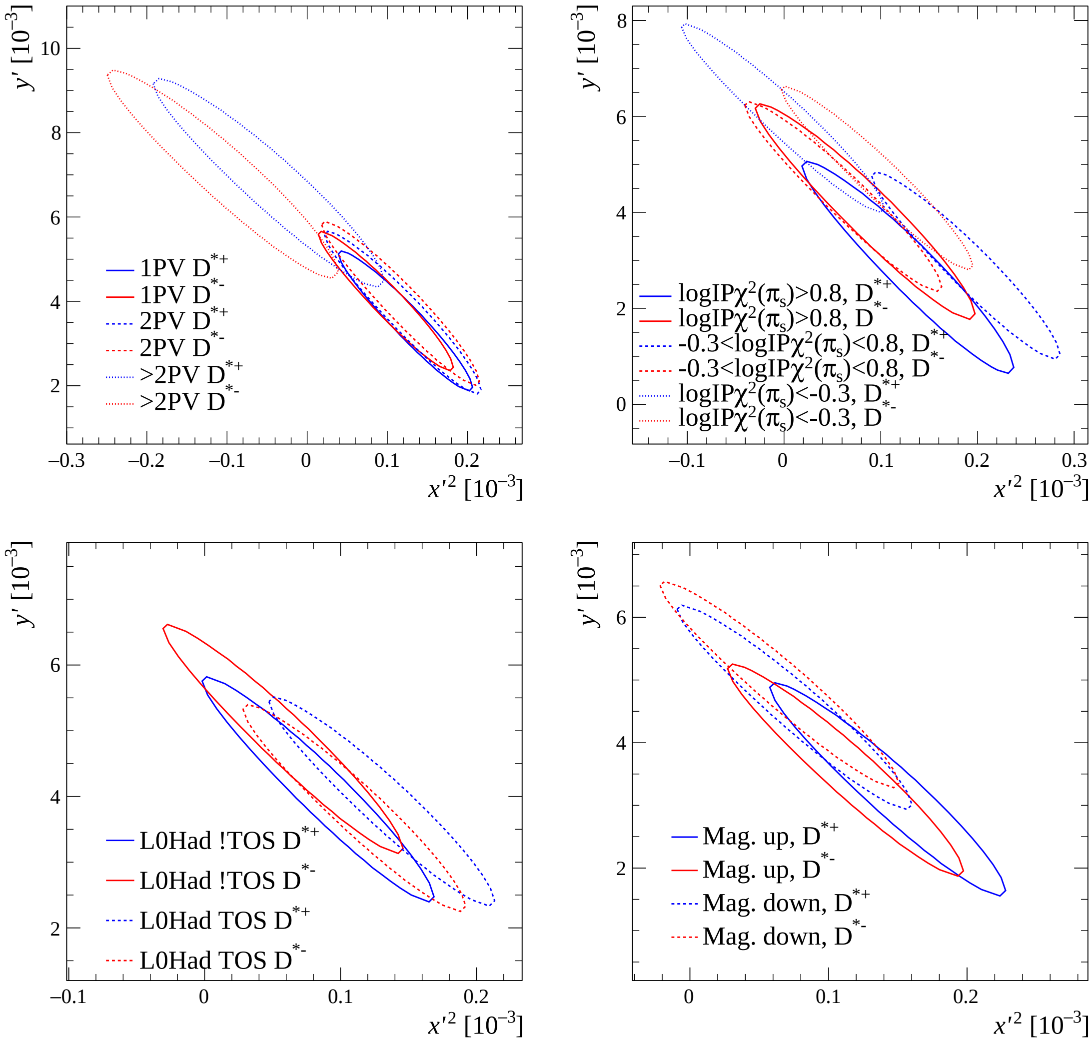

Figure 3.20: Comparison of 68% C.L. (x'^2, y') regions obtained by fitting data for different crosschecks.

Parameter	1 PV	2 PV	>2 PVs
R_D^+ [10^{-3}]	3.581 ± 0.065	3.582 ± 0.076	3.461 ± 0.124
y'^+ [10^{-3}]	3.515 ± 1.094	3.705 ± 1.271	6.310 ± 2.160
x'^{2+} [10^{-3}]	0.125 ± 0.055	0.123 ± 0.064	-0.020 ± 0.116
R_D^- [10^{-3}]	3.576 ± 0.065	3.519 ± 0.076	3.405 ± 0.123
y'^- [10^{-3}]	3.987 ± 1.089	3.924 ± 1.281	7.429 ± 2.180
x'^{2-} [10^{-3}]	0.101 ± 0.055	0.120 ± 0.065	-0.122 ± 0.120
χ^2/ndf = 9.151/12		p-value = 69%	

Table 3.7: Results of the CP violation allowed fit for different number of reconstructed primary vertices.

Parameter	$\log \mathrm{IP}\chi^2(\pi_s) > 0.8$	$-0.3 < \log \mathrm{IP}\chi^2(\pi_s) < 0.8$	$\log \mathrm{IP}\chi^2(\pi_s) < -0.3$
R_D^+ [10^{-3}]	3.641 ± 0.088	3.648 ± 0.078	3.421 ± 0.074
y'^+ [10^{-3}]	2.817 ± 1.457	2.862 ± 1.288	5.937 ± 1.296
x'^{2+} [10^{-3}]	0.133 ± 0.072	0.192 ± 0.064	0.003 ± 0.069
R_D^- [10^{-3}]	3.541 ± 0.088	3.567 ± 0.077	3.498 ± 0.074
y'^- [10^{-3}]	3.977 ± 1.482	4.302 ± 1.304	4.689 ± 1.262
x'^{2-} [10^{-3}]	0.089 ± 0.075	0.065 ± 0.067	0.100 ± 0.065
χ^2/ndf = 23.245/12		p-value = 3%	

Table 3.8: Results of the CP violation allowed fit for different intervals of logarithm of the impact parameter significance of the soft pion.

Parameter	L0Had $\overline{\text{TOS}}$	L0Had TOS
R_D^+ [10^{-3}]	3.555 ± 0.070	3.568 ± 0.060
y'^+ [10^{-3}]	4.084 ± 1.130	3.903 ± 1.049
x'^{2+} [10^{-3}]	0.086 ± 0.056	0.133 ± 0.055
R_D^- [10^{-3}]	3.481 ± 0.070	3.593 ± 0.060
y'^- [10^{-3}]	4.850 ± 1.150	3.805 ± 1.038
x'^{2-} [10^{-3}]	0.061 ± 0.058	0.112 ± 0.054
χ^2/ndf =9.694/6	p-value = 14%	

Table 3.9: Results of the CP violation allowed fit for different Level-0 Trigger decisions.

Parameter	Mag. Up	Mag. Down
R_D^+ [10^{-3}]	3.579 ± 0.067	3.554 ± 0.063
y'^+ [10^{-3}]	3.232 ± 1.122	4.543 ± 1.075
x'^{2+} [10^{-3}]	0.146 ± 0.056	0.078 ± 0.056
R_D^- [10^{-3}]	3.568 ± 0.067	3.515 ± 0.063
y'^- [10^{-3}]	3.539 ± 1.116	4.905 ± 1.086
x'^{2-} [10^{-3}]	0.115 ± 0.056	0.067 ± 0.057
χ^2/ndf = 7.569/6	p-value = 27%	

Table 3.10: Results of the CP violation allowed fit for different magnet polarity.

3.7 Interpretation of the results

The results obtained in this analysis improve the precision on the observables $R_D^{\pm}$, $x'^{2\pm}$ and $y'^{\pm}$ by a factor of ~ 1.5 with respect to the previous LHCb analysis [38]. This is due, on one hand, to the increased statistic (a factor of ~ 2.5 than the prompt dataset [37]), giving an approximate scaling of $\sim 1/\sqrt{N}$, and on the other to the better signal/background discrimination in the WS sample, expressed by the higher value assumed by the score function $S/\sqrt{S+B}$. In particular, the precision on the parameter x'^2, which is related to the mixing parameter x, reaches for the first time the 3σ separation from zero, in the fit for conserved CP symmetry and no direct CP violation fit (see Tab 3.5).

No sign of CP violation either in mixing, which would result in a slope different from zero in the fit shown in Fig. 3.17 (bottom), or in decay, which would result in an intercept to the vertical axis different from zero in the same fit, is seen. In order to test the CP violation hypothesis (no direct CPV and all CPV allowed) against the no CP violation hypothesis, a p-value is computed from the change in χ^2 of the fits and taking into account the difference in the number of degrees of freedom. From the values in Tab. 3.5, one obtains a p-value of 90% for the no direct CPV hypothesis and 95% for the direct and indirect CPV hypothesis, thus confirming the compatibility with the mixing only hypothesis. The direct CP violating asymmetry in DCS decays is found to be $A_D = (0.4 \pm 1.3)\%$, consistent with the no direct CP violation hypothesis.

3.7.1 Comparison with previous LHCb results

In order to combine the results of this analysis with those of the previous LHCb analysis [38], using prompt and semileptonic tagged D^* events from the $3\,\mathrm{fb}^{-1}$ dataset of Run 1, one minimizes a χ^2 expression with $m(n-1)$ degrees of freedom given by

$$\chi^2 = \sum_{i=1}^{n} \sum_{\alpha,\beta=1}^{m} (\hat{p}_\alpha - p_{i\alpha})(V_i^{-1})_{\alpha\beta}(\hat{p}_\beta - p_{i\beta}) \tag{3.25}$$

where i is the index denoting the measurement and α, β the indexes denoting the measured observables, p_i are m-dimensional vectors containing the m measured observables of n disjoint datasets, V_i are the the $m \times m$ covariance matrices corresponding to the p_i and $\hat{p}$ is the vector of free parameters against which χ^2 is minimized. For $n = 2$ disjoint dataset, the above procedure reduces to the calculation of the compatibility between the two measurements, with simplified χ^2 with m degrees of freedom given by

$$\chi^2 = \sum_{\alpha,\beta=1}^{m} (p_{1\alpha} - p_{2\alpha})(V_1 + V_2)^{-1}_{\alpha\beta}(p_{1\beta} - p_{2\beta}). \tag{3.26}$$

Fig. 3.21 shows the compatibility of the mixing parameters x'^2 and y' between Run 1 and Run 2 results, in the limit of CP conservation. The combination of the results from Run 1 and Run 2 is reported in Tab. 3.11. By combining the two datasets, one obtains an improvement of about 50% on the precision of the mixing observables. This has important consequences in the determination of the mixing and CP violation parameters, as outlined in the next section.

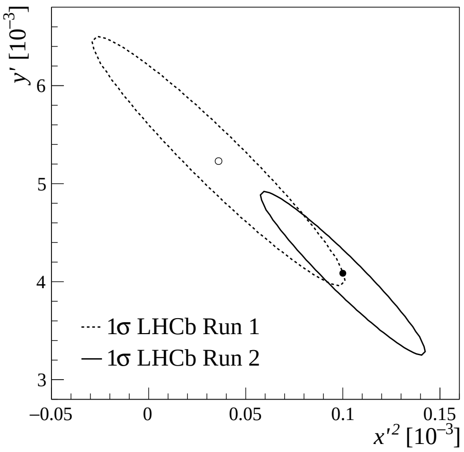

Figure 3.21: Comparison with previous LHCb result [38].

Parameter	Run 1	Run1+Run2	% Error
	(3 fb^{-1} prompt + DT)	(1.9 fb^{-1} prompt)	Improvement
No CP violation			
R_D [10^{-3}]	3.533 ± 0.054	3.540 ± 0.028	48
y' [10^{-3}]	5.23 ± 0.84	4.55 ± 0.46	45
x'^2 [10^{-3}]	0.036 ± 0.043	0.076 ± 0.023	47
	$\chi^2/\text{ndf} = 6.565/3$	p-value = 9%	
No direct CP violation			
R_D [10^{-3}]	3.533 ± 0.054	3.539 ± 0.028	48
$y'+$ [10^{-3}]	5.14 ± 0.91	4.52 ± 0.49	46
x'^2+ [10^{-3}]	0.049 ± 0.050	0.083 ± 0.028	44
$y'-$ [10^{-3}]	5.32 ± 0.91	4.46 ± 0.49	46
x'^2- [10^{-3}]	0.024 ± 0.050	0.076 ± 0.027	46
	$\chi^2/\text{ndf} = 5.135/5$	p-value = 40%	
Direct and indirect CP violation			
R_D+ [10^{-3}]	3.474 ± 0.081	3.533 ± 0.040	51
R_D- [10^{-3}]	3.591 ± 0.081	3.541 ± 0.040	51
$y'+$ [10^{-3}]	5.97 ± 1.25	4.64 ± 0.65	48
x'^2+ [10^{-3}]	0.011 ± 0.065	0.077 ± 0.034	48
$y'-$ [10^{-3}]	4.50 ± 1.21	4.53 ± 0.65	46
x'^2- [10^{-3}]	0.061 ± 0.061	0.073 ± 0.033	46
	$\chi^2/\text{ndf} = 7.385/6$	p-value = 29%	

Table 3.11: Combined LHCb results from Run1 (3 fb^{-1} prompt + doubly tagged) [38] and Run2 (prompt 1.9 fb^{-1}).

3.7.2 Impact on World Average

The impact of the measurement on the mixing and CP violation parameters is then evaluated performing a combination of various experimental observables, before and after including the results here obtained. The combination is performed by minimizing a χ^2 expression similar to Eq. (3.25), where this time the p_i are a function of the measurements, relating the experimental observables to the underlying theoretical parameters governing mixing, while $\hat{p}$ is the set of parameters that are fitted.

The external inputs which are used in the fit are the following

- The HFAG COMBOS world average of y_{CP} and A_Γ [35];
- The mixing and CPV search of Belle in $D^0 \to K^0_S\pi^+\pi^-$ [44] and the measurements of the mixing parameters of BaBar in $D^0 \to K^0_S\pi^+\pi^-$ and $D^0 \to K^0_S K^+K^-$ combined [45];
- The CLEO-c measurement of the mixing parameters and strong-phase difference in $D^0 \to K^+\pi^-$ decays [46];
- The measurement of the mixing parameters $x'^{\pm}$, $y'^{\pm}$, R_D and A_D in $D^0 \to K^+\pi^-$ of LHCb from Run1 with prompt and doubly tagged D^0 decays [38].

In Tab. 3.12 the vale of the mixing and CP violation parameters before and after adding the results from Run 2 are reported. In particular, the improvement in sensitivity on x reaches the $3\,\sigma$ separation from zero for the first time. This confirms that the CP-even mass eigenstate is the heavier one. Improving the sensitivity on x in combination with the observable A_Γ has also consequences for the precision on the CP violation parameter ϕ, since they are related as $A_\Gamma \simeq x \sin\phi$, in the approximation that $|q/p| = 1$ (see Eq. (1.61b)). In Fig. 3.22 the two dimensional contours for $|q/p|$ and ϕ are shown, before and after the inclusion of the Run 2 measurement in the global fit. In conclusion, thanks to this measurement the parameter $|q/p|$ can be better constrained, especially for small values of ϕ, due to the better precision on the mixing parameters, as shown in Eq. (1.53).

Parameter	w/o Run 2	with Run 2
x (%)	0.37 ± 0.15	0.52 ± 0.17
y (%)	0.67 ± 0.07	0.69 ± 0.08
$\delta_{K\pi}$ (°)	15.3 ± 8.1	16.5 ± 8.3
R_D (%)	0.353 ± 0.004	0.351 ± 0.002
A_D (%)	-0.91 ± 1.16	-0.42 ± 0.82
$\lvert q/p\rvert$ (%)	0.867 ± 0.084	0.914 ± 0.108
ϕ (°)	-13.2 ± 9.4	-6.5 ± 9.1
χ^2/ndf	16.613/12	26.501/18

Table 3.12: Results of the global fit for any CP violation allowed, without (left) and including (right) results from Run 2.

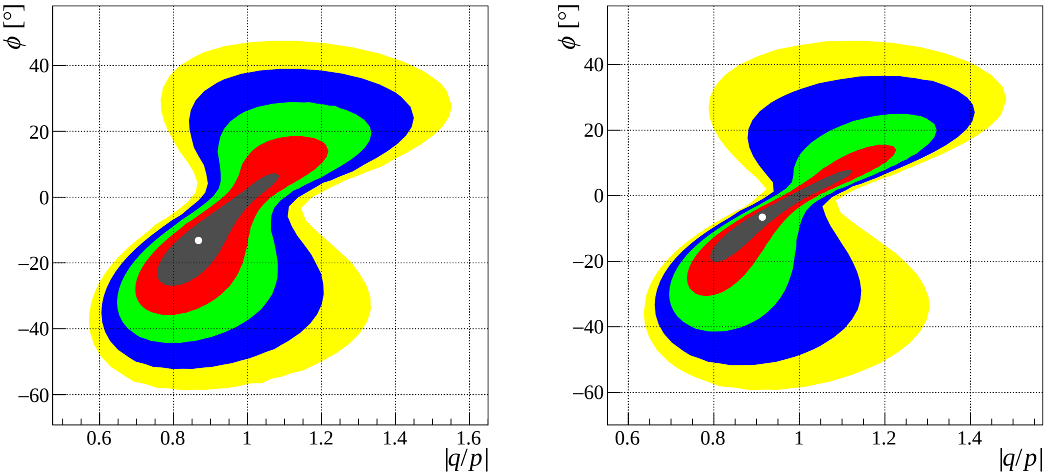

Figure 3.22: Combination of the CP violation parameters before (left) and after adding the LHCb Run 2 results (right), for 1 (dark grey), 2 (red), 3 (green), 4 (blue) and 5 sigma (yellow) contours.

Conclusions

This thesis presents a measurement of the mixing parameters and search for CP violation in the $D^0 - \overline{D}^0$ system, by fitting the time dependence of the ratios of WS to RS decay rates separately for D^0 and $\overline{D}^0$ mesons. The analysis is based on data collected by the LHCb experiment during 2015 and 2016 at $\sqrt{s} = 13\,\text{TeV}$, corresponding to a total $1.9\,\text{fb}^{-1}$ integrated luminosity. For the first time, candidates used to perform the physics analysis were reconstructed directly online at the second stage of the software trigger. In the hypothesis of no CP violation, the results for the mixing parameters are

$$\begin{aligned} R_D &= (3.553 \pm 0.031 \pm 0.010) \times 10^{-3}, \\ y' &= (4.086 \pm 0.52 \pm 0.20) \times 10^{-3}, \\ x'^2 &= (0.100 \pm 0.027 \pm 0.010) \times 10^{-3}, \end{aligned}$$

where the first uncertainty is statistical and the second systematic. In the hypothesis of no direct CP violation, the results for the two independent sets of mixing parameters, evaluated for the D^0 and $\overline{D}^0$ mesons separately, are

$$\begin{aligned} R_D &= (3.553 \pm 0.031 \pm 0.010) \times 10^{-3}, \\ y'^{\pm} &= (4.12 \pm 0.55 \pm 0.23) \times 10^{-3}, \\ x'^{2\pm} &= (0.102 \pm 0.030 \pm 0.012) \times 10^{-3}, \\ y'^{\pm} &= (4.06 \pm 0.55 \pm 0.23) \times 10^{-3}, \\ x'^{2\pm} &= (0.099 \pm 0.030 \pm 0.012) \times 10^{-3}, \end{aligned}$$

while, when allowing for all kind of CP violation, they are

$$\begin{aligned} R_D^+ &= (3.566 \pm 0.044 \pm 0.015) \times 10^{-3}, \\ y'^{\pm} &= (3.92 \pm 0.73 \pm 0.27) \times 10^{-3}, \\ x'^{2\pm} &= (0.111 \pm 0.037 \pm 0.013) \times 10^{-3}, \\ R_D^- &= (3.541 \pm 0.044 \pm 0.015) \times 10^{-3}, \\ y'^{\pm} &= (4.25 \pm 0.73 \pm 0.27) \times 10^{-3}, \\ x'^{2\pm} &= (0.090 \pm 0.038 \pm 0.014) \times 10^{-3}. \end{aligned}$$

The results are compatible with and supersede those of the previous LHCb analysis. In the case of no CP violation allowed and no direct CP violation, x'^2 is measured for the first time different from zero at the level of three standard deviations. When combined with the results of the previous LHCb analysis, one gets a $\sim 50\%$ improvement on the precision of the mixing parameters. No sign of CP violation, either in mixing or in DCS decays, is observed. The main systematic uncertainties have also been analysed and included in the mixing fit. The results are preliminary and additional studies are still ongoing.

The results of this measurement, when published, will significantly improve the precision of the charm mixing parameters, due to its high statistics, and will also help constraining the parameters governing indirect CP violation. In particular, the improvement on the precision of x in combination with the observable A_Γ (from the analysis of neutral charmed mesons decays to CP eigenstates) improves the knowledge of ϕ, expressing CP violation in mixing and decay amplitudes interference if different from zero, while the determination of $x'^{2\pm}$ and $y'^{\pm}$, separately for D^0 and $\overline{D}^0$ mesons, gives strong bounds on the parameter $|q/p|$, expressing CP violation in mixing amplitudes if different from one, especially for small values of ϕ.

Appendix A

Mass fits projections

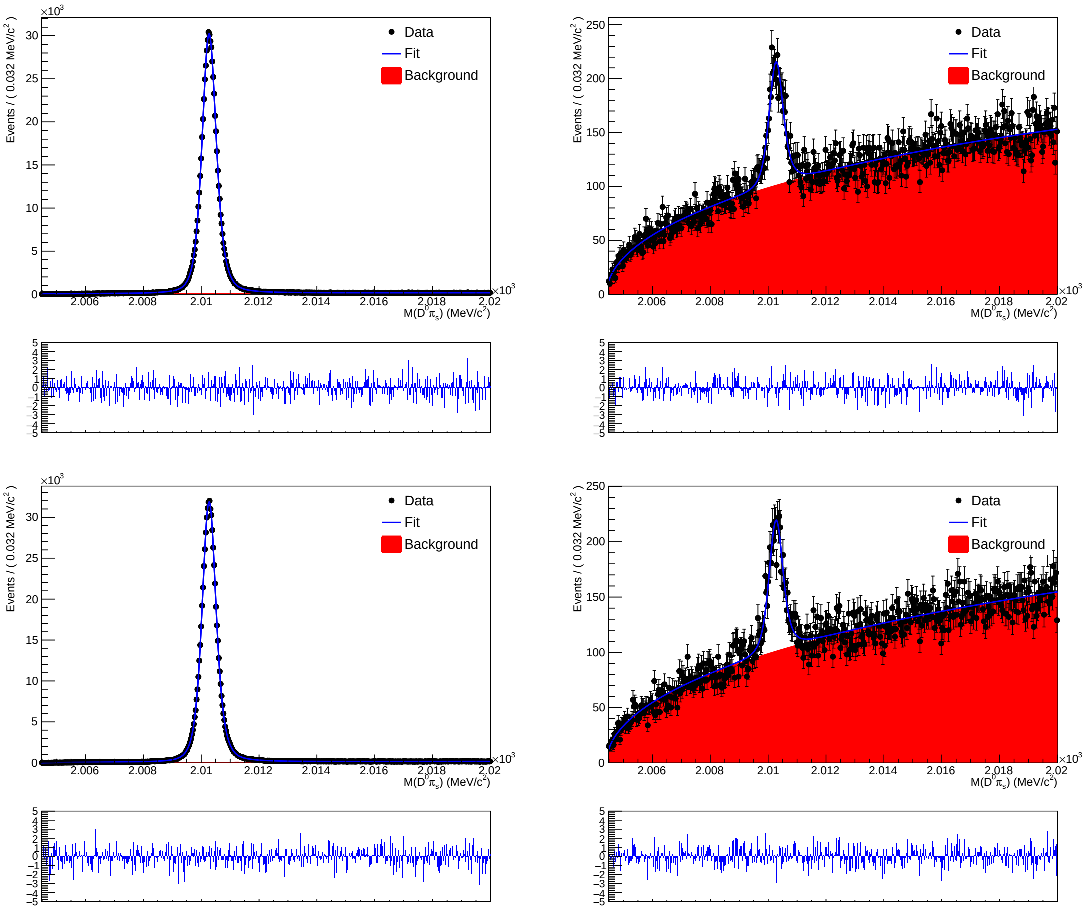

Figure A.1: $D^0\pi_s$ mass distribution for the RS (left) and WS (right) Magnet Up D^0 (top) and $\bar{D}^0$ (bottom) candidates having decay time in the range [0,0.8]τ with fit projection overlaid, in 2015 data.

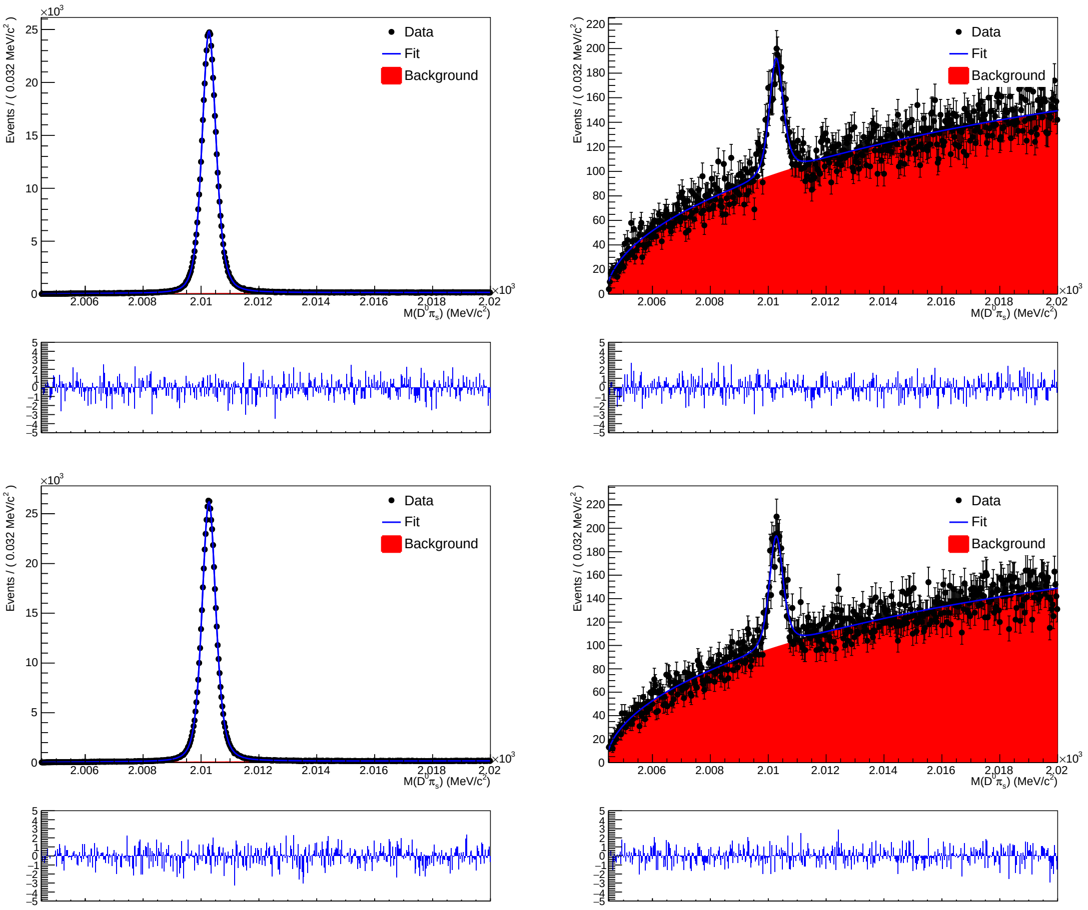

Figure A.2: $D^0\pi_s$ mass distribution for the RS (left) and WS (right) Magnet Up D^0 (top) and $\bar{D}^0$ (bottom) candidates having decay time in the range $[0.8,1]\tau$ with fit projection overlaid, in 2015 data.

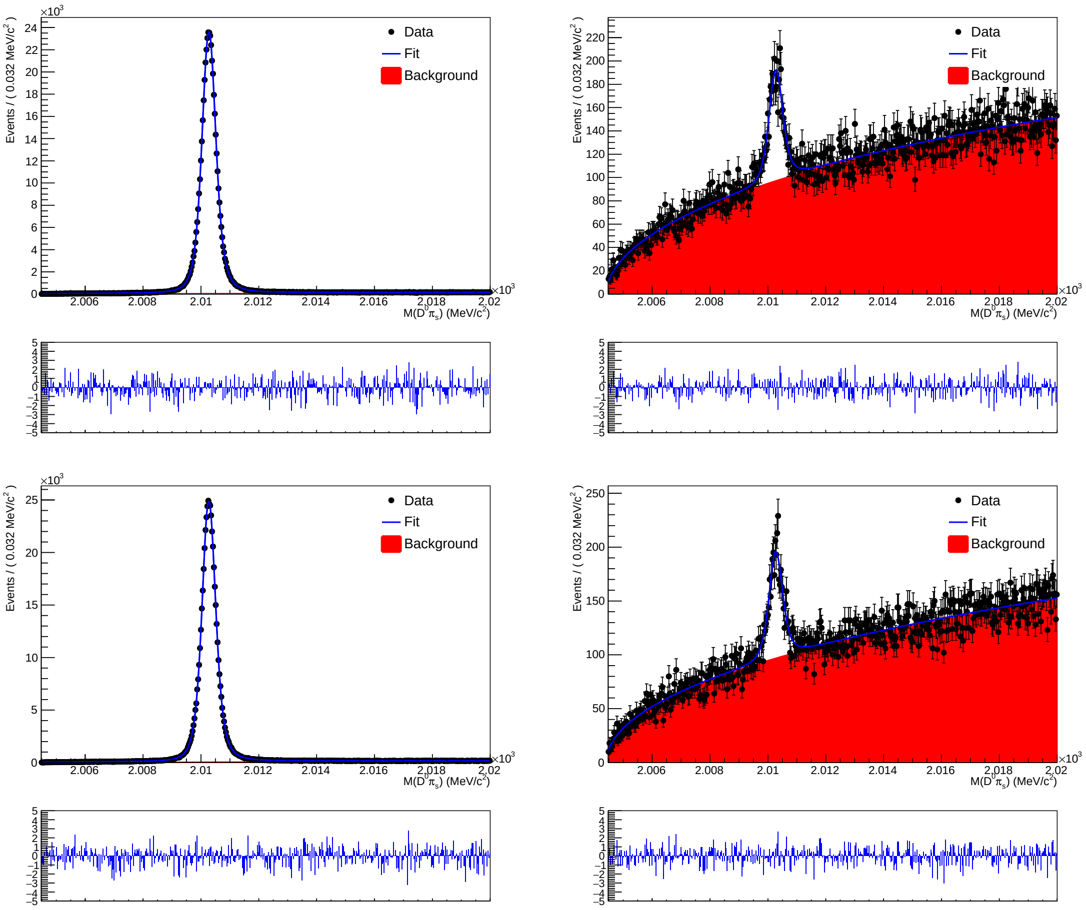

Figure A.3: $D^0\pi_s$ mass distribution for the RS (left) and WS (right) Magnet Up D^0 (top) and $\bar{D}^0$ (bottom) candidates having decay time in the range [1,1.2]τ with fit projection overlaid, in 2015 data.

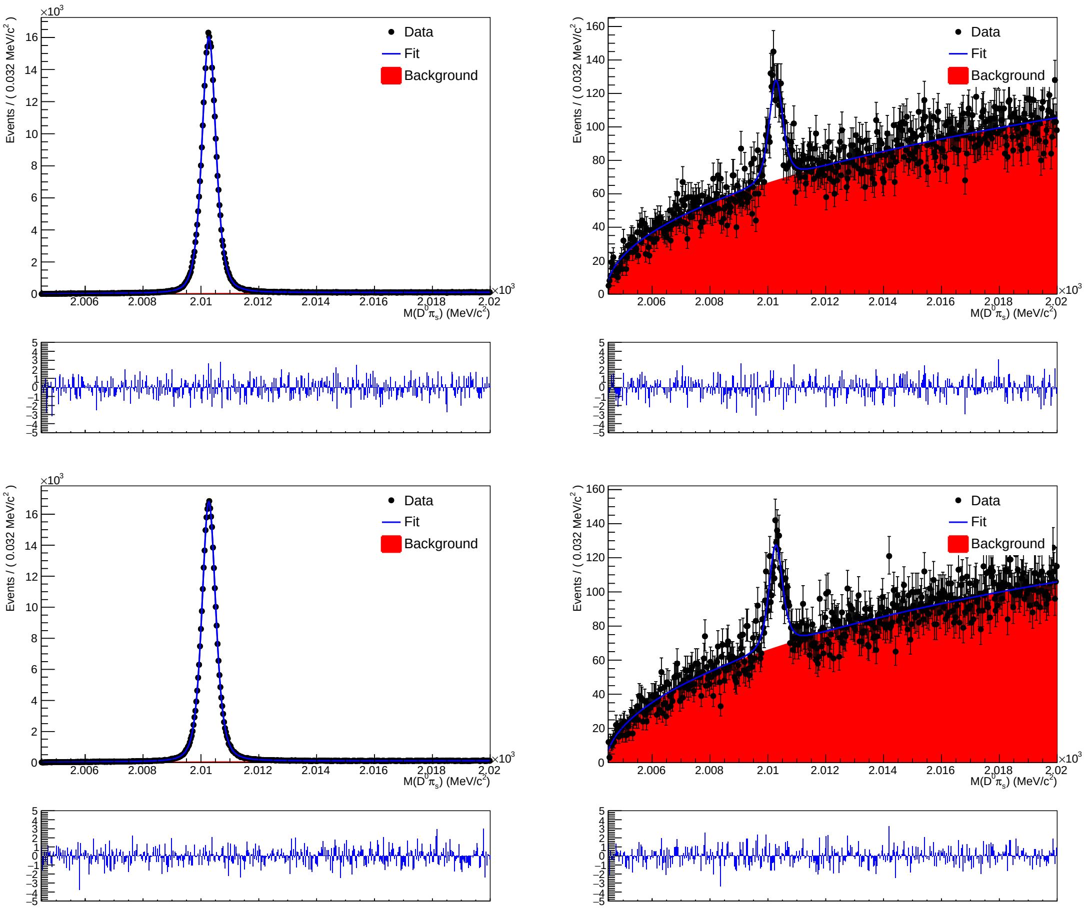

Figure A.4: $D^0\pi_s$ mass distribution for the RS (left) and WS (right) Magnet Up D^0 (top) and $\bar{D}^0$ (bottom) candidates having decay time in the range [1.2,1.35]τ with fit projection overlaid, in 2015 data.

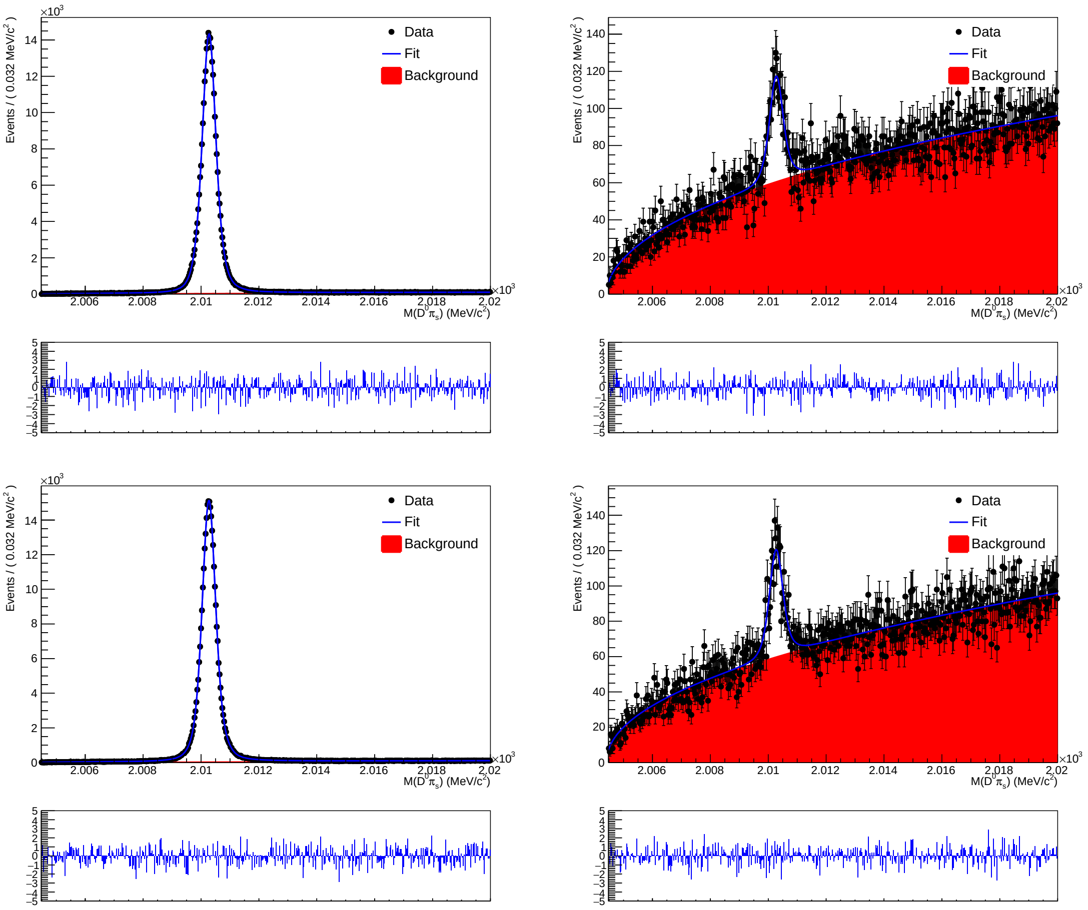

Figure A.5: $D^0\pi_s$ mass distribution for the RS (left) and WS (right) Magnet Up D^0 (top) and $\bar{D}^0$ (bottom) candidates having decay time in the range [1.35,1.5]τ with fit projection overlaid, in 2015 data.

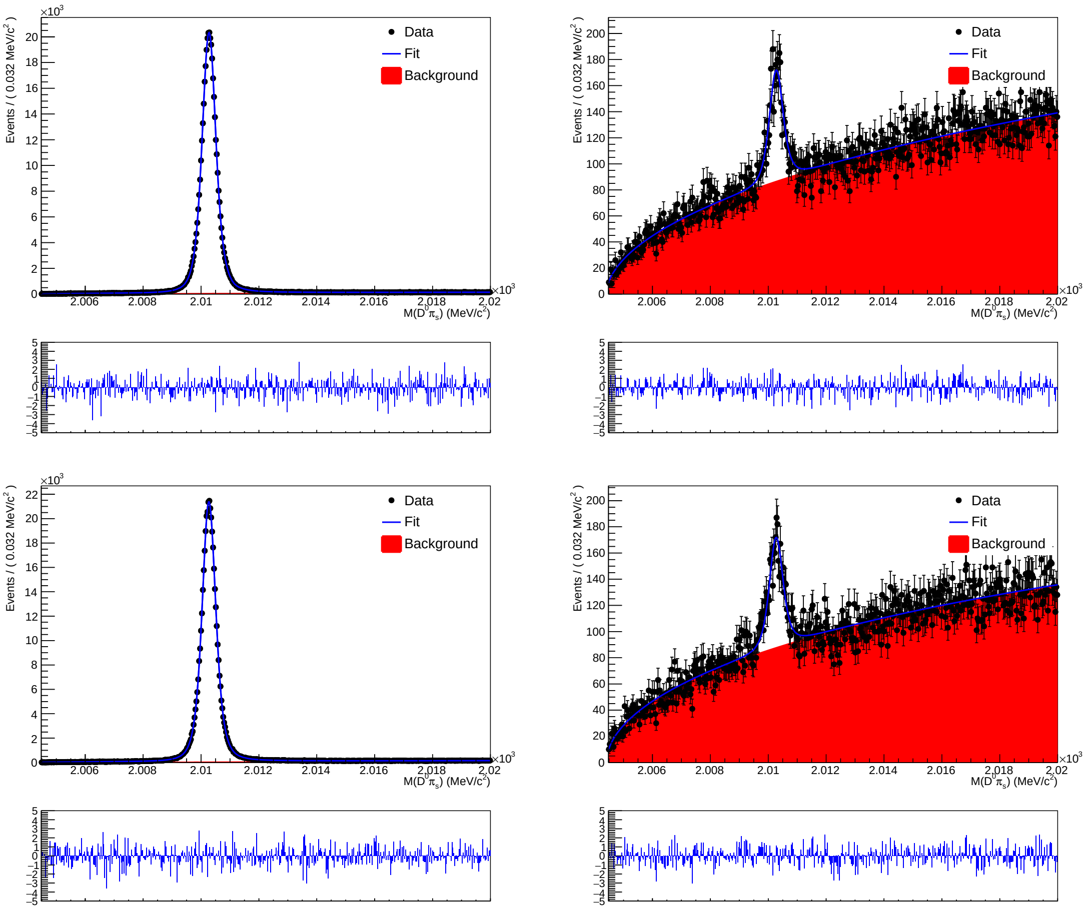

Figure A.6: $D^0\pi_s$ mass distribution for the RS (left) and WS (right) Magnet Up D^0 (top) and $\bar{D}^0$ (bottom) candidates having decay time in the range [1.5,1.75]τ with fit projection overlaid, in 2015 data.

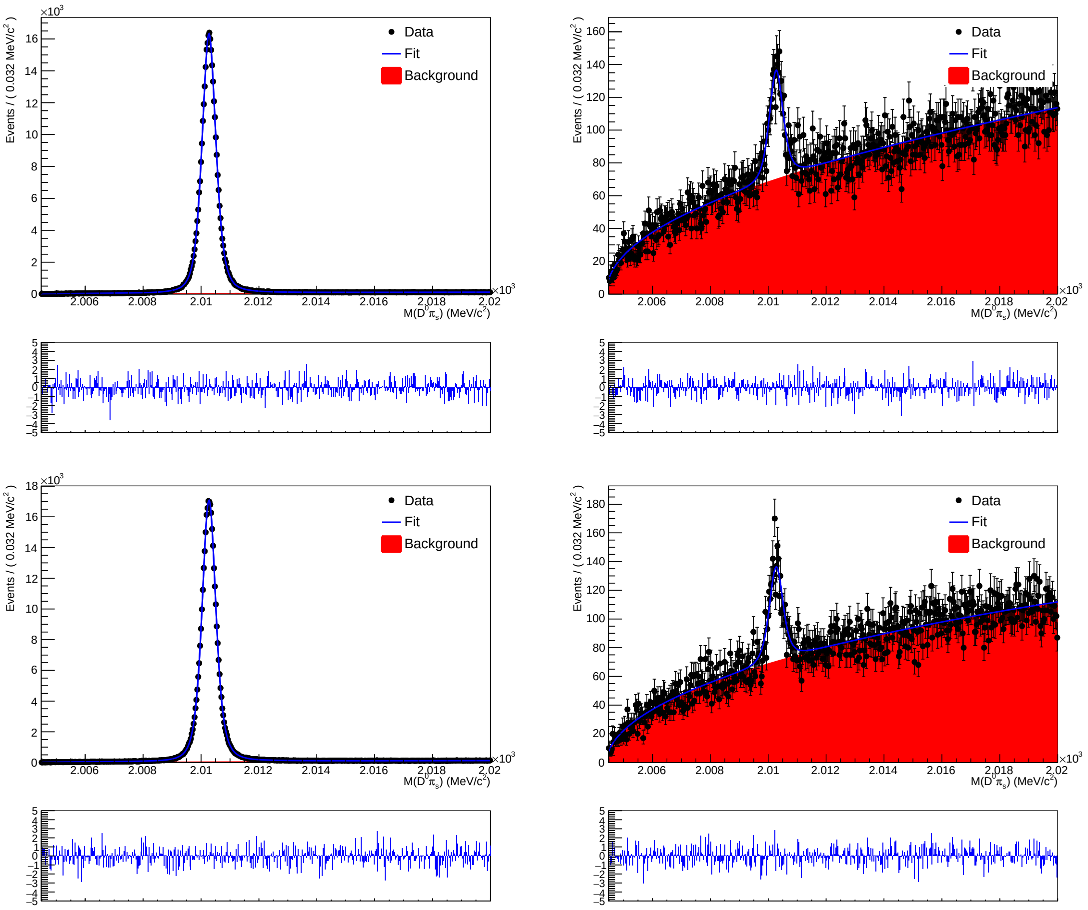

Figure A.7: $D^0\pi_s$ mass distribution for the RS (left) and WS (right) Magnet Up D^0 (top) and $\bar{D}^0$ (bottom) candidates having decay time in the range [1.75,2]τ with fit projection overlaid, in 2015 data.

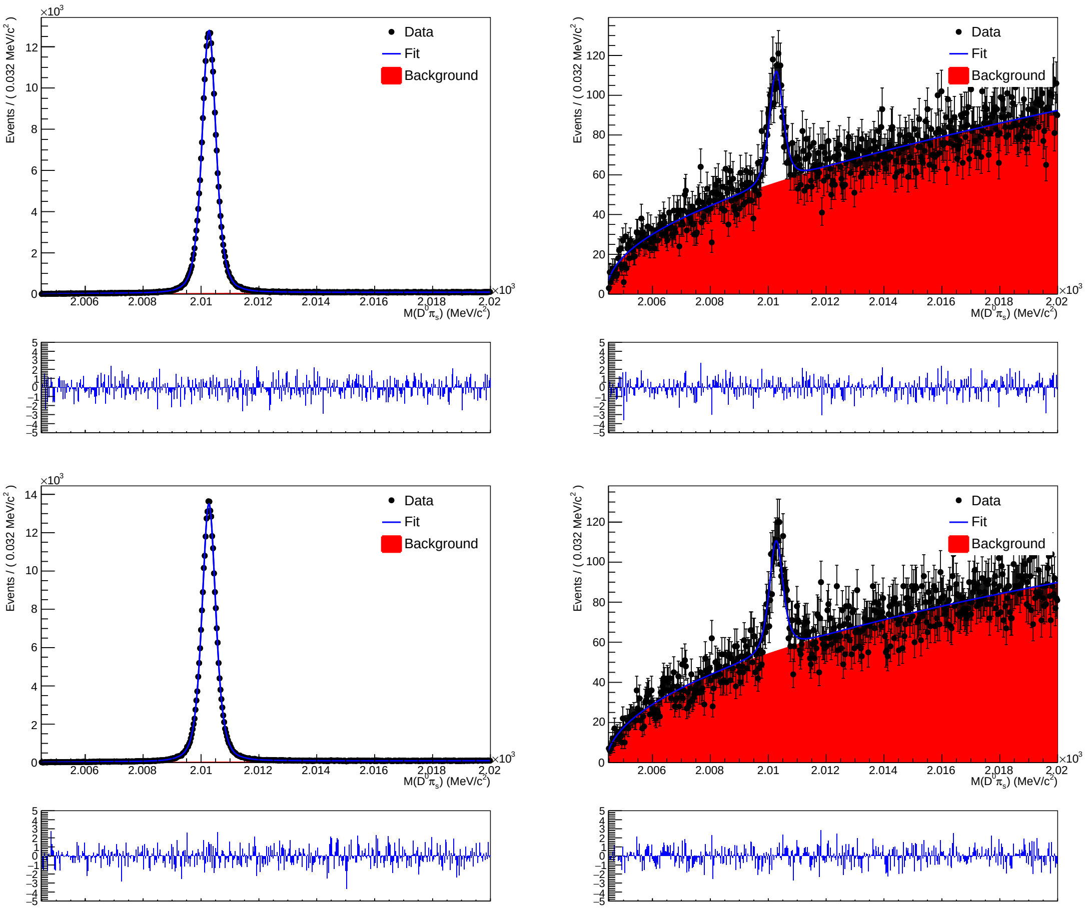

Figure A.8: $D^0\pi_s$ mass distribution for the RS (left) and WS (right) Magnet Up D^0 (top) and $\bar{D}^0$ (bottom) candidates having decay time in the range [2,2.25]τ with fit projection overlaid, in 2015 data.

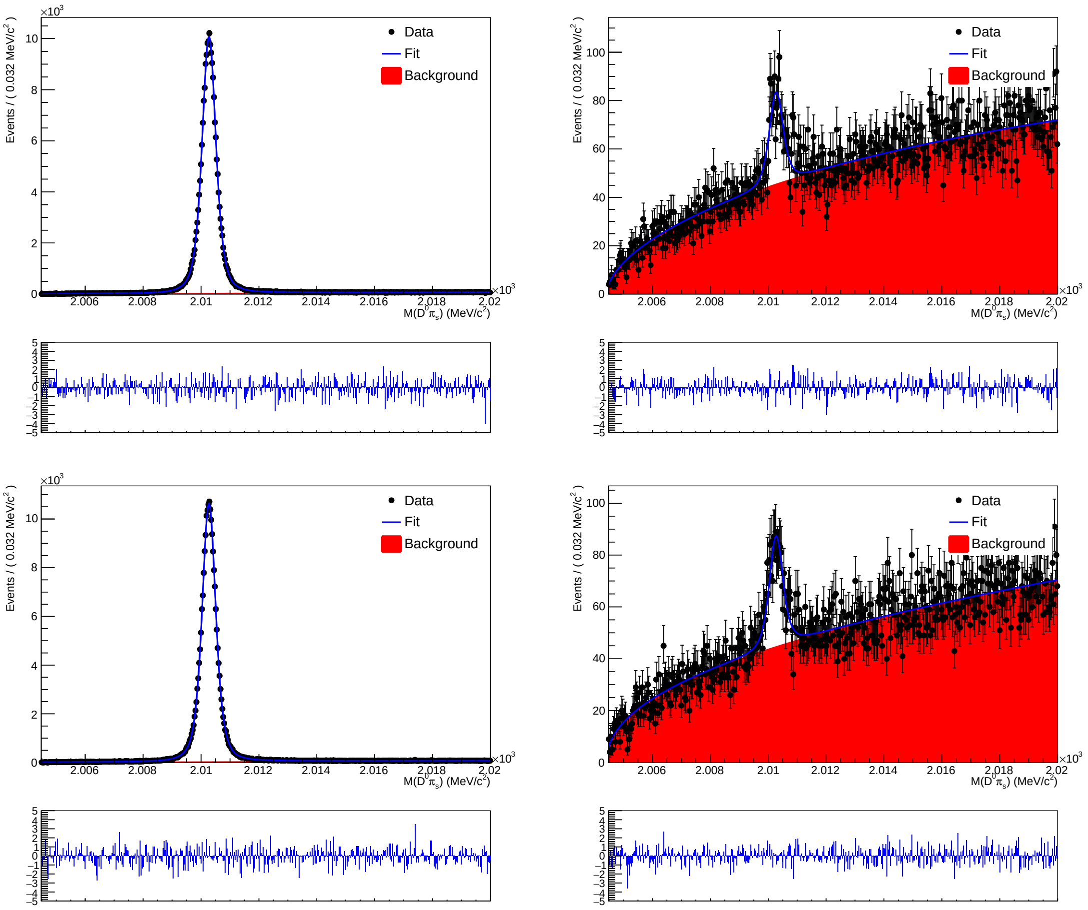

Figure A.9: $D^0\pi_s$ mass distribution for the RS (left) and WS (right) Magnet Up D^0 (top) and $\bar{D}^0$ (bottom) candidates having decay time in the range [2.25,2.5]τ with fit projection overlaid, in 2015 data.

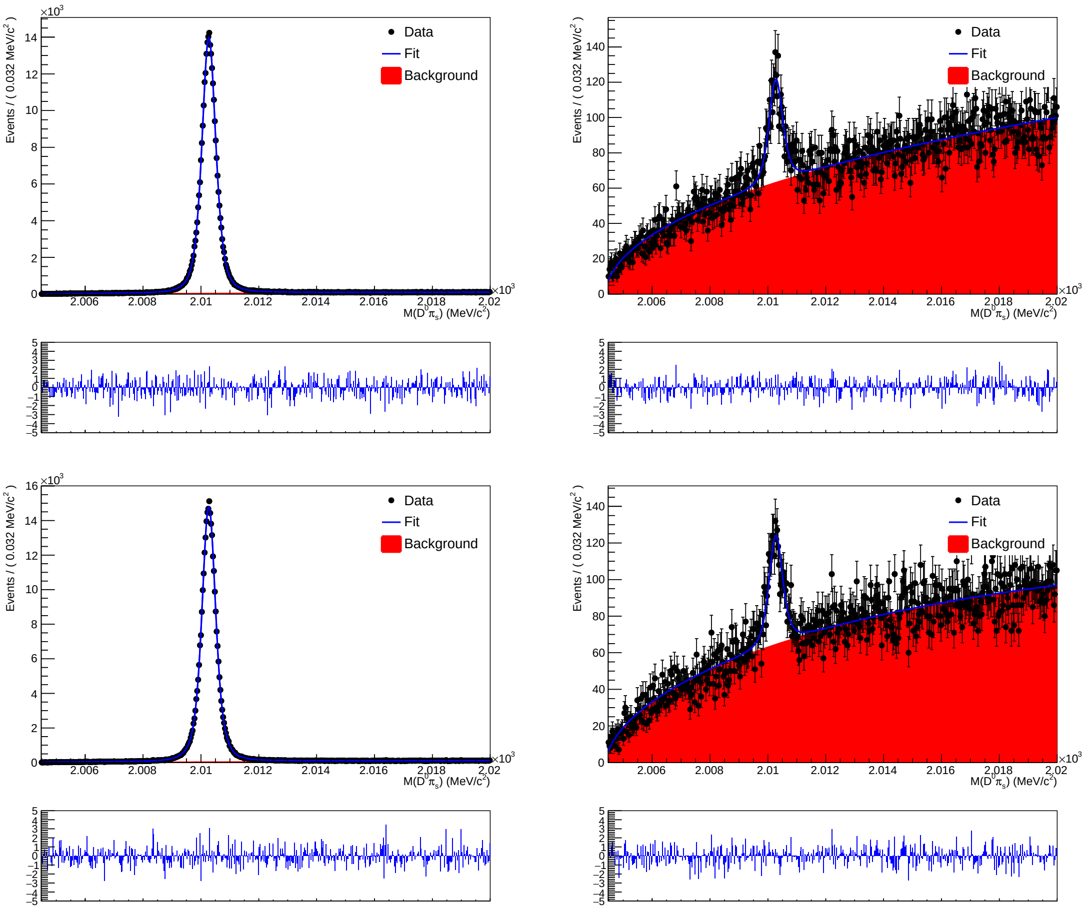

Figure A.10: $D^0\pi_s$ mass distribution for the RS (left) and WS (right) Magnet Up D^0 (top) and $\bar{D}^0$ (bottom) candidates having decay time in the range [2.5,3]τ with fit projection overlaid, in 2015 data.

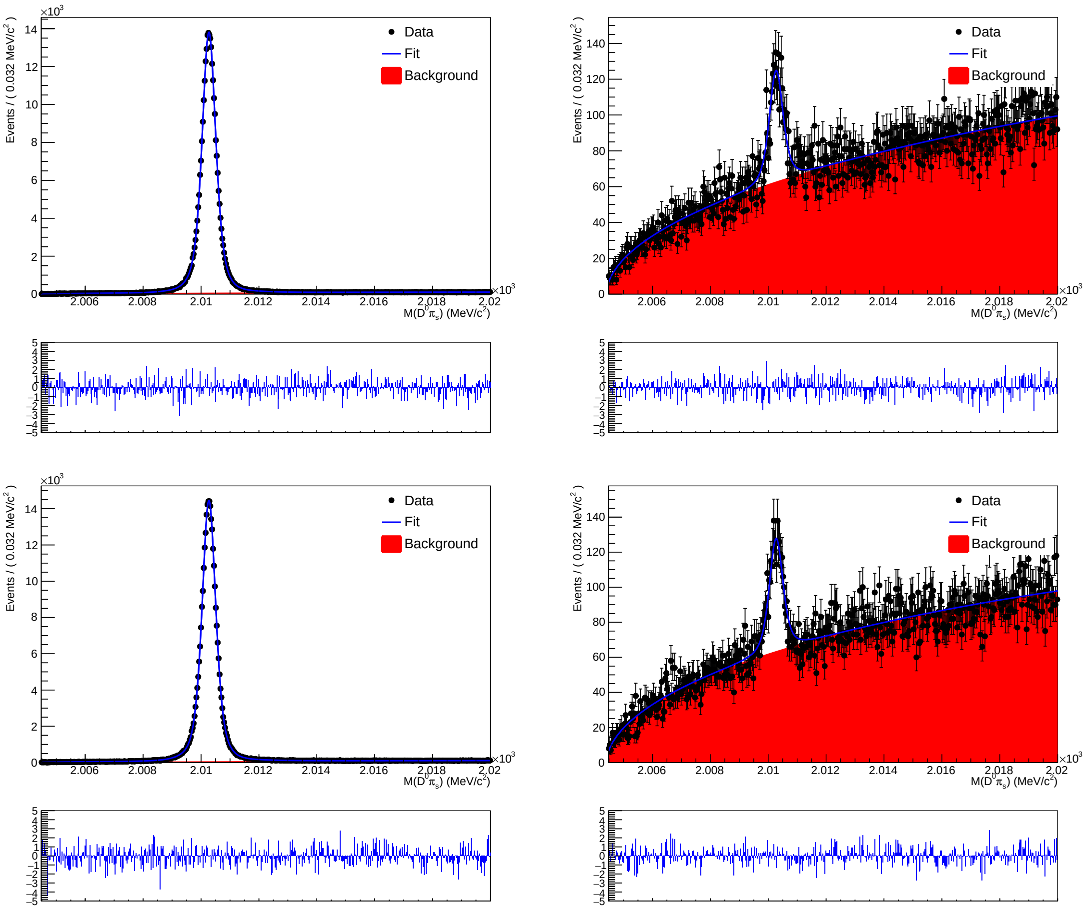

Figure A.11: $D^0\pi_s$ mass distribution for the RS (left) and WS (right) Magnet Up D^0 (top) and $\bar{D}^0$ (bottom) candidates having decay time in the range [3,4]τ with fit projection overlaid, in 2015 data.

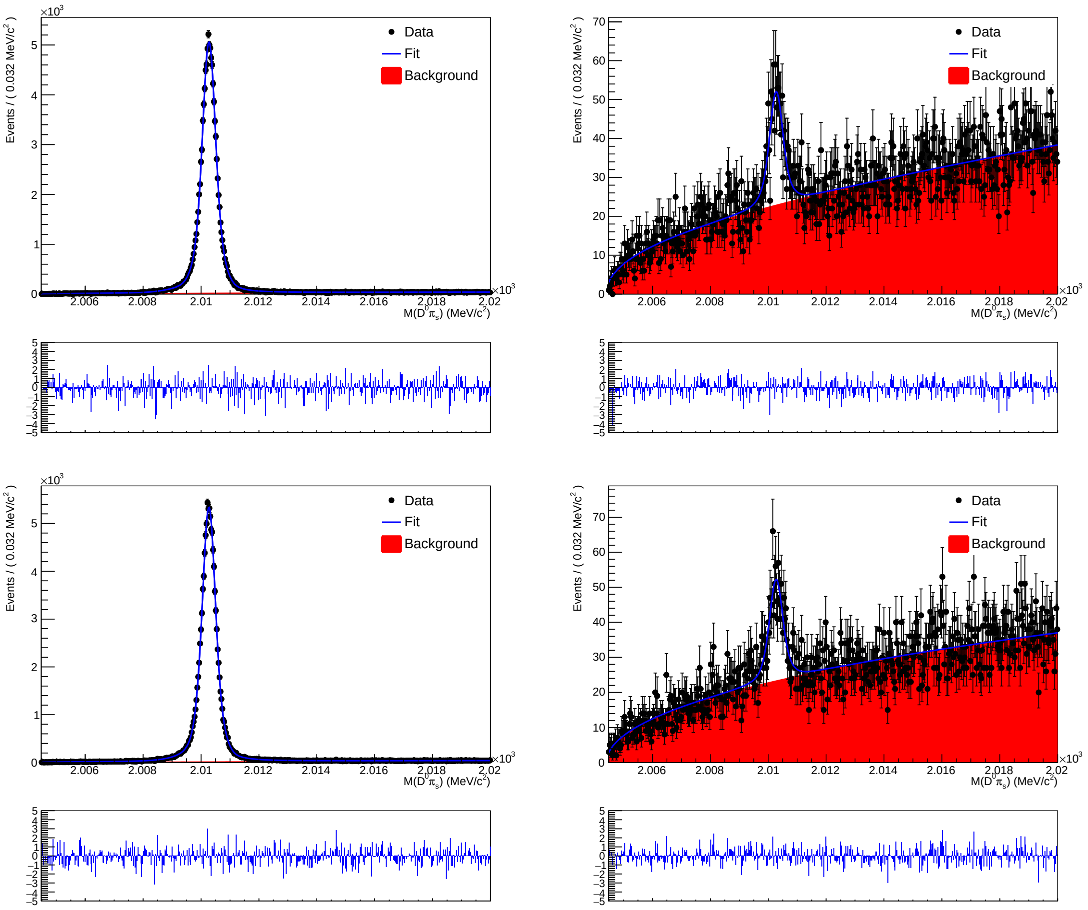

Figure A.12: $D^0\pi_s$ mass distribution for the RS (left) and WS (right) Magnet Up D^0 (top) and $\bar{D}^0$ (bottom) candidates having decay time in the range [4,5]τ with fit projection overlaid, in 2015 data.

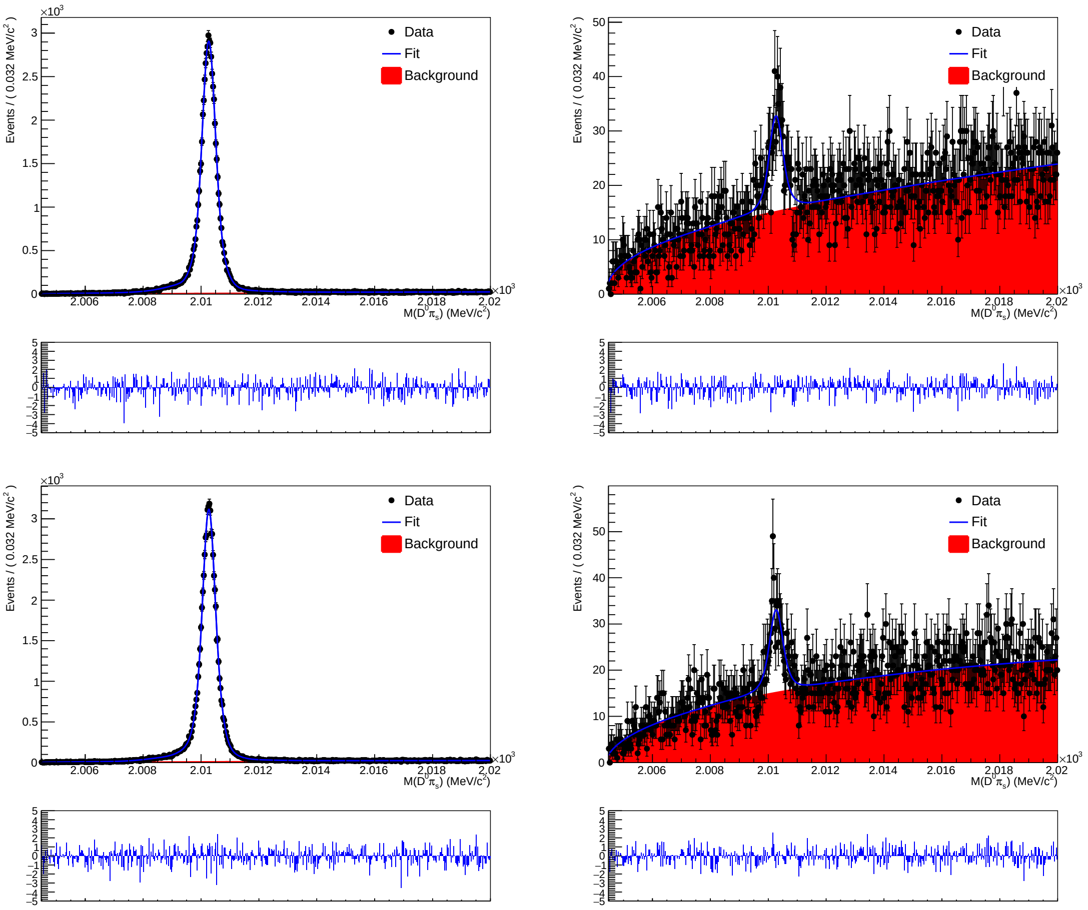

Figure A.13: $D^0\pi_s$ mass distribution for the RS (left) and WS (right) Magnet Up D^0 (top) and $\bar{D}^0$ (bottom) candidates having decay time in the range [5,20]τ with fit projection overlaid, in 2015 data.

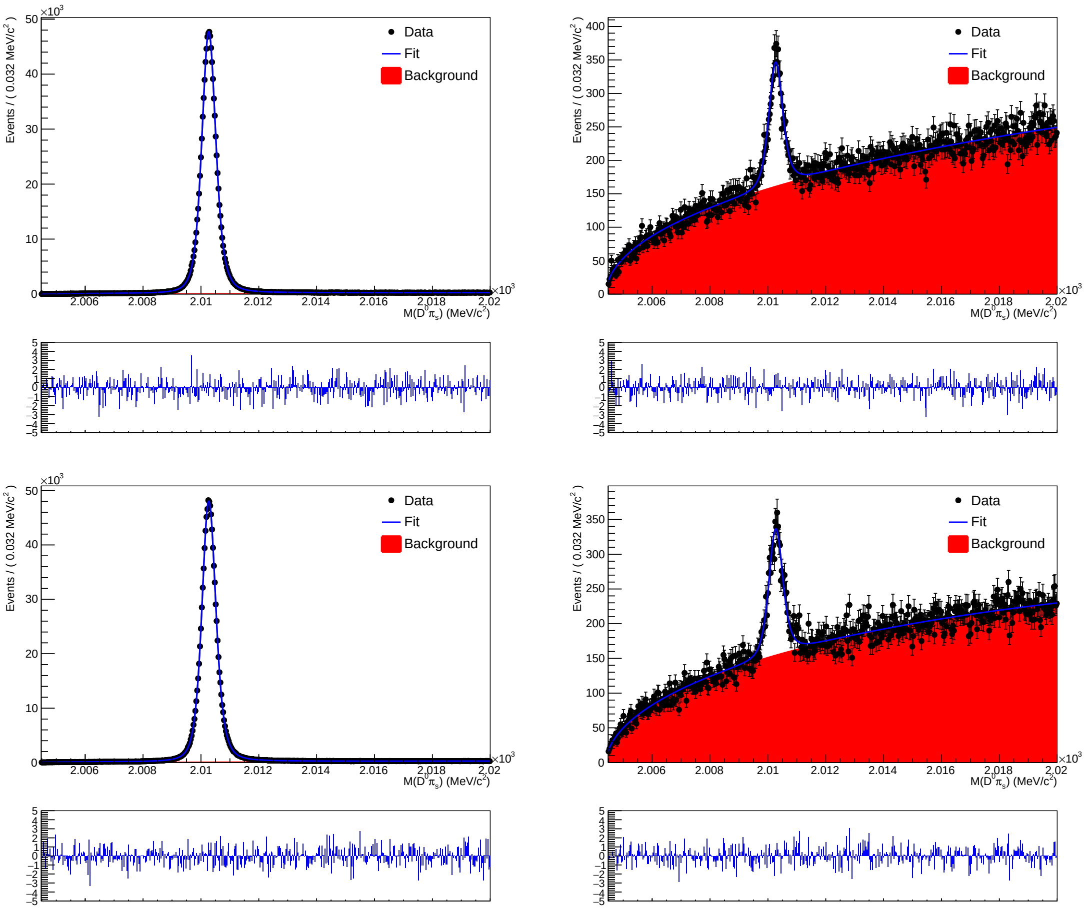

Figure A.14: $D^0\pi_s$ mass distribution for the RS (left) and WS (right) Magnet Down D^0 (top) and $\bar{D}^0$ (bottom) candidates having decay time in the range [0,0.8]τ with fit projection overlaid, in 2015 data.

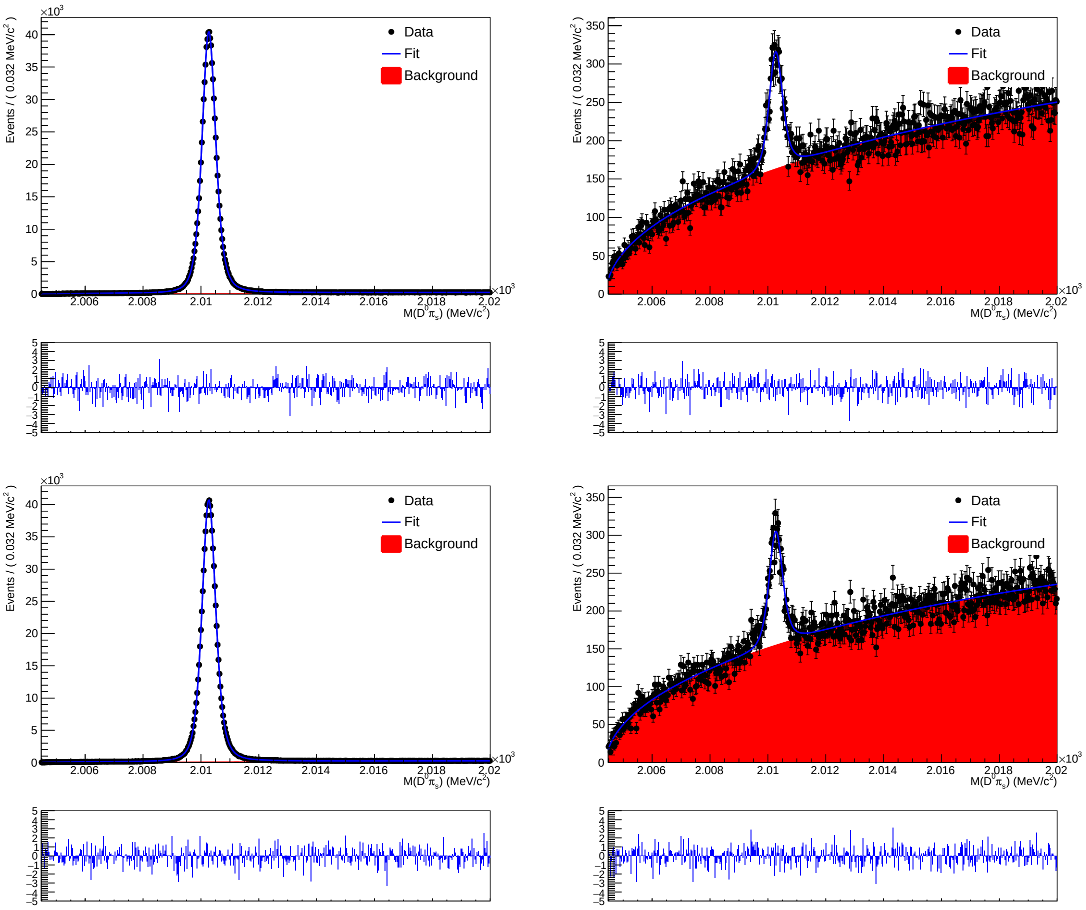

Figure A.15: $D^0\pi_s$ mass distribution for the RS (left) and WS (right) Magnet Down D^0 (top) and $\bar{D}^0$ (bottom) candidates having decay time in the range [0.8,1]τ with fit projection overlaid, in 2015 data.

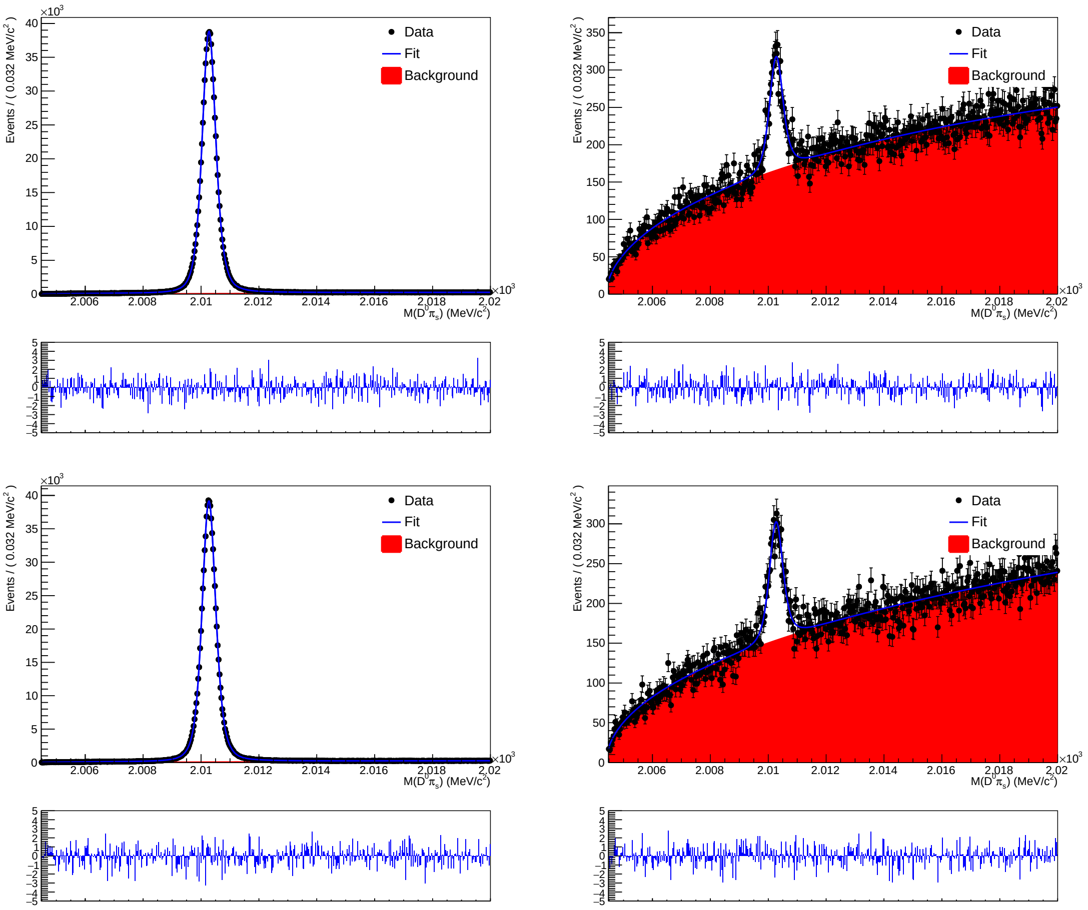

Figure A.16: $D^0\pi_s$ mass distribution for the RS (left) and WS (right) Magnet Down D^0 (top) and $\bar{D}^0$ (bottom) candidates having decay time in the range [1,1.2]τ with fit projection overlaid, in 2015 data.

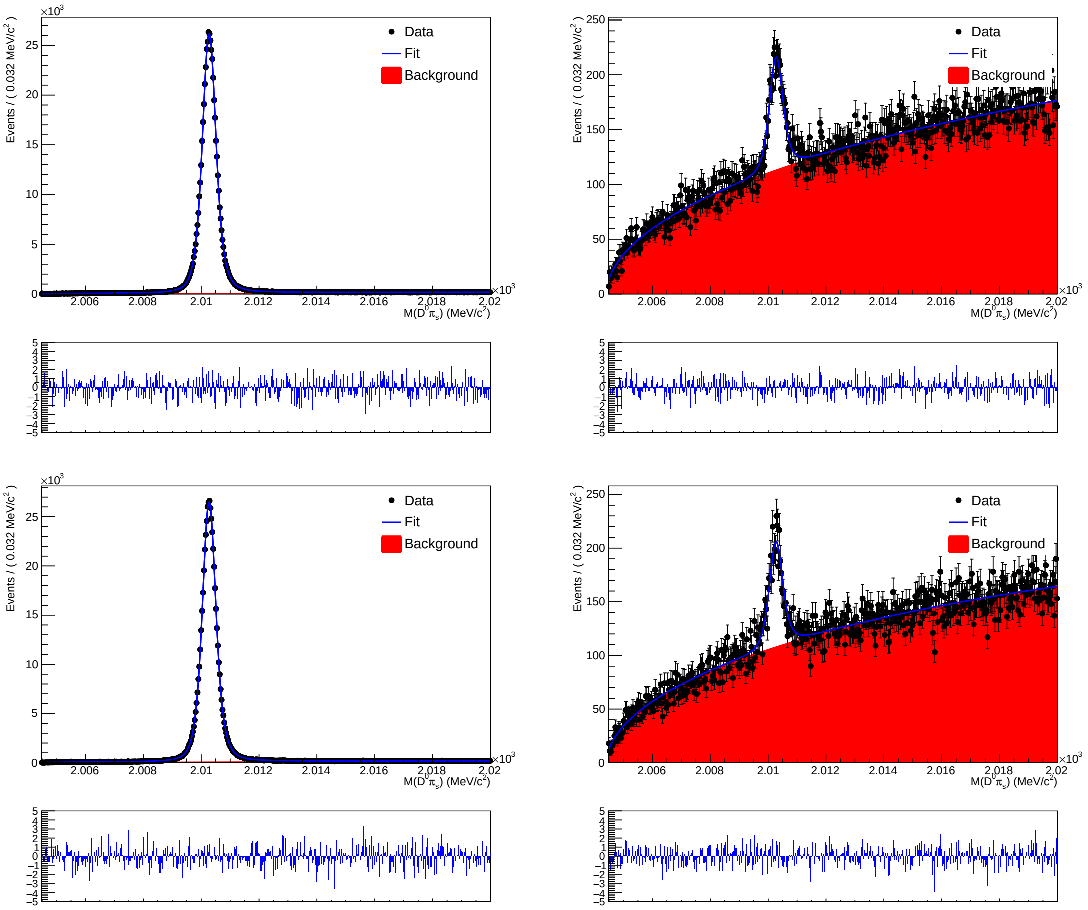

Figure A.17: $D^0\pi_s$ mass distribution for the RS (left) and WS (right) Magnet Down D^0 (top) and $\bar{D}^0$ (bottom) candidates having decay time in the range [1.2,1.35]τ with fit projection overlaid, in 2015 data.

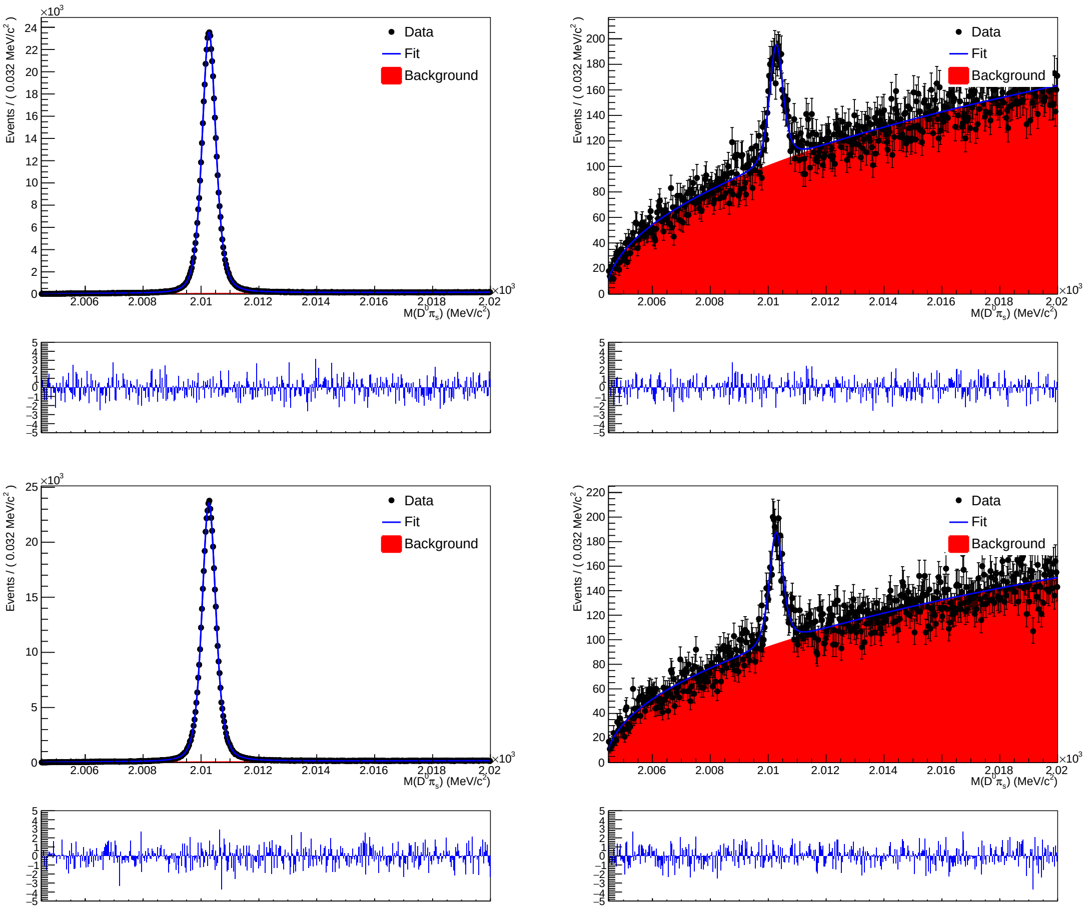

Figure A.18: $D^0\pi_s$ mass distribution for the RS (left) and WS (right) Magnet Down D^0 (top) and $\bar{D}^0$ (bottom) candidates having decay time in the range [1.35,1.5]τ with fit projection overlaid, in 2015 data.

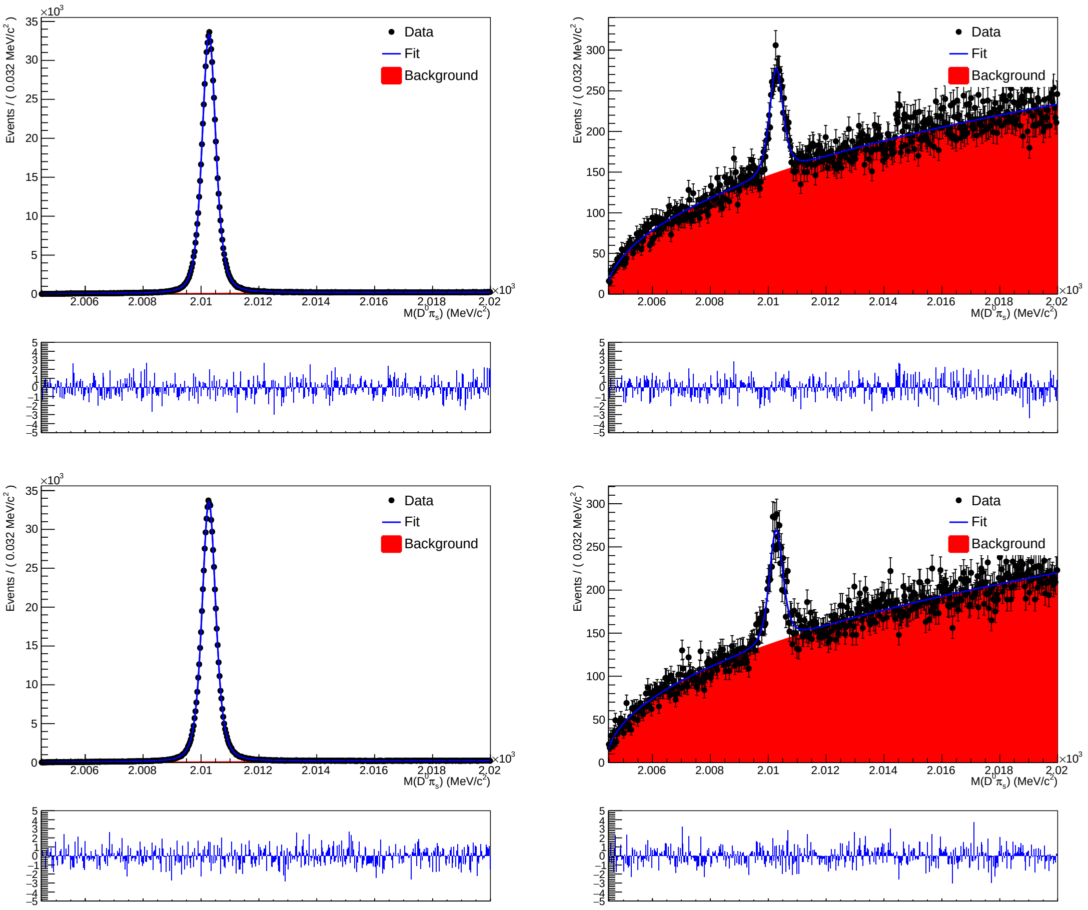

Figure A.19: $D^0\pi_s$ mass distribution for the RS (left) and WS (right) Magnet Down D^0 (top) and $\bar{D}^0$ (bottom) candidates having decay time in the range [1.5,1.75]τ with fit projection overlaid, in 2015 data.

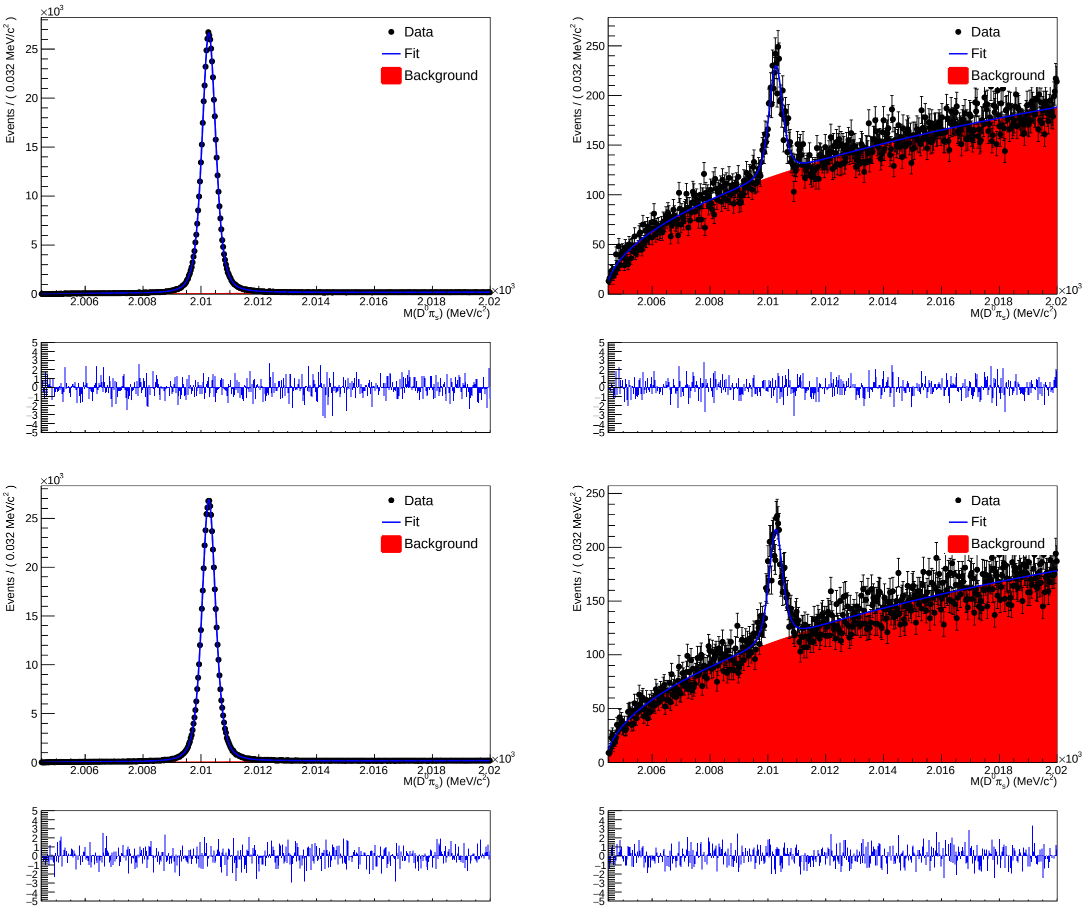

Figure A.20: $D^0\pi_s$ mass distribution for the RS (left) and WS (right) Magnet Down D^0 (top) and $\bar{D}^0$ (bottom) candidates having decay time in the range [1.75,2]τ with fit projection overlaid, in 2015 data.

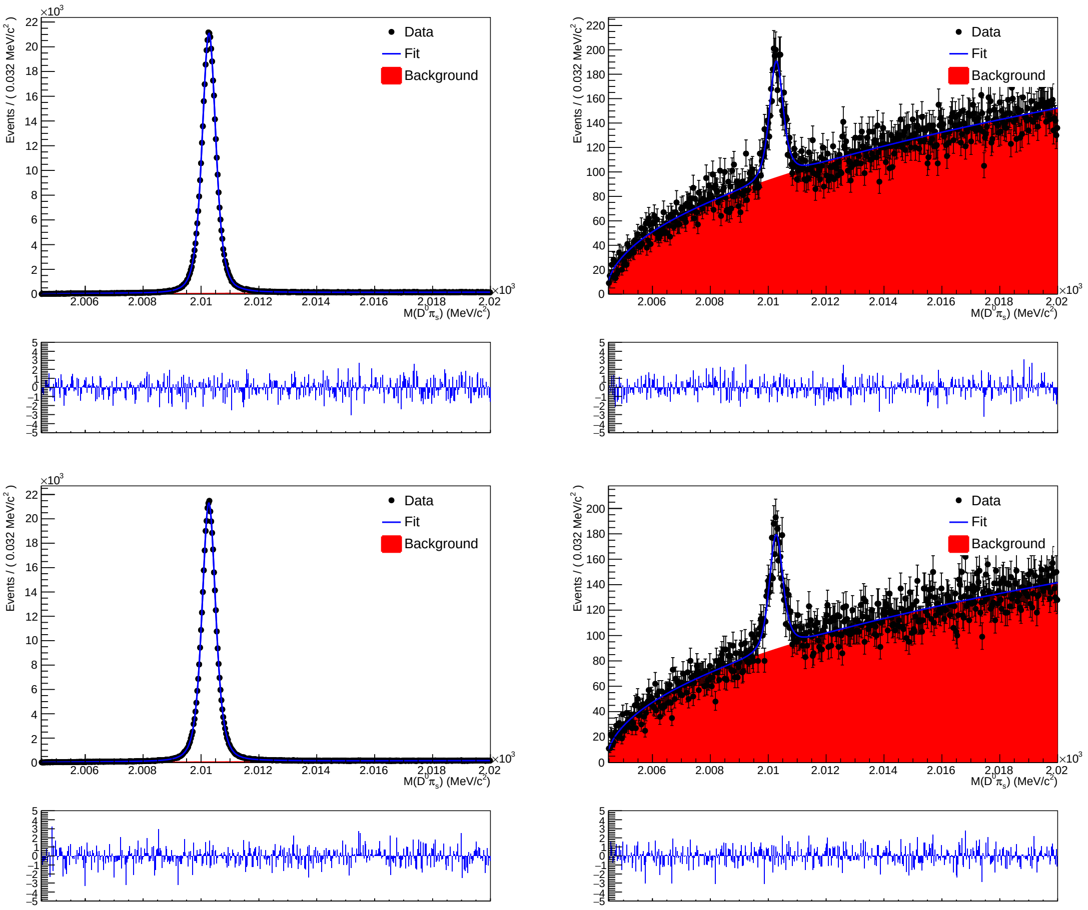

Figure A.21: $D^0\pi_s$ mass distribution for the RS (left) and WS (right) Magnet Down D^0 (top) and $\bar{D}^0$ (bottom) candidates having decay time in the range [2,2.25]τ with fit projection overlaid, in 2015 data.

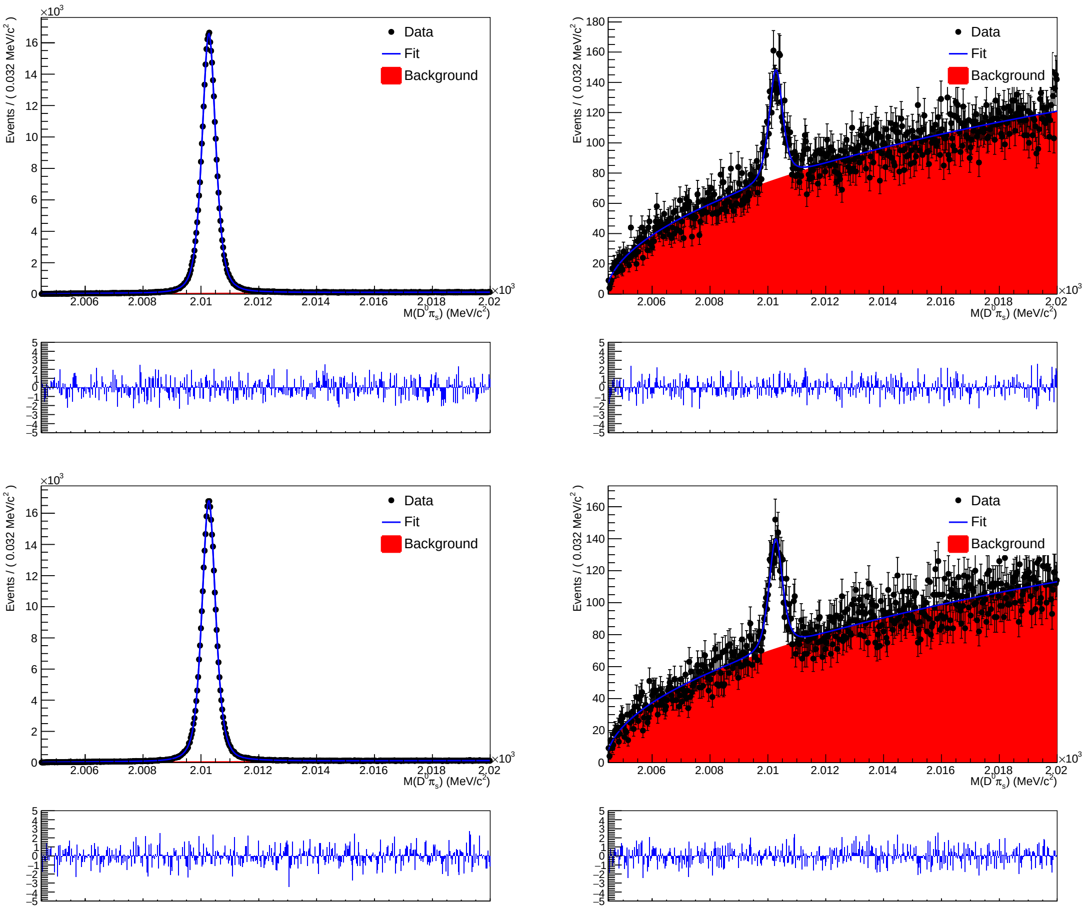

Figure A.22: $D^0\pi_s$ mass distribution for the RS (left) and WS (right) Magnet Down D^0 (top) and $\bar{D}^0$ (bottom) candidates having decay time in the range [2.25,2.5]τ with fit projection overlaid, in 2015 data.

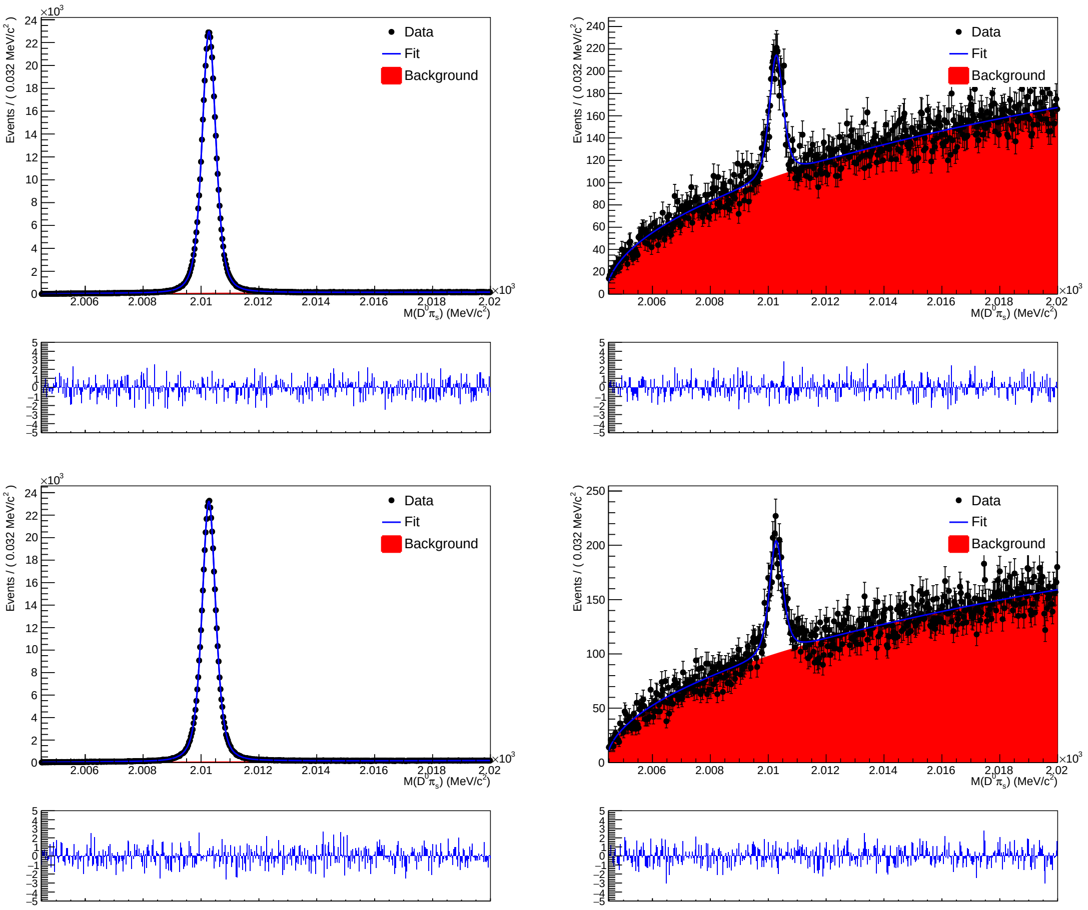

Figure A.23: $D^0\pi_s$ mass distribution for the RS (left) and WS (right) Magnet Down D^0 (top) and $\bar{D}^0$ (bottom) candidates having decay time in the range [2.5,3]τ with fit projection overlaid, in 2015 data.

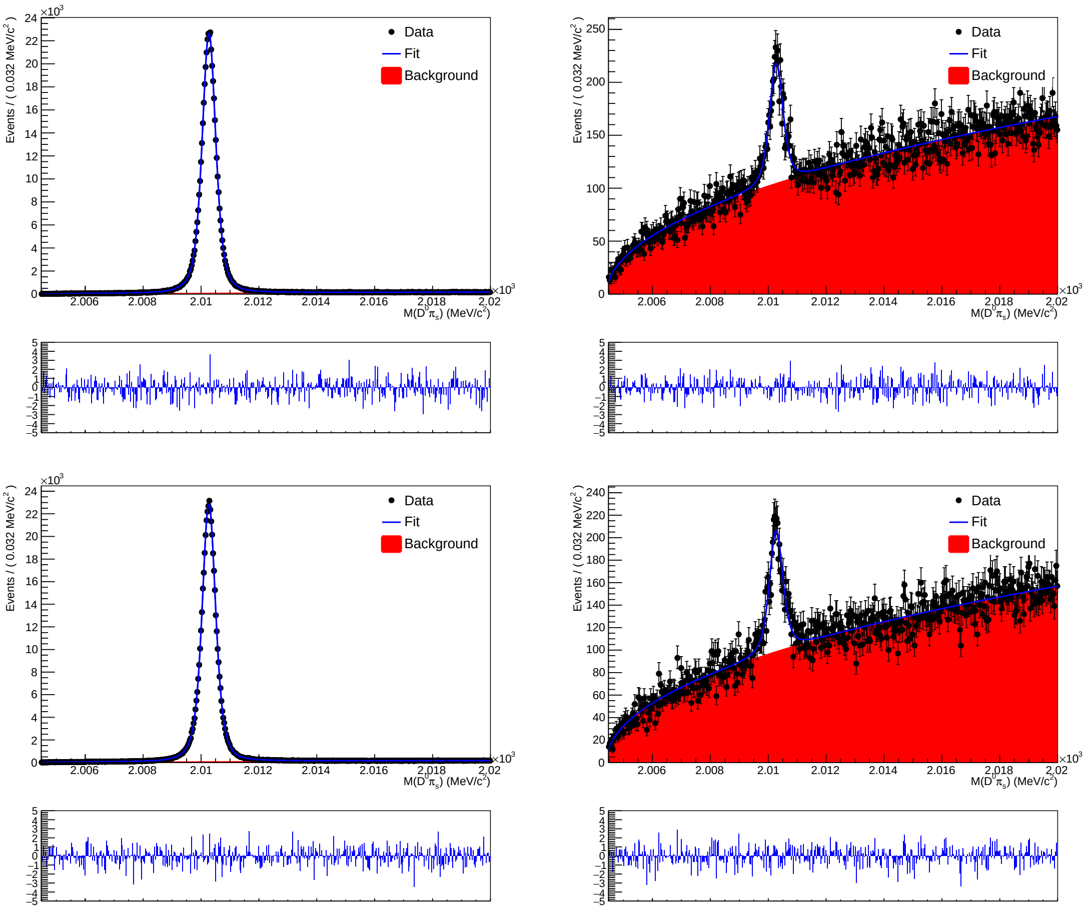

Figure A.24: $D^0\pi_s$ mass distribution for the RS (left) and WS (right) Magnet Down D^0 (top) and $\bar{D}^0$ (bottom) candidates having decay time in the range [3,4]τ with fit projection overlaid, in 2015 data.

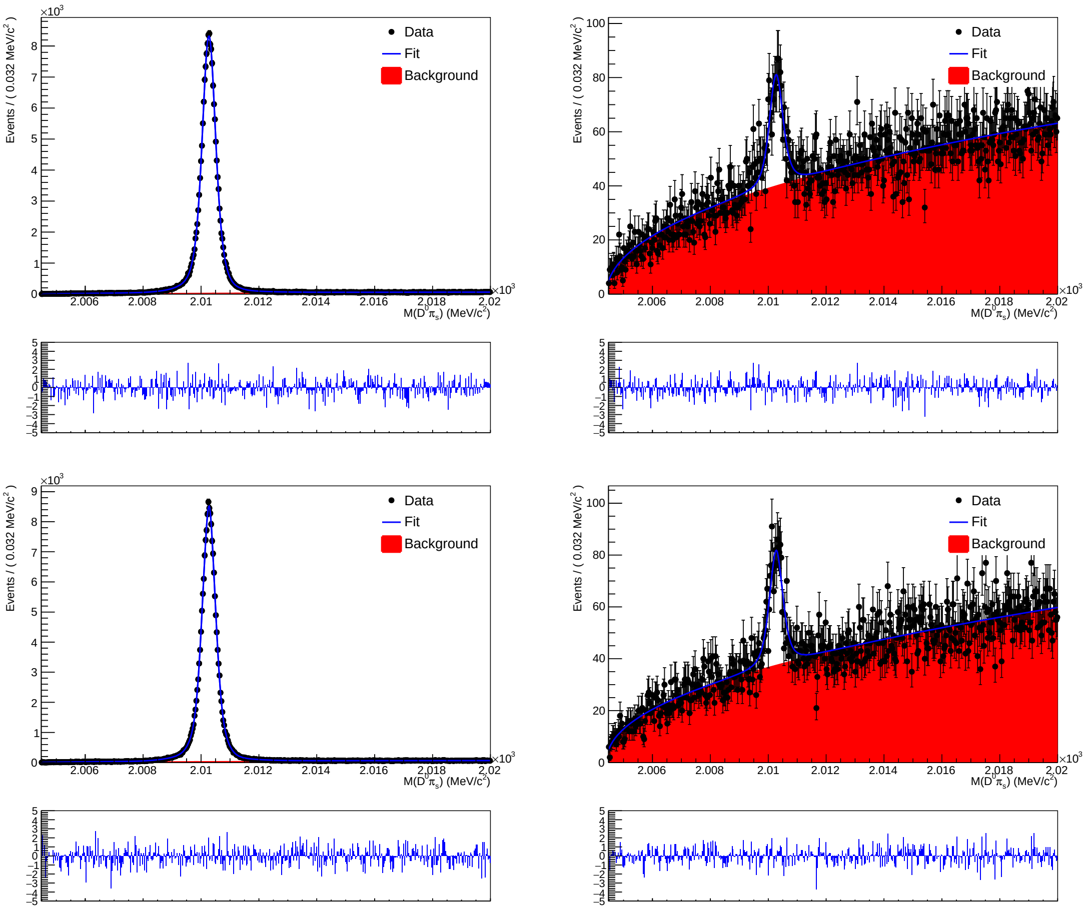

Figure A.25: $D^0\pi_s$ mass distribution for the RS (left) and WS (right) Magnet Down D^0 (top) and $\bar{D}^0$ (bottom) candidates having decay time in the range [4,5]τ with fit projection overlaid, in 2015 data.

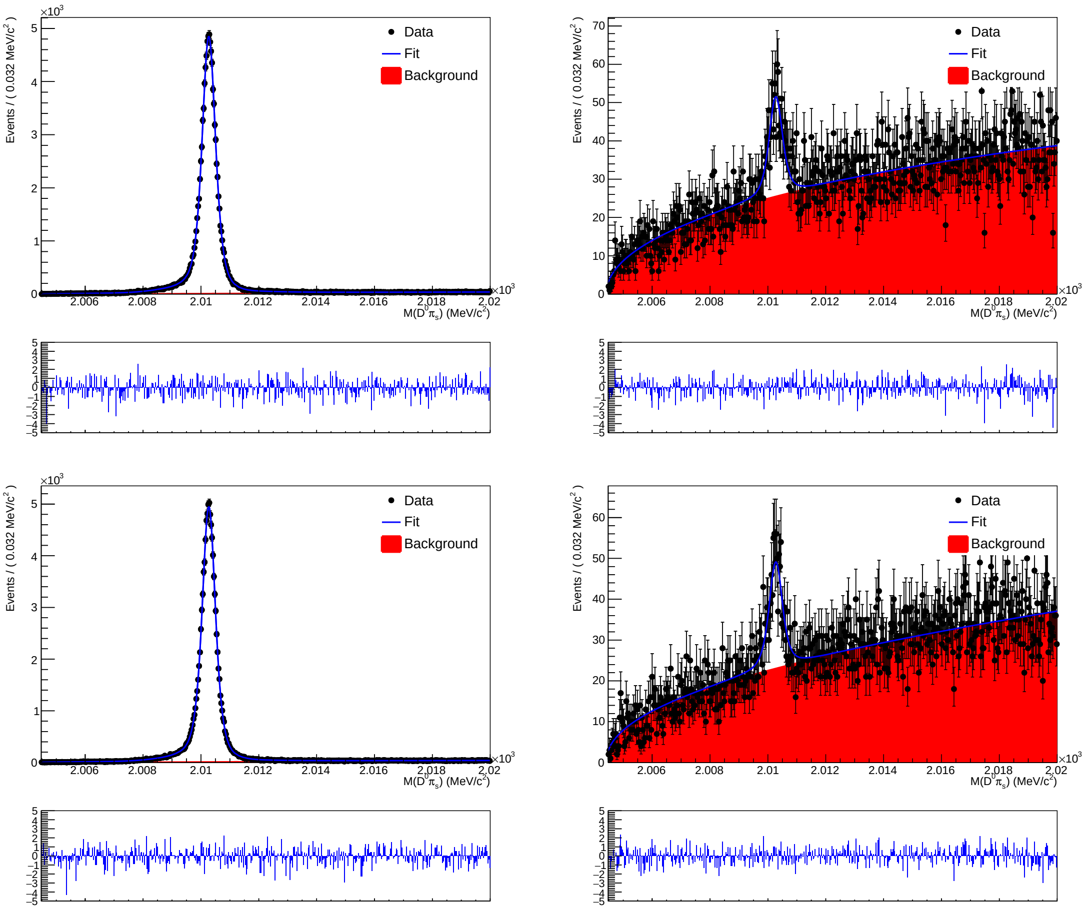

Figure A.26: $D^0\pi_s$ mass distribution for the RS (left) and WS (right) Magnet Down D^0 (top) and $\bar{D}^0$ (bottom) candidates having decay time in the range [5,20]τ with fit projection overlaid, in 2015 data.

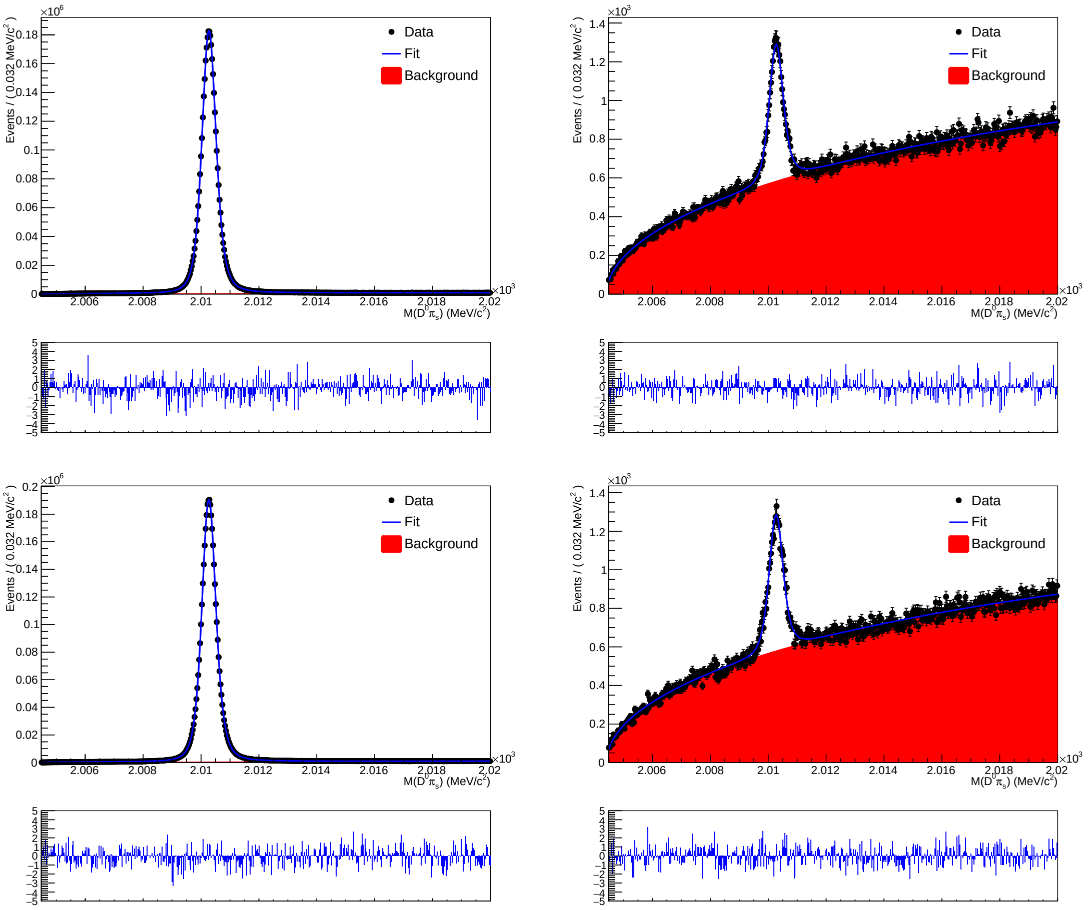

Figure A.27: $D^0\pi_s$ mass distribution for the RS (left) and WS (right) Magnet Up D^0 (top) and $\bar{D}^0$ (bottom) candidates having decay time in the range [0,0.8]τ with fit projection overlaid, in 2016 data.

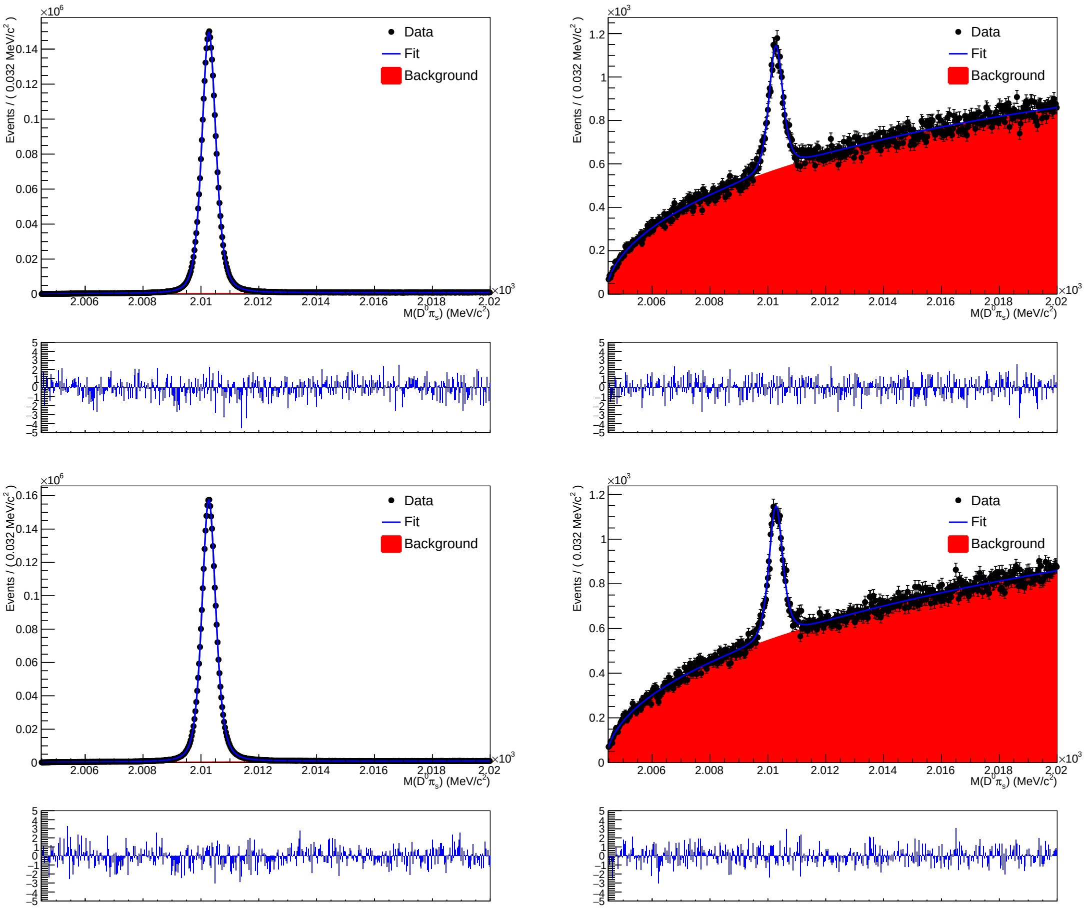

Figure A.28: $D^0\pi_s$ mass distribution for the RS (left) and WS (right) Magnet Up D^0 (top) and $\bar{D}^0$ (bottom) candidates having decay time in the range [0.8,1]τ with fit projection overlaid, in 2016 data.

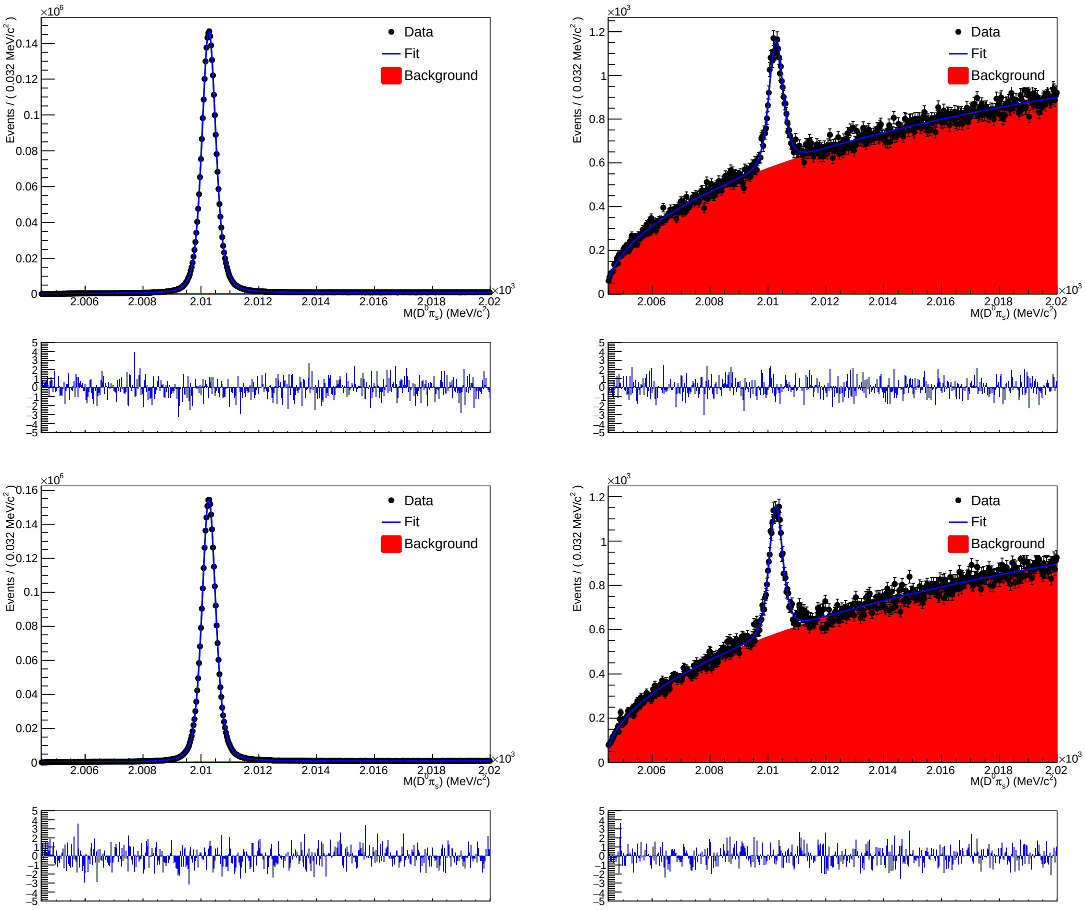

Figure A.29: $D^0\pi_s$ mass distribution for the RS (left) and WS (right) Magnet Up D^0 (top) and $\bar{D}^0$ (bottom) candidates having decay time in the range [1,1.2]τ with fit projection overlaid, in 2016 data.

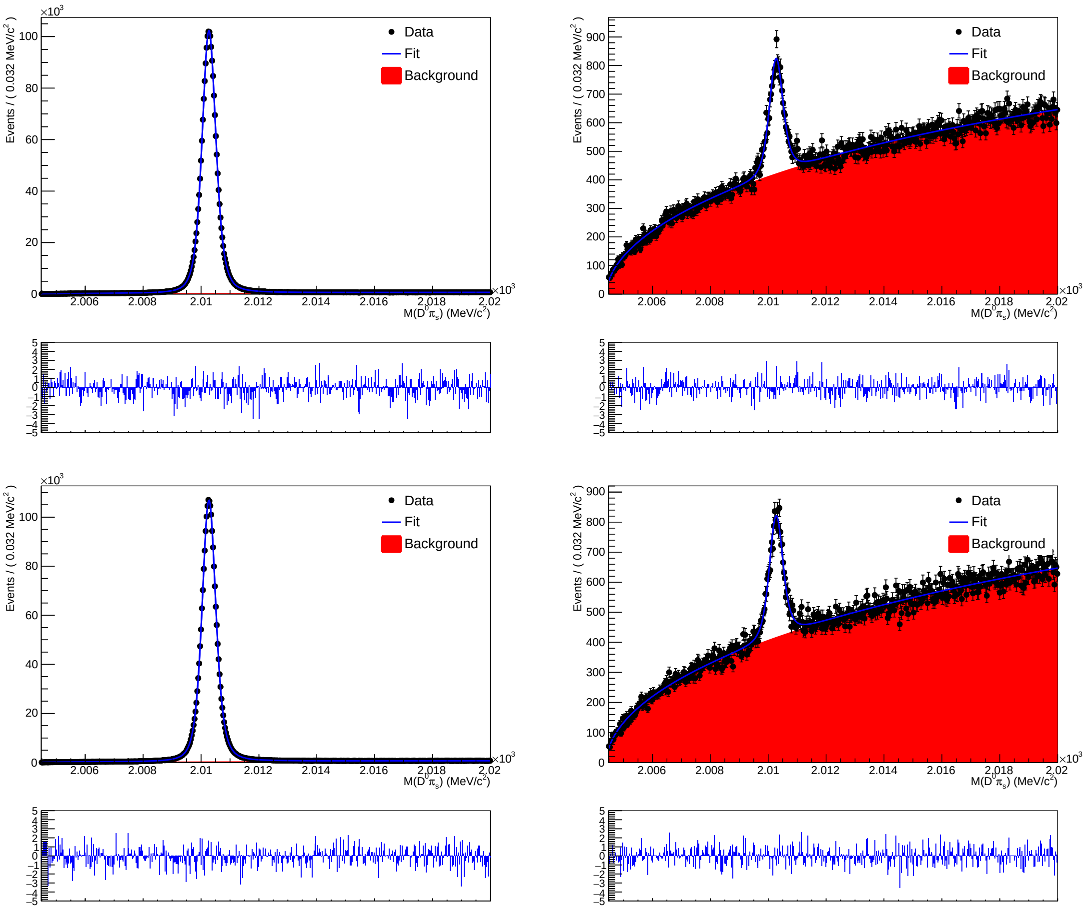

Figure A.30: $D^0\pi_s$ mass distribution for the RS (left) and WS (right) Magnet Up D^0 (top) and $\bar{D}^0$ (bottom) candidates having decay time in the range [1.2,1.35]τ with fit projection overlaid, in 2016 data.

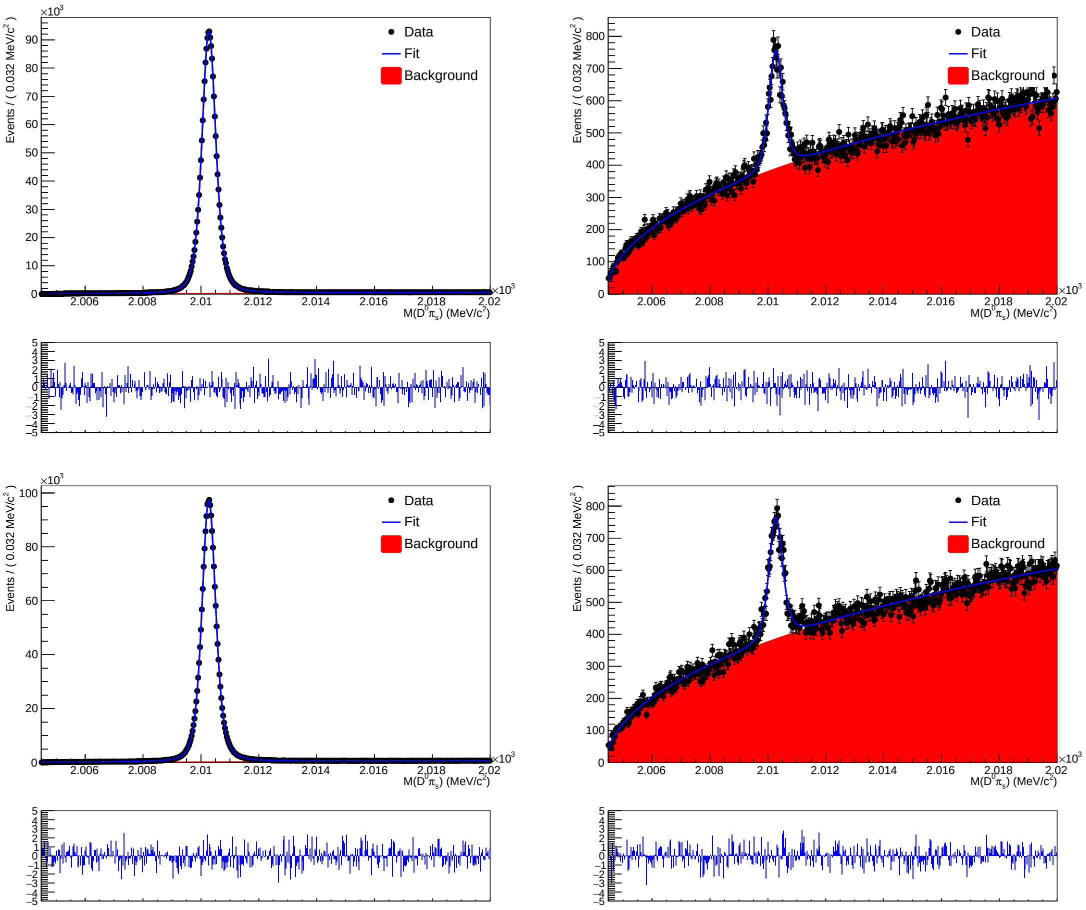

Figure A.31: $D^0\pi_s$ mass distribution for the RS (left) and WS (right) Magnet Up D^0 (top) and $\bar{D}^0$ (bottom) candidates having decay time in the range [1.35,1.5]τ with fit projection overlaid, in 2016 data.

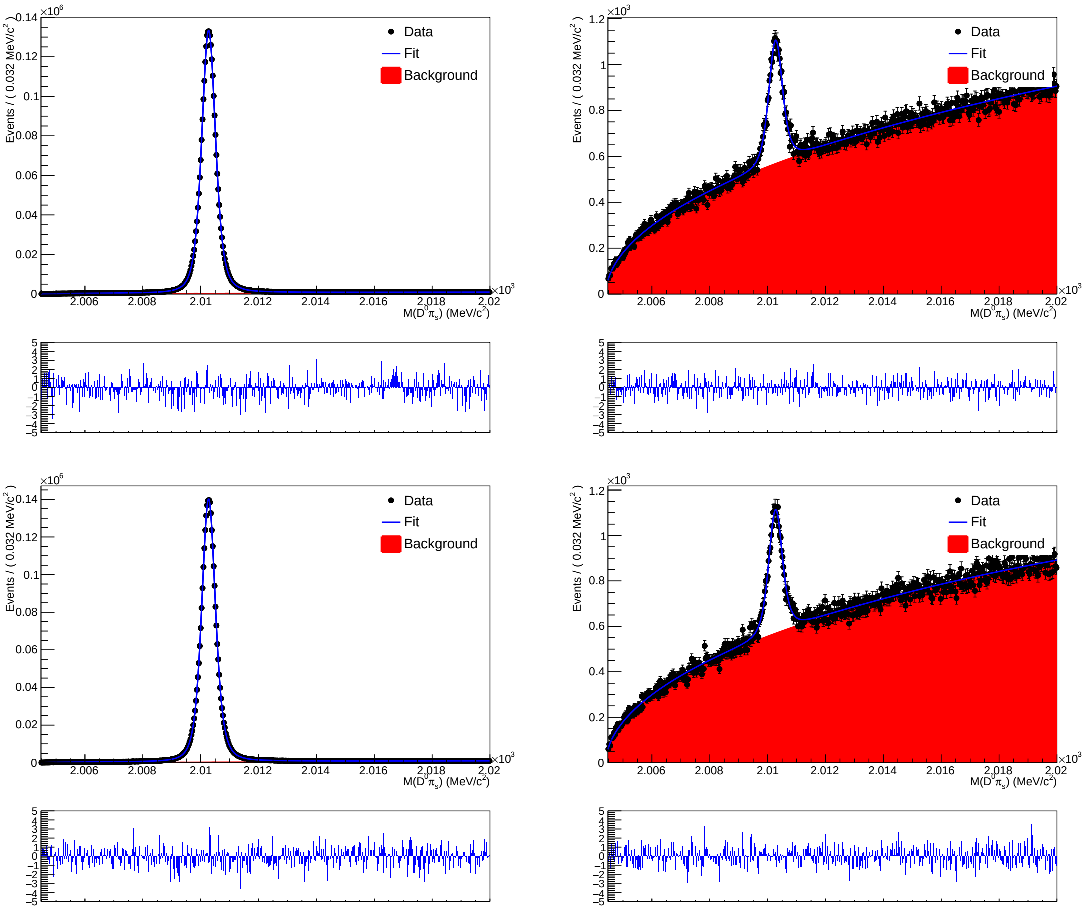

Figure A.32: $D^0\pi_s$ mass distribution for the RS (left) and WS (right) Magnet Up D^0 (top) and $\bar{D}^0$ (bottom) candidates having decay time in the range [1.5,1.75]τ with fit projection overlaid, in 2016 data.

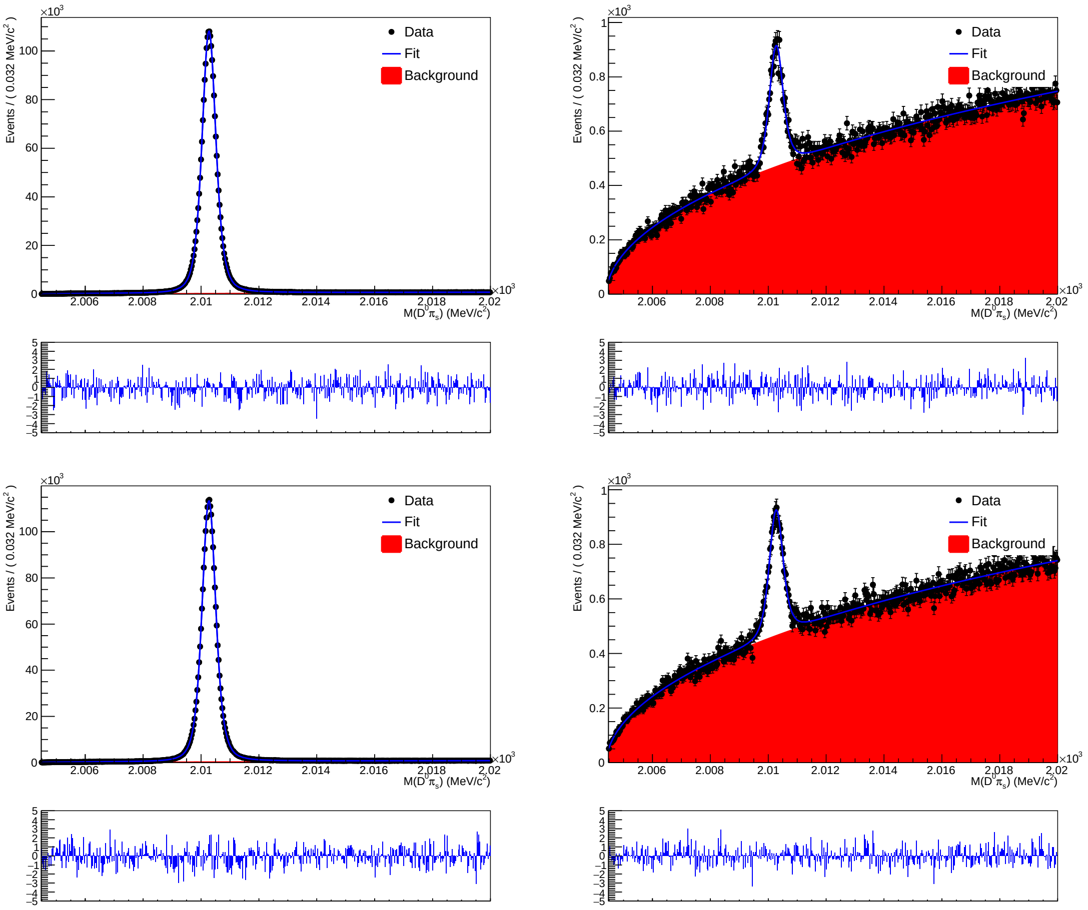

Figure A.33: $D^0\pi_s$ mass distribution for the RS (left) and WS (right) Magnet Up D^0 (top) and $\bar{D}^0$ (bottom) candidates having decay time in the range [1.75,2]τ with fit projection overlaid, in 2016 data.

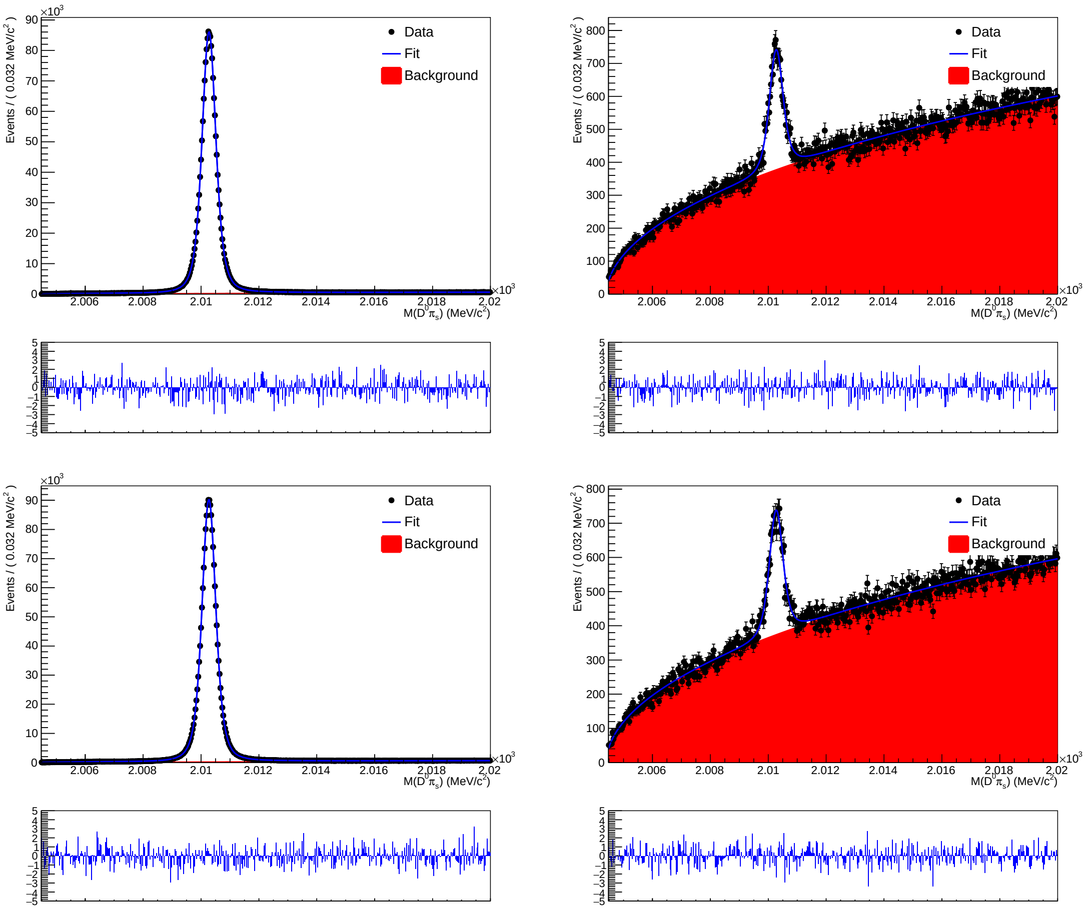

Figure A.34: $D^0\pi_s$ mass distribution for the RS (left) and WS (right) Magnet Up D^0 (top) and $\bar{D}^0$ (bottom) candidates having decay time in the range [2,2.25]τ with fit projection overlaid, in 2016 data.

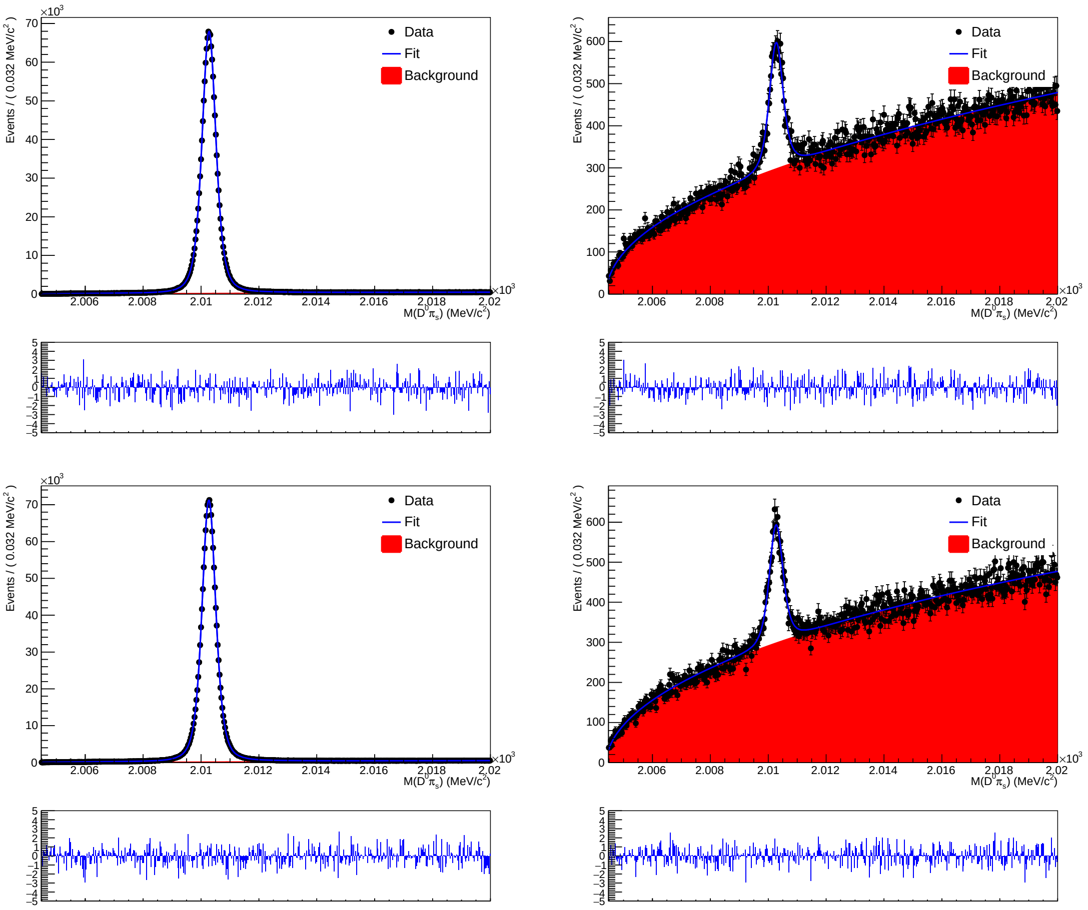

Figure A.35: $D^0\pi_s$ mass distribution for the RS (left) and WS (right) Magnet Up D^0 (top) and $\bar{D}^0$ (bottom) candidates having decay time in the range [2.25,2.5]τ with fit projection overlaid, in 2016 data.

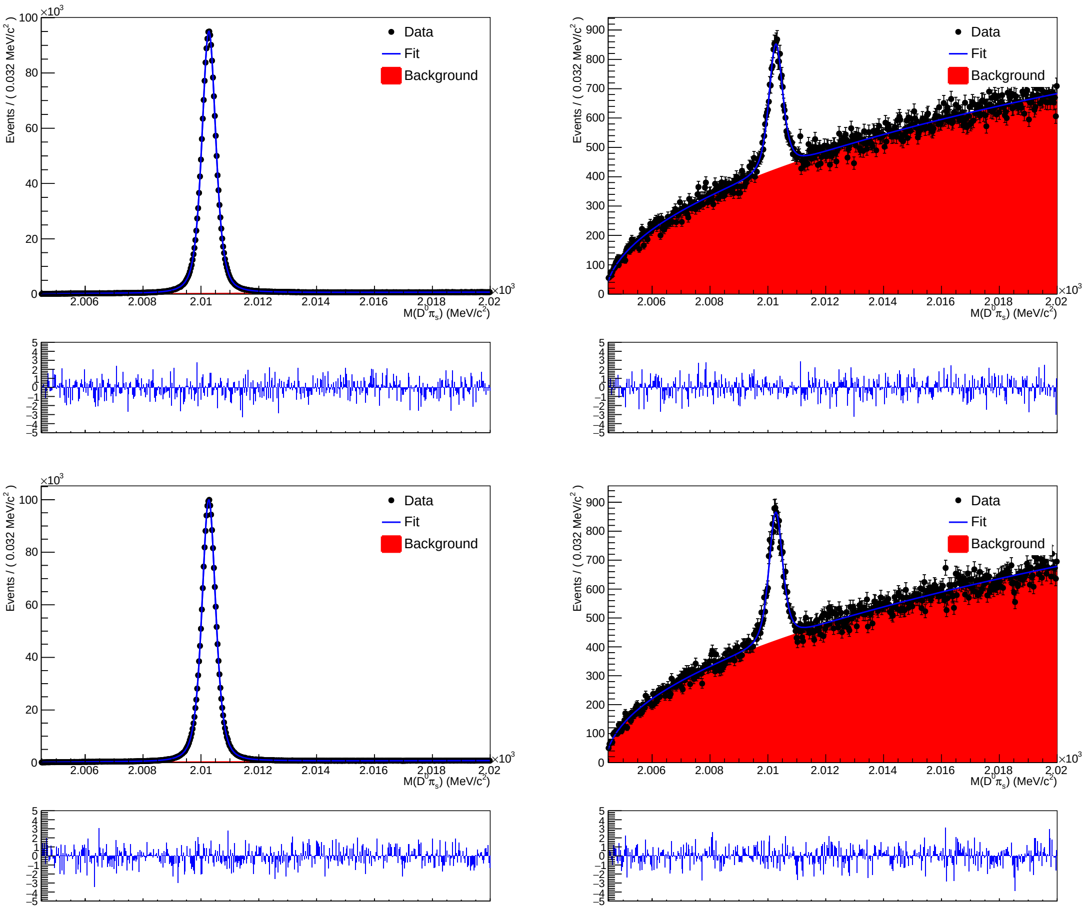

Figure A.36: $D^0\pi_s$ mass distribution for the RS (left) and WS (right) Magnet Up D^0 (top) and $\bar{D}^0$ (bottom) candidates having decay time in the range $[2.5,3]\tau$ with fit projection overlaid, in 2016 data.

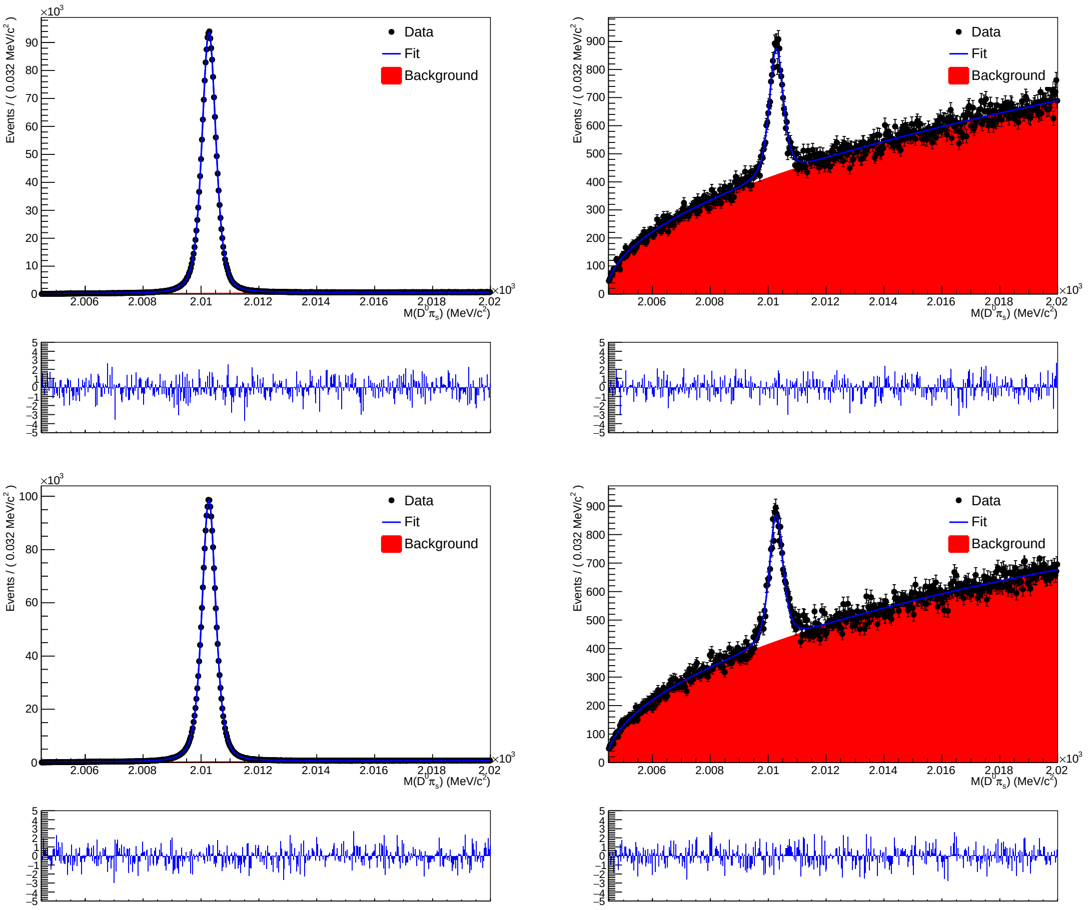

Figure A.37: $D^0\pi_s$ mass distribution for the RS (left) and WS (right) Magnet Up D^0 (top) and $\bar{D}^0$ (bottom) candidates having decay time in the range [3,4]τ with fit projection overlaid, in 2016 data.

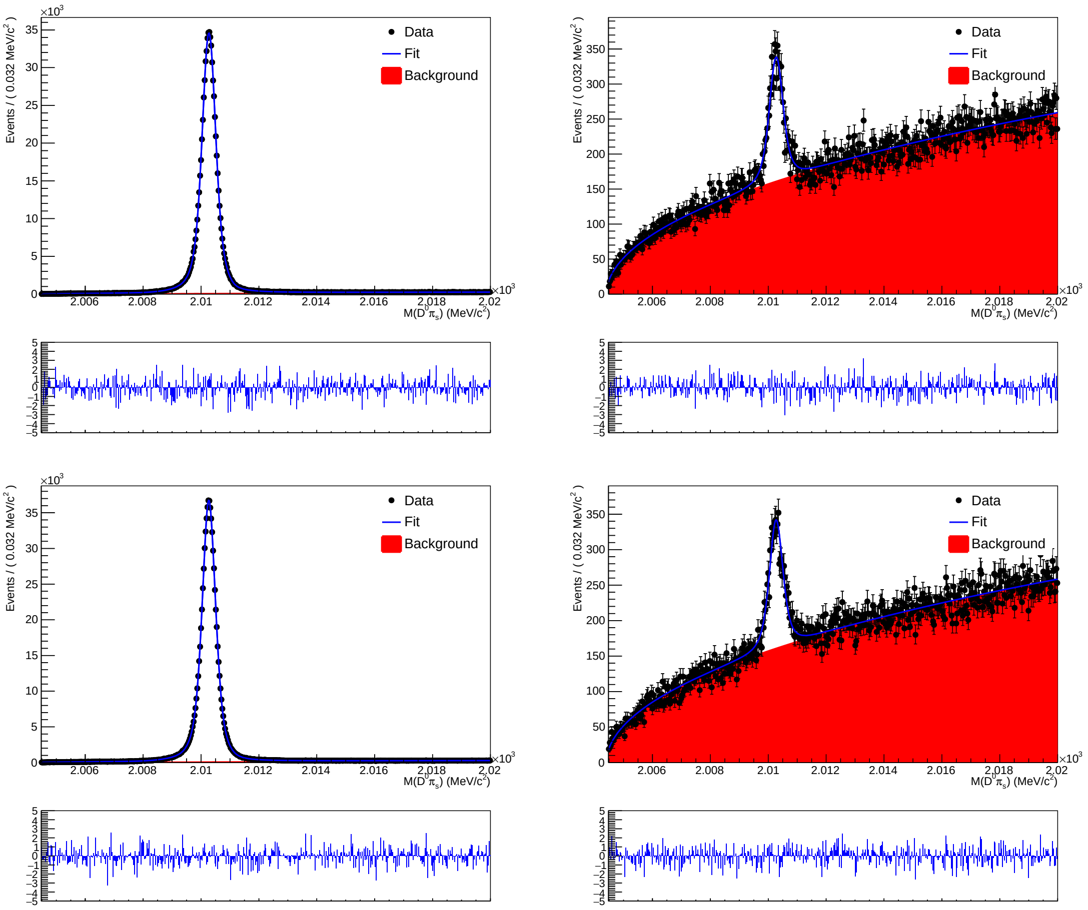

Figure A.38: $D^0\pi_s$ mass distribution for the RS (left) and WS (right) Magnet Up D^0 (top) and $\bar{D}^0$ (bottom) candidates having decay time in the range [4,5]τ with fit projection overlaid, in 2016 data.

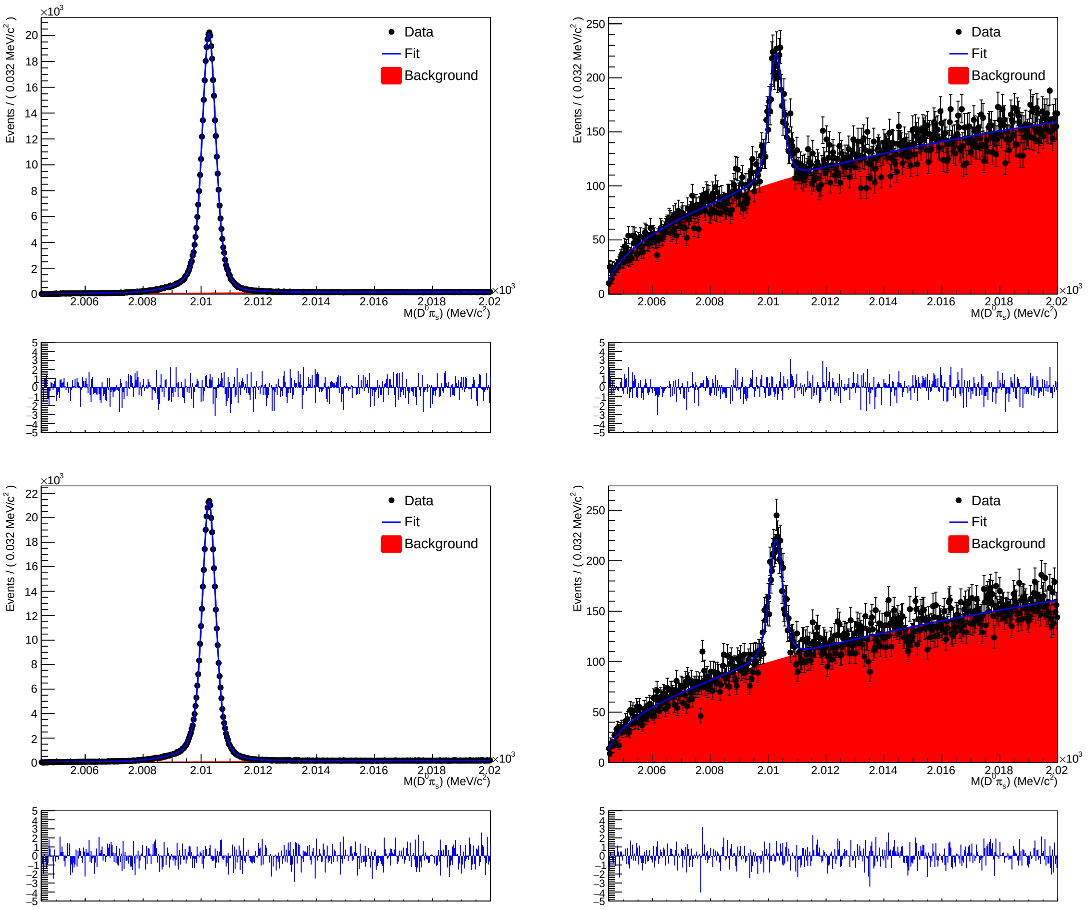

Figure A.39: $D^0\pi_s$ mass distribution for the RS (left) and WS (right) Magnet Up D^0 (top) and $\bar{D}^0$ (bottom) candidates having decay time in the range [5,20]τ with fit projection overlaid, in 2016 data.

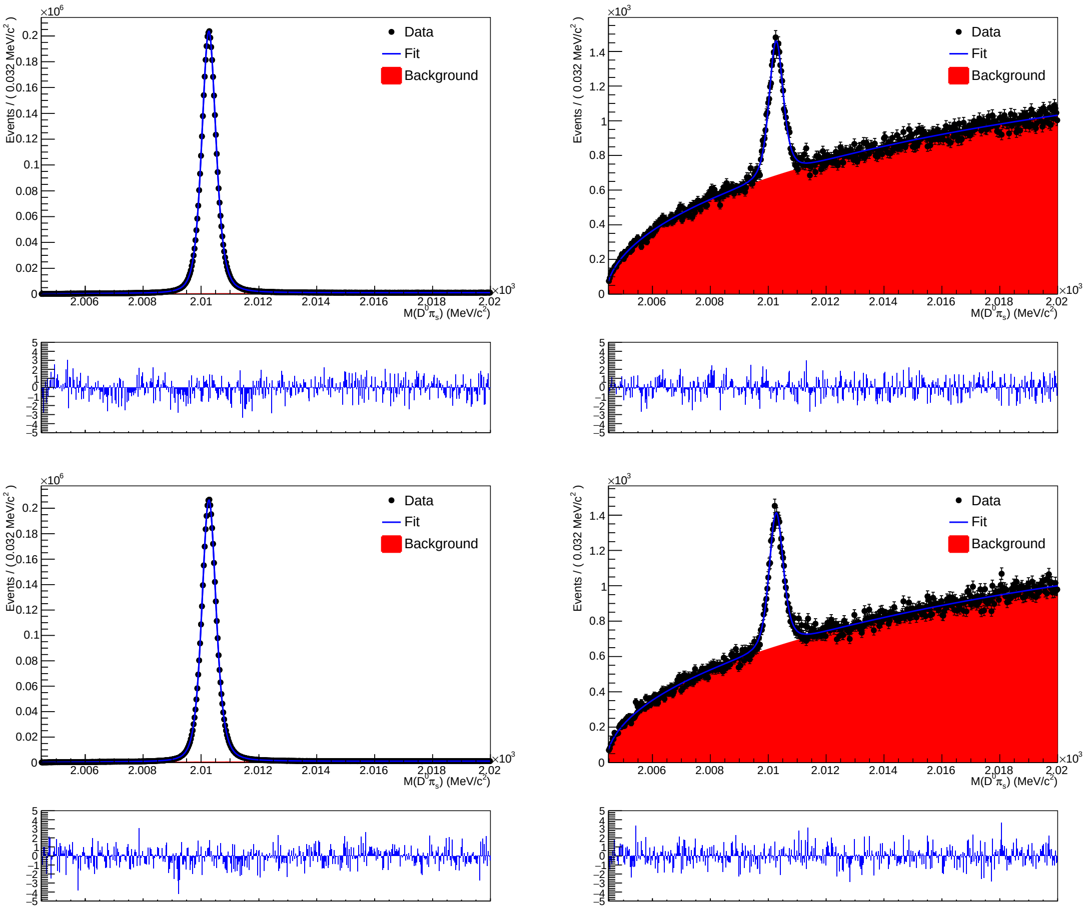

Figure A.40: $D^0\pi_s$ mass distribution for the RS (left) and WS (right) Magnet Down D^0 (top) and $\bar{D}^0$ (bottom) candidates having decay time in the range [0,0.8]τ with fit projection overlaid, in 2016 data.

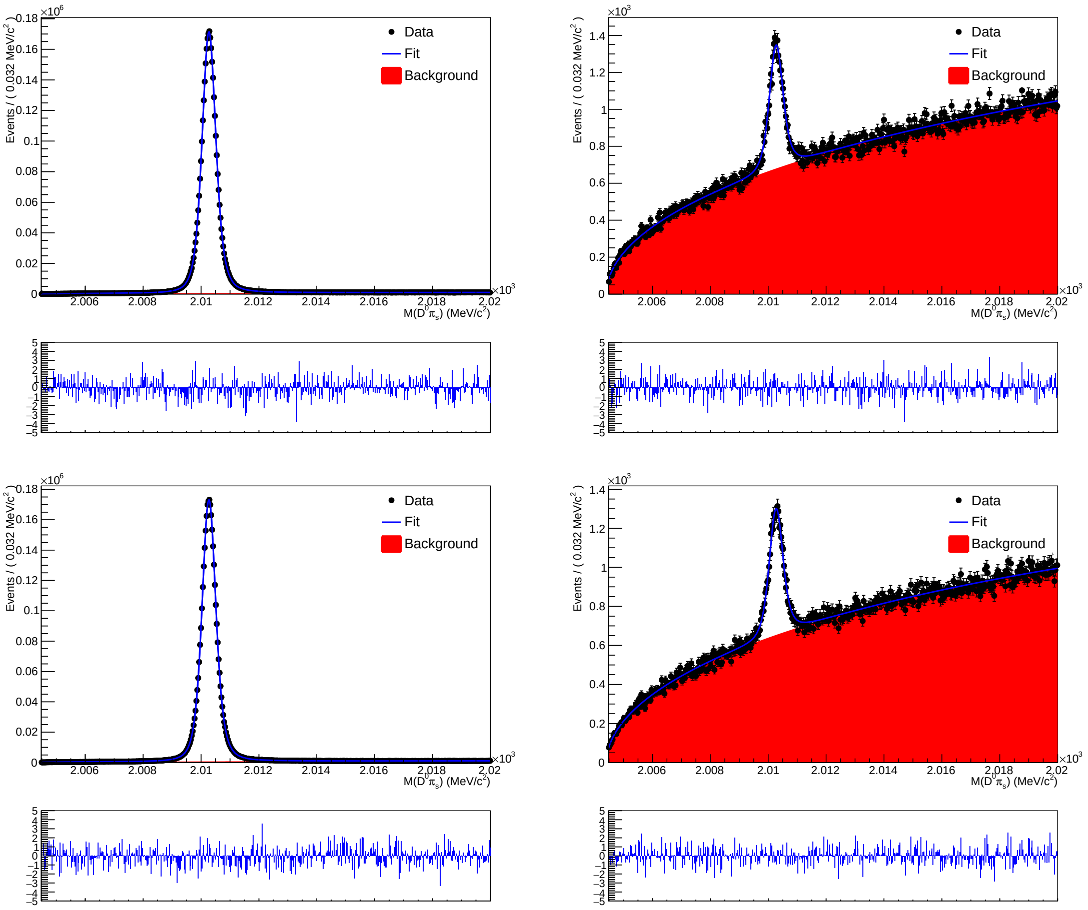

Figure A.41: $D^0\pi_s$ mass distribution for the RS (left) and WS (right) Magnet Down D^0 (top) and $\bar{D}^0$ (bottom) candidates having decay time in the range [0.8,1]τ with fit projection overlaid, in 2016 data.

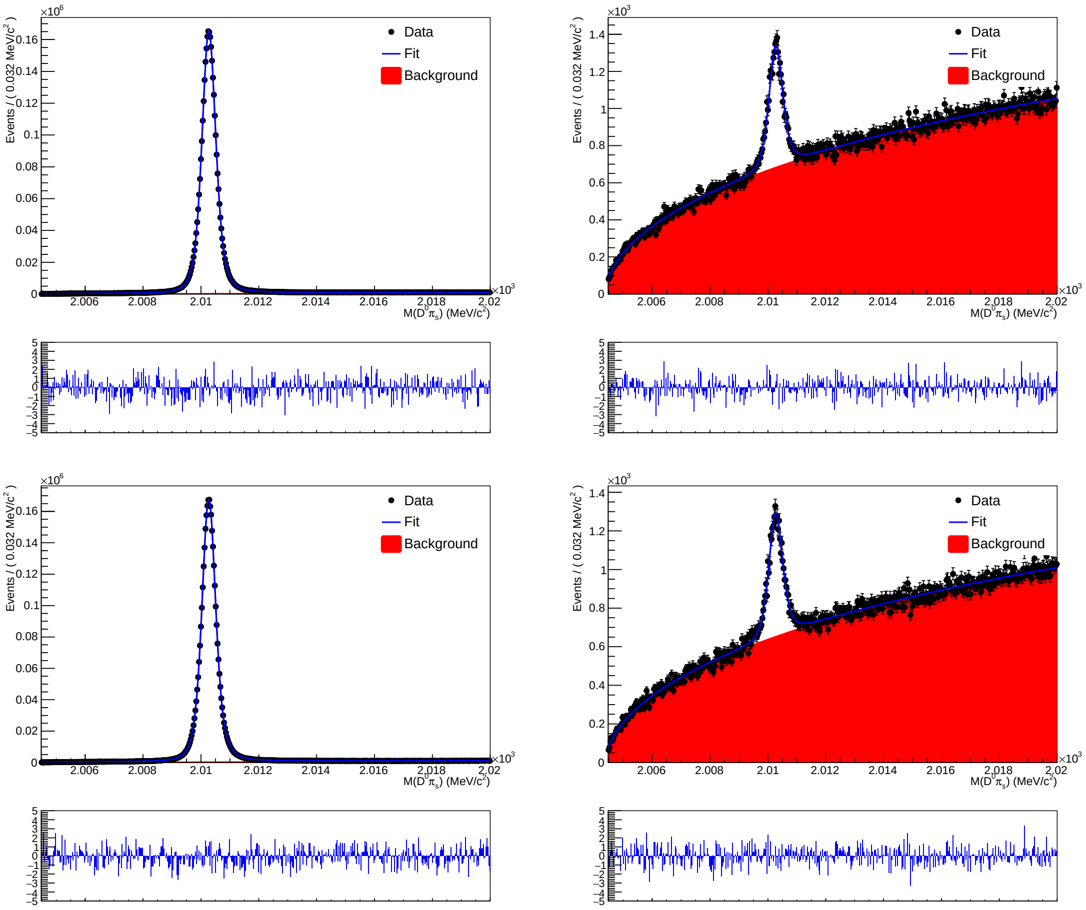

Figure A.42: $D^0\pi_s$ mass distribution for the RS (left) and WS (right) Magnet Down D^0 (top) and $\bar{D}^0$ (bottom) candidates having decay time in the range [1,1.2]τ with fit projection overlaid, in 2016 data.

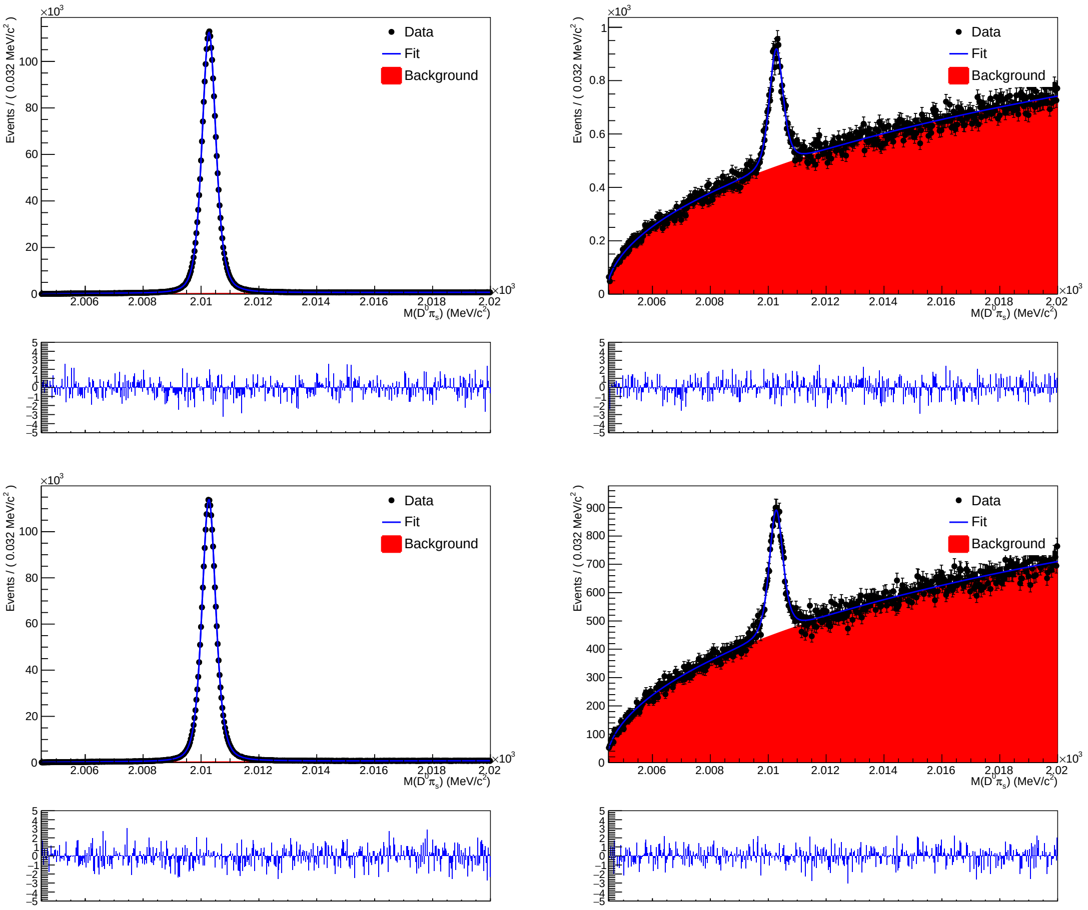

Figure A.43: $D^0\pi_s$ mass distribution for the RS (left) and WS (right) Magnet Down D^0 (top) and $\bar{D}^0$ (bottom) candidates having decay time in the range [1.2,1.35]τ with fit projection overlaid, in 2016 data.

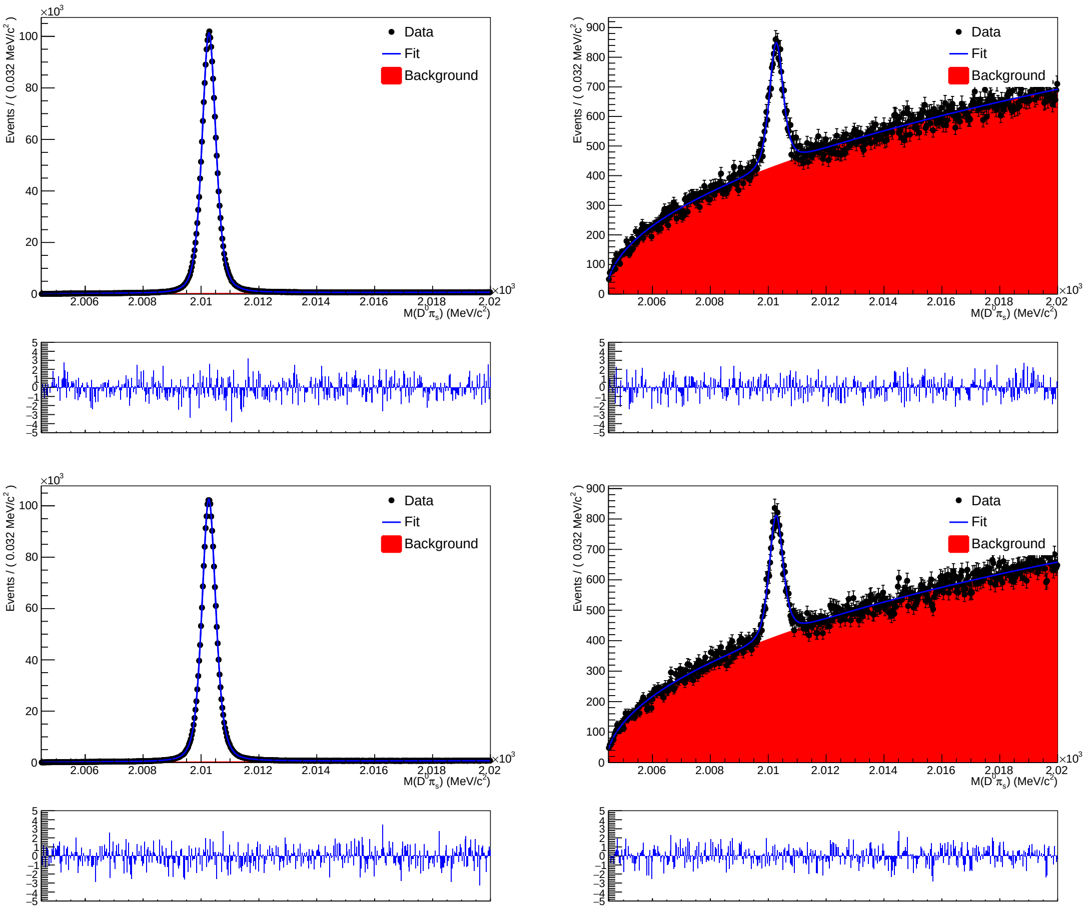

Figure A.44: $D^0\pi_s$ mass distribution for the RS (left) and WS (right) Magnet Down D^0 (top) and $\bar{D}^0$ (bottom) candidates having decay time in the range [1.35,1.5]τ with fit projection overlaid, in 2016 data.

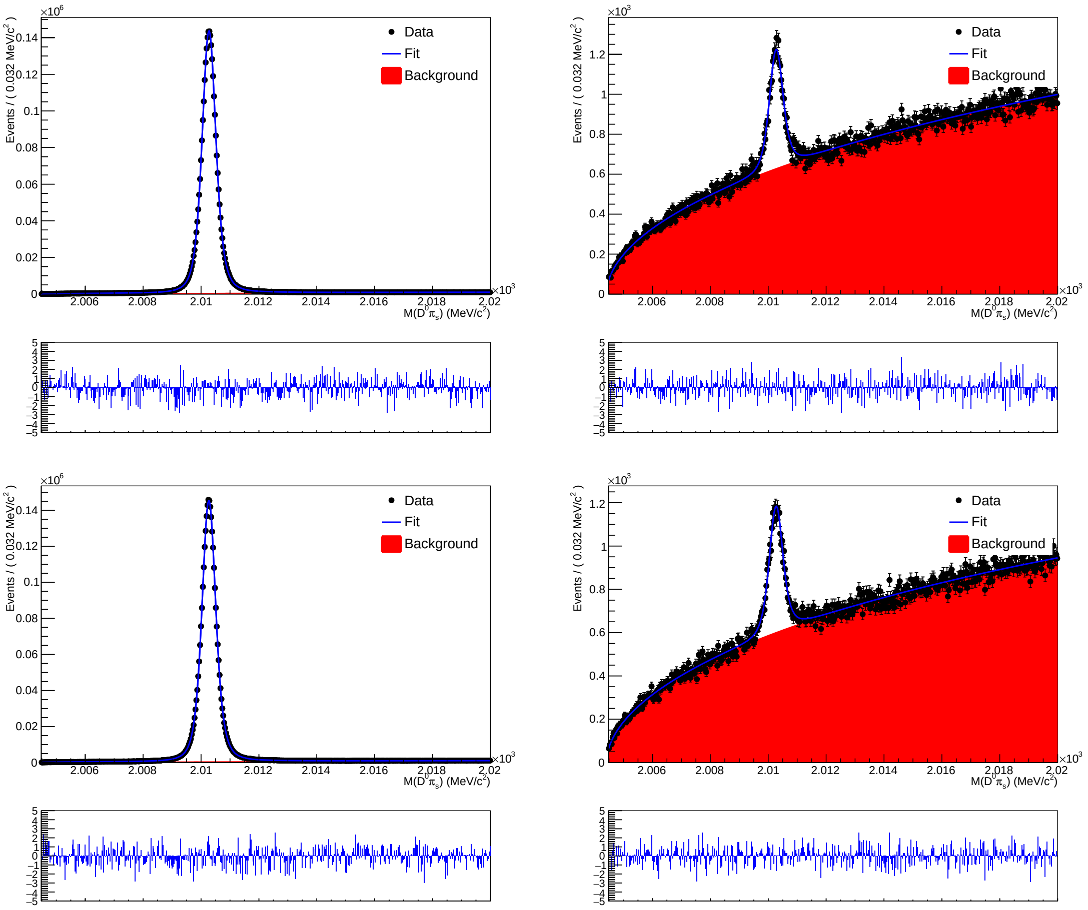

Figure A.45: $D^0\pi_s$ mass distribution for the RS (left) and WS (right) Magnet Down D^0 (top) and $\bar{D}^0$ (bottom) candidates having decay time in the range [1.5,1.75]τ with fit projection overlaid, in 2016 data.

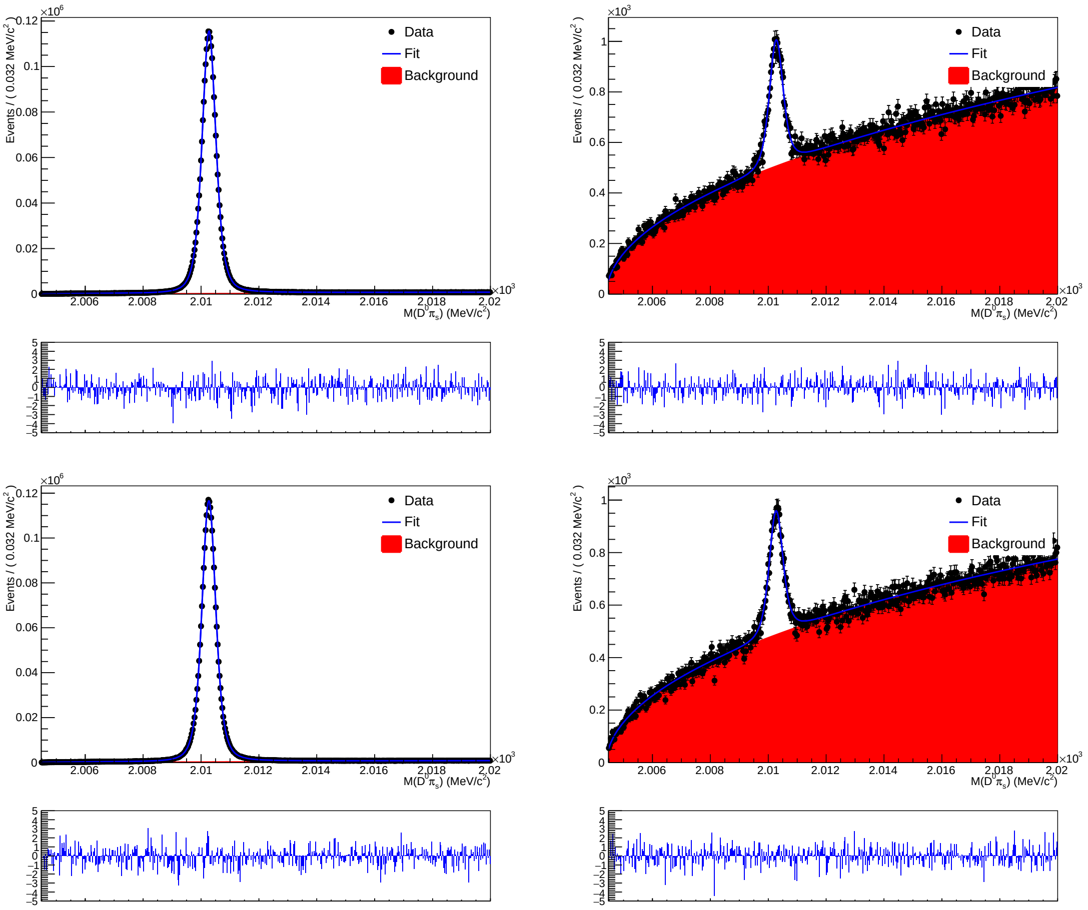

Figure A.46: $D^0\pi_s$ mass distribution for the RS (left) and WS (right) Magnet Down D^0 (top) and $\bar{D}^0$ (bottom) candidates having decay time in the range [1.75,2]τ with fit projection overlaid, in 2016 data.

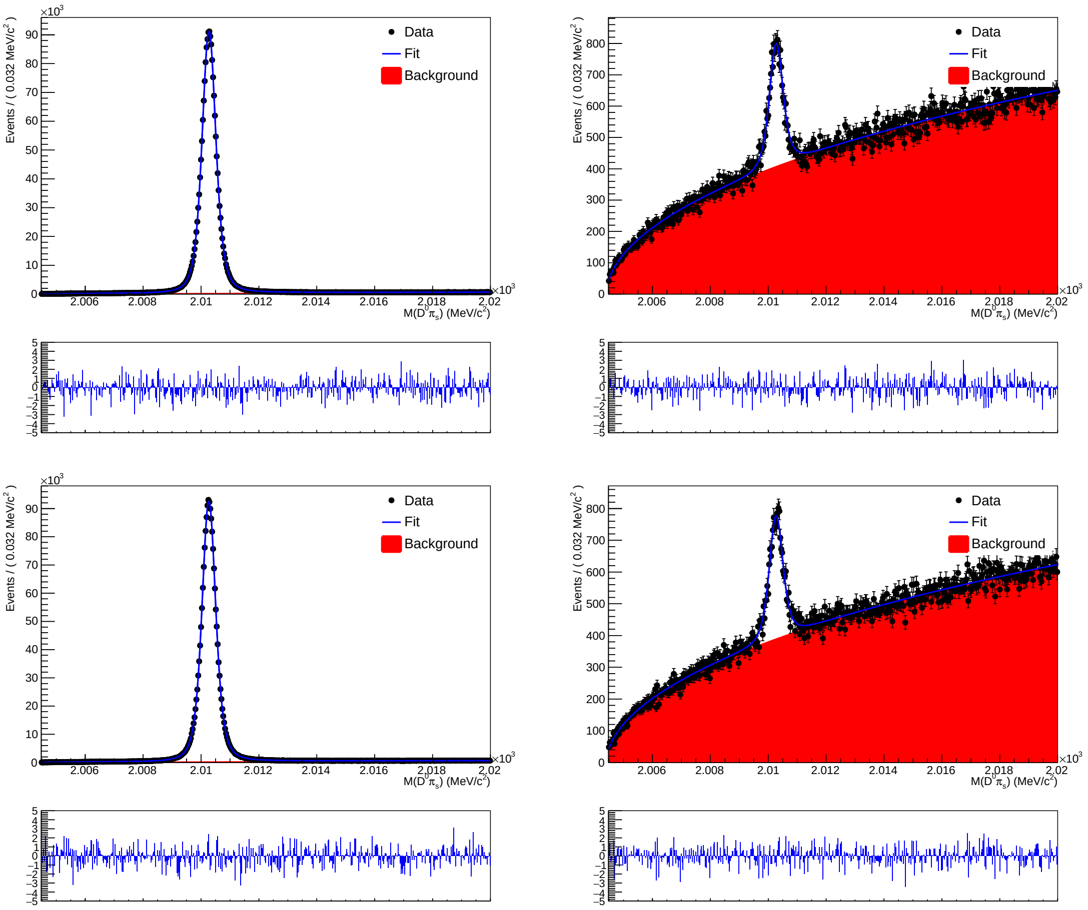

Figure A.47: $D^0\pi_s$ mass distribution for the RS (left) and WS (right) Magnet Down D^0 (top) and $\bar{D}^0$ (bottom) candidates having decay time in the range [2,2.25]τ with fit projection overlaid, in 2016 data.

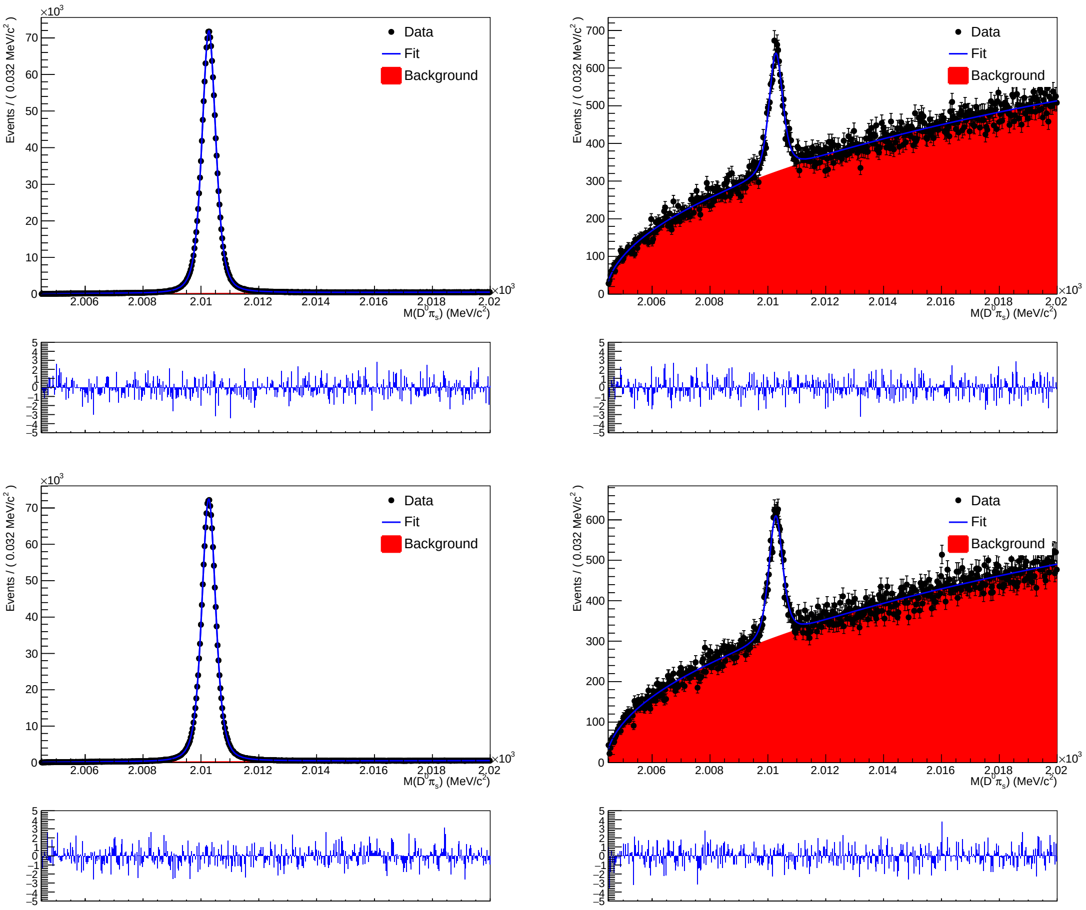

Figure A.48: $D^0\pi_s$ mass distribution for the RS (left) and WS (right) Magnet Down D^0 (top) and $\bar{D}^0$ (bottom) candidates having decay time in the range [2.25,2.5]τ with fit projection overlaid, in 2016 data.

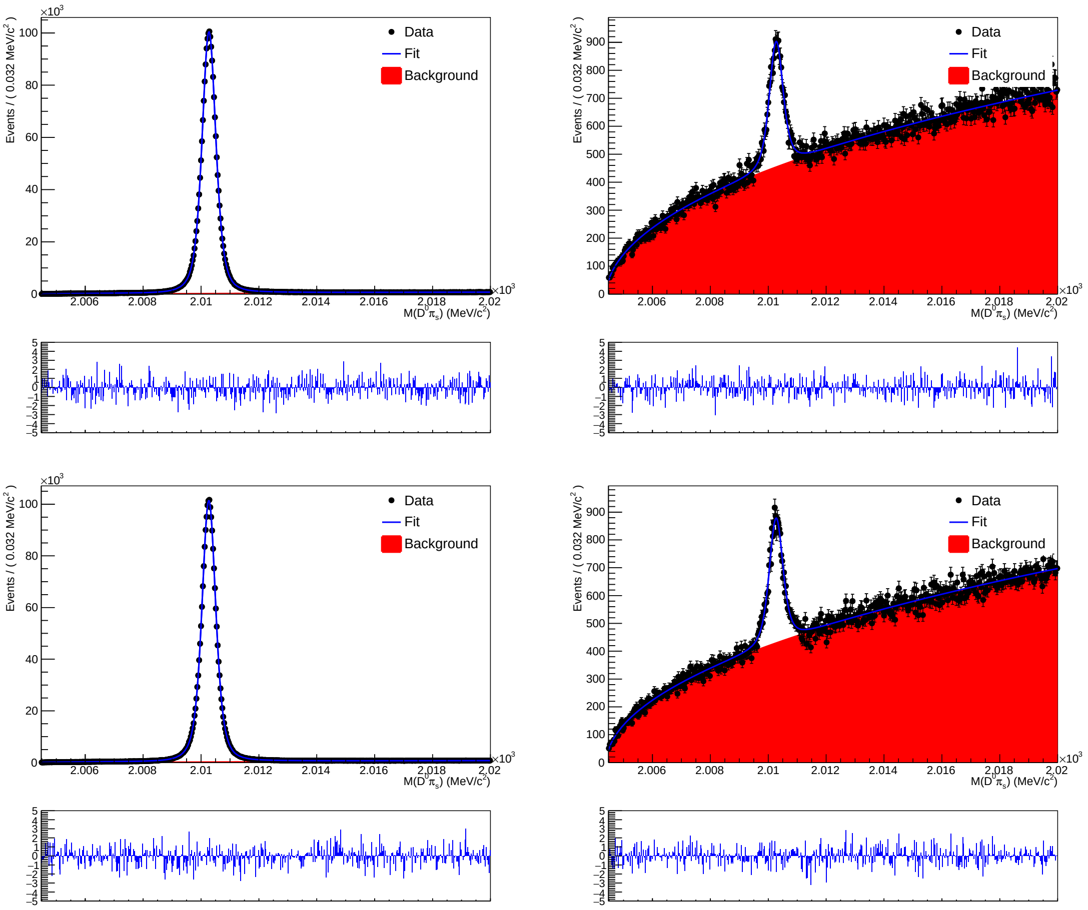

Figure A.49: $D^0\pi_s$ mass distribution for the RS (left) and WS (right) Magnet Down D^0 (top) and $\bar{D}^0$ (bottom) candidates having decay time in the range [2.5,3]τ with fit projection overlaid, in 2016 data.

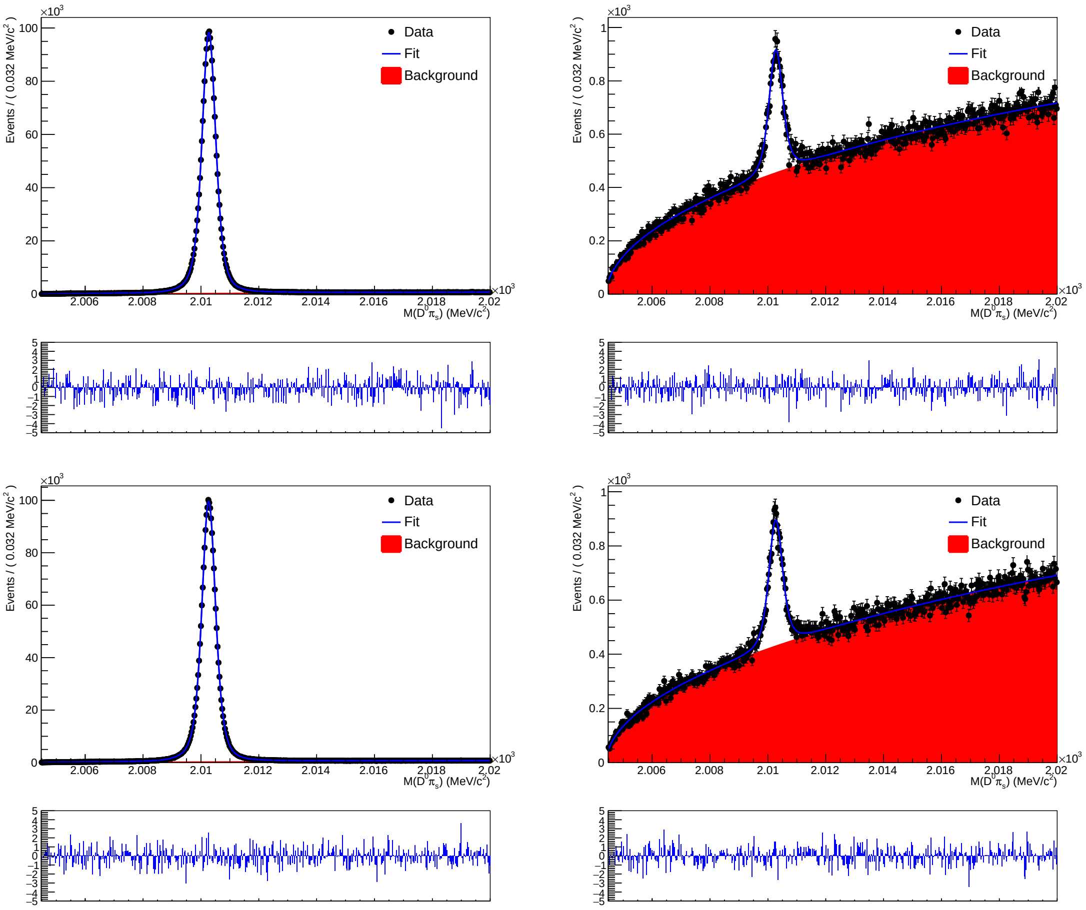

Figure A.50: $D^0\pi_s$ mass distribution for the RS (left) and WS (right) Magnet Down D^0 (top) and $\bar{D}^0$ (bottom) candidates having decay time in the range [3,4]τ with fit projection overlaid, in 2016 data.

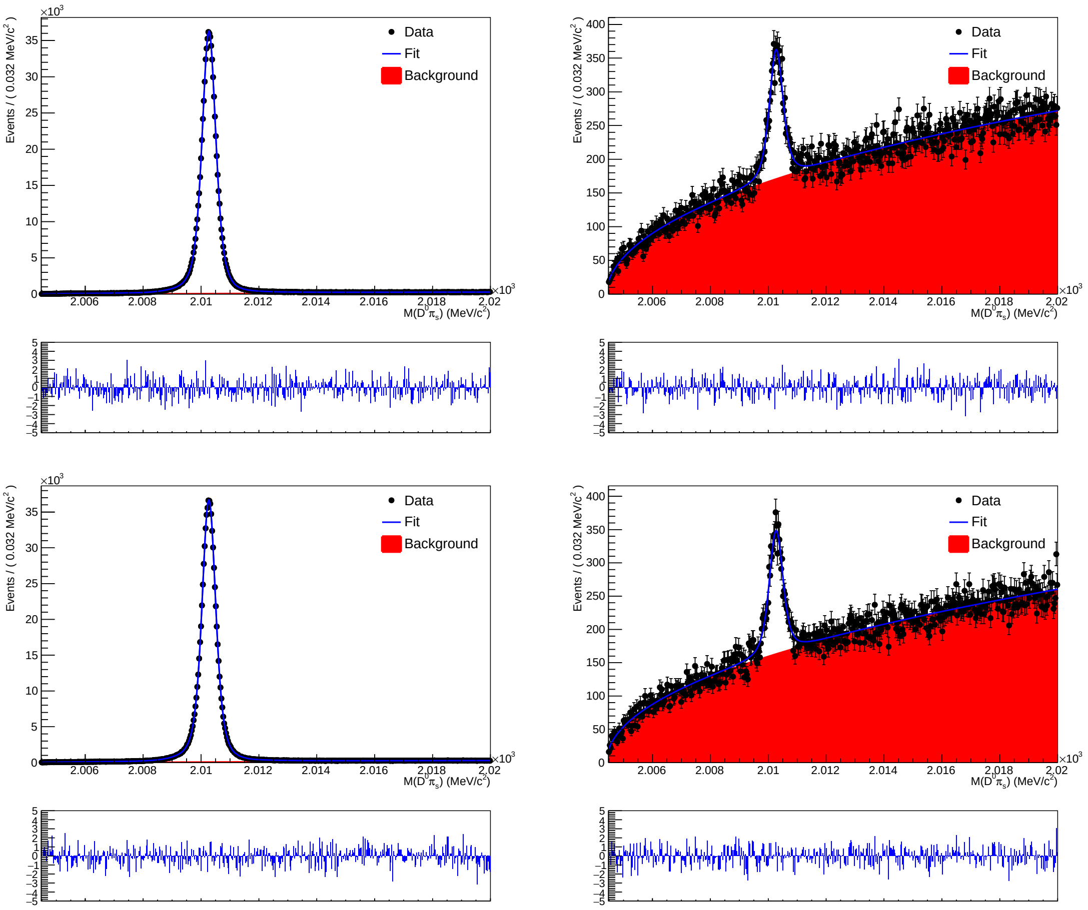

Figure A.51: $D^0\pi_s$ mass distribution for the RS (left) and WS (right) Magnet Down D^0 (top) and $\bar{D}^0$ (bottom) candidates having decay time in the range [4,5]τ with fit projection overlaid, in 2016 data.

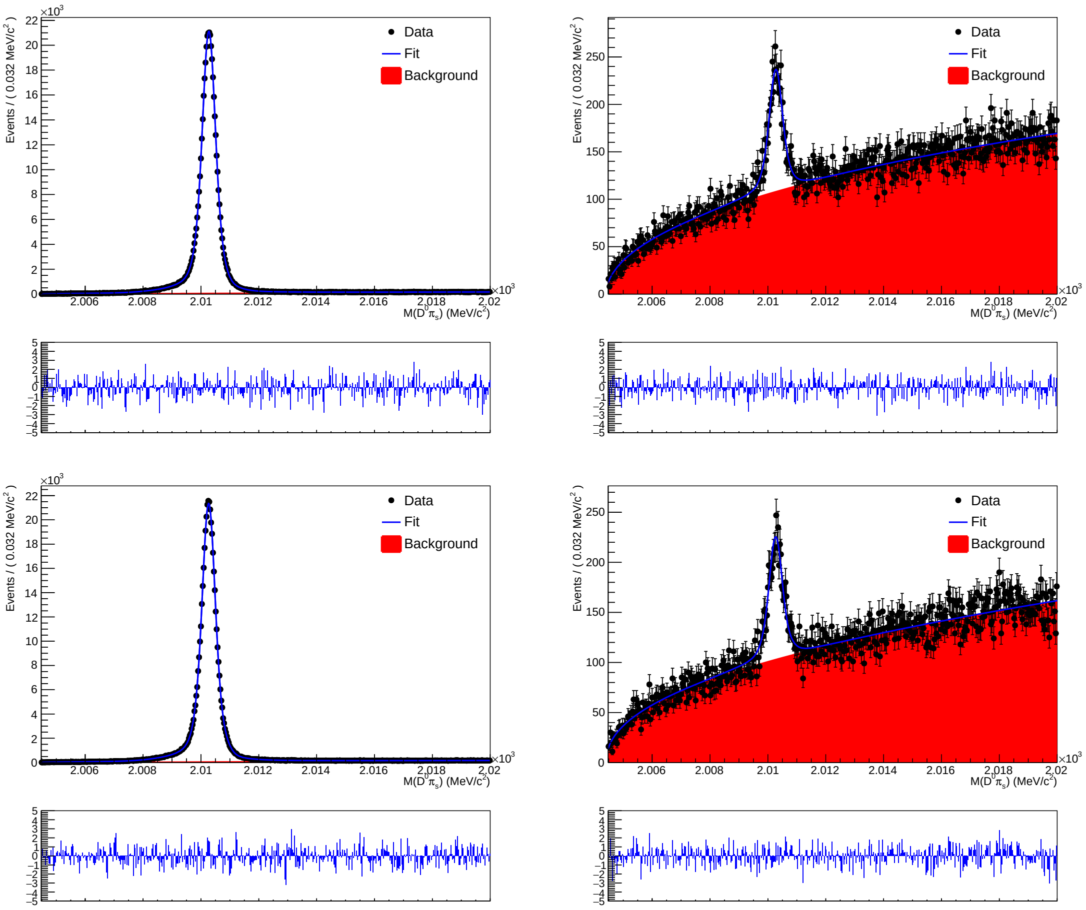

Figure A.52: $D^0\pi_s$ mass distribution for the RS (left) and WS (right) Magnet Down D^0 (top) and $\bar{D}^0$ (bottom) candidates having decay time in the range [5,20]τ with fit projection overlaid, in 2016 data.

Appendix B

Detailed fit results

No CP violation

Parameter	Value	χ^2 constraint
R_D (10^{-3})	3.553 ± 0.032	-
y' (10^{-3})	4.086 ± 0.551	-
x'^2 (10^{-3})	0.100 ± 0.028	-
$a_{K\pi}^{2015}$ (10^{-2})	0.75 ± 0.18	0.69 ± 0.23
$a_{K\pi}^{2016}$ (10^{-2})	0.89 ± 0.08	0.87 ± 0.10
b_0^{2015} (10^{-2})	0.00 ± 0.07	0.00 ± 0.07
b_1^{2015} (10^{-2})	0.03 ± 0.06	0.03 ± 0.06
b_2^{2015} (10^{-2})	0.01 ± 0.03	0.01 ± 0.03
b_3^{2015} (10^{-2})	0.04 ± 0.10	0.04 ± 0.10
b_4^{2015} (10^{-2})	0.17 ± 0.11	0.17 ± 0.11
b_5^{2015} (10^{-2})	1.03 ± 0.19	1.03 ± 0.19
b_6^{2015} (10^{-2})	2.07 ± 0.37	2.05 ± 0.37
b_7^{2015} (10^{-2})	2.73 ± 0.07	2.73 ± 0.07
b_8^{2015} (10^{-2})	3.43 ± 0.11	3.43 ± 0.11
b_9^{2015} (10^{-2})	3.92 ± 0.14	3.92 ± 0.14
b_{10}^{2015} (10^{-2})	5.04 ± 0.12	5.04 ± 0.12
b_{11}^{2015} (10^{-2})	6.21 ± 0.08	6.21 ± 0.08
b_{12}^{2015} (10^{-2})	8.41 ± 0.06	8.40 ± 0.06
b_0^{2016} (10^{-2})	0.00 ± 0.07	0.00 ± 0.07
b_1^{2016} (10^{-2})	0.62 ± 0.17	0.61 ± 0.17
b_2^{2016} (10^{-2})	1.25 ± 0.12	1.24 ± 0.12
b_3^{2016} (10^{-2})	1.60 ± 0.10	1.60 ± 0.10
b_4^{2016} (10^{-2})	2.14 ± 0.10	2.14 ± 0.10
b_5^{2016} (10^{-2})	2.31 ± 0.08	2.31 ± 0.08
b_6^{2016} (10^{-2})	2.63 ± 0.07	2.63 ± 0.07
b_7^{2016} (10^{-2})	3.16 ± 0.06	3.16 ± 0.06
b_8^{2016} (10^{-2})	3.28 ± 0.06	3.28 ± 0.06

Continued on next page

Continued from previous page

Parameter	Value	χ^2 constraint
b_9^{2016} (10^{-2})	5.40 ± 0.15	5.41 ± 0.15
b_{10}^{2016} (10^{-2})	6.15 ± 0.11	6.15 ± 0.11
b_{11}^{2016} (10^{-2})	6.86 ± 0.06	6.86 ± 0.06
b_{12}^{2016} (10^{-2})	9.38 ± 0.06	9.38 ± 0.06
p_0^{2015} (10^{-5})	1.1 ± 0.4	1.1 ± 0.4
p_1^{2015} (10^{-5})	1.3 ± 0.5	1.4 ± 0.5
p_2^{2015} (10^{-5})	1.2 ± 0.4	1.2 ± 0.4
p_3^{2015} (10^{-5})	1.1 ± 0.5	1.2 ± 0.5
p_4^{2015} (10^{-5})	1.0 ± 0.5	1.0 ± 0.5
p_5^{2015} (10^{-5})	1.8 ± 0.6	1.9 ± 0.6
p_6^{2015} (10^{-5})	1.1 ± 0.5	1.1 ± 0.5
p_7^{2015} (10^{-5})	1.2 ± 0.5	1.2 ± 0.5
p_8^{2015} (10^{-5})	0.6 ± 0.5	0.6 ± 0.5
p_9^{2015} (10^{-5})	1.2 ± 0.5	1.2 ± 0.5
p_{10}^{2015} (10^{-5})	1.2 ± 0.5	1.2 ± 0.5
p_{11}^{2015} (10^{-5})	0.7 ± 0.7	0.7 ± 0.7
p_{12}^{2015} (10^{-5})	1.7 ± 1.2	1.8 ± 1.2
p_0^{2016} (10^{-5})	1.3 ± 0.3	1.2 ± 0.3
p_1^{2016} (10^{-5})	0.9 ± 0.3	0.9 ± 0.3
p_2^{2016} (10^{-5})	0.8 ± 0.3	0.9 ± 0.3
p_3^{2016} (10^{-5})	1.1 ± 0.3	1.1 ± 0.3
p_4^{2016} (10^{-5})	1.0 ± 0.3	1.0 ± 0.3
p_5^{2016} (10^{-5})	1.3 ± 0.4	1.3 ± 0.4
p_6^{2016} (10^{-5})	0.8 ± 0.2	0.8 ± 0.2
p_7^{2016} (10^{-5})	0.6 ± 0.2	0.6 ± 0.2
p_8^{2016} (10^{-5})	1.0 ± 0.3	1.0 ± 0.3
p_9^{2016} (10^{-5})	1.3 ± 0.4	1.3 ± 0.4
p_{10}^{2016} (10^{-5})	1.0 ± 0.3	1.0 ± 0.3
p_{11}^{2016} (10^{-5})	1.6 ± 0.5	1.6 ± 0.5
p_{12}^{2016} (10^{-5})	0.9 ± 0.5	0.9 ± 0.5

No direct CP violation

Parameter	Value	χ^2 constraint
R_D (10^{-3})	3.553 ± 0.033	-
y'^{+} (10^{-3})	4.115 ± 0.595	-
x'^{2+} (10^{-3})	0.102 ± 0.033	-
y'^{-} (10^{-3})	4.056 ± 0.594	-
x'^{2-} (10^{-3})	0.099 ± 0.032	-
$a_{K\pi}^{2015}$ (10^{-2})	0.73 ± 0.19	0.69 ± 0.23
$a_{K\pi}^{2016}$ (10^{-2})	0.87 ± 0.10	0.87 ± 0.10
b_0^{2015} (10^{-2})	0.00 ± 0.07	0.00 ± 0.07
b_1^{2015} (10^{-2})	0.03 ± 0.06	0.03 ± 0.06
b_2^{2015} (10^{-2})	0.01 ± 0.03	0.01 ± 0.03
b_3^{2015} (10^{-2})	0.04 ± 0.10	0.04 ± 0.10
b_4^{2015} (10^{-2})	0.17 ± 0.11	0.17 ± 0.11
b_5^{2015} (10^{-2})	1.03 ± 0.19	1.03 ± 0.19
b_6^{2015} (10^{-2})	2.07 ± 0.37	2.05 ± 0.37
b_7^{2015} (10^{-2})	2.73 ± 0.07	2.73 ± 0.07
b_8^{2015} (10^{-2})	3.43 ± 0.11	3.43 ± 0.11
b_9^{2015} (10^{-2})	3.92 ± 0.14	3.92 ± 0.14
b_{10}^{2015} (10^{-2})	5.04 ± 0.12	5.04 ± 0.12
b_{11}^{2015} (10^{-2})	6.21 ± 0.08	6.21 ± 0.08
b_{12}^{2015} (10^{-2})	8.41 ± 0.06	8.40 ± 0.06
b_0^{2016} (10^{-2})	0.00 ± 0.07	0.00 ± 0.07
b_1^{2016} (10^{-2})	0.62 ± 0.17	0.61 ± 0.17
b_2^{2016} (10^{-2})	1.25 ± 0.12	1.24 ± 0.12
b_3^{2016} (10^{-2})	1.60 ± 0.10	1.60 ± 0.10
b_4^{2016} (10^{-2})	2.14 ± 0.10	2.14 ± 0.10
b_5^{2016} (10^{-2})	2.31 ± 0.08	2.31 ± 0.08
b_6^{2016} (10^{-2})	2.63 ± 0.07	2.63 ± 0.07
b_7^{2016} (10^{-2})	3.16 ± 0.06	3.16 ± 0.06
b_8^{2016} (10^{-2})	3.28 ± 0.06	3.28 ± 0.06
b_9^{2016} (10^{-2})	5.40 ± 0.15	5.41 ± 0.15
b_{10}^{2016} (10^{-2})	6.15 ± 0.11	6.15 ± 0.11
b_{11}^{2016} (10^{-2})	6.86 ± 0.06	6.86 ± 0.06
b_{12}^{2016} (10^{-2})	9.38 ± 0.06	9.38 ± 0.06

Continued on next page

Continued from previous page

Parameter	Value	χ^2 constraint
p_0^{2015} (10^{-5})	1.1 ± 0.4	1.1 ± 0.4
p_1^{2015} (10^{-5})	1.3 ± 0.5	1.4 ± 0.5
p_2^{2015} (10^{-5})	1.2 ± 0.4	1.2 ± 0.4
p_3^{2015} (10^{-5})	1.1 ± 0.5	1.2 ± 0.5
p_4^{2015} (10^{-5})	1.0 ± 0.5	1.0 ± 0.5
p_5^{2015} (10^{-5})	1.8 ± 0.6	1.9 ± 0.6
p_6^{2015} (10^{-5})	1.1 ± 0.5	1.1 ± 0.5
p_7^{2015} (10^{-5})	1.2 ± 0.5	1.2 ± 0.5
p_8^{2015} (10^{-5})	0.6 ± 0.5	0.6 ± 0.5
p_9^{2015} (10^{-5})	1.2 ± 0.5	1.2 ± 0.5
p_{10}^{2015} (10^{-5})	1.2 ± 0.5	1.2 ± 0.5
p_{11}^{2015} (10^{-5})	0.7 ± 0.7	0.7 ± 0.7
p_{12}^{2015} (10^{-5})	1.7 ± 1.2	1.8 ± 1.2
p_0^{2016} (10^{-5})	1.3 ± 0.3	1.2 ± 0.3
p_1^{2016} (10^{-5})	0.9 ± 0.3	0.9 ± 0.3
p_2^{2016} (10^{-5})	0.8 ± 0.3	0.9 ± 0.3
p_3^{2016} (10^{-5})	1.1 ± 0.3	1.1 ± 0.3
p_4^{2016} (10^{-5})	1.0 ± 0.3	1.0 ± 0.3
p_5^{2016} (10^{-5})	1.3 ± 0.4	1.3 ± 0.4
p_6^{2016} (10^{-5})	0.8 ± 0.2	0.8 ± 0.2
p_7^{2016} (10^{-5})	0.6 ± 0.2	0.6 ± 0.2
p_8^{2016} (10^{-5})	1.0 ± 0.3	1.0 ± 0.3
p_9^{2016} (10^{-5})	1.3 ± 0.4	1.3 ± 0.4
p_{10}^{2016} (10^{-5})	1.0 ± 0.3	1.0 ± 0.3
p_{11}^{2016} (10^{-5})	1.6 ± 0.5	1.6 ± 0.5
p_{12}^{2016} (10^{-5})	0.9 ± 0.5	0.9 ± 0.5

CP violation allowed

Parameter	Value	χ^2 constraint
R_D^+ (10^{-3})	3.566 ± 0.046	-
R_D^- (10^{-3})	3.541 ± 0.046	-
y'^+ (10^{-3})	3.919 ± 0.777	-
x'^{2+} (10^{-3})	0.111 ± 0.040	-
y'^- (10^{-3})	4.252 ± 0.779	-
x'^{2-} (10^{-3})	0.090 ± 0.040	-
$a_{K\pi}^{2015}$ (10^{-2})	0.72 ± 0.19	0.69 ± 0.23
$a_{K\pi}^{2016}$ (10^{-2})	0.86 ± 0.10	0.87 ± 0.10
b_0^{2015} (10^{-2})	0.00 ± 0.07	0.00 ± 0.07
b_1^{2015} (10^{-2})	0.03 ± 0.06	0.03 ± 0.06
b_2^{2015} (10^{-2})	0.01 ± 0.03	0.01 ± 0.03
b_3^{2015} (10^{-2})	0.04 ± 0.10	0.04 ± 0.10
b_4^{2015} (10^{-2})	0.17 ± 0.11	0.17 ± 0.11
b_5^{2015} (10^{-2})	1.03 ± 0.19	1.03 ± 0.19
b_6^{2015} (10^{-2})	2.07 ± 0.37	2.05 ± 0.37
b_7^{2015} (10^{-2})	2.73 ± 0.07	2.73 ± 0.07
b_8^{2015} (10^{-2})	3.43 ± 0.11	3.43 ± 0.11
b_9^{2015} (10^{-2})	3.92 ± 0.14	3.92 ± 0.14
b_{10}^{2015} (10^{-2})	5.04 ± 0.12	5.04 ± 0.12
b_{11}^{2015} (10^{-2})	6.21 ± 0.08	6.21 ± 0.08
b_{12}^{2015} (10^{-2})	8.41 ± 0.06	8.40 ± 0.06
b_0^{2016} (10^{-2})	0.00 ± 0.07	0.00 ± 0.07
b_1^{2016} (10^{-2})	0.61 ± 0.17	0.61 ± 0.17
b_2^{2016} (10^{-2})	1.25 ± 0.12	1.24 ± 0.12
b_3^{2016} (10^{-2})	1.60 ± 0.10	1.60 ± 0.10
b_4^{2016} (10^{-2})	2.14 ± 0.10	2.14 ± 0.10
b_5^{2016} (10^{-2})	2.31 ± 0.08	2.31 ± 0.08
b_6^{2016} (10^{-2})	2.63 ± 0.07	2.63 ± 0.07
b_7^{2016} (10^{-2})	3.16 ± 0.06	3.16 ± 0.06
b_8^{2016} (10^{-2})	3.28 ± 0.06	3.28 ± 0.06
b_9^{2016} (10^{-2})	5.40 ± 0.15	5.41 ± 0.15
b_{10}^{2016} (10^{-2})	6.15 ± 0.11	6.15 ± 0.11
b_{11}^{2016} (10^{-2})	6.86 ± 0.06	6.86 ± 0.06
b_{12}^{2016} (10^{-2})	9.38 ± 0.06	9.38 ± 0.06

Continued on next page

Continued from previous page

Parameter	Value	χ^2 constraint
p_0^{2015} (10^{-5})	1.1 ± 0.4	1.1 ± 0.4
p_1^{2015} (10^{-5})	1.3 ± 0.5	1.4 ± 0.5
p_2^{2015} (10^{-5})	1.2 ± 0.4	1.2 ± 0.4
p_3^{2015} (10^{-5})	1.1 ± 0.5	1.2 ± 0.5
p_4^{2015} (10^{-5})	1.0 ± 0.5	1.0 ± 0.5
p_5^{2015} (10^{-5})	1.8 ± 0.6	1.9 ± 0.6
p_6^{2015} (10^{-5})	1.1 ± 0.5	1.1 ± 0.5
p_7^{2015} (10^{-5})	1.2 ± 0.5	1.2 ± 0.5
p_8^{2015} (10^{-5})	0.6 ± 0.5	0.6 ± 0.5
p_9^{2015} (10^{-5})	1.2 ± 0.5	1.2 ± 0.5
p_{10}^{2015} (10^{-5})	1.2 ± 0.5	1.2 ± 0.5
p_{11}^{2015} (10^{-5})	0.7 ± 0.7	0.7 ± 0.7
p_{12}^{2015} (10^{-5})	1.7 ± 1.2	1.8 ± 1.2
p_0^{2016} (10^{-5})	1.3 ± 0.3	1.2 ± 0.3
p_1^{2016} (10^{-5})	0.9 ± 0.3	0.9 ± 0.3
p_2^{2016} (10^{-5})	0.8 ± 0.3	0.9 ± 0.3
p_3^{2016} (10^{-5})	1.1 ± 0.3	1.1 ± 0.3
p_4^{2016} (10^{-5})	1.0 ± 0.3	1.0 ± 0.3
p_5^{2016} (10^{-5})	1.3 ± 0.4	1.3 ± 0.4
p_6^{2016} (10^{-5})	0.8 ± 0.2	0.8 ± 0.2
p_7^{2016} (10^{-5})	0.6 ± 0.2	0.6 ± 0.2
p_8^{2016} (10^{-5})	1.0 ± 0.3	1.0 ± 0.3
p_9^{2016} (10^{-5})	1.3 ± 0.4	1.3 ± 0.4
p_{10}^{2016} (10^{-5})	1.0 ± 0.3	1.0 ± 0.3
p_{11}^{2016} (10^{-5})	1.6 ± 0.5	1.6 ± 0.5
p_{12}^{2016} (10^{-5})	0.9 ± 0.5	0.9 ± 0.5

Bibliography

[1] C. S. Wu *et al.*, *Experimental Test of Parity Conservation in Beta Decay*, Phys. Rev. **105** (1957) 1413 .

[2] R. L. Garwin, L. M. Lederman, and M. Weinrich, *Observations of the Failure of Conservation of Parity and Charge Conjugation in Meson Decays: the Magnetic Moment of the Free Muon*, Phys. Rev. **105** (1957) 1415.

[3] T. D. Lee and C. N. Yang, *Question of Parity Conservation in Weak Interactions*, Phys. Rev. **104** (1956) 254.

[4] J. H. Christenson, J. W. Cronin, V. L. Fitch, and R. Turlay, *Evidence for the* 2π *Decay of the* K_2^0 *Meson*, Phys. Rev. Lett. **13** (1964) 138.

[5] S. L. Glashow, *Partial Symmetries of Weak Interactions*, Nucl. Phys. **22** (1961) 579.

[6] S. Weinberg, *A Model of Leptons*, Phys. Rev. Lett. **19** (1967) 1264.

[7] A. Salam, *Weak and Electromagnetic Interactions*, in *Elementary particle theory* (N. Svartholm, ed.), pp. 367–377, Almquist & Wiksell, 1968.

[8] S. L. Glashow, J. Iliopoulos, and L. Maiani, *Weak Interactions with Lepton-Hadron Symmetry*, Phys. Rev. D **2** (1970) 1285.

[9] M. Kobayashi and T. Maskawa, *CP-Violation in the Renormalizable Theory of Weak Interaction*, Progress of Theoretical Physics **49** (1973), no. 2 652, `arXiv:http://ptp.oxfordjournals.org/content/49/2/652.full.pdf+html`.

[10] S. W. Herb *et al.*, *Observation of a Dimuon Resonance at 9.5 GeV in 400-GeV Proton-Nucleus Collisions*, Phys. Rev. Lett. **39** (1977) 252.

[11] CDF collaboration, F. Abe *et al.*, *Observation of top quark production in* $p\bar{p}$ *collisions*, Phys. Rev. Lett. **74** (1995) 2626, `arXiv:hep-ex/9503002`.

[12] D0 collaboration, S. Abachi *et al.*, *Observation of the top quark*, Phys. Rev. Lett. **74** (1995) 2632, `arXiv:hep-ex/9503003`.

[13] NA48 collaboration, V. Fanti *et al.*, *A New measurement of direct CP violation in two pion decays of the neutral kaon*, Phys. Lett. **B465** (1999) 335, `arXiv:hep-ex/9909022`.

[14] KTeV collaboration, A. Alavi-Harati *et al.*, *Observation of direct CP violation in $K_{S,L} \to \pi\pi$ decays*, Phys. Rev. Lett. **83** (1999) 22, `arXiv:hep-ex/9905060`.

[15] BaBar collaboration, B. Aubert *et al.*, *Observation of CP violation in the B^0 meson system*, Phys. Rev. Lett. **87** (2001) 091801, `arXiv:hep-ex/0107013`.

[16] Belle collaboration, K. Abe *et al.*, *Observation of large CP violation in the neutral B meson system*, Phys. Rev. Lett. **87** (2001) 091802, `arXiv:hep-ex/0107061`.

[17] A. D. Sakharov, *Violation of CP Invariance, C Asymmetry, and Baryon Asymmetry of the Universe*, Pisma Zh. Eksp. Teor. Fiz. **5** (1967) 32, [Usp. Fiz. Nauk161,61(1991)].

[18] N. Cabibbo, *Unitary Symmetry and Leptonic Decays*, Phys. Rev. Lett. **10** (1963) 531.

[19] C. Jarlskog, *Commutator of the Quark Mass Matrices in the Standard Electroweak Model and a Measure of Maximal* CP *Nonconservation*, Phys. Rev. Lett. **55** (1985) 1039.

[20] Particle Data Group, C. Patrignani *et al.*, *Review of Particle Physics*, Chin. Phys. **C40** (2016), no. 10 100001.

[21] L. Wolfenstein, *Parametrization of the Kobayashi-Maskawa Matrix*, Phys. Rev. Lett. **51** (1983) 1945.

[22] UTfit, M. Bona *et al.*, *The Unitarity Triangle Fit in the Standard Model and Hadronic Parameters from Lattice QCD: A Reappraisal after the Measurements of Δm_s and $BR(B \to \tau\nu_\tau)$*, JHEP **10** (2006) 081, `arXiv:hep-ph/0606167`.

[23] M. Gell-Mann and A. Pais, *Behavior of Neutral Particles under Charge Conjugation*, Phys. Rev. **97** (1955) 1387.

[24] M. Gersabeck, *Introduction to Charm Physics*, PoS **FWNP** (2015) 001, `arXiv:1503.00032`.

[25] K. Lande *et al.*, *Observation of Long-Lived Neutral V Particles*, Phys. Rev. **103** (1956) 1901.

[26] ARGUS collaboratio, H. Albrecht *et al.*, *Observation of $B^0 - \bar{B}^0$ Mixing*, Phys. Lett. **B192** (1987) 245.

[27] CDF collaboration, A. Abulencia *et al.*, *Observation of $B_s^0 - \overline{B}_s^0$ Oscillations*, Phys. Rev. Lett. **97** (2006) 242003.

[28] Belle collaboration, Starič and others, *Evidence for D^0–$\overline{D}^0$ Mixing*, Phys. Rev. Lett. **98** (2007) 211803.

[29] BaBar collaboration, B. Aubert *et al.*, *Evidence for D^0–$\overline{D}^0$ mixing*, Phys. Rev. Lett. **98** (2007) 211802, `arXiv:hep-ex/0703020`.

[30] CDF collaboration, T. Aaltonen *et al.*, *Evidence for* $D^0-\overline{D}^0$ *Mixing Using the CDF II Detector*, Phys. Rev. Lett. **100** (2008) 121802.

[31] LHCb collaboration, R. Aaij *et al.*, *Observation of* D^0–$\overline{D}^0$ *Oscillations*, Phys. Rev. Lett. **110** (2013) 101802.

[32] C. A. Chavez, R. F. Cowan, and W. S. Lockman, *Charm meson mixing: an experimental review*, Int. J. Mod. Phys. **A 27** (2012) 1230019, `arXiv:1209.5806`.

[33] Y. Nir, *CP violation in meson decays*, in *Particle physics beyond the standard model. Proceedings, Summer School on Theoretical Physics, 84th Session, Les Houches, France, August 1-26, 2005*, pp. 79–145, 2005. `arXiv:hep-ph/0510413`. [79(2005)].

[34] A. L. Kagan and M. D. Sokoloff, *On indirect CP violation and implications for* D^0–$\overline{D}^0$ *and* B_s^0–$\overline{B}_s^0$ *mixing*, Phys. Rev. **D 80** (2009) 076008, `arXiv:0907.3917`.

[35] Y. Amhis *et al.*, *Averages of b-hadron, c-hadron, and* τ*-lepton properties as of summer 2016*, `arXiv:1612.07233`, Updated results at: `http://www.slac.stanford.edu/xorg/hfag/`.

[36] LHCb collaboration, A. A. Alves Jr. *et al.*, *The LHCb detector at the LHC*, JINST **3** (2008) S08005.

[37] LHCb collaboration, R. Aaij *et al.*, *Measurement of* D^0–$\overline{D}^0$ *mixing parameters and search for CP violation using* $D^0 \to K^+\pi^-$ *decays*, Phys. Rev. Lett. **111** (2013) 251801, `arXiv:1309.6534`.

[38] LHCb, R. Aaij *et al.*, *Measurements of charm mixing and CP violation using* $D^0 \to K^\pm\pi^\mp$ *decays*, `arXiv:1611.06143`.

[39] A. Hoecker *et al.*, *TMVA: Toolkit for Multivariate Data Analysis*, PoS **ACAT** (2007) 040, `arXiv:physics/0703039`.

[40] N. L. Johnson, *Systems of frequency curves generated by methods of translation*, Biometrika **36** (1949) 149.

[41] LHCb collaboration, R. Aaij *et al.*, *Observation of* D^0–$\overline{D}^0$ *oscillations*, Phys. Rev. Lett. **110** (2013) 101802, `arXiv:1211.1230`.

[42] H. Gordon, R. W. Lambert, J. van Tilburg, and M. Vesterinen, *A Measurement of the* $K\pi$ *Detection Asymmetry*, Tech. Rep. LHCb-INT-2012-027. CERN-LHCb-INT-2012-027, CERN, Geneva, Feb, 2013.

[43] Particle Data Group, K. A. Olive *et al.*, *Review of particle physics*, Chin. Phys. **C38** (2014) 090001, and 2015 update.

[44] Belle, T. Peng *et al.*, *Measurement of* $D^0-\overline{D}^0$ *mixing and search for indirect CP violation using* $D^0 \to K_S^0\pi^+\pi^-$ *decays*, Phys. Rev. **D89** (2014), no. 9 091103, `arXiv:1404.2412`.

[45] BaBar collaboration, P. del Amo Sanchez *et al.*, *Measurement of* D^0–$\overline{D}^0$ *mixing parameters using* $D^0 \to K^0_\mathrm{S}\pi^+\pi^-$ *and* $D^0 \to K^0_\mathrm{S}K^+K^-$ *decays*, Phys. Rev. Lett. **105** (2010) 081803, `arXiv:1004.5053`.

[46] CLEO collaboration, D. M. Asner *et al.*, *Updated measurement of the strong phase in* $D^0 \to K^+\pi^-$ *decay using quantum correlations in* $e^+e^- \to D^0\overline{D}^0$ *at CLEO*, Phys. Rev. **D 86** (2012) 112001, `arXiv:1210.0939`.

Acknowledgements

I sincerely thank Angelo Carbone and Angelo Di Canto for their patience and for having given me insights into this complex but engaging discipline. Without their teaching, the course of my studies would have been incomplete. I also thank Federico and Fabio for their thoughts as well and closeness during this period. Above all, I am grateful to my parents for their essential support during this five years of studies.